TECHNISCHE UNIVERSITÄT WIEN
Vienna University of Technology

Dissertation

„Alternative production and analysis of porous metal supports for Solid Oxide Fuel Cells"

durchgeführt zum Zweck der Erlangung des akademischen Grades eines Doktors der technischen Wissenschaften unter der Leitung von

Univ.Prof. Dipl.-Ing. Dr.techn. Herbert Danninger
E 164
Institut für Chemische Technologien und Analytik

Eingereicht an der Technischen Universität Wien
Fakultät für Technische Chemie

Harald Gschiel
Matr.Nr.: 0326197
Johann Straußgasse 23
7210 Mattersburg

Wien, am 16.04.2015

Acknowledgement

First of all I would to thank my supervisor Univ.Prof. Dr. Herbert Danninger for his support throughout the past years and guiding me through difficult times of this work. He always had an open door and ear for all kind of problems I had to deal with.

I would also like to thank Univ.Ass. Dr. Christian Gierl-Mayer for his helpful discussions and moreover, for helping me, when I could not see the light at the end of the tunnel.

I have to thank Höganäs AB, especially Per-Olof Larsson and Hilmar Vidarsson for the financial support of this project, for the fruitful discussions and the possibility to work at on a very interesting topic.

Special thanks to Prof. Jose Manuel Torralba and his team at the UC3M in Leganes for letting me work in his laboratories. I really did enjoy my stay in Spain due to all the helpful and friendly colleagues. It was a great experience where I personally did learn a lot.

Furthermore I would like to thank Dr. Erich Halwax and Dr. Klaudia Hradil for the XRD measurements, Dr. Hannes Zbiral for the XRF measurements and Dr. Thomas Konegger for his support with the FIJI software.

Many thanks go to the different working groups at my university (PM, SMET, HLK, BUV). I really enjoyed working there the past years, many of them are considered as my friends and not as colleagues.

Finally I would like to thank my family, especially my parents. They have always been patient and supportive.

Kurzfassung

Brennstoffzellen konvertieren hocheffizient und schadstoffarm chemische Energie in elektrische Energie und werden entweder nach ihrer Betriebstemperatur oder nach dem Elektrolyten eingeteilt. Im Fall der Festoxidbrennstoffzelle (Solid Oxide Fuel Cell, SOFC) besteht der Elektrolyt aus einem festen, dichtem Metalloxid, zumeist yttriumstabilisiertes Zirkonoxid. Die Anode ist üblicherweise ein Ni-ZrO_2 Komposit und die Kathode ein mit Strontium dotiertes $LaMnO_3$.

Ein Brennstoffzellen-Heizgerät kann sowohl Energie als auch Wärme liefern, wobei hier mehrere Brennstoffzellen zu einem Zellstapel aufeinandergeschichtet sind. Einzelne Brennstoffzellen werden in diesem Zellstapel durch einen metallischen Stromsammler unterteilt. Für die mechanische Stabilität der Zelle können entweder der Elektrolyt oder die Elektroden sorgen. Eine Alternative sind metallgestützte Brennstoffzellen, hier werden auf einem ferritischen Metallträger die Funktionsschichten der Zelle dünnschichtig abgeschieden. Der Vorteil dieses metallgestützten Konzepts sind bessere mechanische Eigenschaften (höhere Toleranz gegenüber wiederholten Redox-Zyklen) und Kostenminimierung bei der Fertigung. Üblicherweise wird das Metallsubstrat mittels Folienguss hergestellt und muss Anforderungen wie z.B. offene Porosität für Gasdurchlässigkeit und Oxidationswiderstand in einer H_2/H_2O-Atmosphäre bei einer Temperatur von ca. 900°C erfüllen. Ein weiterer Punkt ist das Angleichen des thermischen Expansionskoeffizienten an den der keramischen Bauteilen der Zelle und, zur einfacheren Herstellung, die Angleichung des Sinterschwundes an den der Keramiken, was einer Schwindung von 15-20% beim Sintervorgang entspricht.

Das Ziel der vorliegenden Arbeit war die Prüfung alternativer pulvermetallurgische Methoden wie Pressen und Sintern, Schüttsintern oder Spritzgießen für die Herstellung eines solchen Metallsubstrats. Die erhaltenen Proben wurden anschließend charakterisiert, wobei der Fokus besonders auf Schwindung, Dichte und Porosität gelegt wurde. Ein wesentliches Ziel war die erwähnte Anpassung des Sinterschwundes an den der keramischen Funktionsschichten, damit Co-Sintern bei der Herstellung möglich wird. Es wurden sowohl ferritische Fe-Cr-Werkstoffe als auch, als Referenz, eine austenitische Fe-Cr-Ni-Variante untersucht, obwohl für Brennstoffzellen eher nur Ni-freie Stähle in Frage kommen.

Die durch einfaches (uniaxiales) Pressen und Sintern hergestellten Proben hatten zu wenig Schwindung. Bei den Schüttsinterungen zeigte sich, dass die Schwindung anisotrop ist und es eine deutliche Differenz beim Schwund in Richtung der Schwerkraft und in den anderen Raumrichtungen gibt. Zusätzlich macht es auch einen Unterschied, ob das Pulver vor dem Sintern nur in die Form vorsichtig geschüttet oder zusätzlich geklopft wird. Die Schwindung des eingerüttelten Pulvers ist deutlich niedriger als die des nur geschütteten Pulvers.

Die besten Resultate konnten beim Metallpulverspritzguss erzielt werden. Es wurde ein Bindersystem aus Polyethylen, Paraffinwachs und Stearinsäure gewählt, und die Beladung betrug 45, 50 und 55 vol%. Es konnte hohe Schwindung von etwa 13% erreicht werden, und die erhaltene Restporosität konnte über die Beladung des Pulver-Binder-Gemisches, d.h. den Pulvergehalt, eingestellt werden. Eine Probe mit 45 vol% Beladung hatte eine Porosität von

24,6% (gemessen mit Hg-Porosimetrie), die Poren waren fein verteilt, und es waren keine Agglomerationen sichtbar. Dies konnte unabhängig vom Grundmaterial sowohl für die ferritischen Stähle als auch für die austenitische Variante festgestellt werden. D.h. der Pulverspritzguss, der in der industriellen Praxis normalerweise für die Fertigung volldichter, komplex geformter Kleinbauteile eingesetzt wird, scheint auch für die Fertigung von hochporösen Komponenten mit definierter Gesamtporosität und Porengeometrie gut geeignet zu sein.

Ein potentiell kritischer Themenbereich konnte durch Thermische Analyse identifiziert werden: DTA-TG-Messungen in feuchtem Wasserstoff, wie er an der Anode von Brennstoffzellen vorkommt, zeigten markante Sauerstoffaufnahme, d.h. die Beständigkeit dieser porösen Träger unter den Betriebsbedingungen von Hochtemperatur-Brennstoffzellen scheint zumindest nicht von vornherein gesichert zu sein; hier sind weitere Untersuchungen erforderlich.

Zusammengefasst kann gesagt werden, dass für die Fertigung des metallischen Trägersubstrats für Sold Oxide Fuel Cells der Metallpulverspritzguss eine realistische Alternative zum Siebdruck zu sein scheint. Ob er auch kommerziell gegen den schon gut etablierten Folienguss konkurrenzfähig ist, bleibt abzuwarten.

Abstract

Fuel cells in general convert chemical energy into electrical energy with very high efficiency and low emission and are classified commonly by the operating temperature or the electrolyte. In case of the Solid Oxide Fuel Cell (SOFC) the electrolyte is made of a solid, nonporous metal oxide, usually yttrium stabilized zirconia. Typically, the anode is a Ni-ZrO_2-cermet and the cathode is Sr-doped $LaMnO_3$.

The SOFC has the highest efficiency in combined heat and power units, where the SOFC is not a single cell anymore; it is a so-called fuel cell "stack", where the interconnector separates the single cells from each other. In order to have mechanical stability in a fuel cell, the single cells can be supported either by the electrolyte or the electrode (anode or cathode). An alternative are porous metal supported cells, where on top of the ferritic FeCr support a thin film cell is deposited. The advantages of this metal supported cell design are better mechanical properties (higher tolerance to thermal cycling) and cost reduction, since the expensive ceramics can be limited to the functional layers. Usually, this FeCr support is manufactured by tape casting and has to fulfil various requirements such as open porosity for gas permeability, oxidation resistance in a H_2/H_2O atmosphere at about 900°C and match of the CTE with the ceramic parts of the cell. For easier manufacturing of the SOFC, to enable co-sintering of support and functional ceramic layers, shrinkage of the support during sintering in the range of that of the ceramics, i.e. about 15-20%, is required.

This work was focused on producing these metal supports by alternative powder metallurgical techniques such as the press-and-sinter route, gravity sintering or metal injection molding. The samples have been characterized with special regard to shrinkage, density and porosity. A major target was adjusting the shrinkage to that of the ceramic functional layers, to enable co-sintering. Both ferritic, Fe-Cr type, steel powder grades as well as, as a reference, an austenitic Fe-Cr-Ni grade were used, although for SOFCs, Ni-free steels are preferred.

The uniaxial pressing and sintering experiments resulted in insufficient shrinkage; for that reason, gravity sintering experiments were performed. The shrinkage is anisotropic, and there is a big difference in shrinkage in direction of the gravity force and in the other directions. There is also a big difference in shrinkage concerning the bulk and the tap starting state. Part of the shrinkage is enforced by gravity, but most part comes from "pseudo-tapping"; i.e. when the powder densifies already before sintering when the boat is put in the furnace because of the small impacts of the sinter boat against the furnace muffle.

The best results could be obtained with metal injection molding (MIM). The ferritic powder was mixed with a binder based on polyethylene, paraffin wax and stearic acid with three different powder loadings (45, 50 and 55 vol%). The shrinkage is rather isotropic and in the range of 13%, which is close to the desired 15-20%. Naturally, the higher the powder loading, the lower the porosity; for example, the sample with a powder loading of 45 vol% has a porosity of 24.6% measured with Hg-porosimetry. But even more important, metallographic investigations showed an evenly distributed pore structure without agglomerations or pore

clusters. This was observed both for the ferritic and the austenitic material. It shows that metal injection molding, which is commonly employed for manufacturing of fully dense, small and complex-shaped precision parts is also well suited for producing highly porous components with defined total porosity and pore geometry.

A potentially critical aspect was identified by thermal analysis: DTA-TG showed that humid hydrogen, as is present at the anodes of SOFCs, causes significant oxidation of the specimens. I.e. the stability of the stainless steel grades used here cannot be taken for granted at service conditions that may occur in SOFCs.

Summarizing it can be said that metal injection molding is a most promising method for producing a porous metal support in an alternative way instead of tape casting, although of course this does not mean that it is also commercially competitive against tape casting which is already a well established process.

Contents

1. Introduction

In the year 2012 the world energy consumption grew by 1.8% and the world energy demand was 12476.6 million tonnes oil equivalent (= 539 Exajoule or about 150.000 TWh); Austria consumed about 33.1 mtoe and Germany 311.7 mtoe. About 90% of the world energy demand is covered by consumption of oil, gas and coal, with problematic consequences like high CO_2- emissions. In the same year, global nuclear power output had the largest decline ever as a response of the tragedy at Fukushima [**1**]. In March 2011 a catastrophic failure of the nuclear power plant in Fukushima took place, as a consequence of an enormous tsunami that cost about 20.000 lives, and once again created doubt that nuclear energy can be mastered safely. But not only since this tragic accident are people looking for alternative electric energy plants.

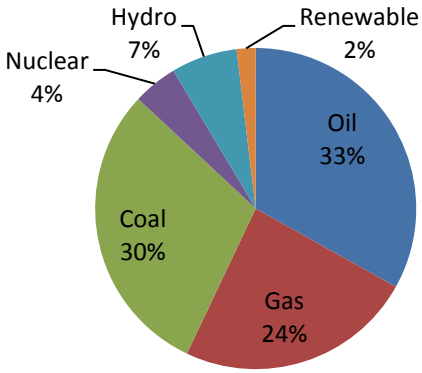

Fig. 1.1: World energy consumption 2012 [1]

Alternatives to nuclear power plants are fossil-, hydro-electric-, wind- or solar energy plants, but it is important that these plants fulfil the environmental guidelines in terms of carbon dioxide emission. In 2012, only 2% of the world energy demand was covered by renewable energy including sources like wind, geothermal, solar, biomass and waste (see Fig. 1.1).

The efficiency of energy conversion makes a contribution to save fossil energy sources and protect the climate. Even at smaller power scales, fuel cell systems are very efficient. Research and development of fuel cell systems are considerably pushed forward in many countries because of their high electrical efficiency, their low emission operation mode, their modular design and the fact that they are very well suited for combined heat and power units[**2**].

A variety of fuel cells - mostly classified by the electrolyte, e.g. Polymer Electrolyte Fuel Cell (PEFC), Alkaline Fuel Cell (AFC), Phosphoric Acid Fuel Cell (PAFC), Molten Carbonate Fuel Cell (MCFC), Solid Oxide Fuel Cell (SOFC) - are in different stages of development. Amongst these, the Solid Oxide Fuel Cell is the fuel cell with the longest continuous development period and characterized by the highest efficiency in combined heat and power units, and it is also suitable for decentralized power supply.

Research areas are widely distributed but there is a strong focus on optimizing the cell components (mainly electrolyte and electrodes) as well as long time stability of the operating fuel cell. Insufficient longtime stability – on the mechanical side as well as on the chemical side - is one major problem which needs to be overcome to make the fuel cell market-ready and competitive. In order to have mechanical stability, the cell can be supported by a so-called porous metal support. These metal supports are usually manufactured by tape casting. The present work, in contrast, is focused on processing these supports by different powder metallurgical techniques such as the press-and-sinter route, gravity sintering or metal injection molding. The samples have been analyzed with special regard to density, porosity.

2. Background

In the year 1839 Robert Grove discovered the principle of a fuel cell, and this principle is still valid today:

A fuel cell is an electrochemical device that continuously converts chemical energy into electrical energy (and some heat) for as long as fuel and oxidant are supplied **[**3**]**.

One principle of fuel cells is that they are not limited by the Carnot-efficiency, only by electrochemical, kinetic or ohmic losses. Additionally, their low noise in operation (no moving parts) and their "green" exhaust gases turns them into a very efficient and low-emission energy conversion technology. It is hoped that the fuel cell then will lead to a clean and efficient power generation in the 21st century.

2.1 Historical background of fuel cells

The fuel cells are certainly no new discovery, already in the year 1839 Sir William Robert Grove invented a H_2/O_2 fuel cell with spongy platinum electrodes and sulphuric acid as an electrolyte. Four cells were connected in series, and DC power was used to electrolyze water (Fig. 2.1).

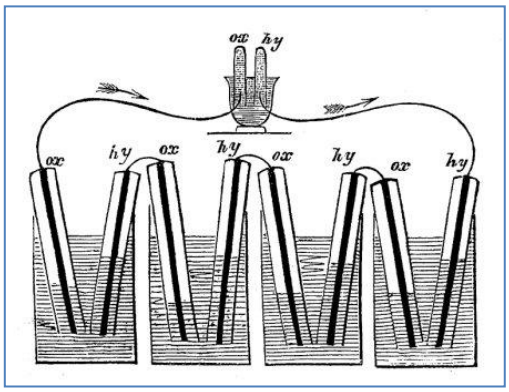

Fig. 2.1: First fuel cell invented by W.R. Grove [3]

Fig. 2.2: Five 100 kW SOFC units at ebay headquarters [4]

Years later, in 1897, Walther Nernst used ZrO_2 doped with 15% Y_2O_3 as an electrolyte in the 'Nernst-Lampe' **[5]**, which is the same electrolyte that is used in Solid Oxide Fuel Cells today. Mond and Langer were the first ones to use porous electrodes and so paved the way for developing acid electrolyte fuel cells, phosphoric acid and proton exchange fuel cells. Bacon then did some pioneering work on developing a 5 kW AFC (Alkaline Fuel Cell), which was later used as an auxiliary power source for NASA's Apollo flights. In NASA's Gemini Space Flights, Polymer Electrolyte Fuel Cell systems were used as well. They served as an auxiliary power source and drinking water source for the astronauts. The operating temperature of the PEMFCs was around 40-80°C.

During that time, fuel cell systems were only able to cover niche positions in high price applications (e.g. space flight, submarine), because of the high cost of production processes and due to the fact that it was only possible to use pure hydrogen as the fuel and pure oxygen as the oxidant. It is clear that - in order to compete with conventional technologies – the aims of reduction of cost as well as the use of natural gas as a feed gas and the high efficiency potential of these systems led to increased research and development. Today the Molten Carbonate Fuel Cell (MCFC) and in particular the Solid Oxide Fuel Cell (SOFC) are considered to gain ground. Numerous demonstration plants and already commercially available fuel cell systems showed the suitability of this technology. Today, worldwide manufacturers for large power generation applications (>100 kW) like Bloom Energy, Versa Power Systems, LG Fuel Cell Systems, Mitsubishi Hitachi Power Systems and small scale power applications like combined heat and power (CHP) units or auxiliary power units (APU) like Hexis, Kyocera or Ceres Power are ready to compete in the energy market.

2.2 Fuel cell types

A variety of fuel cells are in different stages of development. Fuel cells can be classified by the operating temperature, the fuel used for direct utilization and – the most common criterion - by the electrolyte in the fuel cell, for example:

- Polymer Electrolyte Fuel Cell (PEFC)
- Alkaline Fuel Cell (AFC)
- Phosphoric Acid Fuel Cell (PAFC)
- Molten Carbonate Fuel Cell (MCFC)
- Solid Oxide Fuel Cell (SOFC)

Polymer Electrolyte Fuel Cell

Polymer electrolyte fuel cells (PEFC, also called Proton Exchange Membrane fuel cells) consist of a porous anode and cathode (most common: platinum on carbon), and the electrolyte is a gas tight mebrane (most used perfluorosulfonic acid membrane **[6]**, Nafion®) with high ionic conductivity but low electronic conductivity. PEFCs operate at low temperature (below 100°C) and generate a specific power (Wkg^{-1}) and power density (Wcm^{-2}) higher than any other type of fuel cell. These benefits together with fast start-up and system robustness are the reasons that the PEFC has captured attention; it is the leading fuel cell candidate as power sources for transportation, small-scale power generation and portable power. To remain proton conductive, it is necessary to hydrate the Nafion membrane. The whole supporting equipment requirements for these membranes as well as water/cooling management of the cell is a very challenging task especially for portable power **[7,8]**. It is also possible to use methanol instead of hydrogen (direct methanol fuel cell).

Alkaline Fuel Cell

In an Alkaline Fuel Cell (AFC), hydroxyl anions are produced at the cathode side and diffuse through the electrolyte (normally static or circulating 30 – 40 wt% aqueous solution of potassium hydroxide) to the anode and water diffuses the opposite way. The oxygen reduction in alkaline environments is more favorable than in acid environments **[9]**. AFCs also operate well at room temperature with a high efficiency and require smaller amounts of noble metal catalysts. As already mentioned earlier, the first AFC cells were successfully installed in spacecrafts. The major disadvantage of the AFC is the sensitivity to carbon dioxide. Carbonate crystals are formed that can block electrolyte pathways and electrode pores **[10,11]**. As a result, only pure hydrogen and oxygen are utilized in practice **[12]**.

Phosphoric Acid Fuel Cell

The PAFC was the first fuel cell to be commercialized and electrodes, catalysts, bipolar plates are very similar to those of the PEFC. It operates at a temperature around 200°C with molten H_3PO_4 as an electrolyte held in an SiC matrix (about 50 µm thick), sandwiched by the electrodes, Pt/C bonded on PTFE (polytetrafluoroethylene, Teflon®). Appleby **[13]** discovered in 1984 that carbon is stable in this fuel cell environment and made the PAFC economically feasible. Phosporic acid could be used with Pt electrodes at elevated temperatures (above 100°C), but sulfuric acid could not because it would be reduced in the presence of platinum. The PAFC is characterized by a lower performance of a single cell compared to that in an alkaline fuel cell, but it is not as sensitive to carbon impurities. PAFCs suffer from long term degradation (5mV per 1000 hr) due to their highly corrosive electrochemical environment **[14]**. Another critical issue is the water management of the cell.

Molten Carbonate Fuel Cell

MCFCs are being developed for efficient natural gas and coal-based power plants for industrial, electrical, and military applications **[15]**. They have a liquid (molten) mixture of Li_2CO_3, $NaCO_3$ and K_2CO_3 as electrolyte, Ni-based fuel electrode and lithiated NiO as oxygen electrode. Besides their sufficient conductivity of these (state-of-the-art) Ni-based anodes and NiO cathodes, there are major considerations concerning the structural stability and NiO dissolution into the matrix **[16,17]**. A high operating temperature (ca. 650°C) is needed for melting of the electrolyte. Because of the high operating temperature the internal reforming of the fuel is possible, and no noble metal catalysts are required. MCFC plants are already being commercialized (e.g. Fuel Cell Energy in the USA, Ansaldo in Italy, Hitachi, Mitsubishi Electric Company and Toshiba Corporation in Japan); in Germany MTU CFC Solutions are running field tests with a 245 kW power plant and an electrical efficiency of 47% **[18]**. Side note: So far, the cell has not been regarded as reversible, but a very new data by Hu indicates that it may be – at least for short-time experiments **[19]**.

The Solid Oxide Fuel cell is described in more detail in Chapter 2.3.

A summary of major differences of the fuel cells is shown in Table 2.1.

Table 2.1: Summary of major differences of various fuel cells [20]

	PEFC	AFC	PAFC	MCFC	SOFC
Electrolyte	Hydrated Polymeric Ion Exchange Membranes	Mobilized or Immobilized Potassium Hydroxide in asbestos matrix	Immobilized Liquid Phosporic Acid in SiC	Immobilized Liquid Molten Carbonate in $LiALO_2$	Ceramics
Electrodes	Carbon	Transition metals	Carbon-based	Nickel and Nickel Oxide	Perovskite and perovskite / metal cermet
Catalyst	Platinum	Platinum	Platinum	Electrode material	Electrode material
Interconnect	Carbon or metal	Metal	Graphite	Stainless steel or Nickel	Nickel, ceramic, or steel
Operating Temperature	40 - 80 °C	65 - 220 °C	205 °C	650 °C	600-1000 °C
Charge Carrier	H^+	OH^-	H^+	CO_3^{2-}	O^{2-}
External Reformer for hydrocarbon fuels	Yes	Yes	Yes	No, for some fuels	No, for some fuels and cell designs
External shift conversion of CO to H_2	Yes, plus purification to remove trace CO	Yes, plus purification to remove trace CO and CO_2	Yes	No, for some fuels	No, for some fuels and cell designs
Prime Cell Components	Carbon-based	Carbon-based	Graphite-based	Stainless - based	Ceramic
Product Water Management	Evaporative	Evaporative	Evaporative	Gaseous Product	Gaseous Product
Product Heat Management	Process Gas + Liquid Cooling Medium	Process Gas + Electrolyte Circulation	Process Gas + Liquid Cooling medium or steam generation	Internal Reforming + Process Gas	Internal Reforming + Process Gas

2.3 Solide Oxide Fuel Cell

The SOFC is the fuel cell with the longest continuous development period. The following pages will give an overview of the reaction, principle of operation, the materials, design and fabrication, and some examples of commercially available SOFCs or research projects. The electrolyte in this fuel cell is a solid, nonporous metal oxide. Because of the solid electrolyte, the fuel cell can be cast into different shapes, most often tubular or planar. The operating temperature is between 600 and 1000°C. Typically, the anode is Ni-ZrO_2-cermet, and the cathode is Sr-doped $LaMnO_3$. The fuel and the oxidant are fed as gases, which means it is only a two-phase system. The fuel cell reactions occur at the solid electrode/gas interfaces and are shown in Fig. 2.3. The oxygen molecules in the air take up electrons and move as negatively charged ions through the electrolyte to the anode. There they react with hydrogen to form water.

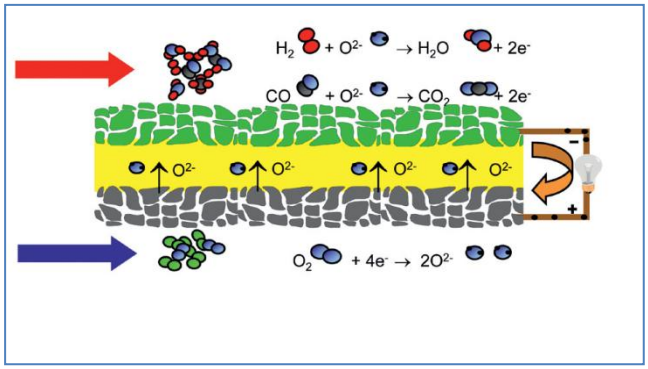

ANODE: $H_2 + O^{2-} \rightarrow H_2O + 2e^-$

$(CO + O^{2-} \leftrightarrow CO_2 + 2e^-)$

CATHODE: $\frac{1}{2} O_2 + 2e^- \rightarrow O^{2-}$

CELL: $H_2 + \frac{1}{2} O_2 \rightarrow H_2O$

Fig. 2.3: Mode of operation of an SOFC [21]

Each component of the fuel cell (anode, electrolyte, cathode, and the interconnect) has to fulfil several functions like proper stability (chemical, phase, morphological, and dimensional) in oxidizing and/or reducing environments in addition to proper conductivity and chemical compatibility with other components **[22]**. The single cell components are now described in detail.

2.3.1 Materials

ELECTROLYTE:

As the name SOFC already evokes, the material used as an electrolyte is a solid oxide ceramic. The ideal electrolyte has to meet a lot of criteria; not only the functions stated above, but it also has to be dense and leak-tight, with high ionic conductivity but low electronic conductivity. Normally the electrolyte should be very thin in order to reduce ionic resistance. Ionic conductivity can only occur if defects are present and vacancies (vice versa the ion) can move from one crystal lattice site to another spot. This movement is thermally activated and consequently strongly temperature dependent (ionic conductivity of YSZ = 10^{-1} S/cm at 1000°C; 10^{-2} S/cm at 700°C). The two simplest types of point defects are Schottky (vacancy

defect) and Frenkel (vacancy created by moving of an ion to an interstitial place) defects. The most common electrolyte is yttrium-stabilized zirconia (YSZ), and already in the year 1943 Baur and Preis **[23]** showed that it could be used in fuel cells and by now, it is the best studied electrolyte as described in numerous journal articles and reviews **[24, 25, 26, 27, 28, 29]**. Pure zirconia undergoes phase transformations from monoclinic (stable < 950 – 1170°C) to tetragonal (stable to about 2370°C) to cubic (melting point 2680°C). The t-m transformation comes along with a volume increase of 3-5% and results in failure of sintered parts. Therefore it is desirable to stabilize the cubic structure at lower temperatures with a dopant like yttrium. Also the ionic conductivity of YSZ increases with increasing dopant concentration due to the increase of oxygen vacancies, reaching a maximum at around 8 - 10 mol% Y_2O_3. Kanert **[30]** has shown that a further increase in dopant concentration leads to a decrease in conductivity, and the reason is that the there are in fact more vacancies but their mobility is then hindered. Other alternative electrolytes are studied and tested, e.g. scandium-doped zirconia (SDZ) which is more conductive than YSZ, but the long term stability is not sufficient. Gadolinium-doped ceria (GDC) is even more conductive, but there is a problem with reduction of GDC in hydrogen at temperatures higher than 600°C. The GDC-electrolyte has reasonable potential in a medium-temperature SOFC, but then all the other cell components still have to be optimized for this particular electrolyte. The performance of perowskite-typed electrolytes like LSGM (lanthanum gallate with strontium doping to the La site and magnesium to the Ga-site of the perovskite; Goodenough **[31]**) is higher than some of the existing fluorite-types (like YSZ and GDC), but the poor chemical compatibility with cathode and anode material is a major drawback. The current status of the most common electrolytes can be seen in Fig. 2.4.

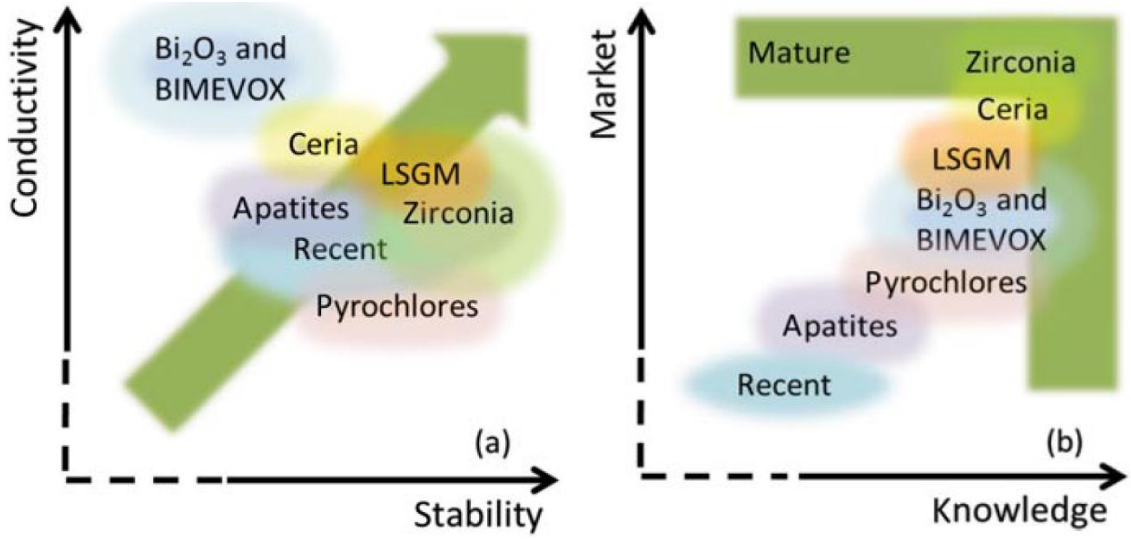

Fig. 2.4: Current status of solid electrolyte[32]

ANODE:

Needless to say that the anode has to be electron conductive and should be stable in the environment (redox, thermally, impurities like sulphur, etc.) and for sintering issues, it must be compatible with the electrolyte and the interconnect materials. Anodes should possess a

catalytic effect on the anode reaction, and they may be required to provide structural support. At the moment performance targets are to provide a power density of about 1 Watt/cm^2 at 0.7 Volts (total cell area specific resistance of about 0.3 Ohm/cm^2), and a current density of about 1.4 A/cm^2. This leads to a total current of 140 A with a cell size of 100 cm^2. The most common anode material is a Ni/YSZ cermet (first invented by Spacil **[33]** in the year 1970), and there are several reasons for that. NiO and YSZ do not react even at 1500°C and can be co-fired at high temperatures, unlike e.g. Co_2O_3 that dissolves into YSZ at lower temperatures. Ni is a good and cheap catalyst and remains metallic in most SOFC conditions. By contrast, Fe would form FeO under H_2/H_2O environments. In the year 1987 Dees **[34]** observed an increase in conductivity at about 30 vol% Ni; below this threshold, ionic conduction through the zirconia phase is dominating, above this threshold a change from ionic conduction to electronic conduction through the Ni phase takes place.

Although the Ni/YSZ cermet is well known and described in the literature, there are some drawbacks for this specific material: NiO shrinks when it is reduced and does not go back to its initial form when it gets reoxidised again ("Ni-coarsening"). Because of this reoxidation the material loses mechanical strength and also active surface area. One method to avoid damage to the cell by this cause is to prepare a porous YSZ substrate with Ni salts (Busawon, [**35**]). Another issue is the sulphur tolerance of the anode. The cell performance is strongly decreased in the presence of sulphur at elevated temperatures (1 ppm at 1000°C **[36, 37]**, or 40 ppm at 700°C **[38]**), and the reason is that the Ni surface gets covered with sulphur **[39]**. Another problem with Ni anodes is the formation of carbon because Ni catalyzes formation of carbon fibers, and this causes electrode instability **[40,41]**. For a better resistance against carbon formation it is possible to coat Ni with CeO_2 **[42]** or to use cerium based ($Ce_{0.6}Gd_{0.4}O_{1.8}$) **[43,44]** or copper based anodes like $CuCeO_2$ instead of nickel **[45,46]**. In this case, Cu is primarily a conductor and Ce the catalyst, but the problem with using Cu is that it is limited to lower temperatures (Cu sinters) and that metal catalysts cannot be used because they would alloy with Cu. In this case, stabilizing the copper with cobalt is helpful. Gross reported that the addition of only 5 vol% cobalt improves the thermal stability significantly **[47]**. Recently, anodes using conducting ceramics have been tested. For example, $La_{0.3}Sr_{0.7}TiO_3$ (LST), $La_{0.8}Sr_{0.2}Cr_{0.5}Mn_{0.5}O_3$ (LSCM) or $Ce_{0.7}Sr_{0.3}VO_3$ (CSV) are tested **[48,49]**; they show a high sulphur and hydrocarbon tolerance and also a long time stability, but the electronic conductivity and the catalytic activity of these anodes are fairly low.

CATHODE:

The requirements for the cathode are similar to those for of the anode. The desired cathode should have low ionic and electronic resistance and high catalytic activity towards oxygen reduction. It should possess chemical stability and low interaction with the electrolyte (YSZ) or interconnect. For sintering issues, a match of the CTE of cathode and electrolyte is required. Long time stability is without doubt needed. Nowadays, the most common materials used as cathodes are lanthanum-based perovskites ($LaMnO_3$). For higher electronic conductivity, doping of the $LaMnO_3$ with various elements like Ba, Ca, Mg, Na, or Ni has

been studied extensively **[50,51,52,53,54]** but as a standard material strontium doped $LaMnO_3$ (LSM) is established, and the reason is the high electronic conductivity in oxidizing atmospheres **[55,56,57,58]**. Doping of $LaMnO_3$ with strontium increases the thermal expansion coefficient **[59]**, but at high temperatures and with YSZ as an electrolyte, LSM reacts with ZrO_2 to $La_2Zr_2O_7$. To minimize this reaction, coating of the YSZ with a $Ce_{0.8}Gd_{0.2}O_2$ layer is possible. Cathodic overpotentials are determined to be one of the main contributors to internal cell/stack losses. Mixed conducting cathodes like LSCF ($La_{0.6}Sr_{0.4}Co_{0.2}Fe_{0.8}O_3$) and LSC (strontium doped $LaCoO_3$) offer lower overpotential but exhibit faster degradation rates than LSM. These types of cathodes are designed for intermediate-temperature SOFC's (700-800°C operating temperature). Another problem at high temperatures is the chromium deposition resulting in a rapid degradation of the cells, but this effect is strongly dependent on the electrolyte/cathode combination **[60]**.

INTERCONNECT:

One of the main functions of the interconnector (IC) is providing the electrodes with gas and transportation of the electrons. The requirements for the interconnector are very tough as listed below:

- High electronic (> 50 S/cm) and thermal (> 10 W/mK) conductivity
- Stability in oxidizing and reducing environments
- Low permeability of anodic and cathodic reactants to minimize their mixing and direct chemical reaction (a leakage of the IC leads to a variation in partial pressure of O_2 and to a decreased fuel cell performance)
- Compatibility of the thermal expansion coefficients of interconnector and fuel cell components (CTE YSZ 10.5 x 10^{-6} per K)
- Chemical stability against the nickel anode on one side and the strontium-doped lanthanum manganate on the other
- Mechanical stability, low cost

Possible alloys for the interconnector are ceramic alloys ($LaCrO_3$), or metallic alloys (nickel or chromium based $95Cr5FeY_2O_3$, ferritic alloys). The advantages of metallic interconnect parts in contrast to the ceramic ones are higher electronic and thermal conductivity, low cost, easy manufacture and good workability. Ceramic interconnects like $LaCrO_3$ are used at high operating temperatures and are well described by Minh **[61]**. There are some industrial metallic interconnect alloys available, e.g., DUCROLLOY (trade mark of Plansee, $95Cr5FeY_2O_3$), Crofer22APU (trade mark of ThyssenKrupp, Fe22Cr), ZMG232 (trade mark of Hitachi, Fe22Cr). Plansee also patented a new alloy called ITM, a ferritic ODS alloy ($Fe26Cr\text{-}Y_2O_3$). Al_2O_3- and SiO_2 –forming alloys are less interesting than Cr_2O_3-forming

ones, because the resulting oxide scale possesses a low electrical conductivity and a high area specific resistance.

Cr-based interconnectors (95Cr5FeY_2O_3): To promote the oxidation resistance and high temperature strength of interconnects, oxide dispersoids (0.1 – 1 mass-%) of reactive elements (Y, Hf, Zr, Ce, La...) can be incorporated into the alloy (**O**xide **D**ispersion **S**trengthened Alloys). The ODS materials are manufactured by elemental mixing of the starting powders or by mechanical alloying, that is, by high-energy ball milling of chromium and oxide powders in a non-oxidizing environment. The RE effect is well known and described in the literature. In case of the Cr5Fe1Y_2O_3 alloy, the oxide scale growth rate and scale spallation tendency is reduced and the cohesiveness of the interface between the oxide scale and the metallic substrate is improved. The direction of mass transport in the chromia scales is altered from predominantly outward chromium diffusion for alloys without Y_2O_3 to inward oxygen diffusion for alloys with Y_2O_3. Some studies even indicate that oxide additives are rather effective in refining the grain size of the surface scales **[62,63]**. One major drawback of the Cr-based interconnectors is the evaporation of Cr or Cr compounds (especially in the presence of water and CO **[64]**) and the high cost because of the high chromium content. To minimize chromium evaporation, coating of the interconnector with strontium doped lanthanum cobaltite is very effective **[65]**. The research then focused on minimizing the Cr content and still fitting the requirements for the interconnects.

Fe-based interconnectors (Fe22Cr, Fe26Cr-Y_2O_3): Advantages of this type of interconnects are the better match of the CTE to other cell components, good mechanical properties and low cost. The Crofer22APU (Fe22Cr; invented by Quadakkers) is a high-temperature ferritic stainless steel, with the addition of 0.4 – 0.20 wt% La; Quadakkers assumed that La does not form intermetallic compounds with Fe and at 800°C it can be dissolved in the α-Fe matrix up to a concentration of around 0.5% **[66]**. At operating temperature the oxide layer of this alloy then consists of a inner Cr_2O_3 scale and a columnar $(Mn,Cr)_3O_4$ spinel outer layer **[67]**. Plansee's ITM interconnect is a ferritic FeCr base alloy, modified by Mo, Ti, Mn and Y for an application temperature up to 850°C. Mechanical properties (yield strength and ultimate tensile strength at elevated temperatures **[68]**) and oxidation resistance are very good and broke the 40.000 h of operation benchmark in a long-time test at the Forschungszentrum Jülich in March 2012 **[69]**.

SEALS:

SOFC seals prevent that the fuel and oxidant are intermixed within the stack, leaking of fuel and oxidant from the stack and sometimes they electrically insulate the cells in a stack. The seal material therefore plays a major role for achieving high performance and low degradation in fuel cells. Therefore this material has to be structurally stable and chemically compatible with other stack components. There are two different types of seals: bonded seals (primarily glasses or glass-ceramics like BaO-Al_2O_3-SiO_2 seals **[70]**) or compressive, non-bonded seals like muscovite or phlogopite mica. In both cases, long time stability of the sealing material is

needed to ensure high performance of the solid oxide fuel cell. Further literature for mechanical testing and leakage tests of the sealants can be found in **[71,72,73,74,75,76]**.

2.3.2 Cell design and support

As already stated above, there are different cell designs possible: tubular (anode- and cathode supported; microtubular), flattened tubular (anode- and cathode supported), or planar (anode-, electrolyte-, and metal-supported). Fig. 2.5 shows an example of the tubular and the flattened design. In this work, the main focus was held on planar (metal supported) fuel cells. This is the reason why only a short overview on the other designs is given. In case of the tubular design, each tube contains one cell, and the single cells can be connected over the interconnector to a bundle or a generator. Siemens/Westinghouse developed a 100-kW cathode-supported high efficient and long-term stable tubular fuel cell for stationary applications that shows only minimal voltage degradation (< 0.1% per 1000 hours). The advantages of the tubular design are the mechanical stability, no sealants required and that the tubes are easier to fabricate than the planar cells **[77]**.

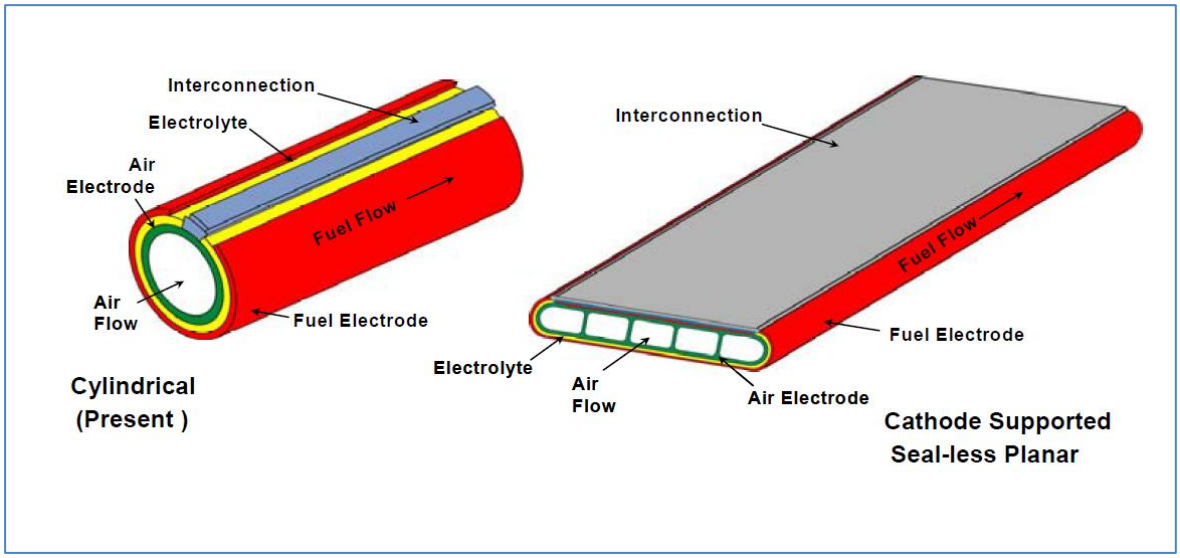

Fig. 2.5: Tubular and flattened tubular design of a SOFC [78]

Flattened tubular cells were invented to increase the cell power density and reduce the ohmic resistance. The cell design is more compact compared to the tubular ones. The current path of electrons is shortened and the seal-less design remains. For more detailed information, Huang **[79]** recently gave a broad overview on (cathode supported) tubular and flattened tubular SOFC's.

The power density of the planar cells is higher than that of tubular cells and in order to increase it, planar single cells are combined to a fuel cell "stack", separated by the interconnector. The mechanical support can come from the electrolyte, the electrodes or by a porous metal support. In case of the electrolyte supported cell, the thickness of the electrolyte is >100 µm, resulting in a high ohmic contribution to resistance (about 0.7 Ω/cm² at 800°C)

and requiring high operating temperature (1000°C). The thickness of the electrodes is about 50 µm, and the concentration polarisation of anode and cathode is low.

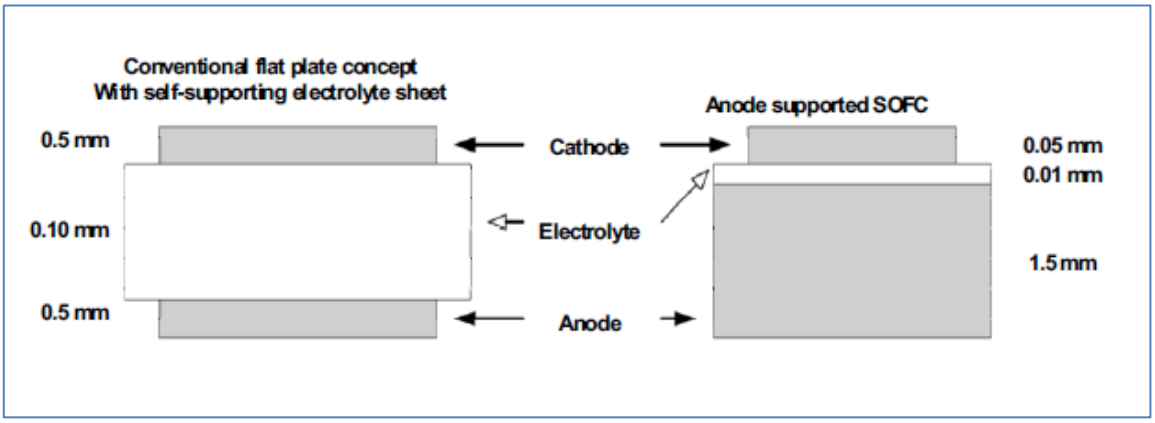

Fig. 2.6: Schematics of electrolyte and anode supported planar SOFC's [80]

As an alternative, the support can come from the electrodes. In this case the anode supported type is preferred for several reasons. First, because of the better diffusion coefficient of hydrogen, second, the easier manufacturing and last, the moderate anode concentration polarization (compared to high cathode concentration polarization for cathode supported cells). The thickness of the anode is about 500 – 1500 µm.

Another alternative in order to get mechanical stability is a metal-supported cell (Fig. 2.7), mostly used for mobile applications.

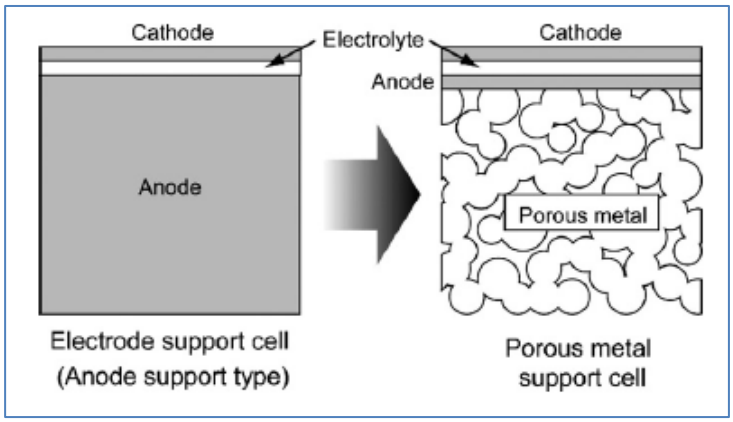

Fig. 2.7: Schematics of anode supported cell and porous metal supported cell [81]

These metal-supported SOFCs are expected to be competitive in the power generation equipment market because of their strength, tolerance to extremely rapid thermal cycling, and the reduced material costs the metal support allows. Since the bulk of the material can be composed of inexpensive material (i.e. ferritic steel), expensive ceramics can be limited to thin functional layers.

Additionally, the metal-supported design allows for easily manufacturable and inexpensive conventional metal joining techniques such as brazing, welding and crimp sealing **[82]**. However, at the interface between the ferritic FeCr support and the Ni-YSZ anode, interdiffusion of iron, nickel and chromium atoms can occur. To limit anode degradation and excessive oxidation due to this interdiffusion, a diffusion barrier layer on basis of CGO, CeO_2 or LSM can be applied on the metal support **[83]**.

The porous metal support is preferably produced by tape casting and has to fulfil various requirements:

- open porosity for gas permeability (fuel gas and reaction gases)

- oxidation resistance in an oxidizing environment and in a H_2/H_2O atmosphere with varying ratios at operating temperature (up to 900°C)

- sufficient mechanical strength (creep strength and also shock resistance - if used as APU in long vehicle trucks)

- match of the CTE with the electrode and electrolyte material to avoid thermal stresses

- high electronic conductivity

- low tendency to interact with the functional ceramics

For the metal supported cell in general, high electrical conductivity and cell robustness are key features in SOFC engineering. Electrical conductivity can be obtained with optimized microstructure for long-range connectivity of respective ionic and electronic conductor chains and maximized active sites and a high density of triple phase boundaries (TPB). This is important because the oxidation of H_2 to H_2O occurs at the electrode/electrolyte/H_2 boundary.

2.3.3 Fabrication methods

As already stated above, there are different cell designs possible: tubular (anode- and cathode supported; microtubular), flattened tubular (anode- and cathode supported), or planar (anode-, electrolyte-, and metal-supported); powder metallurgy is essential for producing parts of the cell and/or the whole cell. Cell fabrication processes contain e.g. sputtering, dip coating, spin coating, spray pyrolysis, electrophoretic / vapor deposition, tape casting or screen printing, and the cost of a fabrication process always is a factor if the cell should be produced economically.

Tubular cells:

Tubular cells can be produced by extrusion of the $LaMnO_3$-cathode, plasma spraying or electrochemical vapor deposition (EVD) of the YSZ-electrolyte and slurry coating or EVD of the Ni-YSZ-anode. For reducing the costs, Kuo **[84]** replaced the EVD-process by a cost-effective atmospheric plasma spraying (APS).

Planar cells:

In case of planar cell design, the manufacturing of fuel cells is also very demanding for powder metallurgy.

- Anode supported cells:

For manufacturing the anode, a slurry of YSZ and NiO powders together with pore formers (graphite or rice starch), solvents (ethanol), binders (polyvinyl butyrate) and dispersants is produced, mixed and then further processed by the tape casting technique. The anode and the electrolyte are sintered together in a single sintering process at about 1400°C for 1 h in air ("co-sintering" or "co-firing", see Fig. 2.8). The cathode is then applied by screen printing and sintering (1250°C, 1h). It is interesting that the reduction from NiO to Ni takes place in the cell (in situ), when the anode is started up the first time and exposed to the fuel. Tape casting and co-sintering of anode and electrolyte are preferred fabrication methods because of their low cost and the good reliability, but there are also some problems involved.

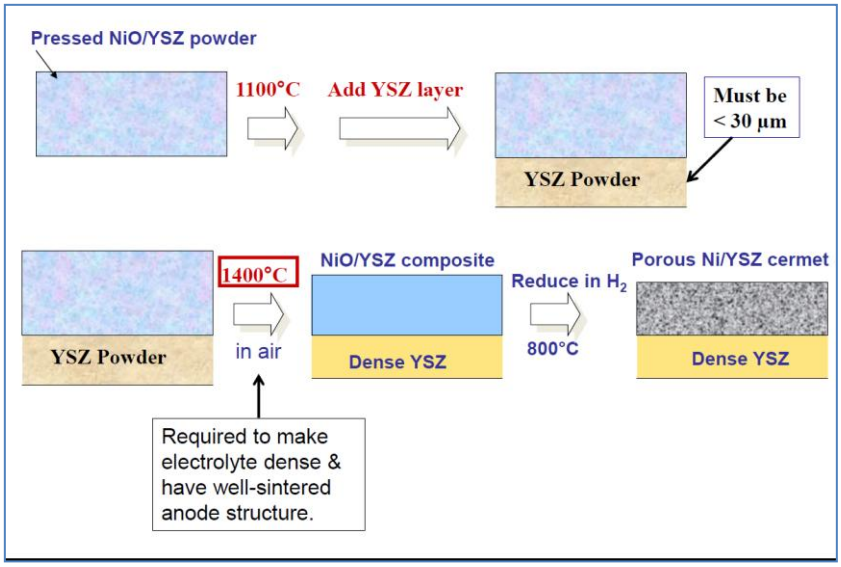

Fig. 2.8: Co-sintering of anode and electrolyte [85]

For manufacturing of these anodes by co-sintering one has to regard the different CTE of Ni and YSZ. The CTE of Ni is higher than that of the ceramics, leading to thermal stresses after co-sintering when the sample is being cooled down. Naturally, this could cause severe damage while operating the cell under thermal cycling conditions. As long as the YSZ electrolyte is less than 30 µm thick, it can take up the strain without fracture and during sintering, the YSZ in the anode bonds to YSZ in the electrolyte, giving a better electrolyte-electrode interface. The layers have to become "dense" (or "shrink") at the same temperature. This often requires presintering of the anode layer by heating it up to 1100°C before adding the electrolyte (see Fig. 2.8). In general, the finished product is influenced by a lot of parameters, e.g. starting powder and particle size distribution **[86,87]**, morphology **[88]**, compacting pressure **[89]**, specific surface and processing parameters (sintering time, atmosphere) **[90]**. Almost ten years ago Jiang **[91]** gave a very good review on this topic. Another problem due to the mismatch of the constituting layers of anode and cathode is that the ceramic foils up (warpage). These curvature effects are monitored and widely reported during co-sintering **[e.g.:92,93]** and described by various models **[94,95]**. Applying pressure during co-sintering could avoid this warpage **[96]**.

- Metal supported cells:

The German Aerospace Center (DLR) in Stuttgart developed a spray concept based on plasma spray technology for manufacturing the entire cell. This spraying process is cost-effective, but even more problems have been encountered in increasing the cell performance and long-term stability, which can be attributed to the inherent gas leakage of plasma sprayed electrolytes. In contrast to this spraying concept, Plansee established a production line for the manufacturing of MSC (Fig. 2.9).

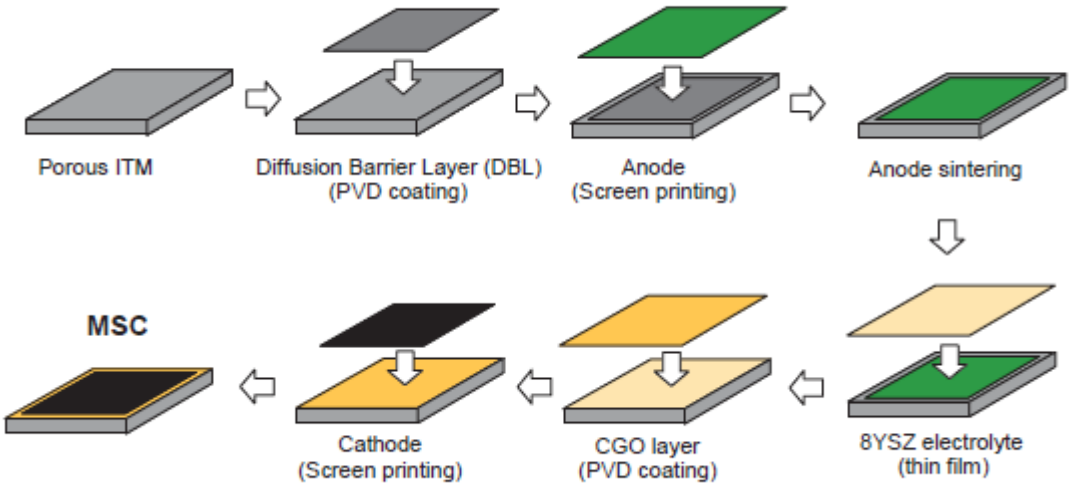

Fig. 2.9: Production line of a thin film MSC [97]

The FeCr support can be produced by tape casting and has a thickness of around 1 mm. To minimize interdiffusion of atoms, a thin film layer as diffusion barrier (~2 µm thick) is applied on top of it (CGO or LSM; by physical vapor deposition or magnetron sputtering). The Ni-YSZ anode is screen printed with reduced pore size, so that at the end the surface is flat enough to apply the 8YSZ electrolyte by sputtering. The electrolyte has to be as gas tight as possible. Finally, another diffusion barrier layer of CGO is deposited, and then the cathode layer is screen printed. The cathode is sintered during the first start-up of the cell [**98**,**99**]. In general, it is very difficult to apply a thin layer on a porous substrate. General levels of porosities of the different layers can be seen in Fig. 2.10. Open porosity is required for efficient gas diffusion from the bulk into reaction sites.

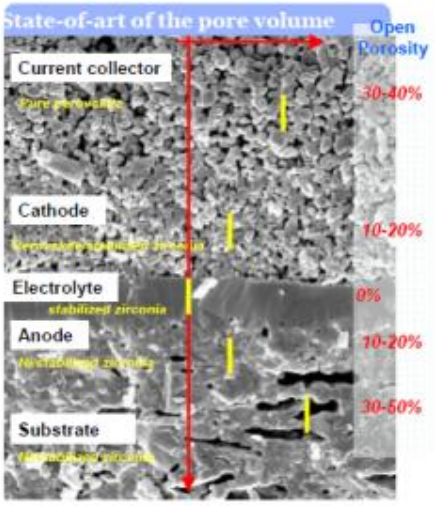

Fig. 2.10: Cross section of a metal supported SOFC [100]

2.3.4 Alternative fabrication methods

As already stated above, a porous metal support gives the required mechanical strength and also acts as a delivery medium for the combustion gases; it is commonly produced by tape casting. The question arises if there are alternative fabrication methods for this support that guarantee economical processing with high reproducibility of the relevant properties. Another question is if co-sintering of the metal support and the ceramic layers is possible. For co-sintering, 15-20% linear shrinkage of the metal support is needed, in an atmosphere other than H_2, because it is obvious that reducing atmosphere will degrade the functional ceramics. The requirements of a porous metal support are already listed in Chapter 2.3.2; in our case, for producing this metal support in an alternative way, 30-50% almost fully open porosity, 15-20% shrinkage of the metal during sintering and also - if possible – dimension of about 100 x 100 x 1 mm should be obtained. Introducing porosity to PM steels is not at all a new issue; there are many ways to get a porous structure, either with powder metallurgical production methods, chemical deposition, melting techniques and others. Strobl has given a review on major processes about manufacturing of metals with a cellular structure **[101]**, Davis has written a compact review especially on metallic foams **[102]**. In this work, various methods for manufacturing this porous metal support have been tried, including:

- uniaxial pressing and sintering using paraffin wax as a spaceholder

- gravity (loose powder) sintering

- special binder systems (polyvinyl alcohol solution, latex binder)

- extrusion molding

- metal injection molding

Properties like defined porosity and permeability also play a role in the field of sintered filters. The separation of solid and liquid particles in a gas is the main application of these metallic filters. The characterization of properties like density, porosity (size and distribution), permeability of the metallic filters is a very important factor **[103]** and some of the test methods can also be applied to porous metal substrates. The methods for characterization of the produced porous metal supports are listened in Chapter 3.13 - 3.18.

3. Experimental details

3.1 Starting powders

The research has started with four different powders provided by Höganäs AB (HAB). The composition of the alloys is shown in Table 3.1. The carbon, oxygen and nitrogen contents were measured at TU Wien, while the other elements were analyzed by Höganäs. There are two different lots of the Fe25Cr20Ni2.5Si grade, the TUW lot has been used for pressing and sintering experiments. MIM and PEM experiments at UC3M have been carried out with lot UC3M. As can be seen in Table 3.1 and Table 3.4, their composition is the same.

Table 3.1: Measured composition of the alloys (metallic alloy elements: data from Höganäs AB, n.m. = not measured)

	Chemical composition (%)								
Alloy	**Cr**	**Ni**	**Mn**	**Si**	**Nb**	**Ti**	**C**	**O**	**N**
Fe25Cr20Ni2.5Si	25,3	20,2	0,1	2,5	n.m	n.m.	0,021	0,16	0,14
Fe18Cr0.3Mn0.5Nb	17,5	0,07	0,28	0,10	0,53	0,03	0,007	0,60	0,03
Fe21Cr	21,1	0,1	0,05	0,16	n.m	n.m	0,049	0,44	0,07
Fe21Cr0.5Nb	21,2	0,08	0,03	0,11	0,43	n.m	0,012	0,44	0,07

The density of the powder was measured by the Ultra-Pyknometer 1000T (Quantachrome). Each powder was measured three times, and then mean value and standard deviation were calculated (Table 3.2). As a reference, iron powder ASC100.29 was measured. The measured density of the iron powder (7.82 g/cm³) is only slightly lower than the theoretical density given for pure iron (7.87 g/cm³). The Fe25Cr20Ni2.5Si (lot TUW) powder has the highest density of all because of its 20 wt% Nickel content, resulting in austenitic structure with higher packing density, while the other three powders have rather the same densities. From the relatively low density levels of the high alloy powders, also of the austenitic one, it can be assumed that within the particles some closed porosity exists.

Table 3.2: Density of the powder measured by using a He-Pycnometer

Alloy	**ρ [g/cm³] Run 1**	**ρ [g/cm³] Run 2**	**ρ [g/cm³] Run 3**	**ρ [g/cm³]**	**Std dev. [g/cm³]**
ASC100.29	7,8240	7,8293	7,8135	**7,8223**	0,0080
Fe25Cr20Ni2.5Si	7,6910	7,6749	7,6640	**7,6766**	0,0136
Fe18Cr0.3Mn0.5Nb	7,5514	7,5464	7,5392	**7,5457**	0,0061
Fe21Cr	7,5892	7,5758	7,5676	**7,5775**	0,0109
Fe21Cr0.5Nb	7,5642	7,5582	7,5440	**7,5555**	0,0104

Also apparent (DIN EN ISO 60) and tap density (DIN EN ISO 3953) and flowability of the four powders were measured. The results are shown in Table 3.3.

All powders have a good flowability (approx. 30 s/50g). Although the Fe25Cr20Ni2.5Si-powder has the smallest particle size, the flowability, measured as 30.5 s/50 g, is quite the same as for the other powders. That means that the shape of these powder particles should be more spherical than the others ones. Therefore the shape of the powder particles is compared by SEM in Fig. 3.1 - Fig. 3.12, where it could be seen that they all have rather the same shape.

The Fe21Cr0.5Nb powder has the highest flowability time (34.4 s/50g) and the lowest apparent density (2.59 g/cm³). The finest powder (Fe25Cr20Ni2. 5Si) has also the lowest tap density (3.2 g/cm³).

Table 3.3: Flowability, apparent and tap density of the powders

Alloy	particle size [µm]	flowability [s/50g]	apparent density [g/cm³]	tap density [g/cm³]
Fe25Cr20Ni2.5Si	< 53	30,5 ± 0,2	2,78 ± 0,03	3,20
Fe18Cr0.3Mn0.5Nb	< 75	30,3 ± 0,4	2,85 ± 0,01	3,42
Fe21Cr	< 75	29,2 ± 0,3	2,78 ± 0,02	3,44
Fe21Cr0.5Nb	< 75	34,4 ± 0,1	2,59 ± 0,01	3,36

The morphology of the powders was studied by scanning electron microscopy. Fig. 3.1 - Fig. 3.6 show the SEM images of Fe25Cr20Ni2.5 Si (left side) and Fe18Cr0.3Mn0.5Nb (right side) at different magnifications. Fig. 3.7 - Fig. 3.12 show the SEM image of Fe21Cr (left) and Fe21Cr0.5Nb (right), the austenitic and ferritic powder look very similar.

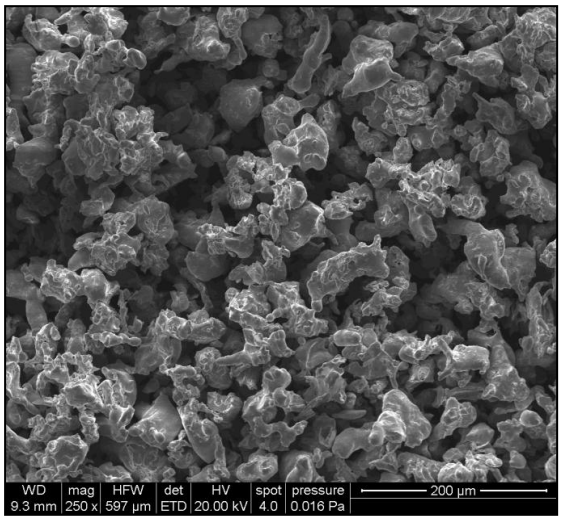

Fig. 3.1 SEM image of Fe25Cr20Ni2.5Si

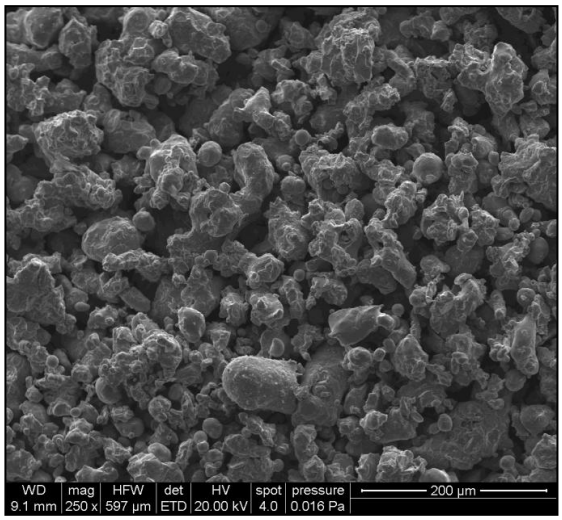

Fig. 3.2: SEM image of Fe18Cr0.3Mn0.5Nb,

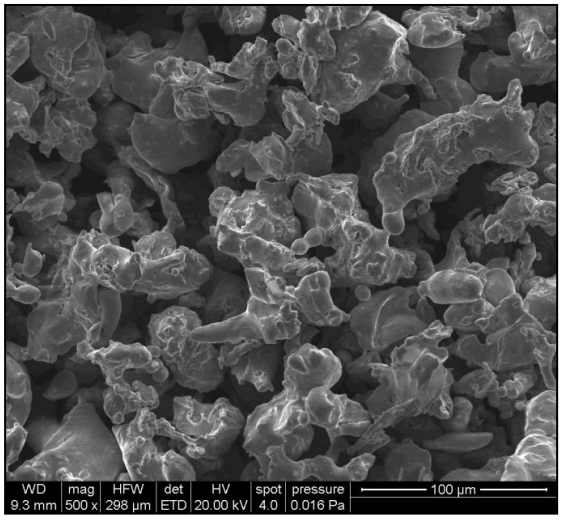

Fig. 3.3: SEM image of Fe25Cr20Ni2.5Si

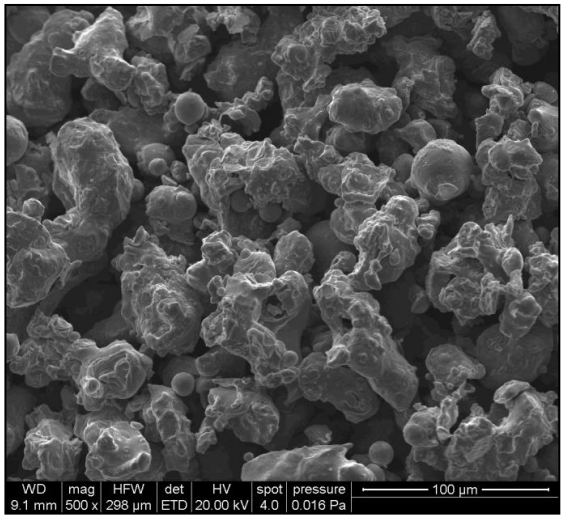

Fig. 3.4: SEM image of Fe18Cr0.3Mn0.5Nb

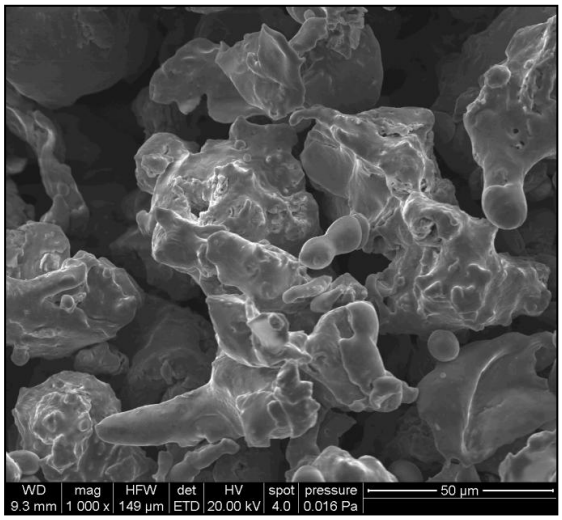

Fig. 3.5: SEM image of Fe25Cr20Ni2.5Si

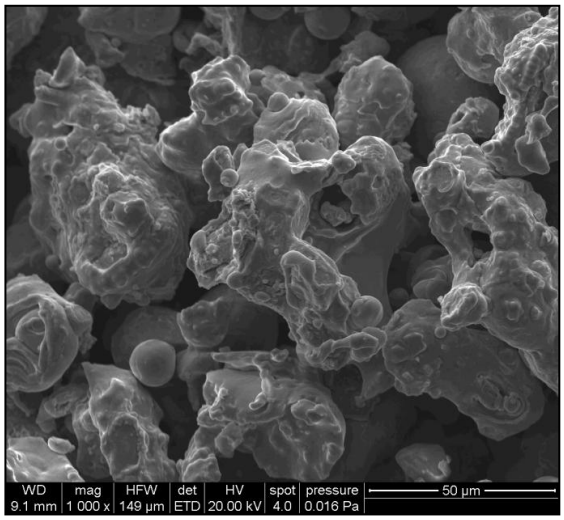

Fig. 3.6: SEM image of Fe18Cr0.3Mn0.5Nb

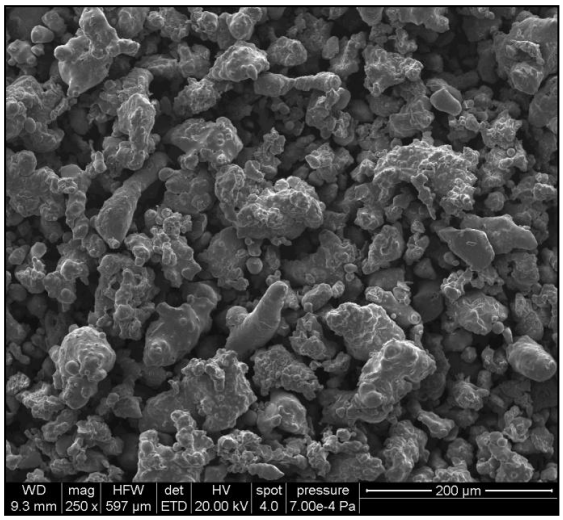

Fig. 3.7: SEM image of Fe21Cr

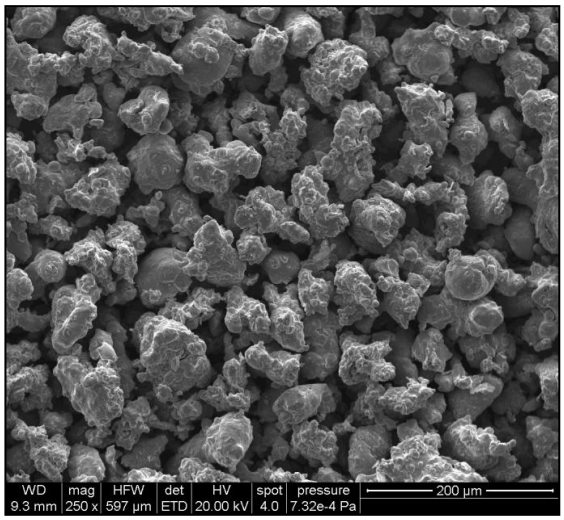

Fig. 3.8: SEM image of Fe21Cr0.5Nb

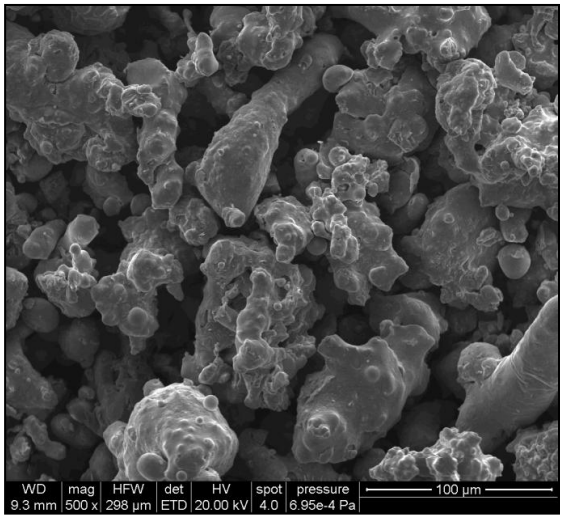

Fig. 3.9: SEM image of Fe21Cr

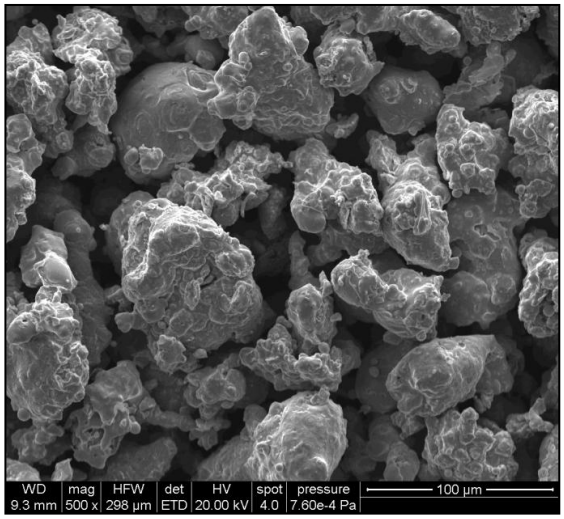

Fig. 3.10: SEM image of Fe21Cr0.5Nb

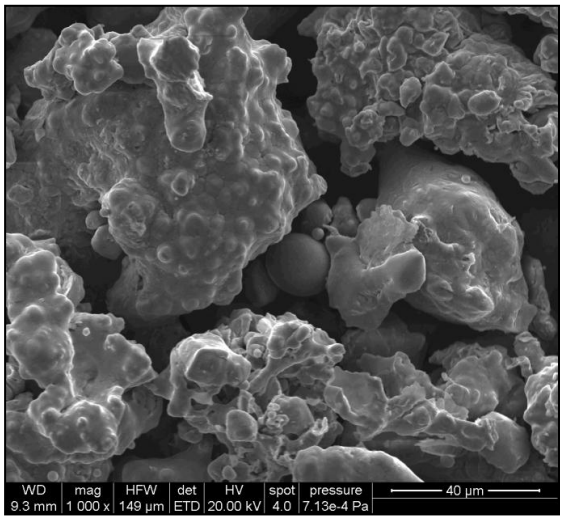

Fig. 3.11: SEM image of Fe21Cr

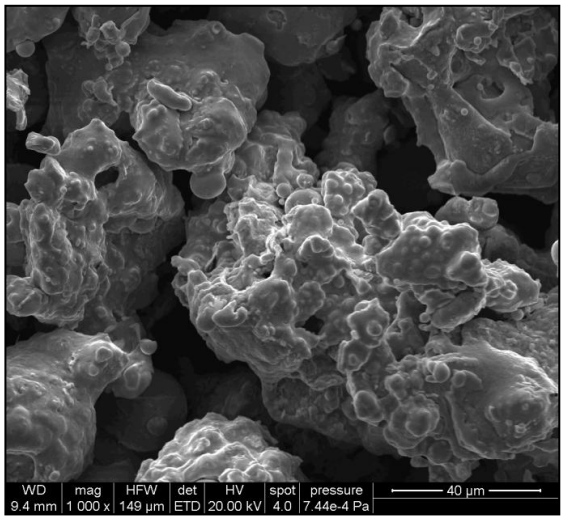

Fig. 3.12: SEM image of Fe21Cr0.5Nb

For the MIM and PEM experiments at University Carlos 3rd in Madrid-Leganes (UC3M) it was decided that one ferritic (430 LHC, <75 µm) and one austenitic (310 B, <53 µm, lot UC3M) powder should be used. The composition of these powders is shown in Table 3.4; the metallic alloying elements have been measured by Höganäs AB, whereas the interstitials (carbon, oxygen and nitrogen) have been measured at UC3M. The austenitic grade is designated 310B; however, regarding the relatively high Si content it is rather equivalent to AISI 314 (1.5 …3.0%Si, as compared to 1.5%Si for AISI 310). In the following, the powders are given by their chemical composition, to avoid confusion with the AISI designations.

Because of the better availability for a higher quantity (~ 100 kg) of the Fe16Cr (AISI 430) powder, it was decided to use the Fe16Cr grade instead of the Fe21Cr one used for the experiments at TUW.

Table 3.4: Measured composition of the base powder (data from Höganäs AB; interstitials measured at UC3M)

	Chemical composition (wt%)	
Element	**Fe16Cr**	**Fe25Cr20Ni2.5Si**
Fe	82,48	51,9
Cr	16,31	25,3
Ni	-	20,2
Si	1,03	2,5
Mn	0,18	0,1
C	0,013	0,021
O	0,20	0,17
N	0,007	0,08

The density of the powder was measured with the He-Pycnometer at UC3M. The measured pycnometric density of the ferritic powder Fe16Cr is 7.6570 ± 0.0116 g/cm³, for the austenitic grade Fe25Cr20Ni2.5Si it is 7.7583 ± 0.0111 g/cm³.

The particle size distribution for the Fe25Cr20Ni (lot TUW) and the Fe21Cr powder was measured at Höganäs AB with a Sympatec Helos particle size analyzer (Table 3.5). The Fe18Cr0.3Mn0.5Nb and Fe21Cr0.5Nb powder were not measured that time because they particle size distribution was expected to be the same. The results for the Fe21Cr grade can be seen in Fig. 3.13.

The ferritic and austenitic powders used for MIM and PEM experiments at UC3M were measured with a Malvern Mastersizer 2000E at UC3M using a wet dispersion of the powder and laser diffraction for analysis. The median values of the four measured powders are shown in Table 3.5. If the median values are compared, there is not a big difference between the four powders.

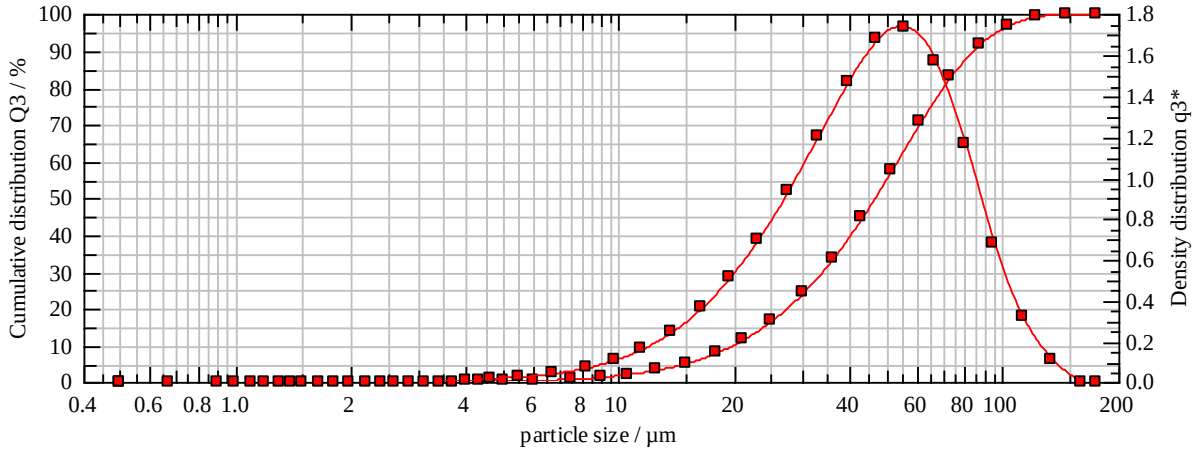

Fig. 3.13: Particle size distribution of the Fe21Cr powder

Table 3.5: Characteristic values of the particle size distribution of two ferritic and two austenitic base powder grades

Powder	Analyzing unit	d(0,1) [µm]	d(0,5) [µm]	d(0,9) [µm]
Fe25Cr20Ni	Malvern (UC3M)	18,82	38,67	71,58
Fe25Cr20Ni	Sympatec (HAB)	19,52	39,17	65,88
Fe16Cr	Malvern (UC3M)	20,02	41,79	78,74
Fe21Cr	Sympatec (HAB)	19,76	46,35	84,22

Fig. 3.14- Fig. 3.19 show the morphology of the powder used for the experiments at UC3M. The images were taken with the scanning electron microscope at UC3M (backscattered electron mode). The ferritic and austenitic powders were produced by water atomization; the irregular shape can be seen in the pictures.

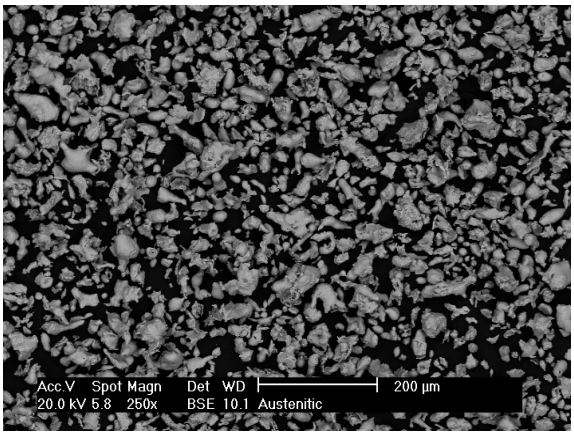

Fig. 3.14: SEM image of Fe25Cr20Ni

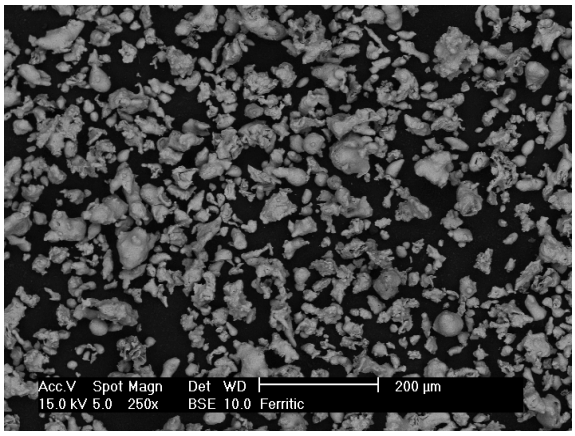

Fig. 3.15: SEM image of Fe16Cr

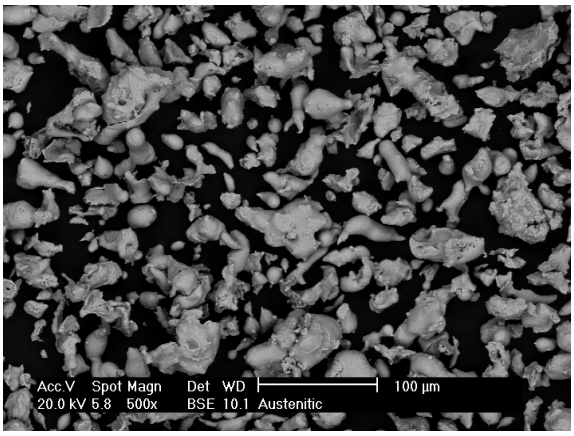

Fig.3.16: SEM image of Fe25Cr20Ni

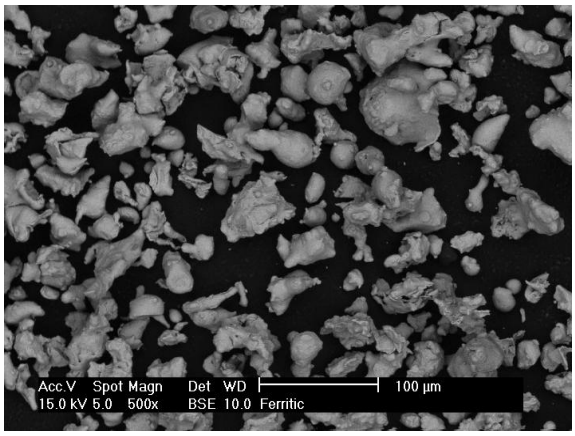

Fig. 3.17: SEM image of Fe16Cr,

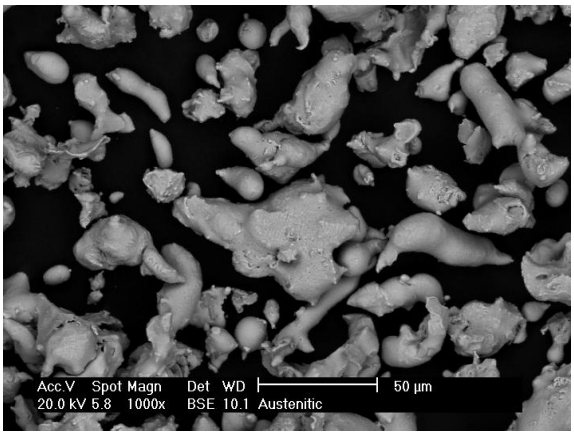

Fig. 3.18: SEM image of Fe25Cr20Ni

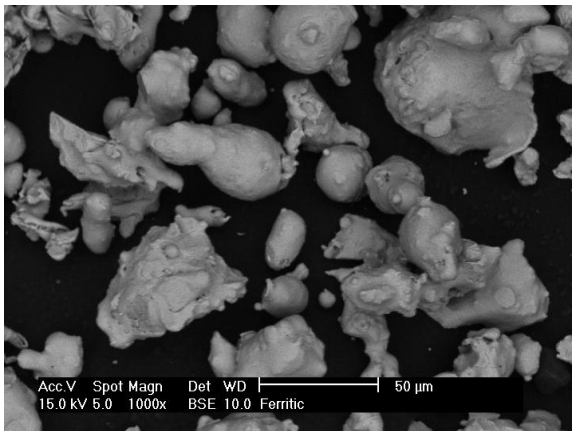

Fig. 3.19: SEM image of Fe16Cr

3.2 Mixing

For uniaxial compaction, the powder was mixed with lubricant (HWC or Kenolube P11) for about 1 hour in a tumbling mixer; typically, dry mixing was performed, except for high lubricant content. In this case the powders were mixed with paraffin wax (usually employed in hardmetal production, density 0.9 g/cm³) as a pressing lubricant, and then they were put in a 250 ml PE flask together with some steel balls. The flask was filled to the top with cyclohexane and put into a turbula mixer for 2.5 hrs. Then the cyclohexane was removed in a rotary evaporator, and the dry powder was sieved through a 315 µm sieve. The powder fraction <315 µm was then pressed in a tool with cylindrical cavity (11.28 mm diameter) or double action pressed in a pressing tool with floating die for Charpy bars ISO 5754.

3.3 Pressing

The starting powder is not commercially available and only produced in small, lab-scale units. Therefore the compressibility of the powder was investigated.

Universal testing machine:

Fig. 3.20: Universal testing machine Zwick 1474

Fig. 3.21: Pressing tool

The samples were mixed with 0.6 wt% HWC and then double action pressed in a tool for cylindrical specimens (cavity diameter 11.27 mm) at 200-800 MPa on a universal testing machine (Fig. 3.20, Zwick 1474 with a Messphysik ME46-NG video extensometer). Normally this machine is used for tensile, compression or bending tests, but can it can also be used for pressing small cylindrical samples under well controlled conditions, and if necessary compressibility curves can be taken. The pressing tool can be seen in Fig. 3.21. This tool has been standard for compactibility tests (Stahleisen-Prüfblatt – 85-69, Verlag Stahleisen GmbH,

Düsseldorf, 1969); now it is no more standard but is still convenient if limited amounts of powders are to be tested.

Hydraulic press:

Fig. 3.22:
Hydraulic press 1500 kN

The powders were either compacted with die wall lubrication (using Multical sizing oil) or mixed with pressing lubricant (Kenolube P11 or paraffin wax) and then the mix was pressed (double action) in a tool with floating die containing a cavity for charpy bars (55 x 10 mm²).

The hydraulic press itself is a 150 ton press from Jessernigg & Urban (Fig. 3.22). The compacting pressure started at 800 MPa and was then successively lowered; the aim was to decrease the pressure as much as possible to attain maximum porosity while retaining sufficient strength.

Pressing lubricants:

HWC: low amount of lubricant (0.6 wt%), dry mixing, cylindrical tool (results can be seen in Chapter 4.1.1)

Kenolube P11: low amount of lubricant (0.6 wt%), dry mixing, Charpy samples (results can be seen in Chapter 4.1.2.1)

Paraffin wax: usually employed in hardmetal production, density 0.9 g/cm³, high amount of lubricant, wet mixing, Charpy samples (results can be seen in Chapter 4.1.2.2)

3.4 Sintering

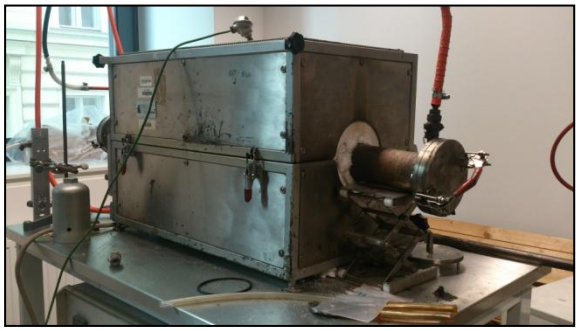

Fig. 3.23: Small laboratory furnace with FeCr-muffle (1.4841) used for dewaxing

After pressing, the green bodies with 0.6% P11 as a pressing lubricant were dewaxed in H_2 for 45 min at 600°C in a tube furnace with gas tight heat resistant steel muffle (EN 1.4841; purging atmosphere Ar 99.999%, flow rate 2.5 l/min; dewaxing atmosphere H_2 99.999%, flow rate 0.5 l/min). At the time the furnace had reached a stable temperature of 600°C, the furnace was opened and the boat with the samples was pushed in. To make sure that there is no oxygen left, the muffle was purged with Argon for further 1-2 minutes, and then the hydrogen valve was opened.

After dewaxing the boat was pushed into the water cooled area (cooling rate ~ 20 K/min) and taken out after cooling. Subsequently the oxygen and nitrogen contents of the specimens were measured.

Fig. 3.24: Large laboratory furnace

Most of the samples were sintered in an SiC rod heated tube furnace with superalloy muffle (Kanthal APM, Fe22Cr7Al) for 60 min isothermal soaking at 1300°C (H_2, 99.999%, flow rate 2 l/min). For cooling down to room temperature, the boat with the samples was pushed into the water cooled exit zone and remained there for about 30 min; the average cooling rate was 40 K/min.

Fig. 3.25: Vacuum furnace

For sintering in vacuum a tube furnace with a ceramic muffle (Pythagoras, Haldenwanger) has been used. The samples were sintered for 1 h at 1300°C; the vacuum was generated by two rotary vane pumps (~ 10^{-4} mbar).

3.5 Gravity sintered samples

In order to get more sintering shrinkage of the samples – and to check which shrinkage is attainable at zero compacting pressure - gravity (loose powder) sintering was tried, as is standard e.g. for manufacturing of porous bronze filters. Therefore the powder was filled into Al_2O_3 crucibles (from the Leco CS analyzer) and then sintered at 1300°C for 1 h in H_2 (99,999%, flow rate 2 l/min). Two different filling techniques (tapped or not tapped) were tried in order to check the impact of the filling on the density and shrinkage. In the first run it was tried not to tap the crucible while filling and while putting it in the furnace (starting from bulk state). In the second run the powder was filled into the crucibles and tapped while filling, in order to get more powder into the crucible, i.e. to start from the tap density and also to have a more stable powder bed. Naturally the mass in the second run is always higher than in the first or second run. Fig. 3.26 shows a comparison of gravity sintered samples before and after sintering.

Fig. 3.26: Comparison of gravity sintered samples before (bottom)and after sintering (top). The shrinkage is evident.

For a more precise measurement of the shrinkage, gravity sintering experiments in an Al_2O_3-boat have been carried out. The dimensions of the boat are (inner diameter): 97.3 x 28.1 x 26.3 mm. Also presintering experiments (two-step sintering) have been tried. Therefore the powder was filled into Al_2O_3-boats (half-full) and heated up to 900°C in argon. The gas was then switched to hydrogen (2 l/min) and the powder was presintered for 30 min at 900°C (1100°C). The powder was then also cooled down in hydrogen atmosphere to room temperature. Final sintering took place at 1300°C for 1 hr in hydrogen. The effect of presintering on the shrinkage was determined.

3.6 Polyvinyl alcohol samples

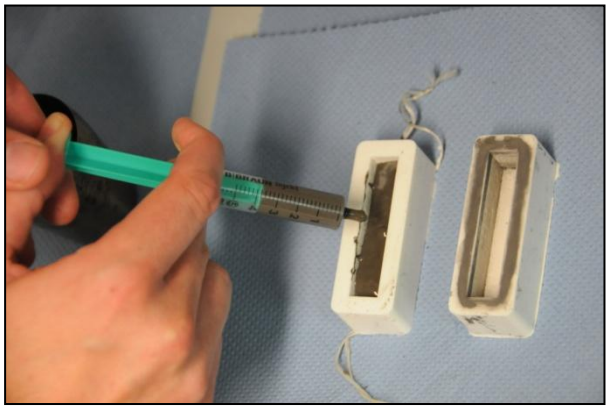

Fig. 3.27: Injection of the slurry into the silicon mold

Another binder system that was tested was a polyvinyl alcohol solution (5.0 wt%) in distilled water. 100 g of Fe21Cr and 12 wt% of the polyvinyl alcohol solution (PVA) were mixed in a cup and stirred into a slurry. The slurry was injected with a syringe into a silicone mold (Fig. 3.27) and put into a drying chamber for approx. 20 hrs at 80°C. The dried samples were heated up in vacuum from room temperature to 1200 – 1300°C (heating rate 10 K/min) and then held for 60 – 360 min.

After that the samples were cooled down to room temperature again as fast as possible (estimated cooling rate: 10 K/min to 800°C, then 5 K/min). Also some sintering experiments under hydrogen were carried out, but the samples tended to break and showed more deformation than the samples sintered in vacuum. The density (green and sintered; volumetric method), linear shrinkage, porosity and metallographic pictures can be seen in Chapter 4.3.1.

3.7 Latex binder samples

Another binder system based on a styrene and butadiene copolymer, Styronal D 517 (from BASF), has been tried. The Fe21Cr powder was mixed with 20 wt% Styronal (white, viscous liquid) and cyclohexane for 2 hrs. Then the liquid was decanted, and the powder was just formed by hand into rectangular shape and dried overnight in a fume hood. Then the sample was dewaxed as described above (600°C, 60 min, Ar flow rate 2 l/min; H_2 flow rate 0.5 l/min) and sintered (1300°C, 60 min, H_2 flow rate 2 l/min). Results are shown in Chapter 4.3.2.

3.8 Feedstock experiments

Feedstock experiments, metal injection molding (MIM) and powder extrusion molding (PEM) were performed at the University Carlos 3rd Madrid (UC3M, Madrid-Leganes).

It was decided that the ferritic Fe16Cr and austenitic Fe25Cr20Ni2.5Si powders, respectively, should be mixed with only one binder system and powder loading first. After that, experiments on a low pressure injection unit (see Fig. 3.28) were started in order to check if samples can be produced from this feedstock. It was planned that if samples could be manufactured with that feedstock successfully, a larger quantity of feedstock should be prepared in order to go on with extrusion or metal injection molding. All feedstocks used for low pressure injection were mixed with a Haake Rheomix lab mixer with following

parameters: feedstock temperature 170°C, mixing time 120 min, and rotation of rotor blades 40 rpm. To evaluate the homogeneity of the powder-binder mixtures, torque measurements were carried out while mixing. The mixture is homogeneous when the torque value reaches a steady state and torque (measured as a resistance against the rotor blades) remains constant with mixing time. After mixing and cooling down to room temperature the feedstock was granulated.

Fig. 3.28: Low pressure injection unit at UC3M

To start with, ferritic powder was mixed with a binder composed of high density polyethylene (HDPE, Dow Plastics) and paraffin wax (PW, pellets, Panreac). The solid loading was 50%; the binder itself consisted of 50 vol% HDPE and 50 vol % PW. The solid loading of the ferritic feedstock was then switched to 45 and 55 vol%, but none of them did work out for the low pressure injection unit either because the feedstock got stuck in the mold.

After that, austenitic powder was mixed with a binder consisting of 47.5 vol% HDPE, 47.5 vol% PW and 5 vol% stearic acid as a surfactant.

The powder loading still remained 50 vol%. Also the austenitic powder-binder system with stearic acid (SA) could not be injected at low pressure, because the feedstock got stuck in the mold again.

In total, more than 10 different feedstocks were produced. For example, polyethylene was replaced by polypropylene or a different kind of paraffin wax was used, but not even one feedstock worked properly for low pressure injection.

A reason for that could be that the maximum injection pressure of the low pressure injection unit could not be raised above 120 psi (8.3 bar), and that is apparently too low for the feedstock. One may argue that the irregular shape of the powder has a strong impact, but also spherical powder (Osprey TI 15) mixed with HDPE and PW could not be injected with this unit. In order to increase the pressure, extrusion molding with a twin screw extruder and standard pressure injection molding have been tried. As a binder system for the austenitic powder, HDPE and paraffin wax and for the ferritic powder HDPE, paraffin wax and stearic acid were chosen.

The first successful high pressure PEM and MIM rounds were performed with the ferritic powder and HDPE, paraffin wax and stearic acid as a binder, made with the Haake Rheomix

lab mixer. After that, injection molding has been tried with the austenitic feedstock (HDPE and paraffin wax as a binder). This feedstock had also been made with the lab mixer and was therefore already available. In order to save time, this feedstock has been chosen for injection. After the successful injection it was decided not to change the binder system, i.e. not to add stearic acid to the austenitic binder system.

3.9 Metal Injection Molding

These experiments were performed on a hydraulic injection molding machine Arburg ALLROUNDER 220S at UC3M. Table 3.6 shows the feedstocks which were then used for manufacturing of MIM parts. For working with the molding machine, a fairly large amount of powder is necessary. Therefore the different powder-binder systems were mixed with the extrusion unit (Rheomexx, twin screw extruder), because the volume of the mixing chamber of the small mixing unit (Haake Rheomix) is only 48 cm^3 while for injection molding around 250 cm^3 are needed. The MIM parameters such as injection pressure and injected volume can be seen in Table 3.7, a comparison of the green and sintered MIM samples can be seen in Fig. 3.29.

Table 3.6: Feedstocks for MIM and PEM samples
(PE: high density polyethylene; PW: paraffin wax; SA: stearic acid)

Powder	Binder	composition feedstock (vol%)			
		powder	HDPE	PW	SA
Fe16Cr	PE + PW + SA	55	21,35	21,35	2,3
Fe16Cr	PE + PW + SA	50	23,75	23,75	2,5
Fe16Cr	PE + PW + SA	45	26,1	26,1	2,8
Fe25Cr20Ni2.5Si	PE + PW	55	22,5	22,5	-
Fe25Cr20Ni2.5Si	PE + PW	50	25,0	25,0	-
Fe25Cr20Ni2.5Si	PE + PW	45	27,5	27,5	-

It is remarkable that for the austenitic sample the injection pressure decreases with increasing powder loading.

Table 3.7: Injection parameters for metal injection molding

Powder	powder loading (vol%)	Injection pressure (bar)	Injection volume (cm^3)
Fe16Cr	45	700	5,0
Fe16Cr	50	950	3,6
Fe16Cr	55	1200	4,0
Fe25Cr20Ni2.5Si	45	700	4,8
Fe25Cr20Ni2.5Si	50	800	4,0
Fe25Cr20Ni2.5Si	55	500	6,0

Fig. 3.29 Comparison of green (above) and sintered MIM parts (1300°C, 60 min, vacuum)

Further on, all MIM parts were debinded (two-step debinding, solvent and thermal) and then sintered at 1300°C for 60 min in vacuum at Leganes. The exact procedure will be described below.

In Fig. 3.30 - Fig. 3.33 SEM images (fracture surface) of the MIM green parts are shown. The green parts were broken by hand and then immediately examined by SEM at UC3M (without sputtering). It can be seen that the molten binder coats the surface of the sample.

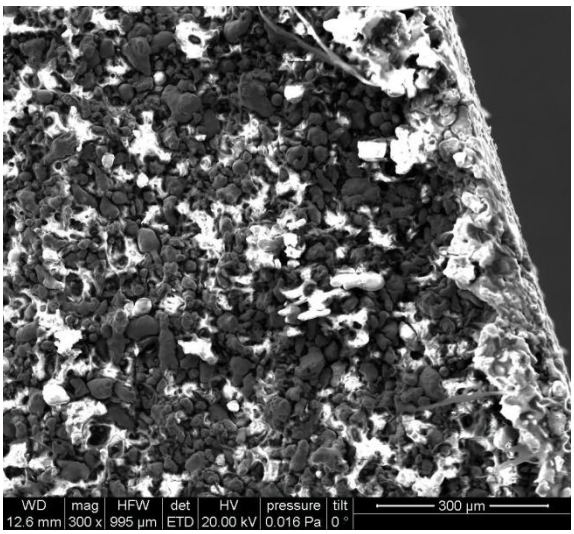

Fig. 3.30: SEM image (fracture surface) of an austenitic MIM sample (green part) with 50 vol% powder loading

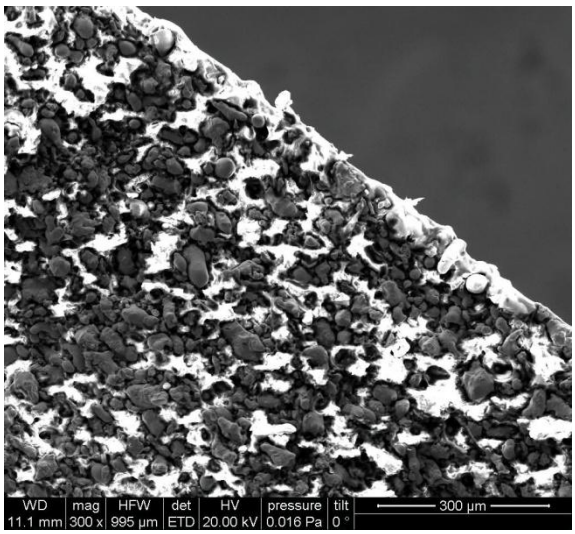

Fig. 3.31: SEM image (fracture surface) of a ferritic MIM sample (green part) with 50 vol% powder loading

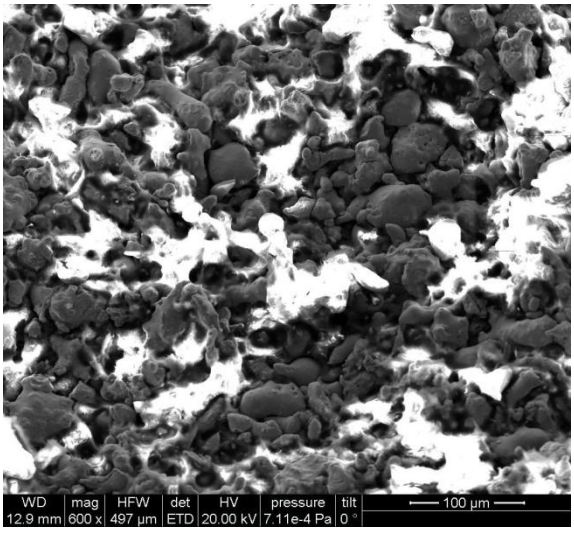

Fig. 3.32: SEM image (fracture surface) of an austenitic MIM sample (green part) with 50 vol% powder loading

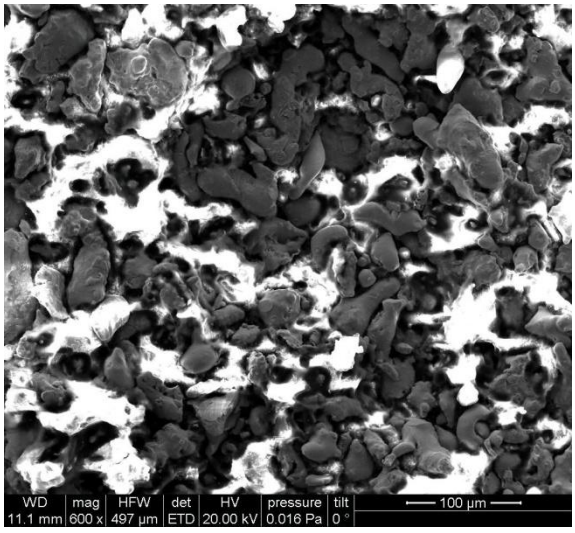

Fig. 3.33: SEM image (fracture surface) of a ferritic MIM sample (green part) with 50 vol% powder loading

3.10 Powder Extrusion Molding

The powder extrusion was done at UC3M with a Haake Rheomexx twin screw extruder using a cylindrical nozzle. The feedstock temperature was set at 170°C. In order to get a homogeneous feedstock, the powder and the binder were just filled into the cavity of the Rheomexx, without premixing, and then extruded twice without the nozzle. In the third round, the nozzle was put on the device, and the samples were extruded to cylindrical rods (average length: 40-50 mm, diameter: 7-8 mm).

The debinding and sintering process was done exactly the same way as for the MIM samples and is described in Chapter 3.11. Fig. 3.34 shows a comparison of the green and sintered samples. The shrinkage is evident. In Fig. 3.35 a ferritic PEM sample is shown after thermal debinding; evidently cracks can occur during thermal debinding. Typically, one out of four samples was cracked while debinding (an example is shown in Fig. 3.35, top left specimen), regardless of the binder content or base powder used. This percentage is valid for all sinter runs.

Fig. 3.34: Comparison of PEM samples (ferritic, 55 vol% powder loading); green (above) and sintered (below, 1300°C, 60 min, vacuum) state

Fig. 3.35: PEM samples (ferritic + 50 vol% powder loading) after thermal debinding.

3.11 Debinding and sintering of MIM/PEM parts

The debinding procedure is based on the knowhow of UC3M, and also DSC and TGA measurements of green parts were performed, the curves are shown in Fig. 4.71 and in Fig. 4.72. The debinding was carried out in two steps (solvent and thermal). First, the green samples were dewaxed in cyclohexane at 60°C for 5 hrs and then dried overnight in a drying chamber at 70°C. For the following thermal debinding, the samples were heated from room temperature to 300°C, held for 1 hour, then to 475°C with a holding time of 1 hour and finally to 550°C and held at that temperature for one hour before cooling down to room temperature

again. The heating and cooling rates were set at 5°C/min, the atmosphere was compressed air. The carbon, oxygen and nitrogen contents were determined by LECO measurements.

After debinding the samples were sintered at 1300°C for 1 hour in high vacuum (~ $2*10^{-5}$ mbar at high temperature) at UC3M. The heating and cooling rates were set at 5°C/min. For comparison, some samples were also sintered at 1300°C in H_2 (99,999%, flow rate 2 l/min) for 60 minutes at TUW in the large laboratory furnace.

3.12 Plates Höganäs

Very thin austenitic and ferritic plates with a thickness around 0.40 mm produced by tape casting have been handed out by Höganäs AB for further analysis at TUW (see Fig. 3.36 and Fig. 3.37). The chemical composition measured with XRF spectrometry at TUW can be seen in Table 4.32. DTA/TG-QMS measurements were performed in wet and dry hydrogen (flow rate: ca. 10 ml/min). Therefore the samples were heated up from 40°C to 1590°C and then cooled down back to 50°C (20 K/min).

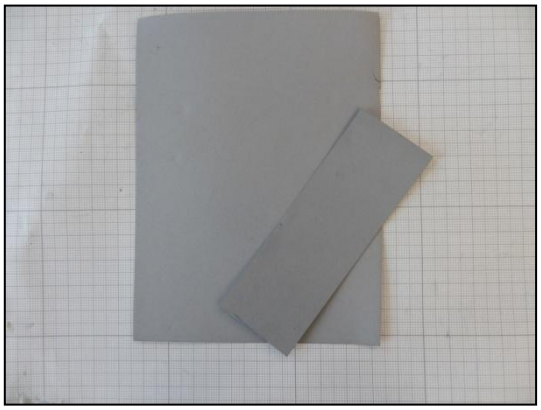

Fig. 3.36: Tape cast plates from Höganäs

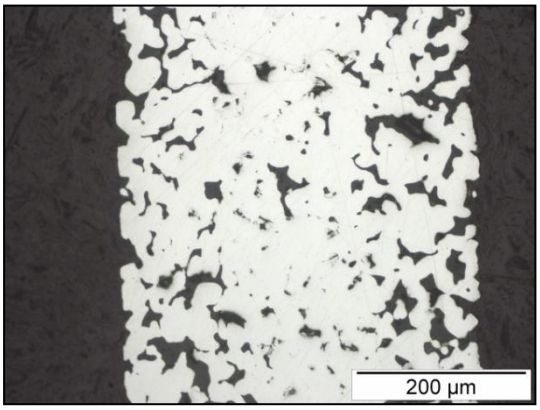

Fig. 3.37: Cross section of the plates; the thickness is around 400 µm

For annealing tests in the dilatometer the samples were heated up from room temperature to 600°C, 700°C, 800°C and 900°C, held there for 1 hour in wet hydrogen and then cooled back to room temperature (see Fig. 3.38). For creating a wet hydrogen atmosphere, the hydrogen passed through a gas washing flask filled with distilled water (22°C).

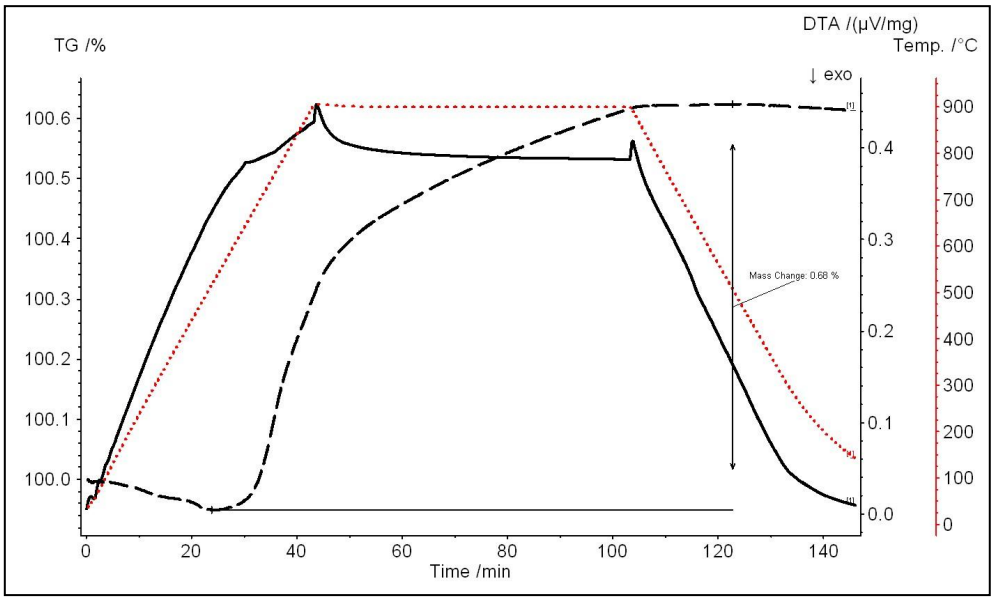

Fig. 3.38: DTA/TG-measurement of the ferritic plate (threshold 900°C, 1h, wet H_2). The broken black line stands for TG measurements, the solid black line for DTA measurements

3.13 Characterization

Measuring the density or porosity, resp. of metallic filters can be done by water displacement method (DIN EN ISO 2738). This method has also been suitable for measuring the density of the metal substrates and is described in detail in Chapter 3.13.2. An alternative method for measuring the density is by gamma radiation, because the capability of absorption is depending on the density of the parts. A well defined beam passes through the samples, where it is partly absorbed and the attenuation is measured by a detector [**104**]. In this work, the measurement by water displacement method worked out well and there was no need to analyze samples by this special technique.

Another way of measuring the pore size is either by mercury intrusion, gas adsorption, electro acoustic spectroscopy or by capillary flow porometry. In this work the method of choice was mercury intrusion because the analysis could be done “in-house” at TUW at the Institute of Building Construction and Technology

In this work, most of the time the values of the density are given as absolute values and not relative values. The reason is that at this high porosity levels, there is no big difference of the theoretical density.

3.13.1 Density by volumetric method

The density was calculated by measuring the dimensions with a sliding caliper (accuracy 0.01 mm) and the weight (laboratory balance, accuracy 0.1 mg). The density was then calculated by using the following formula:

$$\rho_{green} = m / (l * b * h)$$

ρ_{green} ... green density [g/cm³]
m ... mass [g]
l ... length [cm]
b ... width [cm]
h ... height [cm]

If not mentioned otherwise, the green densities were measured by the volumetric method.

3.13.2 Density by water displacement method

For measuring the density by the water displacement method (Archimedes principle, DIN ISO 3369), the samples were soaked in a water-repellent fluid (commercial water stop spray) for approx. 5 minutes (to avoid water penetration of the open pores). Then they were taken out and sprayed once more, to make sure that they were 100% water repellent. After that they were dried overnight, the weight of the samples in air and in water were measured the following morning. The displacement in air was regarded irrelevant and was ignored.

$$\rho_{sintered} = (m_a / m_a - m_w) * 0.998$$

$\rho_{sintered}$ ... sintered density [g/cm³]
m_A ... weight in air [g]
m_W ... weight in water [g]
0.998 ... density of water at 23°C [g/cm³]

If not mentioned otherwise, the sintered densities were measured by the water displacement method. In the following, mostly absolute density values are given; since however the theoretical (pore-free) density data of the steel grades used are very similar, the relative density is not shown, also because the total porosity data are presented anyhow.

3.13.3 Total porosity

The total porosity was calculated by the following equation:

$$P = (1 - \rho_{sintered} / \rho_{theoretical}) * 100$$

P ... Porosity [%]
$\rho_{theoretical}$ ... theoretical density of the material measured by He-pycnometry [g/cm³]

The measured density with the He-Pycnometer was taken as theoretical density. It can be assumed that within the particles some closed porosity exits, but at these high porosity levels (> 30%), the resulting error can be disregarded.

3.13.4 Open porosity

The volume of the sample was measured by the Ultra-Pyknometer 1000T (Quantachrome). Helium was used as an inert gas because due to its small atomic dimensions it is able to penetrate even the finest open pores to assure maximum accuracy (Fig. 3.39).

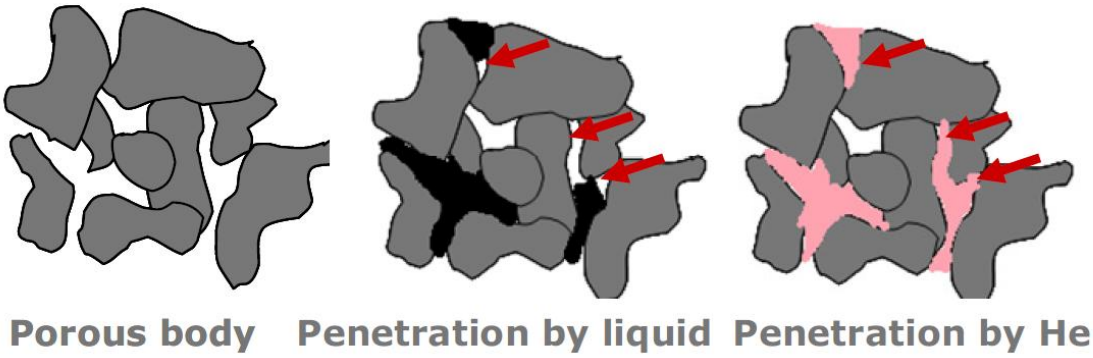

Fig. 3.39: Comparison of the pore penetration by liquids and He during pycnometry [105]

The measurement is accomplished by employing Archimedes' principle of fluid displacement and Boyle-Mariotte's to determine the volume. Boyle-Mariotte's law defines that the product of the pressure of a gas and the volume are constant at a given temperature. If the sample chamber is now pressurized to some pressure above ambient (18 psi), the state of the system is given by

$$P_2(V_C - V_P) = n\,R\,T$$

V_C	...	volume of the sample chamber
V_P	...	volume of the sample
P_2	...	pressure of the gas above ambient
n	...	total number of moles of gas
R	...	gas constant
T	...	gas temperature

If the valve opens to connect an added volume V_A, the pressure will decrease to the value P_3 (approx. 16 psi) due to the higher volume.

$$P_2(V_C - V_P) = P_3\,(V_C - V_P + V_A)$$

This equation can be changed to:

$$V_P = V_C + \frac{V_A}{1 - (P_2 / P_3)}$$

The instrument calibrates the values for the added volume V_A and the volume of the sample chamber V_C and by knowing the weight of the sample the density can be calculated easily [**106**].

Each powder was measured three times and then mean value and standard deviation were calculated.

3.13.5 Dimensional change

The dimensional change of the samples was determined by measuring the length before and after sintering.

$$\Delta l = [(l_s - l_g) / l_g] * 100$$

Δl ... dimensional change (%)
l_s ... length of the sintered part [mm]
l_g ... length of the green part [mm]

3.14 Metallographic investigation

The samples were cut into small pieces either with a water cooled Al_2O_3-cutting disk (Struers Accutom 50) or by hand with a hacksaw and then embedded in a hot mounting resin (Struers Multifast), polished (220 µm – 9 µm – 3 µm) and - due to the high porosity of the samples - they were impregnated with a synthetic resin (Struers, Epofix resin + hardener).The impregnation unit can be seen in Fig. 3.40. Then they were polished once more and photos (of the pore structure) were taken with an optical microscope.

Fig. 3.40: Impregnation unit at TU Wien

3.15 Optical investigation

3.15.1 Light optical microscope

The samples were investigated under an inverted optical microscope (OLYMPUS GX 51) with the analySIS 5.0 Soft Imaging Software. The microscope is used for standard optical studies for magnifications from 50 - 1000x and suited for bright-field, dark-field and polarized light optical analysis.

3.15.2 Scanning electron microscope (SEM)

With scanning electron microscopy it is possible to gather information especially of the surface, particle size or morphology, crystal orientation or texture (with EBSD) **[107]**. In this work, the morphology of the powders was studied by scanning electron microscopy (using a SEM FEI Quanta 200 at Vienna University of Technology and a PHILIPS XL-30 at UC3M, Madrid-Leganes). The SEM FEI Quanta 200 uses a tungsten filament as electron source, and for image data a secondary electron detector or backscattered electron detector can be used. Elemental analysis can be done with an energy dispersive spectrometer.

3.16 Chemical and structural analysis

3.16.1 XRF measurements

To characterize the metallic alloying elements of some samples at the Vienna University of Technology a wavelength dispersive XRF spectrometer (Panaytical Axios Advanced) with a Rhodium X-ray tube anode (Rh Kα radiation) has been used.

3.16.2 XRD measurements

XRD measurements have been carried out at the X-Ray Center at TU Wien. XRD analysis has been done using a PANalytical X'Pert PRO Bragg-Brentano X-ray powder diffractometer with a CuKα1 (λ = 1.5406 Å) wavelength and an X'Celerator detector. Typical conditions of measurements were continuous scans of flat specimens (scan region 2θ = 5-90°). For qualitative phase analysis the X'Pert High Score 4.1 software and for quantitative phase analysis the TOPAS 4.1 program based on the Rietveld method was used. The Rietveld code essentially is a non-linear least-squares algorithm where a model diffraction pattern that has contributions from both diffractometer and sample is fitted against the observed diffraction pattern.

3.16.3 Carbon/Sulfur content

The carbon and sulfur content was measured with a LECO CS 230 analyzer (Fig. 3.41).

0.1 – 1 g of the sample is put together with tungsten (as accelerator material) into an Al_2O_3-crucible. The combustion chamber is purged with oxygen, and then a constant O_2-flow is adjusted. The inductive elements of the sample and the accelerator couple with the high frequency field of the furnace. The heat and the pure oxygen atmosphere generate combustion of the sample. During combustion, the carbon of the sample forms CO or CO_2. Carbon monoxide is converted in the catalytic heater assembly to CO_2 and this is detected by IR-spectrometry. Sulfur-bearing elements react to SO_2 which is also measured in the IR-cell **[108]**.

Fig. 3.41: Leco CS230 Determinator

3.16.4 Nitrogen/Oxygen content

The nitrogen and oxygen content was determined with a LECO TC400 analyzer through hot fusion gas analysis in He atmosphere. The sample is put into a graphite crucible, and high current passes through the crucible, heating it to about 2000°C. During a first outgassing step, the gases trapped in the graphite are removed, then the sample is inserted into the crucible. At high temperature, reduction of present oxides by the carbon of the crucible takes place, the elements reacting to carbon monoxide or dioxide. Carbon monoxide is converted into carbon dioxide which is then detected by the IR cell. After detection, the CO_2 is removed with Lecosorb and resulting water vapor with Anhydrone. The remaining nitrogen is then detected by the TC (thermal conductivity) cell **[109]**.

3.16.5 Hg-Porosimetry

Hg-Porosimetry measurements of specific samples have been carried out on a POROTEC Pascal Mercury Porosimeter at the TU Wien (Institute of Building Construction and Technology). With this intrusion technique, it is possible to obtain information about pore size / volume distribution, mean pore radius, total pore volume, specific pore surface, and particle size.
The analysis is based on intrusion of Hg into the solid material porous structure under controlled pressurization **[110]**.

Fig. 3.42: POROTEC Hg-Porosimeter

The applied pressure is inversely proportional to the pore radius. The Washburn-equation [**111**] gives the pressure needed for intrusion:

$$p = (2 \gamma \cos \theta) / r$$

p...pressure [Nm^{-2})]
γ...surface tension of mercury [Nm^{-1}]
θ...contact angle [°]
r...pore radius [m

The pressure is then incrementally increased and the corresponding volume of mercury entering the specimen is measured, and a distribution of the pore size can be calculated.

3.17 Thermal analysis

In this work, samples were investigated by a range of thermoanalytical methods such as dilatometry (DIL), thermogravimetry (TG) and differential thermal analysis (DTA) combined with mass spectroscopy (MS).

3.17.1 Dilatometry

For highly precise measurement of dimensional changes of solids at a programmed temperature change with a negligible sample strain, dilatometry is the method of choice **[112]**.

In order to obtain the dimensional changes of the sample, dilatometer runs were carried out using a pushrod dilatometer Netzsch 402 DIL with Al_2O_3 measuring system and Proteus software. The samples were double action pressed at 400 MPa (with die wall lubrication) and then cut into 10 x 10 mm^2 pieces. Measurements were carried out perpendicular to the pressing direction. In the dilatometer runs, the samples were heated up with 10 K/min from 30°C to 1300°C, then held isothermally for 60 min at 1300°C and after that cooled down from 1300°C to 30°C with 10 K/min. The atmosphere was hydrogen (99.999% purity, flow rate 37.5 ml/min).

3.17.2 Differential thermal analysis / Thermogravimetry

For thermogravimetric measurements, the weight is plotted as a function of temperature, and/or over a function of time at constant heating rate. The change in mass can be caused by e.g. reduction of (surface) oxides.

In the differential thermal analysis a sample and a reference specimen (thermal conductivity and heat capacity should be nearly the same as in the test sample) undergo the same temperature/time profile, and the difference in temperature (ΔT) between both is monitored. Usually, temperature (or time) is plotted on the x-axis and the ΔT is plotted on the y-axis **[113]**.

Thermogravimetric Analysis (TG) and Differential Thermal Analysis (DTA) were performed on a simultaneous thermal analyzer Netzsch STA 449 equipped with a Netzsch Aeolos mass spectrometer (QMS) for atmosphere analysis. The sample temperature was measured with a WRe thermocouple, since this thermocouple can be used in H_2, in contrast to the common PtRh-Pt types. For creating a wet hydrogen atmosphere, the hydrogen passed through a gas washing flask filled with distilled water (room temperature about 22°C).

3.18 Image analysis

Bevor going into detail about image analysis it has to be said that there is a very good review on the sequence of image acquisition, processing, analysis and output made by Paciornik and de Pinho Mauricio **[114]**. Recently, the techniques of image analysis have been valued as powerful tools in the fuel cell research. Simwonis introduced this technique for the evaluation of Ni-YSZ anode degradation **[115]**. Furthermore it is possible to obtain information about phase fraction and grain size, and even more, it is possible to build 3D structures of the fuel and air electrode having 2D images as input **[116]**. In this work, porosity quantification by image analysis has been carried out for the samples with the software program *Fiji*, an open source image processing program based on *ImageJ*. To calculate the porosity, the photo image was first converted into a grayscale picture, then a threshold was set automatically by the program (below threshold pixels are black; all other pixels set to white). In the next step, an area fraction was analyzed by the program, i.e. the program calculates the percentage of all "black" parts in the image. Pores that are cut by edges are included (see Fig. 3.44).

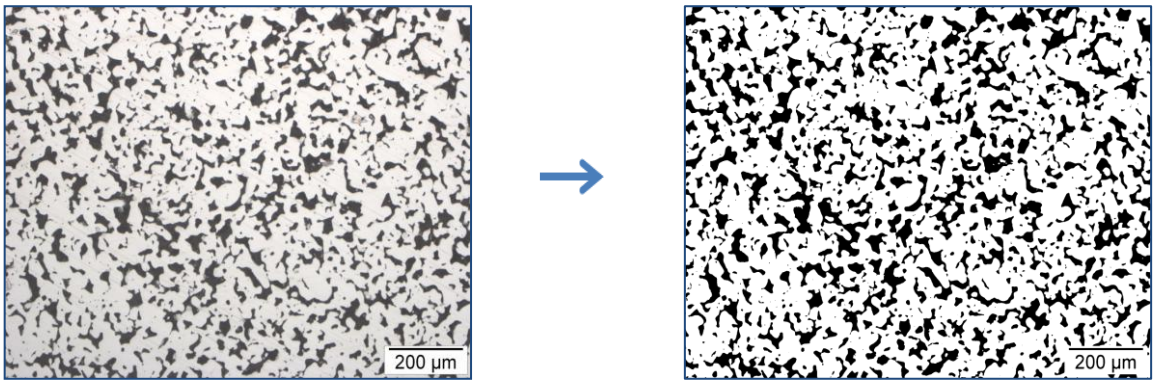

Fig. 3.43: Left: unmodified microscope image **right: grayscale image**

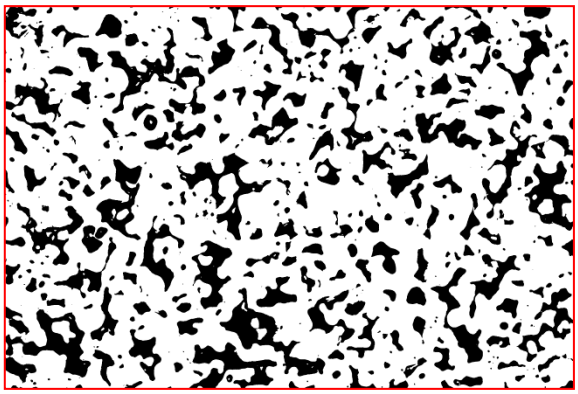

Fig. 3.44: Edges were included for area porosity calculations

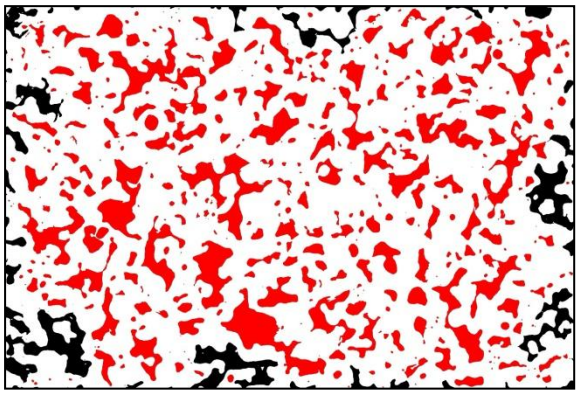

Fig. 3.45: Exclude edges for pore sizee distribution calculations

Pore size distribution calculations are possible by using basic geometrical parameters like surface area, Feret diameter or perimeter of the pores. In this work, most samples show a network of interconnected pores, so for these calculations the parameter surface area of the pores has been used. Pores that are cut by edges are not included (see Fig. 3.45).

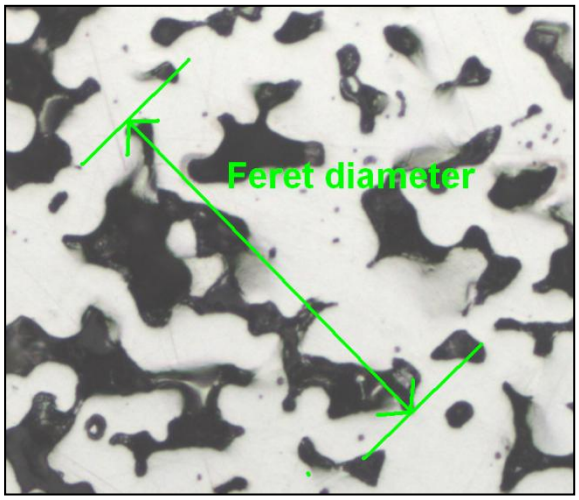

Fig. 3.46: Example for the Feret diameter of a pore

For comparison, calculations have also been made with the Feret diameter.

The Feret diameter is the longest distance between any two points along the selection boundary, also known as the maximum caliper [**117**].

In this work, the Feret diameter is referred to the maximum caliper of pores and not particles (Fig. 3.46). All results for the image analysis are shown in chapter 4.7.

4. Results & Discussion

It was tried to manufacture a porous metal support by alternative manufacturing routes like pressing and sintering, gravity sintering, by using different binder systems, powder extrusion molding or metal injection molding. Tape cast plates were handed out by Höganäs for further investigation. The obtained results are described in the following.

4.1 Pressed samples

The four starting powders (Fe21Cr, Fe21Cr0.5Nb, Fe18Cr0.3Mn0.5Nb, Fe25Cr20Ni2.5Si – lot TUW) are not all commercially available and in part only produced in small, lab-scale units. Therefore the compressibility of the powder has been investigated.

4.1.1 Compressibility tests (cylindrical tool)

In order to gather some information about the compressibility of the powders, cylindrical samples were pressed. One major advantage of this small pressing tool is that only a small amount of powder (~ 5 g) is necessary to produce a sample. After pressing and sintering, the green and sintered density was measured.

The starting powders (Fe21Cr, Fe21Cr0.5Nb, Fe18Cr0.3Mn0.5Nb, Fe25Cr20Ni2.5Si) were mixed with 0.6% HWC as pressing lubricant and then pressed (double action) in the small cylindrical tool (diameter: 11.27 mm) with 200-800 MPa, the green densities (Archimedes method) are shown in Fig. 4.1.

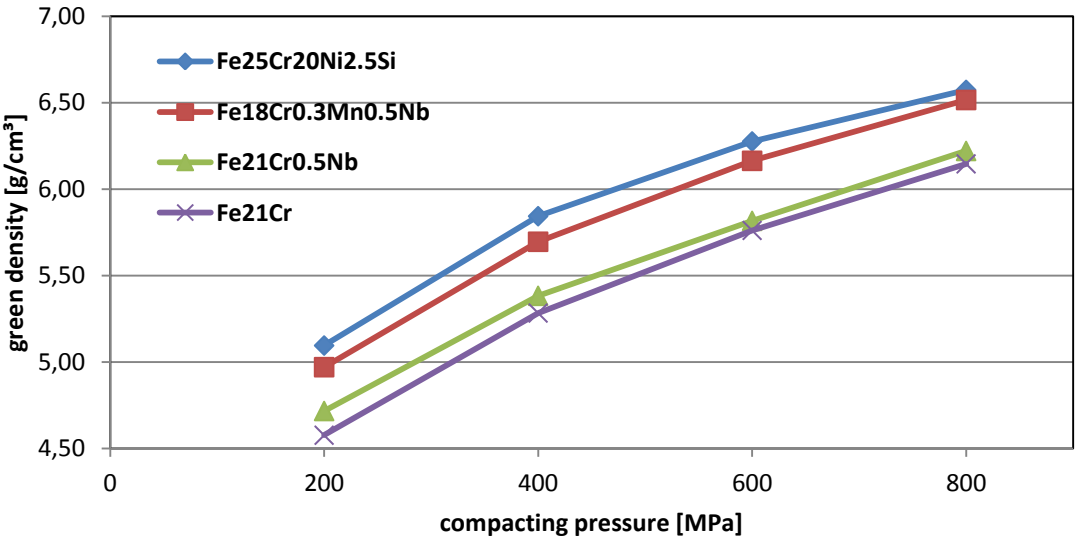

Fig. 4.1: Compactibility curves of stainless steel powders, compacted with 0.6% HWC

After pressing, the samples were dewaxed for 30 min at 600°C (Ar 99.999%, flow rate 1 l/min, small laboratory furnace) and then sintered for 60 min isothermally at 1300°C (H_2, 99.999%, flow rate 1 l/min, large laboratory furnace). The sintered densities (Archimedes method) are shown in Table 4.1 and Fig. 4.2.

Table 4.1: Comparison of green and sintered density (Dewaxed at 600°C in Ar for 30 min; sintered 1 h 1300°C in H_2) .

Sample	compacting pressure (MPa)	green density [g/cm³]	sintered density [g/cm³]
Fe25Cr20Ni2.5Si	200	5,10	6,16
	400	5,84	6,51
	600	6,28	6,83
	800	6,57	7,06
Fe18Cr0.3Mn0.5Nb	200	4,97	6,11
	400	5,70	6,30
	600	6,16	6,62
	800	6,52	6,91
Fe21Cr	200	4,58	5,87
	400	5,28	5,89
	600	5,76	6,19
	800	6,15	6,54
Fe21Cr0.5Nb	200	4,72	6,00
	400	5,38	6,01
	600	5,82	6,39
	800	6,22	6,73

Once more, the Fe21Cr alloy has the lowest sintered density of all samples. The shape of the graphs for Fe21Cr and Fe21CrNb is quite surprising, in particular the very small difference between 200 and 400 MPa. Nevertheless, these experiments were made just to check the compressibility with a small amount of powder, therefore the significance of these preliminary tests should not be overestimated.

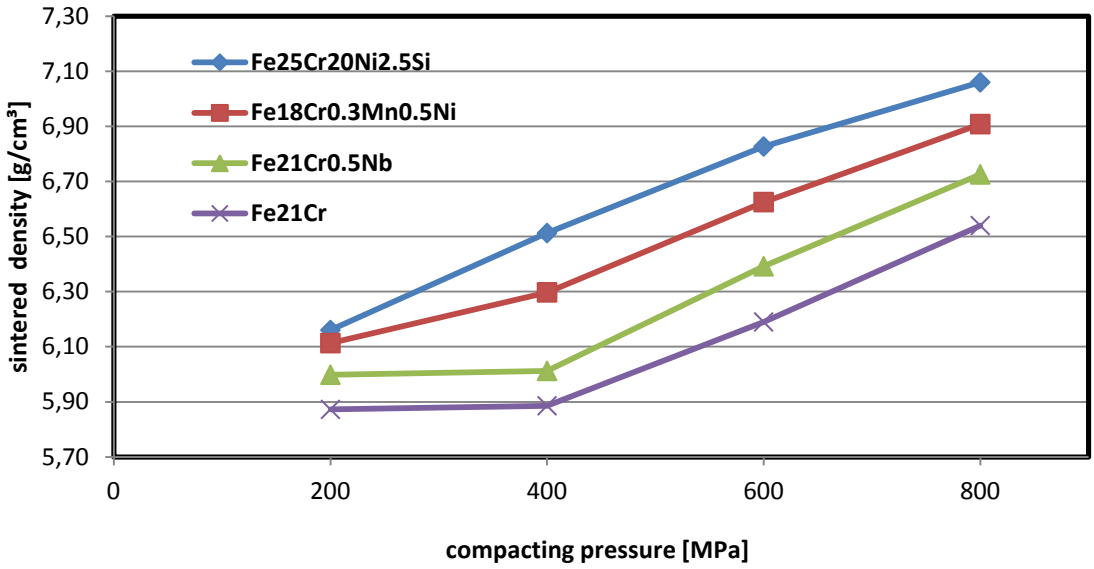

Fig. 4.2: Comparison of the sintered density (cylindrical samples). Dewaxed at 600°C in Ar, sintered for 1 h at 1300°C in H_2

Fig. 4.3 and Fig. 4.4 show a comparison of green and sintered densities of the alloys. It is evident that the densification during sintering decreases with higher green density, but also after compaction at 800 MPa, sintering results in quite significant increase of the density.

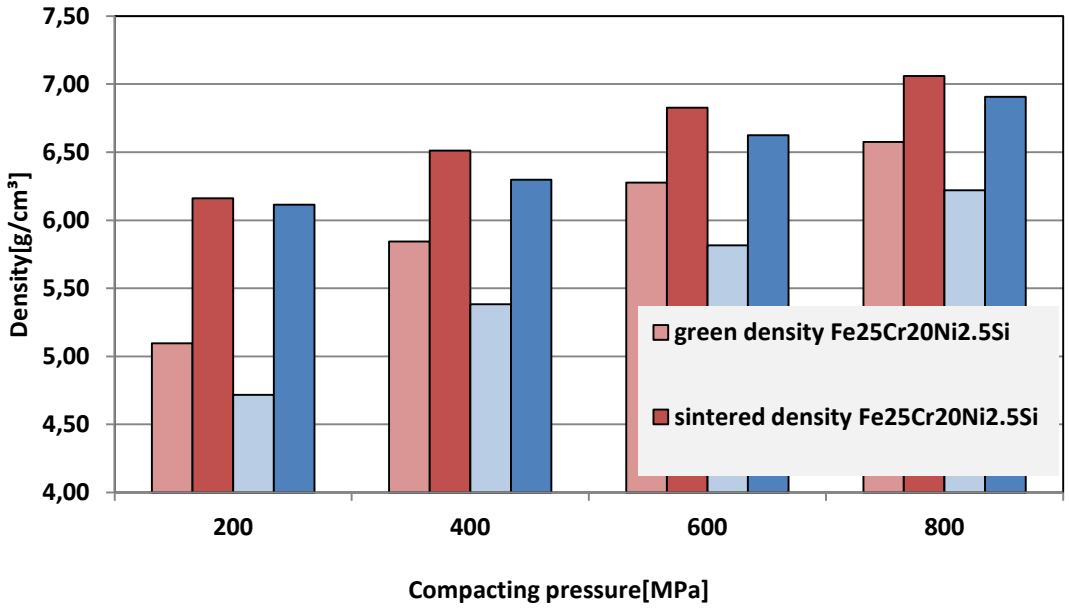

Fig. 4.3: Comparison of green and sintered density of Fe25Cr20Ni2.5Si and Fe18Cr0.3Mn0.5Nb. Dewaxed at 600°C in Ar, sintered 1 h at 1300°C in H_2.

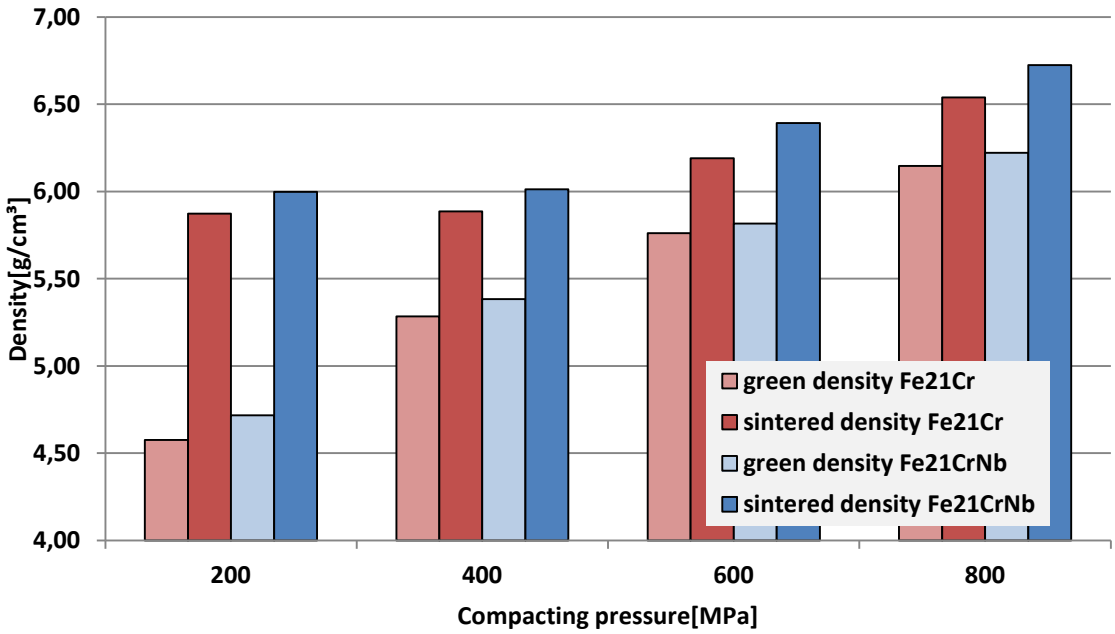

Fig. 4.4: Comparison of the green and sintered density of Fe21Cr and Fe21Cr0.5Nb. Dewaxed at 600°C in Ar, sintered 1 h at 1300°C in H_2.

In order to see the input of the compacting pressure and the sintering process on the density obtained, the green and sintered densities of Fe25Cr20Ni and Fe21Cr are shown (Fig. 4.5). In any case it is evident that also at the highest compacting pressure, sintering at 1300°C results in considerable increase of the density.

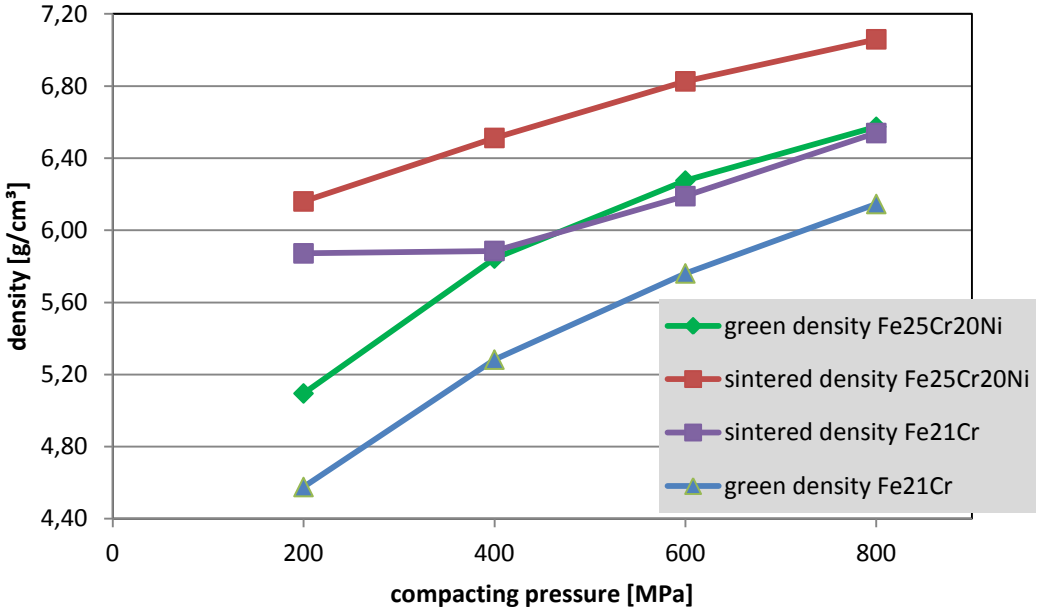

Fig. 4.5: Comparison of green and sintered density of Fe25Cr20Ni and Fe21Cr. Dewaxed 600°C Ar, sintered for 1 h at 1300°C in H_2.

Since it was only necessary to check the compressibility of the base powders, no further analysis (e.g. metallographic) has been carried out with the small billets, and it was decided to go on with pressing and sintering of Charpy bars (55 x 10 mm^2).

4.1.2 Charpy samples

4.1.2.1 Low amount of pressing lubricant

The powders were either mixed with 0.6% Kenolube P11 as a pressing lubricant and then pressed (double action) or compacted with die wall lubrication (using Multical sizing oil) into the die for Charpy bars (55 x 10 mm^2). The compacting pressure started at 800 MPa maximum, the aim was to decrease the pressure as much as possible. As a reference, iron powder (ASC100.29) was used (compacted only with die wall lubrication) and then compared to the other samples. After pressing, the green density was calculated by measuring the dimensions and weight of the Charpy samples (volumetric method).

Using die wall lubrication, it was possible to lower the compacting pressure to 100 MPa, with pressing lubricant to 150 MPa minimum. It was not possible to reduce the compacting pressure any further since then the green compacts disintegrated on ejection.

Green density:

The green densities (volumetric method) of the die wall lubricated powders are shown in Fig. 4.6 and especially the lower pressure range in Fig. 4.7. It is remarkable that once more the samples with higher alloy element content have higher green densities than the Fe21Cr samples. Over the whole compacting pressure from 100-800 MPa, the Fe21Cr powder has rather the same green densities (absolute and relative) as the Fe21Cr0.5Nb, and the Fe18Cr0.3Mn0.5Nb has nearly the same green density as the austenitic Fe25Cr20Ni2.5Si powder (see Table 4.2).

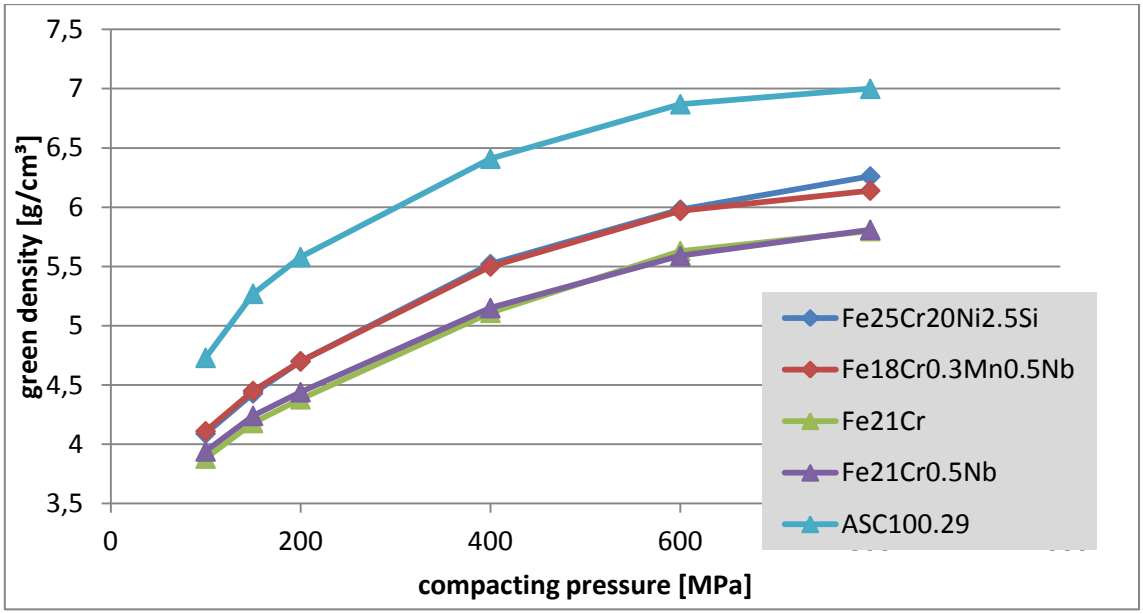

Fig. 4.6: Green density as a function of compacting pressure (die wall lubrication)

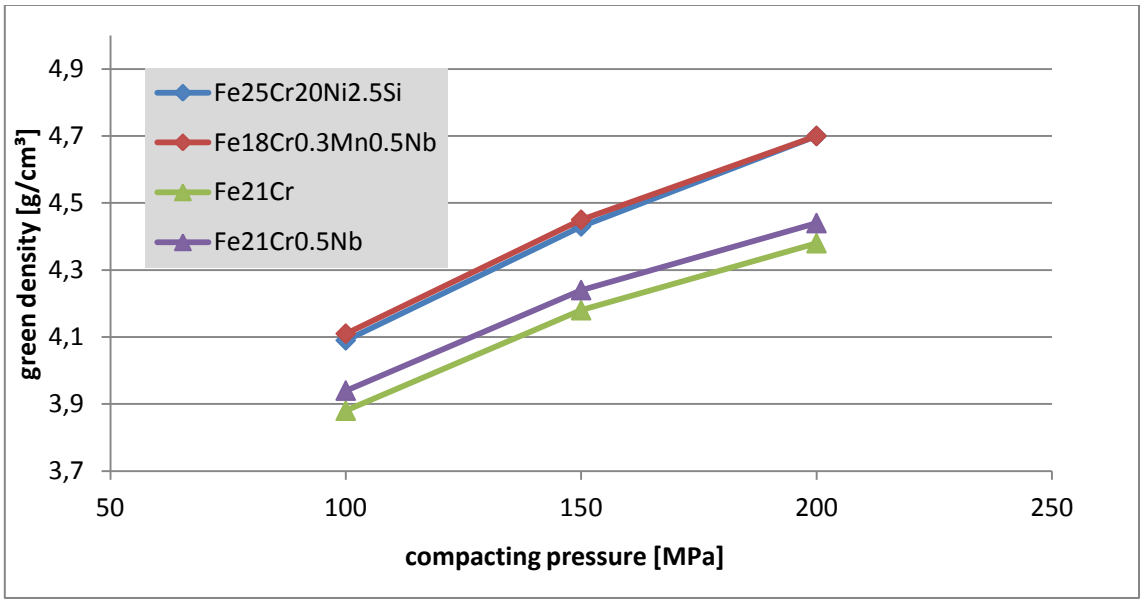

Fig. 4.7: Green density, die wall lubrication, compacting pressure 100 – 200 MPa

Table 4.2 shows the green density data (Charpy samples, die wall lubrication, volumetric method). The theoretical density is given by the measurements of the powder density by using the He-pycnometer. The porosity was calculated through:

Porosity [%] = $(1 - (\rho_{Green} / \rho_{Pycnometer})) * 100$

With die wall lubrication, a porosity of nearly 50% after pressing with a compacting pressure of 100 MPa could be achieved.

Table 4.2: Green density and porosity (Charpy samples, die wall lubrication)

Powder	Compacting pressure [MPa]	ρ_{GREEN} [g/cm³]	ρ_{THEORY} (He-Pycnom.) [g/cm³]	ρ [in % of theory]	Porosity [%]
Fe25Cr20Ni2.5Si	800	6,26	7,68	81,5	18,5
Fe18Cr0.3Mn0.5Nb	800	6,14	7,55	81,3	18,7
Fe21Cr	800	5,80	7,58	76,5	23,5
Fe21Cr0.5Nb	800	5,81	7,56	76,9	23,1
ASC100.29	800	7,00	7,82	89,5	10,5
Fe25Cr20Ni2.5Si	600	5,98	7,68	77,8	22,2
Fe18Cr0.3Mn0.5Nb	600	5,97	7,55	79,0	21,0
Fe21Cr	600	5,63	7,58	74,2	25,8
Fe21Cr0.5Nb	600	5,59	7,56	74,0	26,0
ASC100.29	600	6,87	7,82	87,8	12,2
Fe25Cr20Ni2.5Si	400	5,52	7,68	71,8	28,2
Fe18Cr0.3Mn0.5Nb	400	5,50	7,55	72,8	27,2
Fe21Cr	400	5,11	7,58	67,4	32,6
Fe21Cr0.5Nb	400	5,15	7,56	68,1	31,9
ASC100.29	400	6,41	7,82	82,0	18,0
Fe25Cr20Ni2.5Si	200	4,70	7,68	61,2	38,8
Fe18Cr0.3Mn0.5Nb	200	4,70	7,55	62,3	37,7
Fe21Cr	200	4,38	7,58	57,8	42,2
Fe21Cr0.5Nb	200	4,44	7,56	58,7	41,3
ASC100.29	200	5,58	7,82	71,4	28,6
Fe25Cr20Ni2.5Si	150	4,43	7,68	57,6	42,4
Fe18Cr0.3Mn0.5Nb	150	4,45	7,55	58,9	41,1
Fe21Cr	150	4,18	7,58	55,2	44,8
Fe21Cr0.5Nb	150	4,24	7,56	56,1	43,9
ASC100.29	150	5,27	7,82	67,4	32,6
Fe25Cr20Ni2.5Si	100	4,09	7,68	53,2	46,8
Fe18Cr0.3Mn0.5Nb	100	4,11	7,55	54,4	45,6
Fe21Cr	100	3,88	7,58	51,1	48,9
Fe21Cr0.5Nb	100	3,94	7,56	52,1	47,9
ASC100.29	100	4,73	7,82	60,5	39,5

In contrast, Fig. 4.8 shows the green density of the powders with 0.6% Kenolube P11 as a pressing lubricant. The lowest compacting pressure was set to 150 MPa, still lower pressure yielded too fragile compacts and they disintegrated on ejection, which shows the well known adverse effect of lubricant on the green strength. Once more, the ferritic powders have lower green densities.

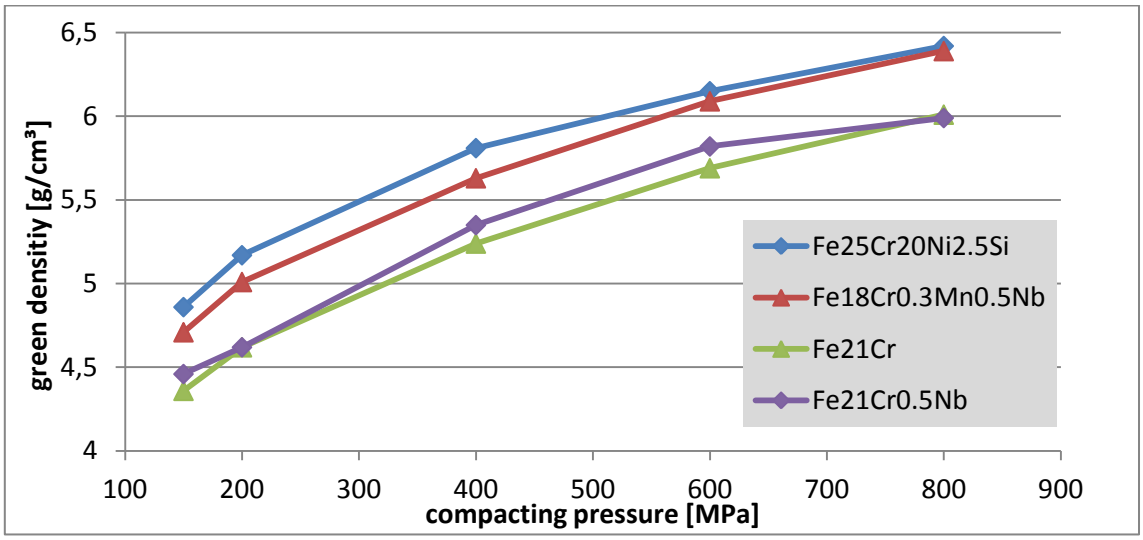

Fig. 4.8: Green density as a function of compacting pressure, compacted with 0.6% P11 admixed

Table 4.3 shows the green density data (Charpy samples, volumetric method) for compaction with pressing lubricant. With admixed lubricant, after pressing with the minimum possible compacting pressure of 150 MPa, a maximum porosity of about 40% is achieved.

Table 4.3: Green density and porosity (Charpy samples, compacted with 0.6% P11)

Sample	Powder	Comp. pressure [MPa]	ρ_{GREEN} [g/cm³]	ρ_{THEORY} (He-Pycnom.) [g/cm³]	ρ [in % of theory]	Porosity [%]
A8	Fe25Cr20Ni2.5Si	800	6,42	7,68	83,6	16,4
B8	Fe18Cr0.3Mn0.5Nb	800	6,39	7,55	84,6	15,4
C8	Fe21Cr	800	6,01	7,58	79,3	20,7
D8	Fe21Cr0.5Nb	800	5,99	7,56	79,2	20,8
A6	Fe25Cr20Ni2.5Si	600	6,15	7,68	80,1	19,9
B6	Fe18Cr0.3Mn0.5Nb	600	6,09	7,55	80,6	19,4
C6	Fe21Cr	600	5,69	7,58	75,1	24,9
D6	Fe21Cr0.5Nb	600	5,82	7,56	77,0	23,0
A4	Fe25Cr20Ni2.5Si	400	5,81	7,68	75,7	24,3
B4	Fe18Cr0.3Mn0.5Nb	400	5,63	7,55	74,6	25,4
C4	Fe21Cr	400	5,24	7,58	69,1	30,9
D4	Fe21Cr0.5Nb	400	5,35	7,56	70,8	29,2
A2	Fe25Cr20Ni2.5Si	200	5,17	7,68	67,4	32,6
B2	Fe18Cr0.3Mn0.5Nb	200	5,01	7,55	66,3	33,7
C2	Fe21Cr	200	4,62	7,58	60,9	39,1
D2	Fe21Cr0.5Nb	200	4,73	7,56	62,6	37,4
A15	Fe25Cr20Ni2.5Si	150	4,86	7,68	63,3	36,7
B15	Fe18Cr0.3Mn0.5Nb	150	4,71	7,55	62,3	37,7
C15	Fe21Cr	150	4,36	7,58	57,5	42,5
D15	Fe21Cr0.5Nb	150	4,46	7,56	58,9	41,1

With die wall lubrication, the compacting pressure could be lowered to 100 MPa, with admixed pressing lubricant to 150 MPa. Also for the same compacting pressure the green density of die wall lubricated samples is lower than it is when using a pressing lubricant, indicating that in this low to moderate density range the lubricating effect of P11 absolutely outweighs the effect of the space occupied by P11, which would inhibit densification. In the range of 150-800 MPa, the difference of the green density between the die lubricated samples and the samples with pressing lubricant is around 0.2 g/cm³. This can be seen in Fig. 4.9 and Table 4.4.

Table 4.4: Comparison of green density of die wall lubricated samples (Multical) and those compacted with pressing lubricant (0.6% P11)

Powder	Comp. pressure [MPa]	Green density [g/cm³]	
		Multical	P11
Fe25Cr20Ni2.5Si	800	6,26	6,42
Fe25Cr20Ni2.5Si	600	5,98	6,15
Fe25Cr20Ni2.5Si	400	5,52	5,81
Fe25Cr20Ni2.5Si	200	4,7	5,17
Fe25Cr20Ni2.5Si	150	4,43	4,86
Fe25Cr20Ni2.5Si	100	4,09	-
Fe18Cr0.3Mn0.5Nb	800	6,14	6,39
Fe18Cr0.3Mn0.5Nb	600	5,97	6,09
Fe18Cr0.3Mn0.5Nb	400	5,5	5,63
Fe18Cr0.3Mn0.5Nb	200	4,7	5,01
Fe18Cr0.3Mn0.5Nb	150	4,45	4,71
Fe18Cr0.3Mn0.5Nb	100	4,11	-
Fe21Cr	800	5,8	6,01
Fe21Cr	600	5,63	5,69
Fe21Cr	400	5,11	5,24
Fe21Cr	200	4,38	4,62
Fe21Cr	150	4,18	4,36
Fe21Cr	100	3,88	-
Fe21Cr0.5Nb	800	5,81	5,99
Fe21Cr0.5Nb	600	5,59	5,82
Fe21Cr0.5Nb	400	5,15	5,35
Fe21Cr0.5Nb	200	4,44	4,62
Fe21Cr0.5Nb	150	4,24	4,46

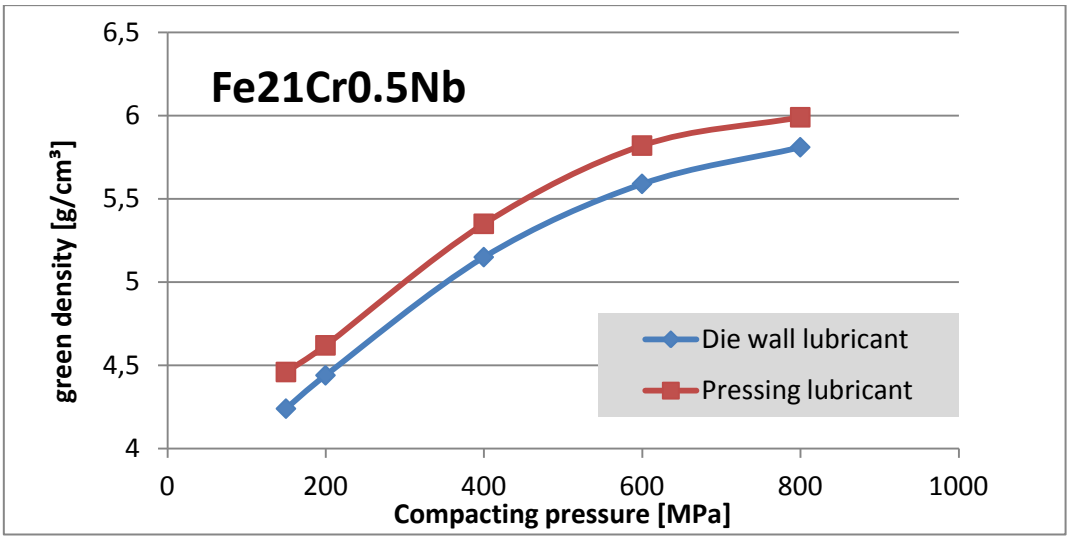

Fig. 4.9: Green density of Fe21Cr0.5Nb powder compacts, differently lubricated.

Sintered density:

After pressing, the green bodies compacted with die wall lubrication were sintered for 60 min isothermally at 1300°C (H_2, 99.999%, flow rate 2 l/min, large laboratory furnace). The sintered densities (volumetric method) are shown in Fig. 4.10 and Table 4.5. The lower the compacting pressure, the lower the sintered density was. The lowest sintered density obtained in this experiment was at 4.82 (4.90 resp.) g/cm³ for the Fe21Cr (Fe21Cr0.5Nb) sample.

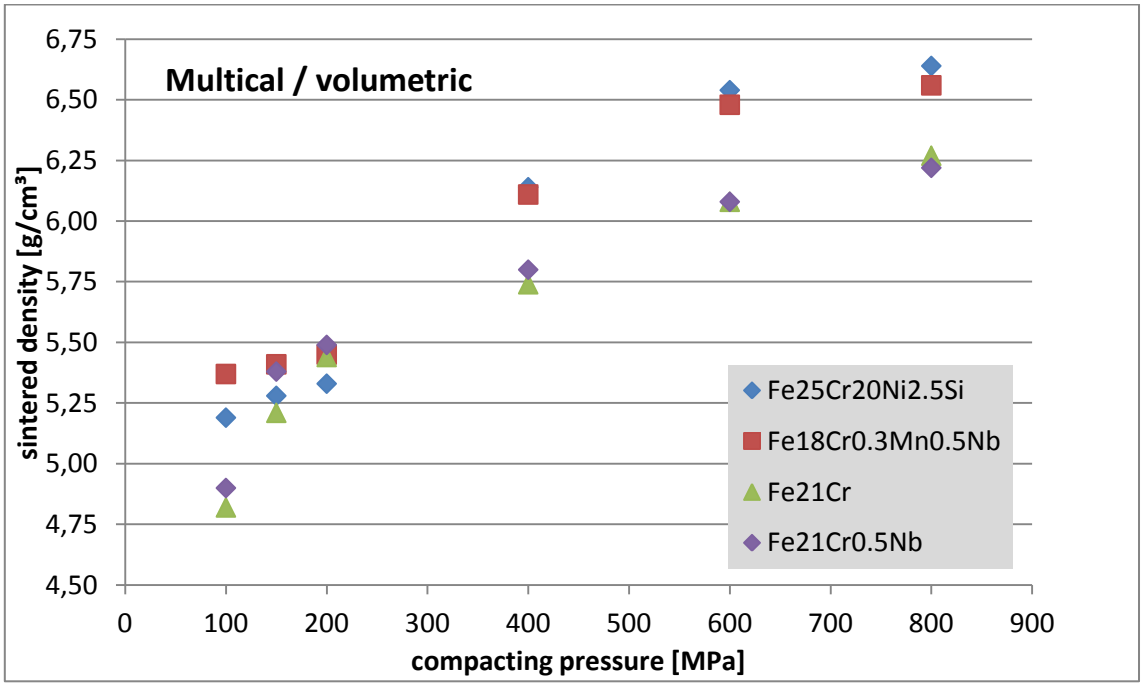

Fig. 4.10: Sintered density (volumetric method, compacted with die wall lubrication). Sintered 1 h at 1300°C in H_2

The correlation of sintered density and compacting pressure of the Charpy samples with P11 as a pressing lubricant can be seen in Fig. 4.11 and Table 4.5. The samples were dewaxed for 60 min at 600°C in Ar/H_2, and then sintered for 1 h at 1300°C in H_2. The samples were not easy to handle, for example, the austenitic sample compacted at 150 MPa fell apart during the measurement of the length. Once more, the ferritic sample compacted at 150 MPa has the lowest density (5.17 g/cm³). In contrast to the die wall lubricated parts, a difference between the ferritic samples Fe21Cr and Fe21Cr0.5Nb and the other ones in the lower compacting pressure range could not be seen. A few measuring points in this diagram are missing. The reason is that these samples were not sintered. These four (missing) samples compacted at 800 or 600 (Fe21Cr) MPa were taken out after the dewaxing process in order to measure the carbon, oxygen and nitrogen content in the as-dewaxed state since pickup esp. of carbon could not be excluded.

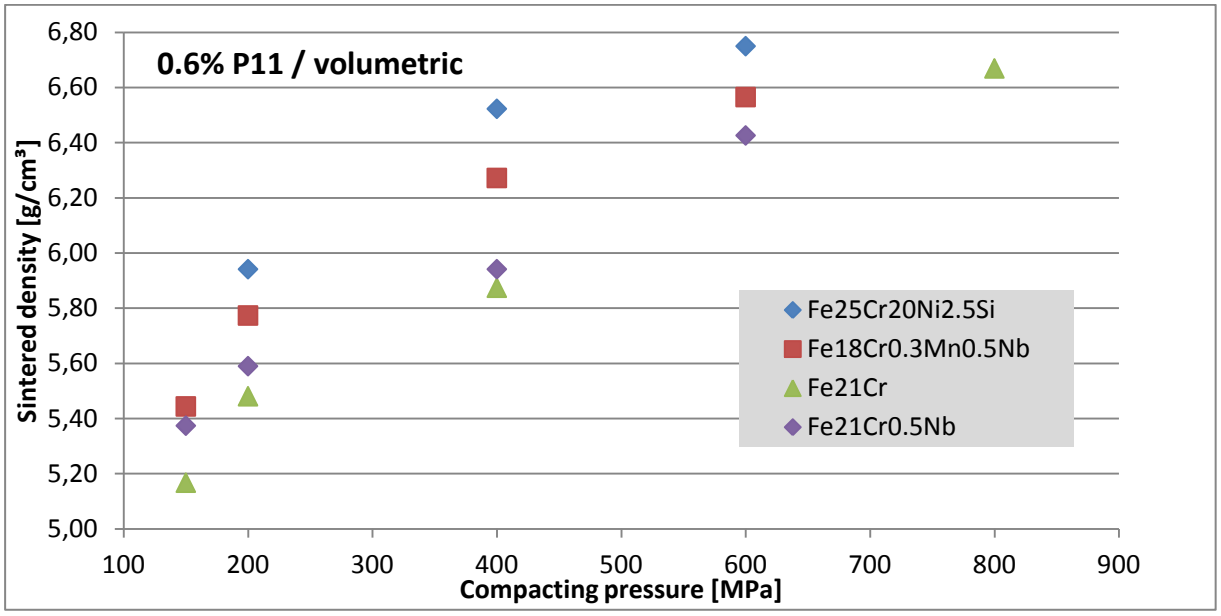

Fig. 4.11: Sintered density (Charpy samples pressed with lubricant, volumetric method). Dewaxed at 600°C Ar/H_2, sintered 1 h 1300°C in H_2

The sintered density was also measured with the Archimedes (water displacement) method, but the correlation between sintered density and compacting pressure was not very good. Surprisingly, a better correlation could be obtained with the volumetric method.

Comparison of green and sintered density:

A comparison of green and sintered density values (volumetric method) is shown in Table 4.5. The green as well as the sintered densities of the samples with pressing lubricant (P11) are higher than the densities of the die wall lubricated samples. As already mentioned before, with die wall lubrication it was possible to lower the compacting pressure to 100 MPa minimum, with pressing lubricant only to 150 MPa.

Table 4.5: Comparison of green (ρG) and sintered (ρS) density

Sample	Powder	Comp. pressure [MPa]	Multical		Kenolube P11	
			ρG [g/cm³]	ρS [g/cm³]	ρG [g/cm³]	ρS [g/cm³]
A8	Fe25Cr20Ni2.5Si	800	6,26	6,64	6,42	
A6	Fe25Cr20Ni2.5Si	600	5,98	6,54	6,15	6,75
A4	Fe25Cr20Ni2.5Si	400	5,52	6,14	5,81	6,52
A2	Fe25Cr20Ni2.5Si	200	4,70	5,33	5,17	5,94
A15	Fe25Cr20Ni2.5Si	150	4,43	5,28	4,86	
A1	Fe25Cr20Ni2.5Si	100	4,09	5,19		
B8	Fe18Cr0.3Mn0.5Nb	800	6,14	6,56	6,39	
B6	Fe18Cr0.3Mn0.5Nb	600	5,97	6,48	6,09	6,56
B4	Fe18Cr0.3Mn0.5Nb	400	5,50	6,11	5,63	6,27
B2	Fe18Cr0.3Mn0.5Nb	200	4,70	5,45	5,01	5,77
B15	Fe18Cr0.3Mn0.5Nb	150	4,45	5,41	4,71	5,44
B1	Fe18Cr0.3Mn0.5Nb	100	4,11	5,37		
C8	Fe21Cr	800	5,80	6,27	6,01	6,67
C6	Fe21Cr	600	5,63	6,08	5,69	
C4	Fe21Cr	400	5,11	5,74	5,24	5,87
C2	Fe21Cr	200	4,38	5,44	4,62	5,48
C15	Fe21Cr	150	4,18	5,21	4,36	5,17
C1	Fe21Cr	100	3,88	4,82		
D8	Fe21Cr0.5Nb	800	5,81	6,22	5,99	
D6	Fe21Cr0.5Nb	600	5,59	6,08	5,82	6,43
D4	Fe21Cr0.5Nb	400	5,15	5,80	5,35	5,94
D2	Fe21Cr0.5Nb	200	4,44	5,49	4,62	5,59
D15	Fe21Cr0.5Nb	150	4,24	5,38	4,46	5,37
D1	Fe21Cr0.5Nb	100	3,94	4,90		

Fig. 4.12 - Fig. 4.15 show a comparison of green and sintered density of the die wall lubricated Charpy samples. As mentioned above, the densities of the ferritic samples Fe21Cr and Fe21Cr0.5Nb are lower than those of the other two samples.

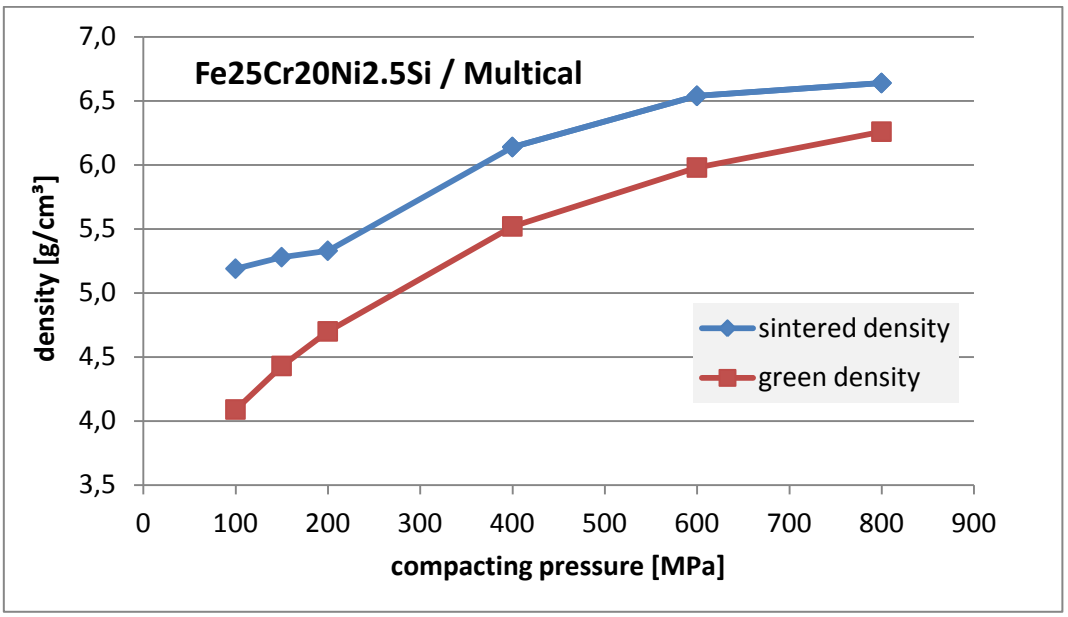

Fig. 4.12: Green and sintered density of the Fe25Cr20Ni2.5Si sample, die wall lubricated, sintered 60 min 1300°C. H_2

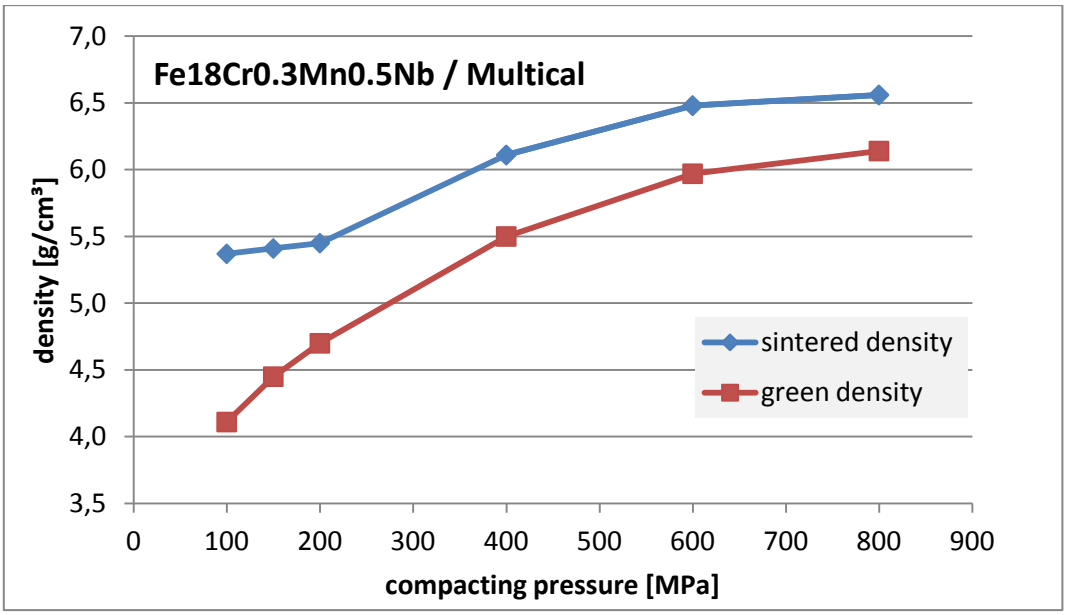

Fig. 4.13: Green and sintered density of the Fe18Cr0.3Mn0.5Nb sample; die wall lubricated, sintered 60 min 1300°C, H_2

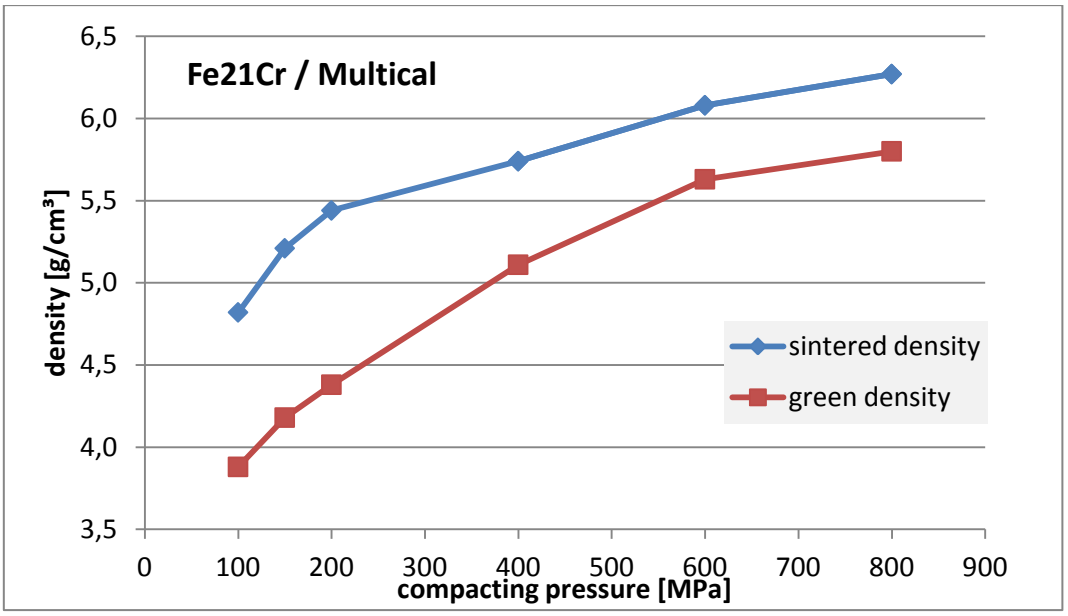

Fig. 4.14: Green and sintered density of the Fe21Cr sample, die wall lubricated, sintered 60 min 1300°C, H_2

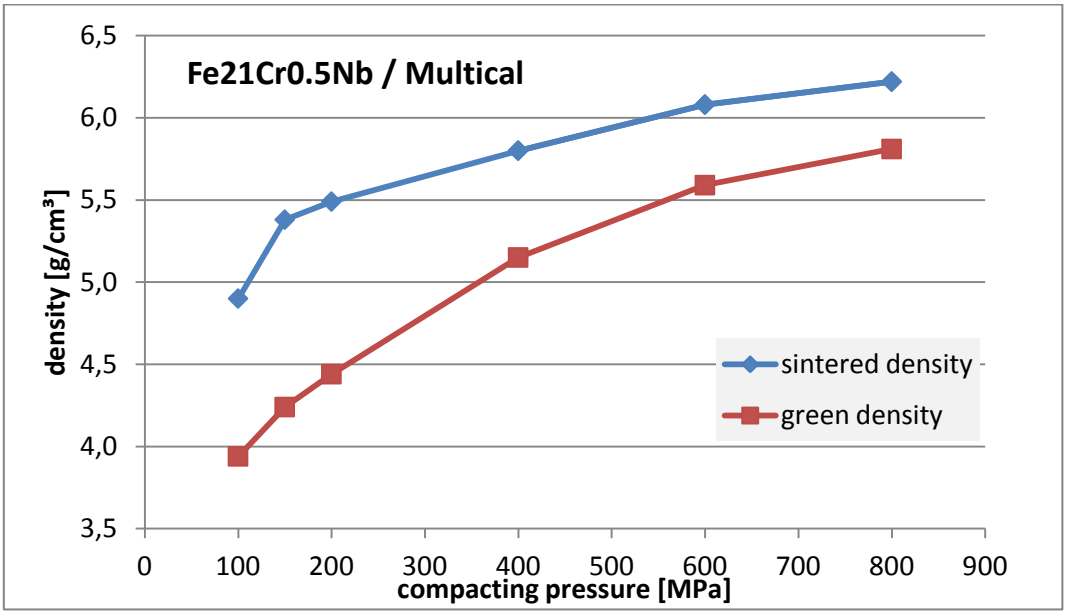

Fig. 4.15: Green and sintered density of the Fe21Cr0.5Nb sample, die wall lubricated, sintered 60 min 1300°C, H_2

Fig. 4.16 - Fig. 4.19 show a comparison of green and sintered density of the Charpy samples compacted with 0.6% P11 as a pressing lubricant. Once more, the ferritic powders Fe21Cr and Fe21Cr0.5Nb have a lower density than the other samples. The shape of the graph for all four powders looks the same and common for iron base powders.

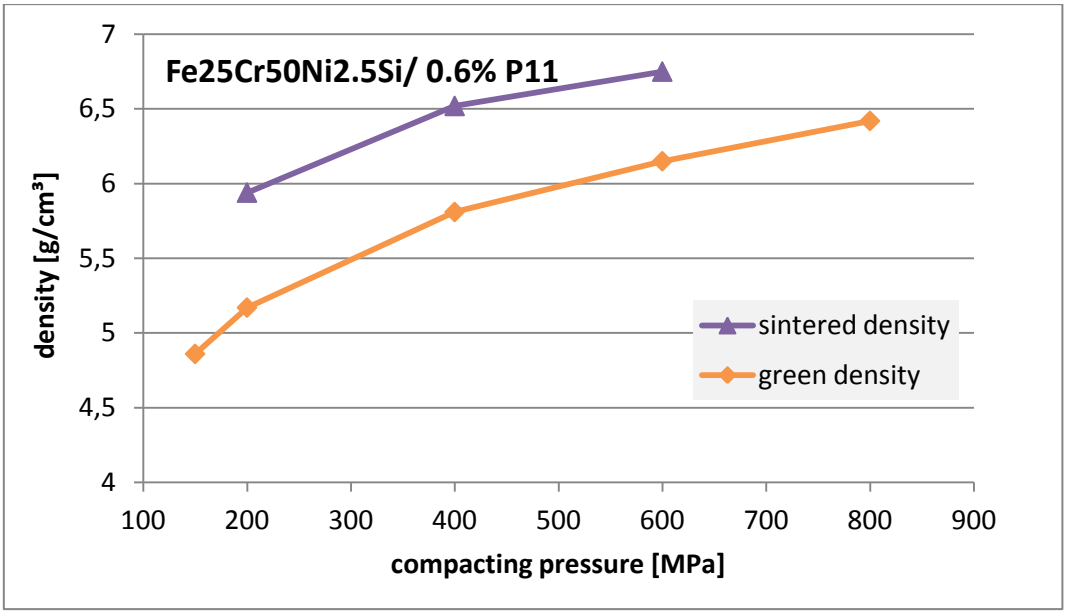

Fig. 4.16: Green and sintered density of the Fe25Cr20Ni2.5Si sample, compacted with 0.6% P11, dewaxed at 600°C in Ar/H_2, sintered 60 min 1300°C, H_2

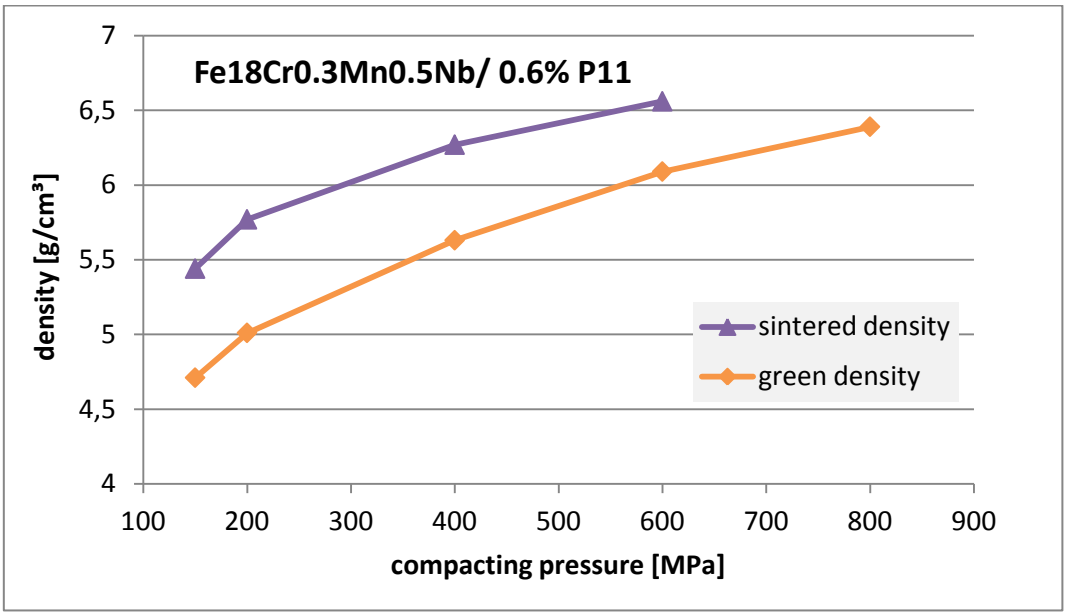

Fig. 4.17: Green and sintered density of the Fe18Cr0.3Mn0.5Nb sample, compacted with 0.6% P11,
dewaxed at 600°C in Ar/H_2, sintered 60 min 1300°C, H_2

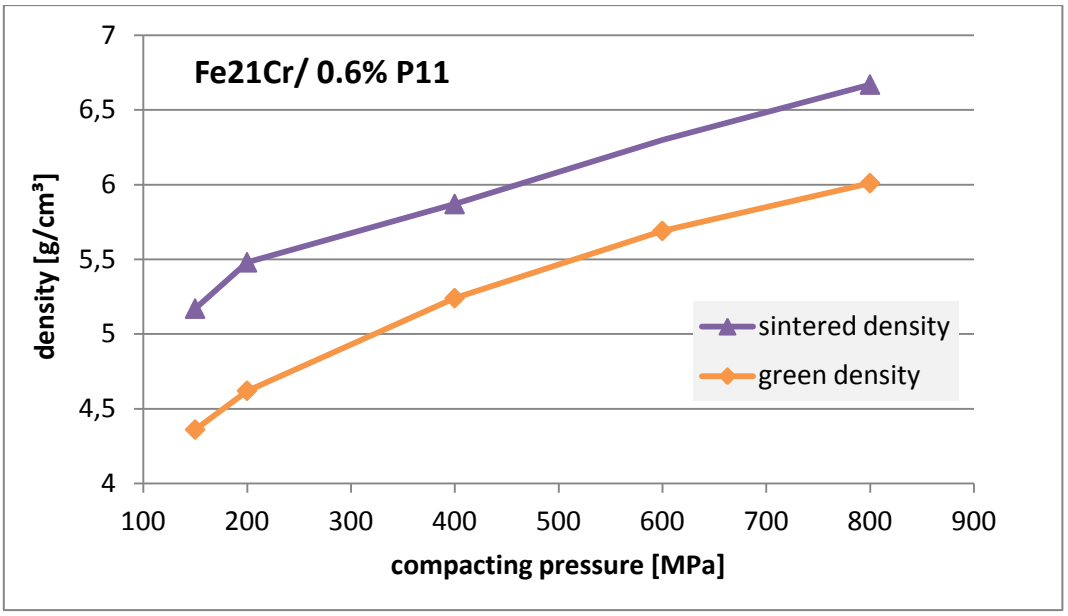

Fig. 4.18: Green and sintered density of the Fe21Cr sample, compacted with 0.6% P11, dewaxed at 600°C in Ar/H_2, sintered 60 min 1300°C, H_2

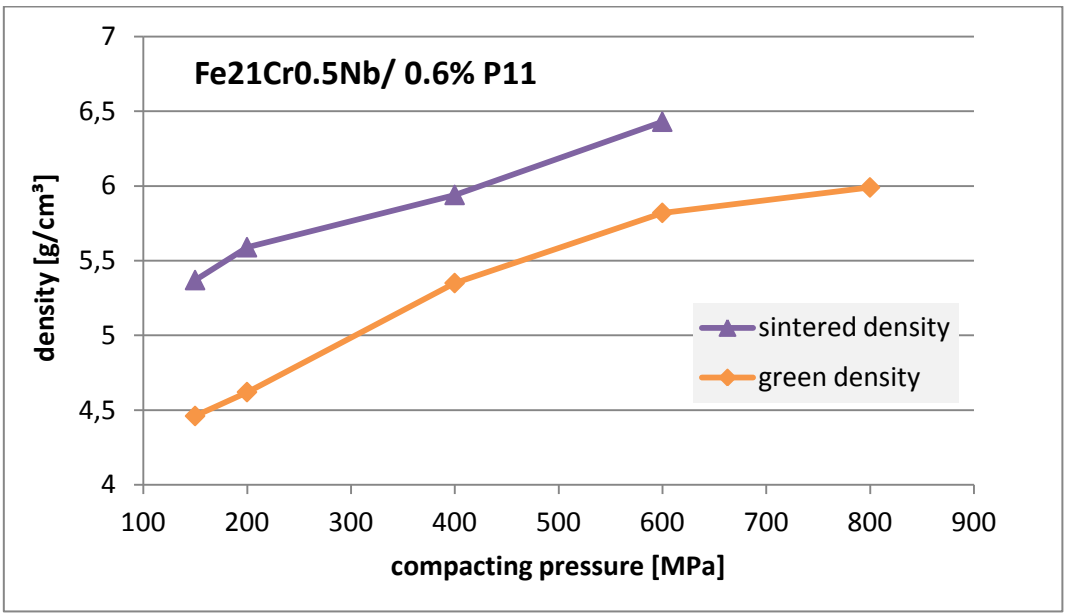

Fig. 4.19: Green and sintered density of the Fe21Cr0.5Nb sample, compacted with 0.6% P11, dewaxed at 600°C in Ar/H_2, sintered 60 min 1300°C, H_2

Porosity and metallographic images of the sintered samples:

Table 4.6 shows the porosity of the sintered samples. Of course, the lower the compacting pressure, the higher is the porosity. The porosity of the austenitic sample Fe25Cr20Ni is lower than that of the ferritic ones, related to the higher green density of the austenitic samples (see Table 4.5). In the range of 150-400 MPa the porosity for both ferritic samples Fe21Cr and Fe21Cr is the same with pressing lubricant and with die wall lubrication. If porosity above 30% is needed, it is only possible to do it with die wall lubrication. For example, for the Fe21Cr0.5Nb sample a porosity of 36% could be attained after compacting at 100 MPa with die wall lubrication.

Table 4.6: Porosity of all samples (die wall lubricated with Multical / compacted with 0.6% P11)

Powder	Comp. Pressure [MPa]	Multical		Kenolube P11	
		ρS [g/cm³]	Porosity (%)	ρS [g/cm³]	Porosity (%)
Fe25Cr20Ni2.5Si	800	6,64	13,5	not sintered**	-
Fe18Cr0.3Mn0.5Nb	800	6,56	13,1	not sintered**	-
Fe21Cr	800	6,27	17,3	6,67	12,0
Fe21Cr0.5Nb	800	6,22	17,7	not sintered**	-
Fe25Cr20Ni2.5Si	600	6,54	14,8	6,75	12,1
Fe18Cr0.3Mn0.5Nb	600	6,48	14,2	6,56	13,0
Fe21Cr	600	6,08	19,8	not sintered**	-
Fe21Cr0.5Nb	600	6,08	19,6	6,43	15,0
Fe25Cr20Ni2.5Si	400	6,14	20,0	6,52	15,1
Fe18Cr0.3Mn0.5Nb	400	6,11	19,1	6,27	16,9
Fe21Cr	400	5,74	24,3	5,87	22,5
Fe21Cr0.5Nb	400	5,80	23,3	5,94	21,4
Fe25Cr20Ni2.5Si	200	5,33	30,6	5,94	22,6
Fe18Cr0.3Mn0.5Nb	200	5,45	27,8	5,77	23,5
Fe21Cr	200	5,44	28,3	5,48	27,7
Fe21Cr0.5Nb	200	5,49	27,4	5,59	26,1
Fe25Cr20Ni2.5Si	150	5,28	31,3	not sintered**	-
Fe18Cr0.3Mn0.5Nb	150	5,41	28,4	5,44	27,9
Fe21Cr	150	5,21	31,2	5,17	31,8
Fe21Cr0.5Nb	150	5,38	28,9	5,37	28,9
Fe25Cr20Ni2.5Si	100	5,19	32,5	not possible*	-
Fe18Cr0.3Mn0.5Nb	100	5,37	28,9	not possible*	-
Fe21Cr	100	4,82	36,4	not possible*	-
Fe21Cr0.5Nb	100	4,90	35,2	not possible*	-

*not possible: parts disintegrate on ejection

**not sintered: because of C/O/N-control after dewaxing

Metallography of the pressed samples:

Because of the fact that the shrinkage of the pressed samples is not in the required range (15 – 20%), not all of them were investigated by light microscope. For that reason only the Fe21Cr sample pressed with 150 and 400 MPa (die wall lubricated, porosity is 31.2% and 24.3%, resp.) are shown. At a magnification of 100x the difference in the porosity is clearly visible, but it has to be pointed out that the pores are rather finely distributed.

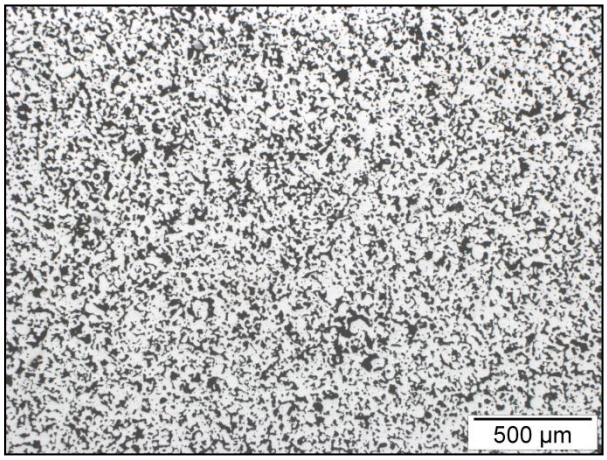

Fig. 4.20: Fe21Cr, pressed with 150 MPa, 31,2% porosity, 50x

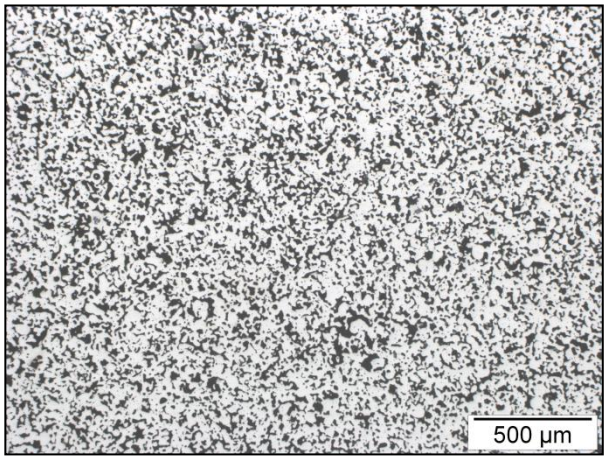

Fig. 4.21: Fe21Cr, pressed with 400 MPa, 24,3% porosity, 50x

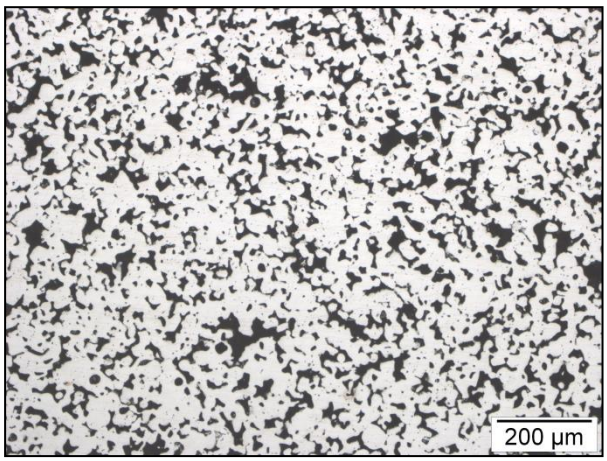

Fig. 4.22: Fe21Cr, pressed with 150 MPa, 31,2% porosity, 100x

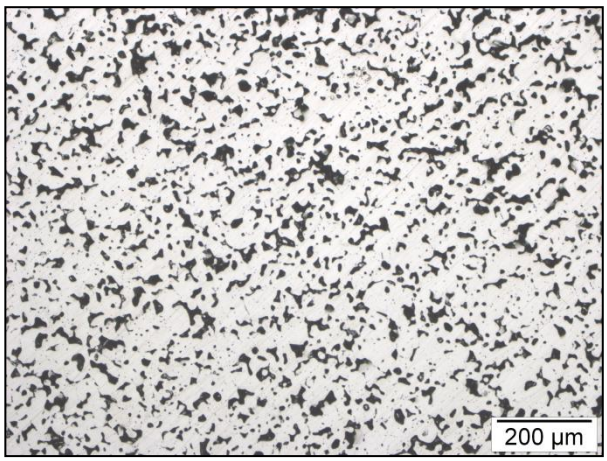

Fig. 4.23: Fe21Cr, pressed with 400 MPa, 24,3% porosity, 100x

- Effect of compacting pressure on the shrinkage:

Fig. 4.24: Green and sintered bodies of the Fe21Cr sample

Fig. 4.24 shows the green and sintered bodies of the Fe21Cr Charpy sample (die wall lubricated). The shrinkage of this sample is about 7.7% (linear). The general values of the shrinkage are shown in The question then was if higher shrinkage could be attained if the compacting pressure is further reduced, which however means that the compacts cannot be handled any more, being too fragile.

Table 4.7. There it could be seen that it is better to compact with die wall lubrication than with a pressing lubricant, in order to obtain higher shrinkage, but not more than 8% shrinkage could be achieved. However, as mentioned above the shrinkage of a ferritic metal support of a SOFC should be in the range of 15 – 20%.

The question then was if higher shrinkage could be attained if the compacting pressure is further reduced, which however means that the compacts cannot be handled any more, being too fragile.

Table 4.7: Comparison of the shrinkage of die wall lubricated samples (Multical) and samples admixed with pressing lubricant (Kenolube P11), sintered 60 min 1300°C, H_2)

Sample	Powder	compacting pressure [MPa]	shrinkage (Multical) [%]	shrinkage (Kenolube P11) [%]
A8	Fe25Cr20Ni2.5Si	800	2,1	not sintered
A6	Fe25Cr20Ni2.5Si	600	2,5	2,9
A4	Fe25Cr20Ni2.5Si	400	3,5	3,5
A2	Fe25Cr20Ni2.5Si	200	4,8	5,1
A15	Fe25Cr20Ni2.5Si	150	6,0	not possible
A1	Fe25Cr20Ni2.5Si	100	6,8	not possible
B8	Fe18Cr0.3Mn0.5Nb	800	2,1	not sintered
B6	Fe18Cr0.3Mn0.5Nb	600	2,6	2,6
B4	Fe18Cr0.3Mn0.5Nb	400	4,0	3,8
B2	Fe18Cr0.3Mn0.5Nb	200	5,7	5,4
B15	Fe18Cr0.3Mn0.5Nb	150	6,8	5,6
B1	Fe18Cr0.3Mn0.5Nb	100	9,1	not possible
C8	Fe21Cr	800	2,6	3,5
C6	Fe21Cr	600	2,9	not sintered
C4	Fe21Cr	400	4,4	3,8
C2	Fe21Cr	200	6,8	6,1
C15	Fe21Cr	150	7,7	6,4
C1	Fe21Cr	100	7,6	not possible
D8	Fe21Cr0.5Nb	800	2,4	not sintered
D6	Fe21Cr0.5Nb	600	2,8	3,9
D4	Fe21Cr0.5Nb	400	3,8	4,1
D2	Fe21Cr0.5Nb	200	7,5	5,9
D15	Fe21Cr0.5Nb	150	8,2	6,6
D1	Fe21Cr0.5Nb	100	7,6	not possible

Dimensional change of the pressed samples:

The shrinkage of the samples has also been analyzed with the Dilatometer.

The samples were pressed at 400 MPa (only die wall lubricated), cut in 10 x 10 mm² pieces, and the measurements were carried out perpendicular to the pressing direction. As can be seen below (Fig. 4.26), the samples were heated up from 30°C to 1300°C (10 K/min), then held isothermally for 60 min at 1300°C, and after that cooled down with 10K/min to 30°C again, all in hydrogen atmosphere.

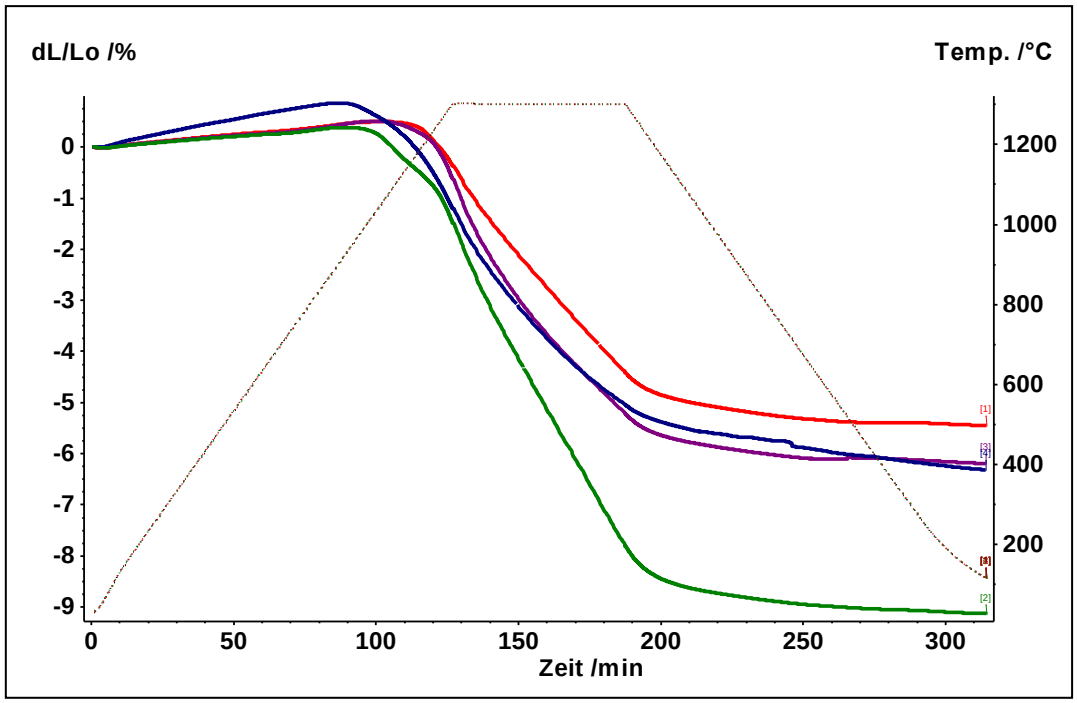

Fig. 4.25: Dilatometer run of all four samples, Fe25Cr20Ni2.5Si (blue), Fe18Cr0.3Mn0.5Nb (red), Fe21Cr (green) and Fe21Cr0.5Nb (purple) in H_2 atmosphere. Compacted at 400 MPa

The austenitic sample (blue line) has the highest expansion (~ 0.9%) of all four samples while heating up, and it starts to shrink before the ferritic samples. The Fe21Cr sample (green line) has the highest shrinkage at the isothermal stage, with 9.5%. While cooling down a slight shrinkage is visible due to thermal contraction of about 1%.

For a better comparison of the different dilatometric graphs and to compare the shrinkage at 1300°C, it was tried to divide the graphs into four different regions (steps).

Step 1) only for Fe25Cr20Ni and Fe21Cr: start of shrinkage to the first inflection point
Step 2) step before isothermal sintering
Step 3) isothermal sintering at 1300°C
Step 4) cooling down from 1300°C – 30°C

For better illustration, the dilatometer graph of the Fe21Cr sample is shown below (Fig. 4.26), the graphs of each sample individually are shown in the appendix.

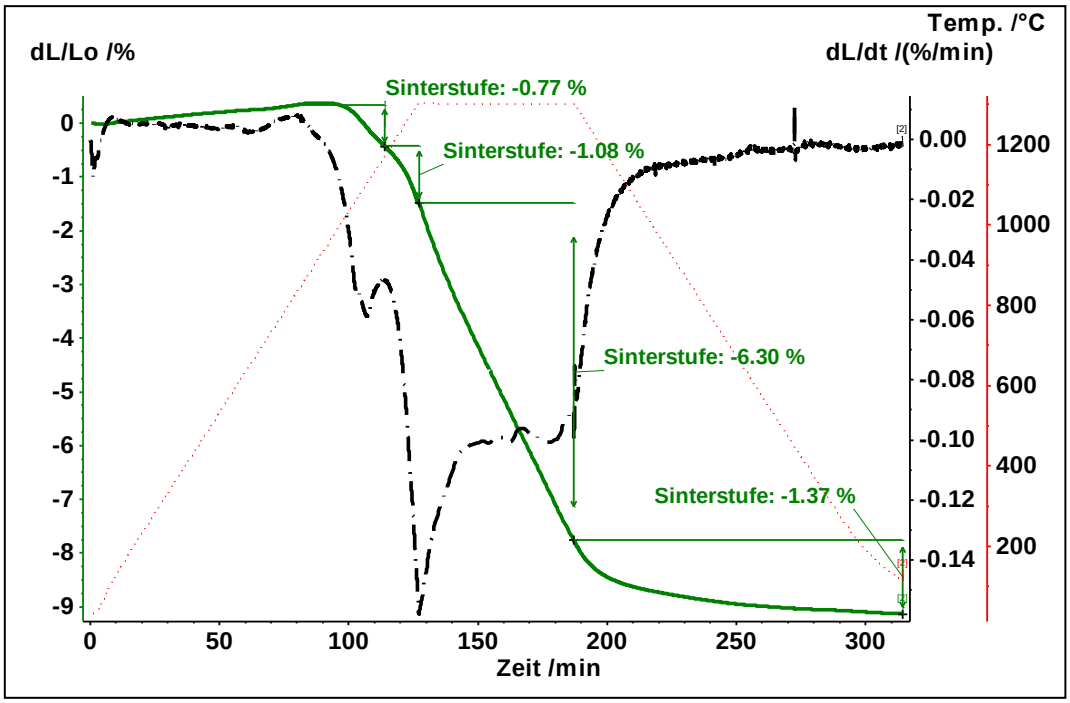

Fig. 4.26: Dilatometric graph of Fe21Cr (green line) and first derivative (broken black line)

The shrinkage during the different steps and the total shrinkage as well as expansion are shown in Table 4.8.

Table 4.8: Values of expansion and shrinkage of all four samples

Sample	Shrinkage					max. expansion (%)
	step 1	step 2	step 3	step 4	Σ	
Fe25Cr20Ni2.5Si	-0,32	-1,61	-4,03	-1,29	**-7,25**	0,88
Fe18Cr0.3Mn0.5Nb		-0,91	-4,07	-1,02	**-6,00**	0,51
Fe21Cr	-0,77	-1,08	-6,30	-1,37	**-9,52**	0,41
Fe21Cr0.5Nb		-1,08	-4,81	-0,86	**-6,75**	0,52

With 6.3% the Fe21Cr sample has the highest shrinkage at the isothermal sintering window. Further it can be seen, that after a sintering time of 60 minutes there is still shrinkage possible (step 4). In order to get higher shrinkage of the samples, extending the sintering time could be a viable option. Because of the rather “insufficient” shrinkage of the pressed samples, the influence of the sintering time was then later studied with the gravity sintered samples (results can be seen in Chapter 4.2.1.2).

C/O/N control of the pressed samples:

Carbon, oxygen and nitrogen content were controlled and measured from the powder and after dewaxing and sintering of the samples.

The carbon content (Table 4.9) for the samples compacted with lubricant is of course higher than that of the die wall lubricated ones. The Fe18Cr0.3Mn0.5Nb sample as well as the powder have very low carbon content. The Fe25Cr20Ni2.5Si powder (and samples) has the highest carbon content, but this can be explained by the higher carbon solubility in the austenitic lattice. Both ferritic samples Fe21Cr and Fe21Cr0.5Nb have fairly the same carbon content after sintering (0.01%).

Table 4.9: Carbon content of the powder and samples

wt%C				
Sample	**Powder**	**P11 dewaxed**	**P11 sintered**	**Multical sintered**
Fe25Cr20Ni2.5Si	0,0212 ± 0,0012	0,0555 ± 0,0029	0,0345 ± 0,0035	0,0188 ± 0,0039
Fe18Cr0.3Mn0.5Nb	0,0071 ± 0,0002	0,0436 ± 0,0005	0,0124 ± 0,0008	0,0062 ± 0,0033
Fe21Cr	0,0108 ± 0,0001	0,0807 ± 0,0025	0,0178 ± 0,0017	0,0100 ± 0,0045
Fe21Cr0.5Nb	0,0124 ± 0,0007	0,0455 ± 0,0009	0,0145 ± 0,0004	0,0098 ± 0,0054

The oxygen content (Table 4.10) of the austenitic powder (0.16 wt%) is very low compared to the others (~ 0,56 wt%), but after sintering the content (for die wall lubricated samples) is ten times higher than for the ferritic ones.

The initial oxygen content for all powders and the content after dewaxing is nearly the same, which means that there is hardly any oxidation during the dewaxing process. But surprisingly, the oxygen content after dewaxing and after sintering for the samples with P11 only decreases slightly compared to the die wall lubricated samples in which almost all oxygen is removed during sintering.

Table 4.10: Oxygen content of the powder and samples

wt%O				
Sample	**Powder**	**P11 dewaxed**	**P11 sintered**	**Multical sintered**
Fe25Cr20Ni2.5Si	0,163 ± 0,002	0,198 ± 0,002	0,602 ± 0,196	0,542 ± 0,036
Fe18Cr0.3Mn0.5Nb	0,610 ± 0,003	0,627 ± 0,005	0,598 ± 0,070	0,045 ± 0,001
Fe21Cr	0,465 ± 0,006	0,440 ± 0,004	0,328 ± 0,027	0,0381 ± 0,019
Fe21Cr0.5Nb	0,566 ± 0,004	0,577 ± 0,002	0,538 ± 0,086	0,038 ± 0,14

The nitrogen content (Table 4.11) for the ferritic powders is low. The initial nitrogen content of the austenitic powder is 0.132% and after sintering 0.0043%, so the mass loss due to N_2 formation is much more pronounced for the austenitic sample than it is for the ferritic ones which contain only little nitrogen from the beginning.

Table 4.11: Nitrogen content of powder and sample

wt%N				
Sample	**Powder**	**P11 dewaxed**	**P11 sintered**	**Multical sintered**
Fe25Cr20Ni2.5Si	0,132 ± 0,001	0,135 ± 0,007	0,0638 ± 0,0021	0,0043 ± 0,0019
Fe18Cr0.3Mn0.5Nb	0,033 ± 0,001	0,0385 ± 0,001	0,0099 ± 0,0007	0,0010 ± 0,0002
Fe21Cr	0,048 ± 0,001	0,0759 ± 0,002	0,0141 ± 0,0012	0,0073 ± 0,0003
Fe21Cr0.5Nb	0,089 ± 0,003	0,0861 ± 0,002	0,0131 ± 0,0013	0,0066 ± 0,0008

4.1.2.2 High content of pressing lubricant

As could be seen above, by using low contents of pressing lubricant the shrinkage also is very low. The idea then was to raise the amount of pressing lubricant and use it as a spaceholder, so that during the sintering process carbon dissolves and ideally enhances the shrinkage.

Different amounts of pressing lubricant ($\rho_{\text{paraffin wax}}$ = 0.9 g/cm³) and different pressing tools were used. An overview can be seen in Table 4.12. The samples pressed with the cylindrical tool were mixed 2.0 and 6.0 wt% paraffin wax (= 14 resp. 44 vol%); these samples were then used for metallographic investigations.

Table 4.12: Overview of the samples with high content of pressing lubricant

Sample	admixed paraffin wax (wt%)	initial carbon content (wt%C)	compacting pressure (MPa)	pressing tool
Fe21Cr	2,0	1,7	100 - 400	cylindrical
Fe21Cr	6,0	4,2	100 - 400	cylindrical
Fe21Cr	2,7	2,0	100 - 400	Charpy
Fe21Cr	7,8	6,0	100 - 400	Charpy

The Charpy samples were mixed with 2.7 and 7.8 wt% paraffin wax (= 19 resp. 57 vol%), and they were used to measure green (volumetric method) and sintered (water displacement method) density as well as the linear shrinkage (results shown in Table 4.13 and Fig. 4.27).

Table 4.13: Green density, sintered density and shrinkage (lin.) of the samples with admixed paraffin wax [n.m = not measured]

Sample	compacting pressure (MPa)	green density [g/cm³]	sintered density [g/cm³]	theoretical density (g/cm³)	porosity [%]	linear shrinkage (%)
Fe21Cr + 2.7 wt% PW	100	4,07	4,60	7,54	39,0	5,4
Fe21Cr + 2.7 wt% PW	150	4,30	4,92	7,54	34,7	4,9
Fe21Cr + 2.7 wt% PW	200	4,54	4,99	7,54	33,8	4,7
Fe21Cr + 2.7 wt% PW	400	5,19	5,65	7,54	25,1	2,4
Fe21Cr + 7.8 wt% PW	100	4,31	4,57	7,19	36,4	4,0
Fe21Cr + 7.8 wt% PW	150	4,47	4,7	7,19	34,6	3,5
Fe21Cr + 7.8 wt% PW	200	4,63	n.m.	7,19	n.m.	n.m.
Fe21Cr + 7.8 wt% PW	400	4,85	n.m.	7,19	n.m.	n.m.

The Charpy samples mixed with 2.7 wt% paraffin wax were good to handle and did not break while dewaxing or sintering, while the samples with 7.8 wt% paraffin wax were very tricky to handle and disintegrated (after dewaxing) or broke (after sintering).

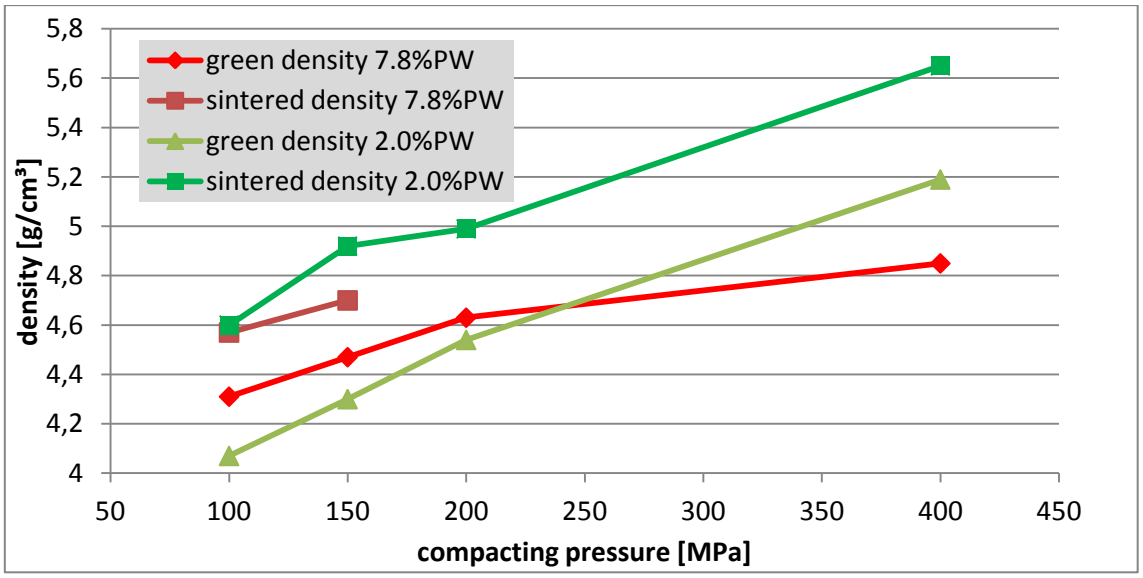

Fig. 4.27: Green and sintered density of the paraffin wax samples

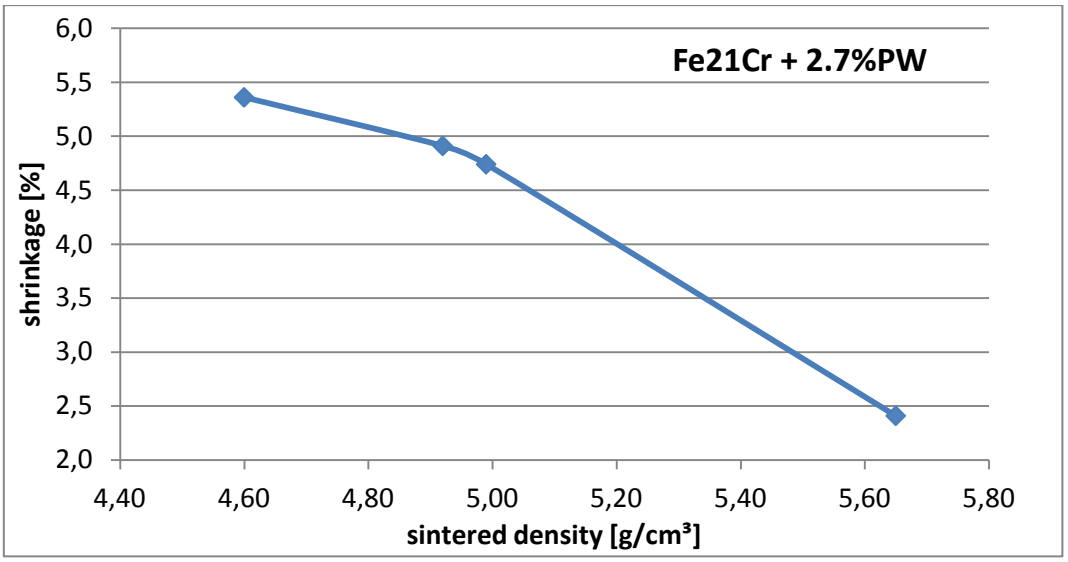

Fig. 4.28: Shrinkage depending on sintered density of the Fe21Cr + 2.7% PW sample

Fig. 4.28 demonstrates the shrinkage of the Fe21Cr + 2.7 wt% paraffin wax sample. It is obvious that lower compacting pressure leads to lower density, but even if the samples are compacted at very low pressure (100 MPa), the shrinkage of only 4-5% is insufficient if co-sintering with the functional ceramic layers of the SOFC is aimed at.

Metallographic investigations on all samples show that the pore size and pore distribution for samples is not heavily depending on the compacting pressure. They all look rather similar. That is the reason why right here only images of the samples compacted with 100 MPa are shown at different magnifications.

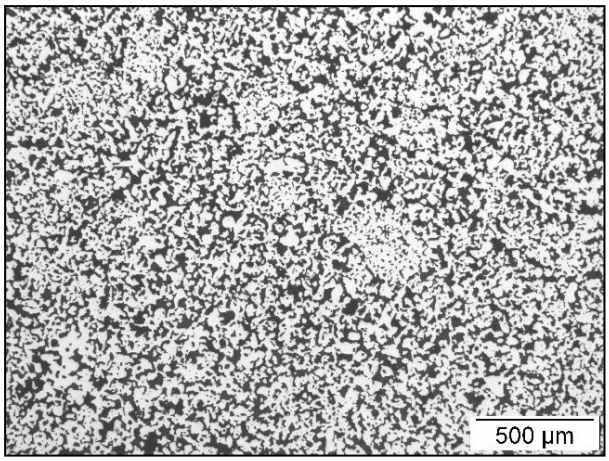

Fig. 4.29: Fe21Cr + 2% PW, 50x, 100 MPa, dewaxed and sintered, 39% P

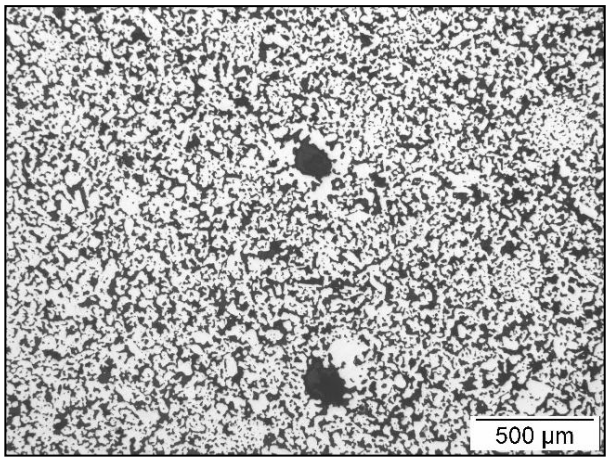

Fig. 4.30: Fe21Cr + 2% PW, 50x, 100 MPa, dewaxed and sintered, 39% P

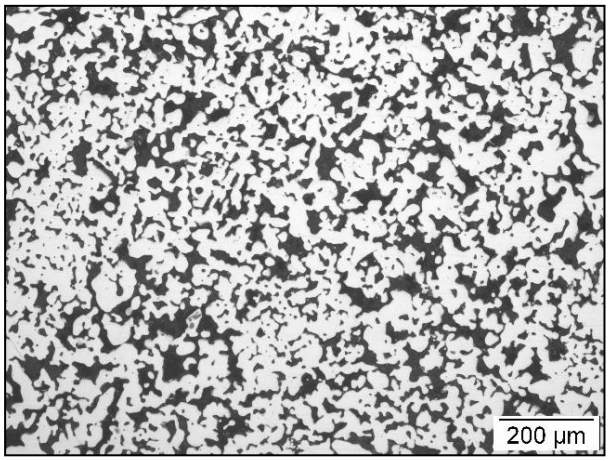

Fig. 4.31: Fe21Cr + 2% PW, 100x, 100 MPa, dewaxed and sintered, 39% P

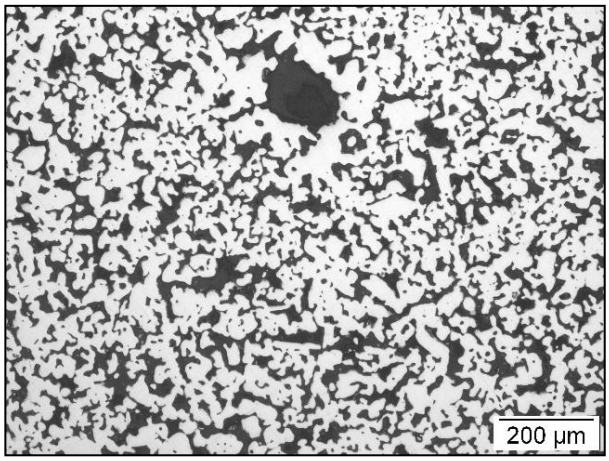

Fig. 4.32: Fe21Cr + 2% PW, 100x, 100 MPa, dewaxed and sintered, 39% P

Fig. 4.29 shows that the pores are homogeneously distributed and there are also some densification centers visible with around 500 µm size.

In Fig. 4.30 some big pores can be seen. It may be possible that these pores result from agglomerations of wax while mixing, and while dewaxing these agglomerations form voids. The powder was already mixed for 2.5 hours, and longer mixing time could decrease the sintering activity.

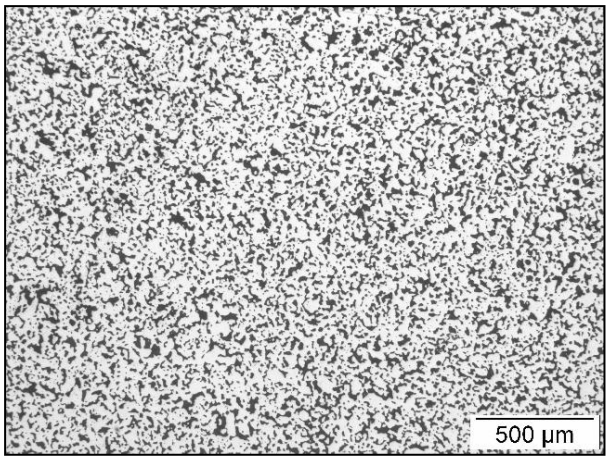

Fig. 4.33: Fe21Cr + 6% PW, 50x, 100 MPa, dewaxed and sintered, 36% P

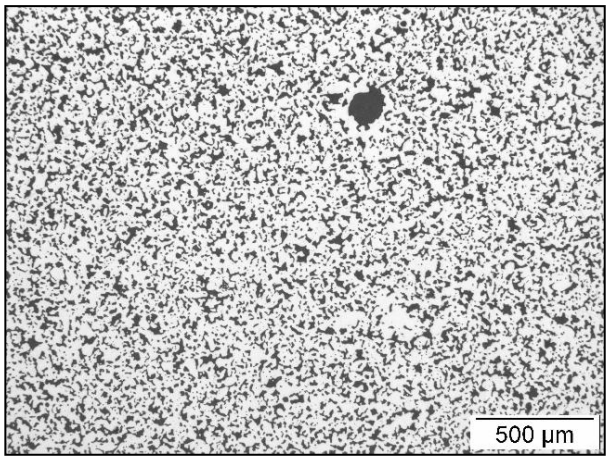

Fig. 4.34: Fe21Cr + 6% PW, 50x, 100 MPa, dewaxed and sintered, 36% P

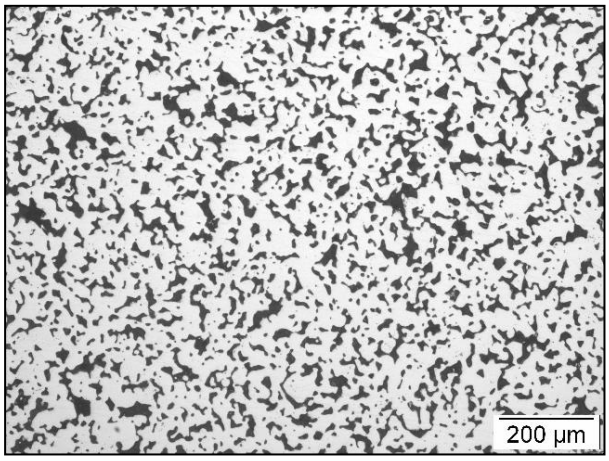

Fig. 4.35: Fe21Cr + 6% PW, 100x, 100 MPa, dewaxed and sintered, 36% P

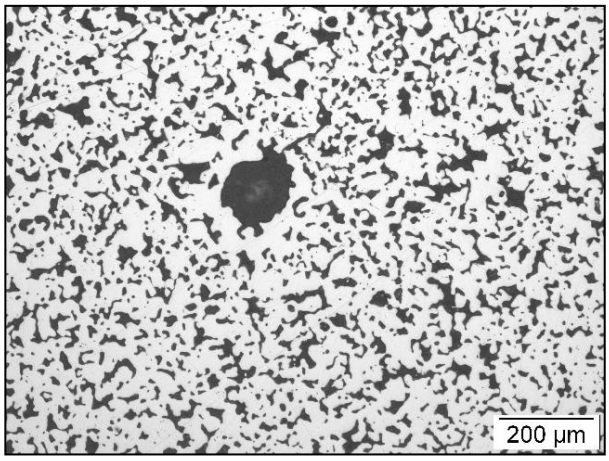

Fig. 4.36: Fe21Cr + 6% PW, 100x, 100 MPa, dewaxed and sintered, 36% P

Fig. 4.33 shows that the pores are finely distributed, but there are also some remaining clusters left (see Fig. 4.36). These pores most probably result from agglomerates of wax while mixing, and while dewaxing these agglomerates form local voids. These voids could be to some degree detrimental for the mechanical stability of the porous metal support.

All in all it could be shown that with raising the amount of lubricant the sintered density decreased, and because of the agglomerations of wax, clusters of pores after dewaxing are visible. But the major disadvantage was the decrease of shrinkage, even at a compacting pressure of 100 MPa only 4% of linear shrinkage could be achieved, and that is far away from the desired 15-20%. To sum it up, the idea of paraffin wax as a spaceholder did not work out. It was then decided to switch to lower compacting pressure without lubricant – so gravity sintering was the next option.

4.2 Gravity sintered samples

4.2.1 Gravity sintering in an Al_2O_3 crucible

4.2.1.1 Influence of starting state

The powder was filled into Al_2O_3 crucibles (with or without tapping) and then sintered for 60 min at 1300°C in H_2. The process is described in detail in chapter 3.5. The starting state for the powder filled without tapping is not directly the apparent density; it is more somewhere between apparent and tap density. The reason is if the crucible is put in the furnace for sintering, densification of the powder takes place because of the small impacts of the sinter boat against the muffle ("pseudo-tapping"). This densification process is investigated in chapter 4.2.2.

The density of the sintered samples was measured by the water displacement method; because of the irregular shape of the samples volumetric measurements were not possible. However, one has to keep in mind that – as was found with the low-pressure compacted specimens - at these very high porosity levels some water might penetrate the pores despite intense impregnation, and therefore a too high density tends to be measured.

The results are shown in Table 4.14. Not surprisingly, the density of the tap-filled samples is always higher than that of the samples filled without tapping.

Table 4.14: Density of the gravity sintered samples (1300°C, 1 h, H_2)

Powder	starting state	m_{AIR} [g]	m_{H2O} [g]	density [g/cm³]	$V_{SINTERED}$ [cm³]
Fe25Cr20Ni2.5Si	bulk	12,5414	9,6335	4,31	2,91
Fe25Cr20Ni2.5Si	tap	14,5452	11,6726	5,06	2,87
Fe18Cr0.3Mn0.5Nb	bulk	13,2105	9,6660	3,73	3,54
Fe18Cr0.3Mn0.5Nb	tap	15,6134	11,6278	3,92	3,99
Fe21Cr	bulk	13,7739	10,3141	3,98	3,46
Fe21Cr	tap	16,1462	12,478	4,40	3,67
Fe21Cr0.5Nb	bulk	13,1855	9,4405	3,52	3,75
Fe21Cr0.5Nb	tap	15,3001	11,2623	3,79	4,04

In order to calculate the linear shrinkage, the sample height after sintering was measured and compared to the crucible height and then calculated by:

Linear shrinkage (heigth) = $((h_{crucible} - h_{sintered\ sample}) / h_{crucible})*100$

Because of the irregular shape of the sintered samples only the height and not the diameter was taken to measure the shrinkage. The results for the linear shrinkage (by height) are shown in Table 4.15. Except for the austenite, the linear shrinkage of the tap-filled samples is around 7 %, of the samples filled without tapping approx. 14% (which of course also includes the effect of "pseudo-tapping" during inserting the crucibles into the furnace). The linear

shrinkage of the austenitic sample is higher than that of the ferritic samples, and the reason is that the smaller particle size of the austenite (< 53 µm to < 75 µm) leads to more densification and higher shrinkage. Otherwise the shrinkage of the ferritic powder should be higher than that of the austenitic powder because of the higher self-diffusion of the ferrite. The self diffusion effect should outweigh the effect of the powder size.

Table 4.15: Linear shrinkage (height) of the gravity sintered samples (density shown in Tab. 4.14)

Powder	starting state	crucible height [mm]	sample height (after sintering) [mm]	shrinkage (lin.) [%]
Fe25Cr20Ni2.5Si	bulk	18,35	14,61	**20,4**
Fe25Cr20Ni2.5Si	tap	18,35	15,53	**15,4**
Fe18Cr0.3Mn0.5Nb	bulk	18,35	15,66	**14,7**
Fe18Cr0.3Mn0.5Nb	tap	18,35	17,08	**6,9**
Fe21Cr	bulk	18,35	15,87	**13,5**
Fe21Cr	tap	18,35	17,01	**7,3**
Fe21Cr0.5Nb	bulk	18,35	15,75	**14,2**
Fe21Cr0.5Nb	tap	18,35	17,00	**7,4**

The sintered samples were also measured with the He pycnometer, and the resulting density was compared to the powder density (also measured with He pycnometry). The comparison is shown in Table 4.16. Except for three measurements, the powder density is hardly higher than the sintered pycnometric density. That means that there is almost exclusively open porosity in the sintered parts (with the possible exception of the closed internal pores mentioned above, which are possibly contained by the powder particles), which is of course a requirement for a porous metal support for an SOFC.

Table 4.16: Comparison of the pycnometric density of powder and gravity sintered samples

Powder	density powder [g/cm³]	density sintered parts [g/cm³]	Δρ
Fe25Cr20Ni2.5Si	7,68	7,64	0,04
Fe25Cr20Ni2.5Si	7,68	7,67	0,00
Fe18Cr0.3Mn0.5Nb	7,55	7,53	0,02
Fe18Cr0.3Mn0.5Nb	7,55	7,56	-0,02
Fe21Cr	7,58	7,60	-0,02
Fe21Cr	7,58	7,64	-0,06
Fe21Cr0.5Nb	7,56	7,50	0,06
Fe21Cr0.5Nb	7,56	7,47	0,09

The porosity of the samples can be seen in Table 4.17. The porosity of the ferritic samples is higher than that of the austenitic one. Even more important is the distribution of the pores. Light microscopic images of the samples can be seen in chapter 0.

Table 4.17: Porosity of the gravity sintered samples

Powder	starting state	sintered density [g/cm ³]	powder density [g/cm³]	porosity [%]
Fe25Cr20Ni2.5Si	bulk	4,31	7,68	43,8
Fe25Cr20Ni2.5Si	tap	5,06	7,68	34,1
Fe18Cr0.3Mn0.5Nb	bulk	3,73	7,55	50,6
Fe18Cr0.3Mn0.5Nb	tap	3,92	7,55	48,1
Fe21Cr	bulk	3,98	7,58	47,5
Fe21Cr	tap	4,40	7,58	42,0
Fe21Cr0.5Nb	bulk	3,52	7,56	53,4
Fe21Cr0.5Nb	tap	3,79	7,56	49,9

4.2.1.2 Influence of sintering time

The powder was filled into the crucible without tapping and sintered at 1300°C in H_2 for 30, 45, 60, 75 and 90 minutes. After sintering, the height of the samples was measured. The crucible height was set at 18.35 mm. The linear shrinkage along the vertical axis was then calculated through:

Linear shrinkage [%] = $[1 – (h_{sample} / h_{crucible})] * 100$

The results are shown in Table 4.18 and Fig. 4.37.

Table 4.18: Sintering experiments using the four base powders and different sintering times

Powder	mass [g]	Sintering time [min]	sample height [mm]	shrinkage (linear) [%]
Fe25Cr20Ni2.5Si	12,01	30	14,96	18,5
Fe25Cr20Ni2.5Si	12,05	45	14,52	20,9
Fe25Cr20Ni2.5Si	12,54	60	14,61	20,4
Fe25Cr20Ni2.5Si	12,98	75	14,22	22,5
Fe25Cr20Ni2.5Si	12,76	90	14,19	22,7
Fe18Cr0.3Mn0.5Nb	13,79	30	16,31	11,1
Fe18Cr0.3Mn0.5Nb	12,81	45	15,54	15,3
Fe18Cr0.3Mn0.5Nb	13,21	60	15,66	14,7
Fe18Cr0.3Mn0.5Nb	13,33	75	15,56	15,2
Fe18Cr0.3Mn0.5Nb	13,39	90	15,02	18,1
Fe21Cr	12,35	30	16,60	9,5
Fe21Cr	12,93	45	16,61	9,5
Fe21Cr	13,77	60	15,87	13,5
Fe21Cr	13,04	75	15,56	15,2
Fe21Cr	13,06	90	15,20	17,2
Fe21Cr0.5Nb	13,16	30	16,92	7,8
Fe21Cr0.5Nb	13,32	45	15,99	12,9
Fe21Cr0.5Nb	13,18	60	15,75	14,2
Fe21Cr0.5Nb	13,00	75	15,88	13,5
Fe21Cr0.5Nb	12,86	90	15,18	17,3

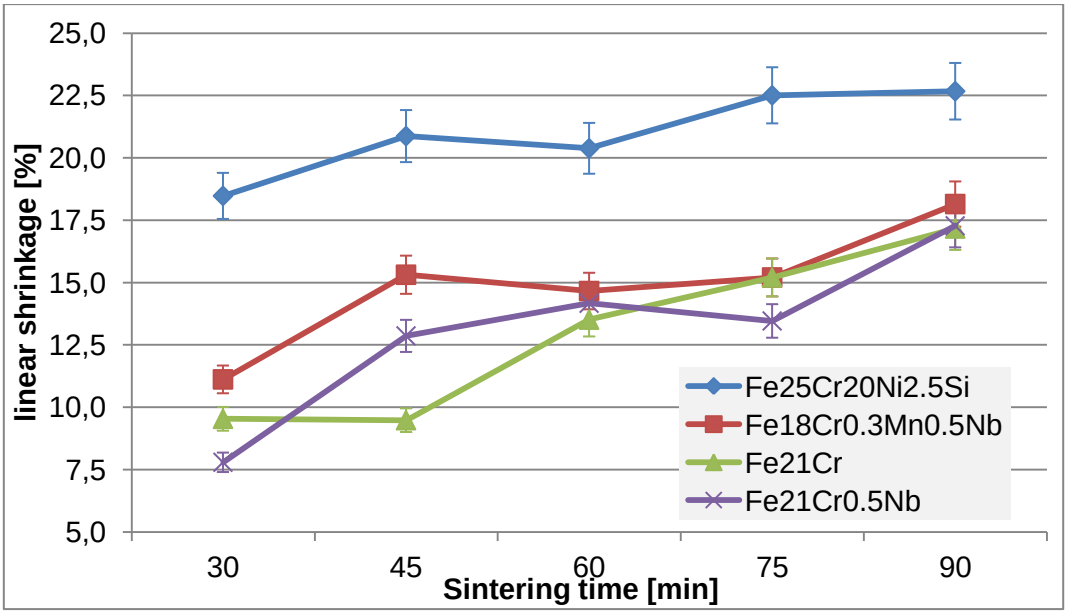

Fig. 4.37: Shrinkage as a function of sintering time

The austenitic sample has the highest shrinkage, starting already at about 18% (after 30 min) and increasing to about 22.5% after 90 min sintering time. It seems that after 75 min, the sintering time has no significant effect on the shrinkage any more for the austenitic sample. This is in contrast to the ferritic samples, where also after a sintering time of 90 min an increase of the shrinkage could be extrapolated. After a sintering time of 90 min, all three ferritic samples have nearly the same shrinkage (~ 17.5%). For the Fe21Cr and the Fe18Cr0.3Mn0.5Nb samples a linear shrinkage of about 15% could be attained after a sintering time of 75 min, which is necessary for co-sintering with all other SOFC parts. To measure the shrinkage in every direction more precisely and in particular to assess the effect of "pseudo-tapping", gravity sintering experiments in an Al_2O_3 boat have been carried out.

4.2.2 Gravity sintering in an Al_2O_3 boat

First of all, two presintering experiments with Fe21Cr powder were carried out. Therefore the powder was filled into Al_2O_3-"boats" (half-full) and heated up to 900°C in argon. The gas was then switched to hydrogen (2 l/min) and the powder was presintered for 30 min at 900°C. The powder was then also cooled down in hydrogen atmosphere. After the presintering, a blue discoloration of the sample can be seen (see Fig. 4.38), because below a certain temperature even fairly dry hydrogen can have an oxidizing effect. It was then decided to do the cooling down for presintering in argon atmosphere.

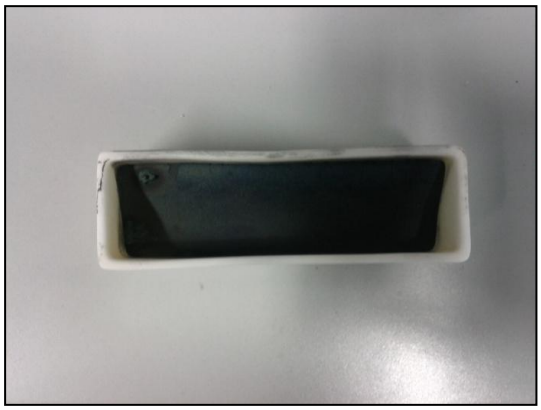

Fig. 4.38: Presintered Fe21Cr powder (900°C, 30 min, H_2)

Fig. 4.39: Fe21Cr sample after final sintering at 1300°C, 60 min, H_2 (presintered at 900°C)

Fig. 4.40: Presintered Fe21Cr powder (1100°C, 30 min, H_2)

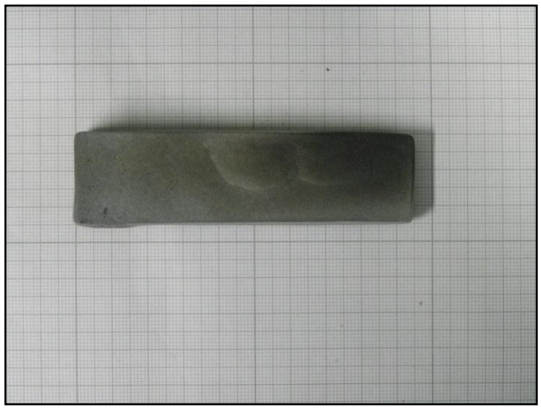

Fig. 4.41: Fe21Cr sample after final sintering at 1300°C, 60 min, H_2 (presintered at 1100°C)

After presintering the Fe21Cr powder for 30 min at 900°C, the powder was still loose and no sinter bonds had been formed, and therefore the temperature for presintering was raised to 1100°C, while the parameters for the final sintering remained the same (1300°C, 60 min, H_2, 2 l/min). After the final sintering the length of the sample was measured and the shrinkage of the sample (rectangular to the gravity force; in direction of the longitudinal axis of the sinter boat) was obtained. For the sample presintered at 900°C a shrinkage of 3.4%, for the sample presintered at 1100°C a shrinkage of 3.1% was measured. It seems that presintering of powder counteracts with the shrinkage. The shrinkage in direction to the gravity force could not be measured because the uneven height of the samples (see Fig. 4.38). The uneven height of the sample is more a consequence of the rearrangement of the powder while putting it in the furnace than an anisotropic shrinkage.

It was then tried to measure the "real" starting state of the powder without tapping, but after "pseudo-tapping". Therefore the powder was filled into the Al2O3 boat and then the boat was pushed through the cold furnace carefully like in a normal sinter run. The height of the powder was measured before and after the run. This procedure was repeated 10 times with all four powders. The height of the powder was about 2.5 mm lower after the run (= 10% lower

than the filling height of the powder at the start), which indicates the effect of "pseudo-tapping". The powder mass and the volume of the boat have been measured, so the "starting density" of the powder before sintering can be calculated easily. In case of the Fe21Cr0.5Nb powder, this results in a "starting state" density of 2.80g/cm³, and that is about 10% higher than the apparent density of the (2.56 g/cm³). An increase of about 10% in density in contrast to the apparent density could be observed for every powder.

In order to measure the shrinkage more precisely, gravity sintering experiments for both powder grades (austenitic and ferritic) have been carried out. Therefore the powder was filled into Al_2O_3 boats up to the edge, and it was tried not to tap the crucible while filling and while putting it in the furnace. In order to do so, the powder was poured on a paper first and from the paper one just let it trickle into the Al_2O_3 boat. While putting it into the furnace, it was tried not to touch the sidewalls of the muffle. In case of sintering starting from tapped density, the powder was put on a sieving stack in order to do the tapping uniformly. The sintering again was performed at 1300°C for 60 min in hydrogen. The dimension of the samples was measured after sintering and the shrinkage was calculated by:

$$\text{Linear shrinkage [\%]} = [1 - (l_{sintered} / l_{boat})] * 100$$

In Table 4.19 the measured shrinkage can be seen. For the ferritic and the austenitic sample there is a big difference concerning the shrinkage of the height. The shrinkage in direction to the gravity force for the ferritic sample is 5.6% higher for the bulk sintered than for the tapped sintered samples (austenitic: 9% higher resp.). This could mean that the around 5-10% are enforced by "pseudo-tapping" and gravity. As could be shown above, the major part of the shrinkage is enforced by "pseudo-tapping" and not by gravity. The shrinkage of the height of the ferritic samples is markedly higher than the shrinkage in the other directions. But this can be easily explained because the ferritic powder stuck to the ceramic sinter case which inhibited shrinkage in the horizontal plane. To remove the sintered body, the ceramic case had to be destroyed. The shrinkage in height is higher than in the other directions. It is assumed that the densification process of the powder takes place from the top to the bottom and since no powder can get lost, the powder from the top "heads" to the width.

Table 4.19: Shrinkage of the gravity sintered samples (1300°C, 60 min, H_2)

	shrinkage (%)		
Sample	**Length**	**width**	**height**
Fe21Cr bulk	2,4	6,4	16,0
Fe21Cr tapped	0,5	8,6	10,4
Fe25Cr20Ni2.5Si bulk	7,1	11,5	22,8
Fe25Cr20Ni2.5Si tapped	6,7	10,1	13,6

Metallographic investigations

In the following images only the longitudinal plane (perpendicular to the gravity force) of the gravity sintered samples is shown. The distribution of pores in the cross section is also very fine.

Fe25Cr20Ni2.5Si (1300°C, H_2, 60min)

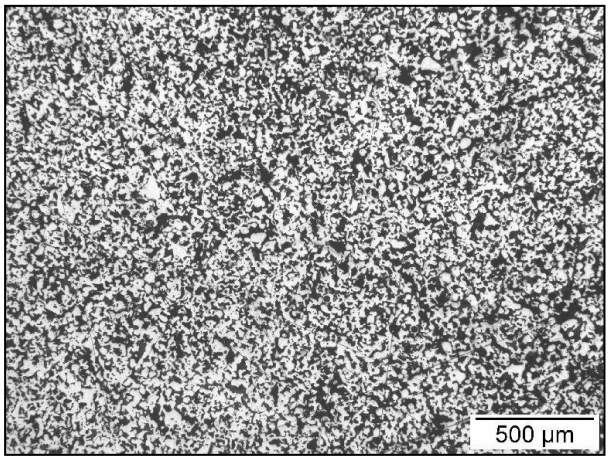

Fig. 4.42: Fe25Cr20Ni2.5Si, bulk state, longitudinal plane, 50x, 44% P

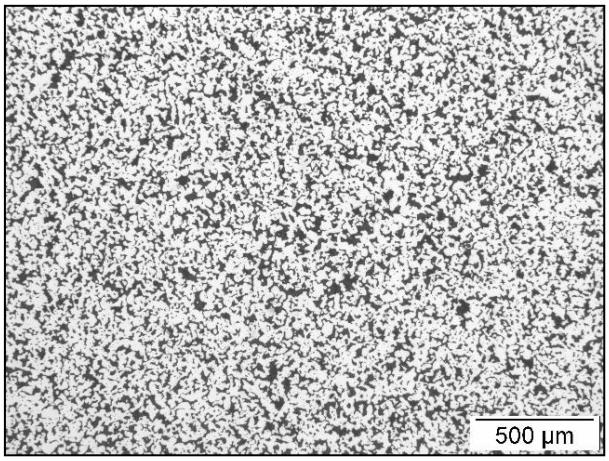

Fig. 4.43: Fe25Cr20Ni2.5Si, tapped state, longitudinal plane, 50x, 34% P

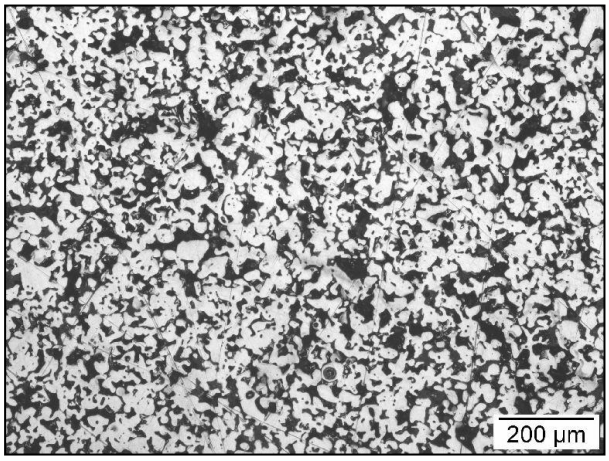

Fig. 4.44: Fe25Cr20Ni2.5Si, bulk state, longitudinal plane, 100x, 44% P

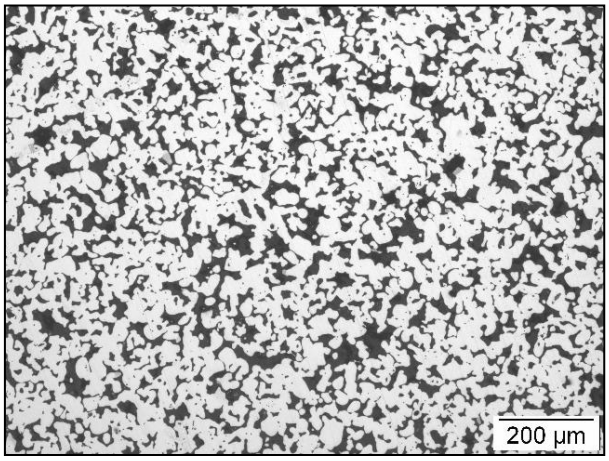

Fig. 4.45: Fe25Cr20Ni2.5Si, tapped state, longitudinal plane, 100x, 34% P

The porosity in this austenitic sample is about 44%. The pores in this austenitic sample are homogeneously distributed, and agglomerations of pores are only slightly visible.

Naturally, the sintered density of the gravity sintered samples started from tapped state is higher than the one for the samples started from the bulk state. Therefore also the porosity is considerably lower. The porosity of the Fe25Cr20Ni2.5Si sample started from the tapped state is about 34% (44% resp. for the bulk state) and again the pores are finely distributed, and no agglomerations are visible.

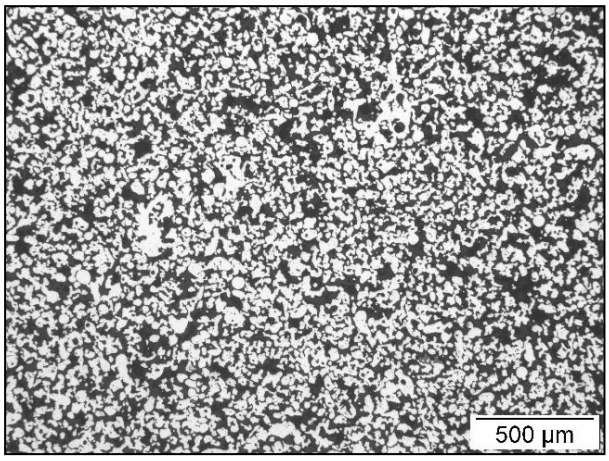

Fig. 4.46: Fe18Cr0.3Mn0.5Nb, bulk state, longitudinal plane, 50x, 51% P

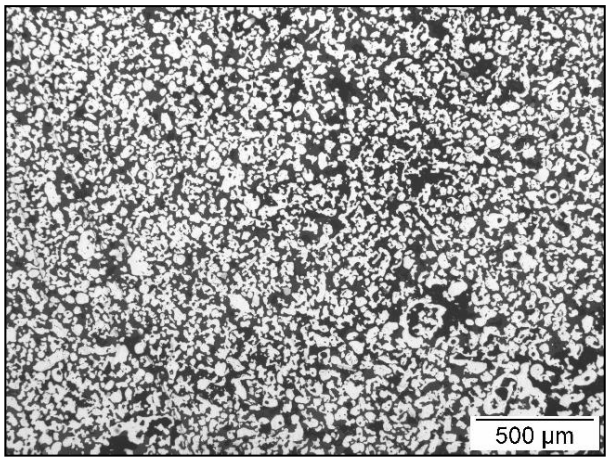

Fig. 4.47: Fe18Cr0.3Mn0.5Nb, tapped state, longitudinal plane, 50x, 48% P

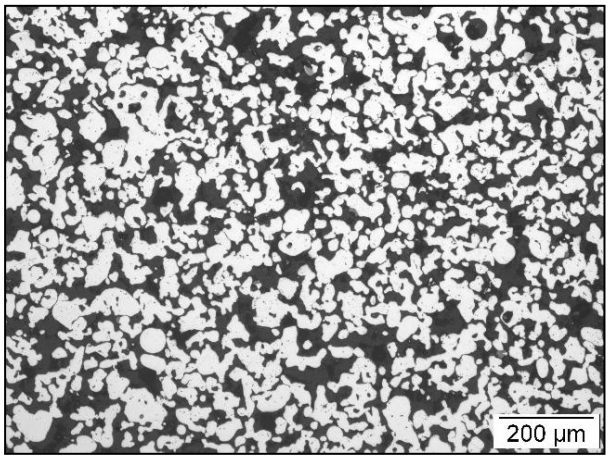

Fig. 4.48: Fe18Cr0.3Mn0.5Nb, bulk state, longitudinal plane, 100x, 51% P

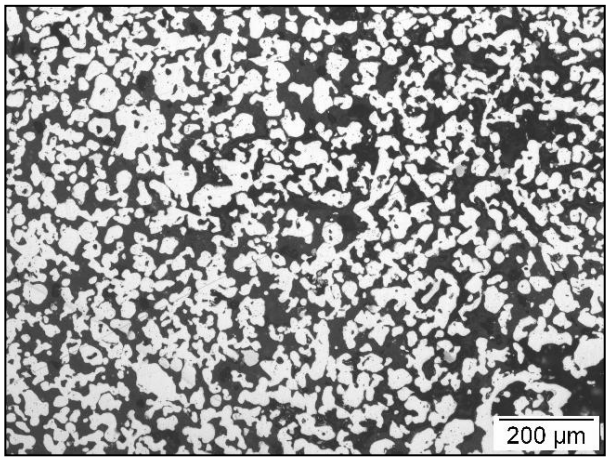

Fig. 4.49: Fe18Cr0.3Mn0.5Nb, tapped state, longitudinal plane, 100x, 48% P

The porosity in the Fe18Cr0.3Mn0.5Nb sample (sintered at 1300°C, 60min, H_2) is about 51%, and the distribution of the pores is again very fine. There is no big difference to the tapped state, but the porosity is higher than the one for the austenitic sample.

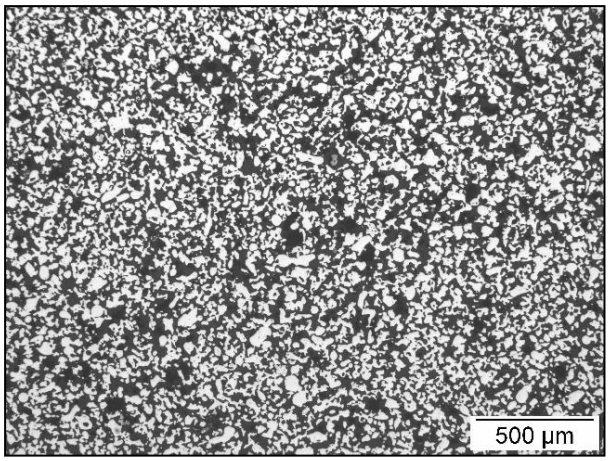

Fig. 4.50: Fe21Cr, bulk state, longitudinal plane, 50x, 48% P

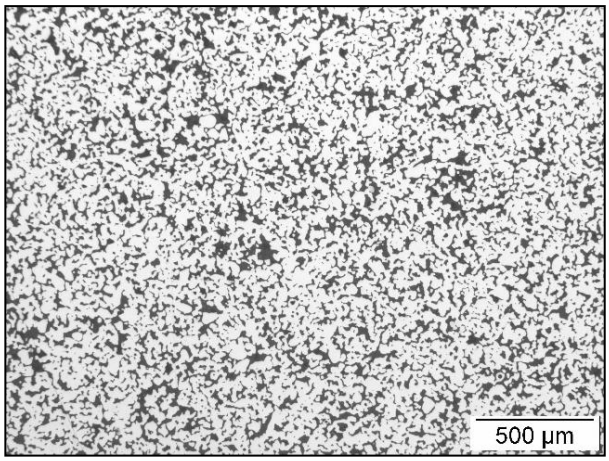

Fig. 4.51. Fe21Cr, tapped state, longitudinal plane, 50x, 42% P

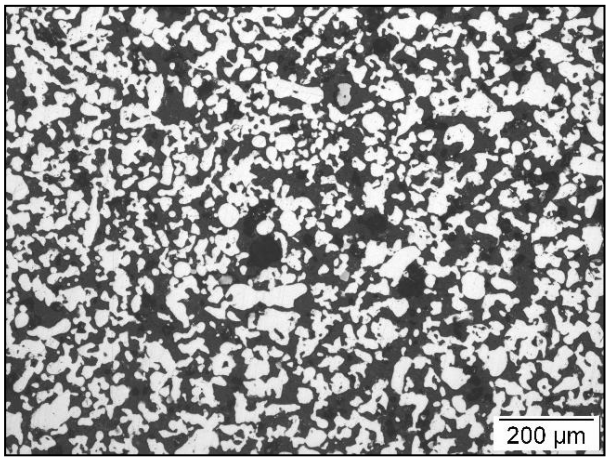

Fig. 4.52: Fe21Cr, bulk state, longitudinal plane, 100x, 48% P

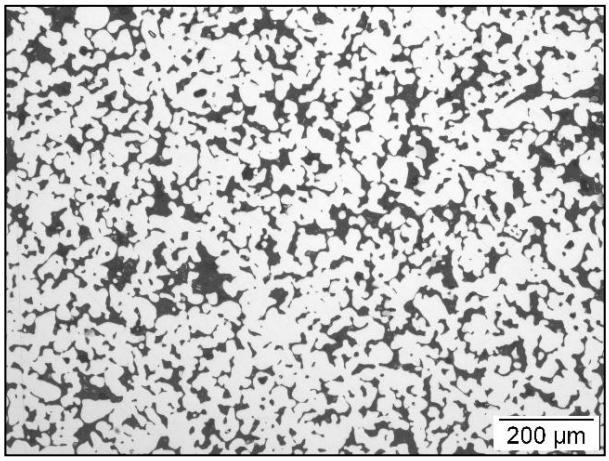

Fig. 4.53: Fe21Cr, tapped state, longitudinal plane, 100x, 42% P

The porosity of the Fe21Cr sample in the bulk state is about 48% and the pores are again well distributed with hardly any agglomerations. This is also valid for the tapped state with 42% porosity.

Fe21Cr0.5Nb (1300°C, H_2, 60min)

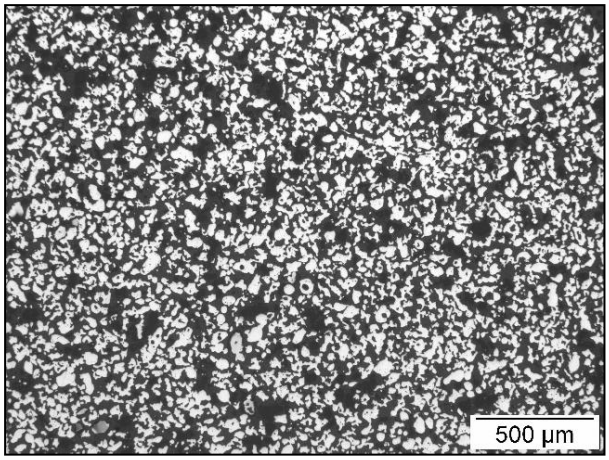

Fig. 4.54: Fe21Cr0.5Nb, bulk state, longitudinal plane, 50x, 53% P

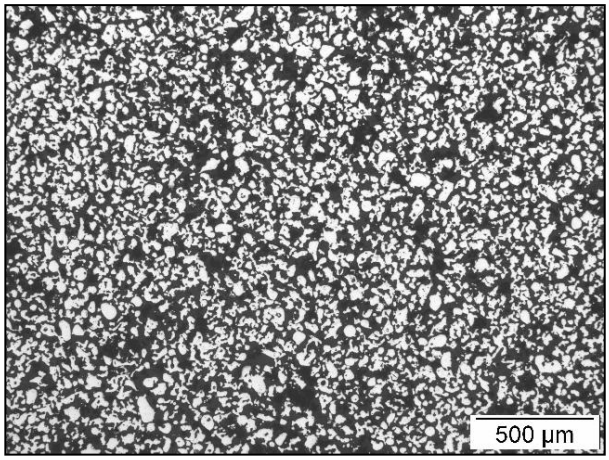

Fig. 4.55: Fe21Cr0.5Nb, tapped state, 50x, longitudinal plane, 50% P

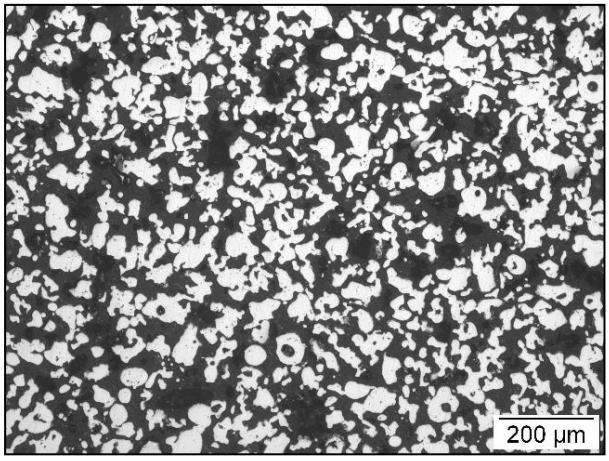

Fig. 4.56: Fe21Cr0.5Nb, bulk state, longitudinal plane, 100x, 53% P

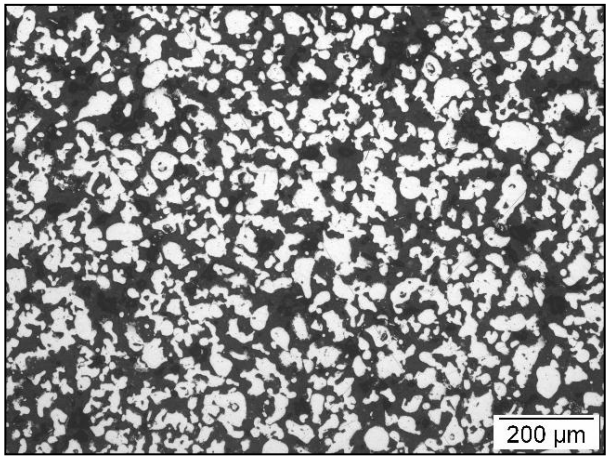

Fig. 4.57: Fe21Cr0.5Nb, tapped state, 100x, longitudinal plane, 50% P

The porosity of this sample is about 53%, the pores are finely distributed. Some small agglomerations of pores can be seen. The porosity of the Fe21Cr0.5Nb sample is about 50%, the distribution is rather fine.

Gravity sintering is a promising method for fabrication of this porous metal support. First the powder was filled into Al_2O_3 crucibles and the effect of tapping the powder on the density and shrinkage has been investigated. It could be shown that the sintered density of the tapped powder is higher than that of the untapped one. The shrinkage (measured by height; in the crucibles) for the untapped ferritic samples is by 7% higher than that of the tapped powder, and also longer sintering time leads to higher shrinkage. To measure the shrinkage more precisely, gravity sintering experiments in Al_2O_3 boats have been carried out. There it could be seen that the shrinkage is anisotropic. For the Fe21Cr sample shrinkage of 16.0% in height, but only 6.4% in width and 2.4% in length were obtained. Metallographic investigations of

the samples show that the pores are finely distributed, even at 50% porosity. The austenitic sample has higher densities than the ferritic ones, resulting in lower porosity.

4.3 Binder experiments

4.3.1 Polyvinyl alcohol solution system

A binder system based on polyvinvyl alcohol (PVA) was tested. The powder and the PVA distilled in water were stirred and the slurry was injected into a silicone mold. The dried PVA samples were sintered in vacuum at 1200 – 1300°C for 60 – 360 min. After that the samples were cooled down to room temperature again as fast as possible (detailed description in Chapter 3.5). Also some sintering experiments in hydrogen were carried out, but the samples tended to break and showed more deformation than the samples sintered in vacuum.

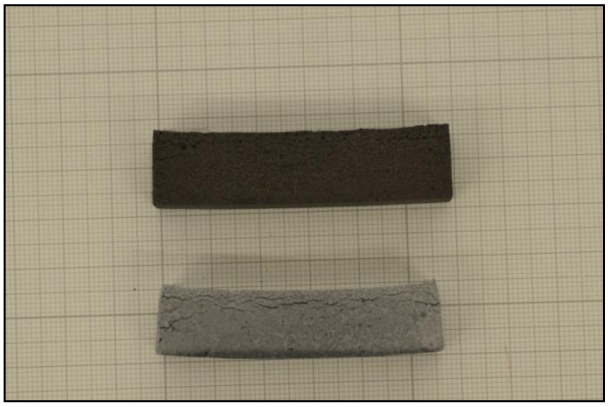

Fig. 4.58: Fe21Cr + PVA before (above) and after (below) sintering in vacuum.

Table 4.20 shows the density (green and sintered; volumetric method), linear shrinkage and porosity of the samples that were chosen for the following metallographic investigations. The specimens differed in sintering parameters, otherwise they were identical.

Table 4.20: Characteristics of the PVA samples chosen for metallographic investigations. Starting powder Fe21Cr

Sample	sintering temperature [°C]	sintering time	green density [g/cm³]	sintered density [g/cm³]	linear shrinkage [g/cm³]	porosity [%]
PVA 7	1250	60	2,44	2,63	3,2	65,0
PVA 13	1250	180	2,78	3,26	4,9	57,0
PVA 19	1200	60	2,90	3,08	2,1	59,4
PVA 23	1300	60	2,75	3,08	5,9	59,4
PVA 27	1250	360	2,9	3,42	5,9	54,9

All five samples were studied by light microscopy, but the pore size and pore distribution did not depend strongly on sintering time and temperature. This is the reason why only images of the samples PVA 7 (1250°C, 60 min) and PVA 27 (1250°C, 360 min) are shown.

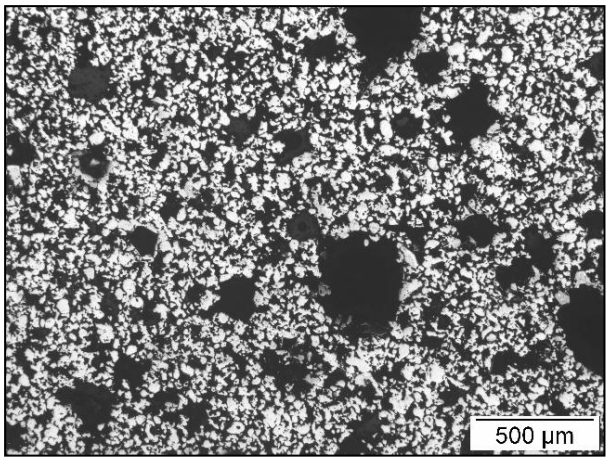

Fig. 4.59: Fe21Cr + PVA, 50x, sintered (1250°C, 60 min, vacuum), 65% P

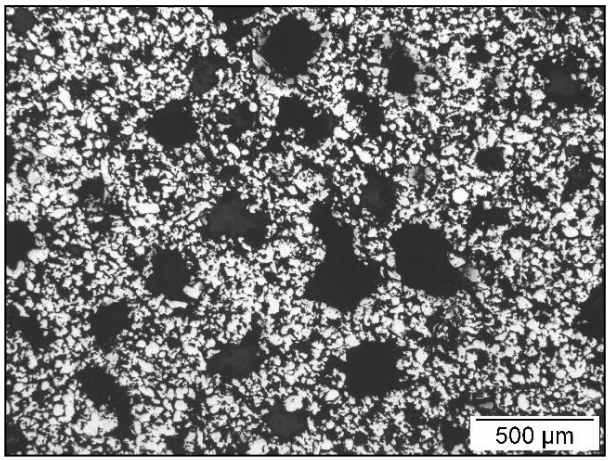

Fig. 4.60: Fe21Cr + PVA, 50x, sintered (1250°C, 60 min, vacuum), 65% P

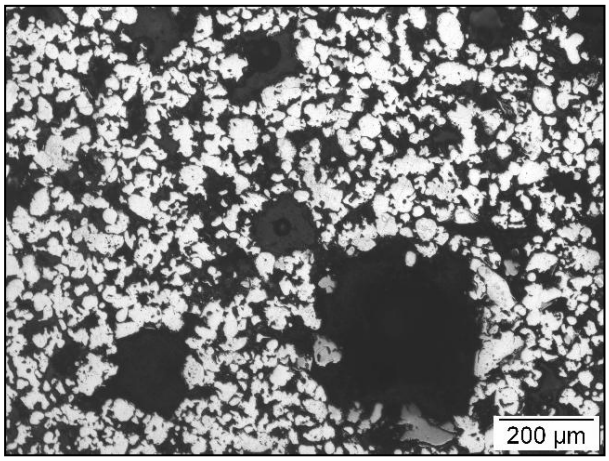

Fig. 4.61: Fe21Cr + PVA, 100x, sintered (1250°C, 60 min, vacuum), 65% P

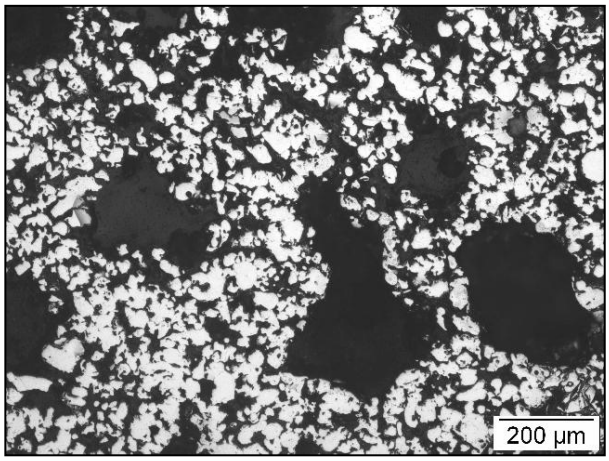

Fig. 4.62: Fe21Cr + PVA, 100x, sintered (1250°C, 60 min, vacuum), 65% P

The PVA Nr. 7 sample (1250°C, 60 min, vacuum) shows the highest porosity of all samples, with 65%. There are however numerous large pores all over the sample, which is detrimental for the mechanical properties.

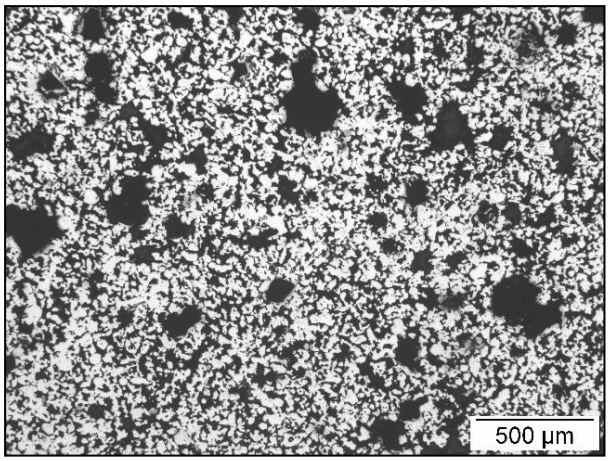

Fig. 4.63: Fe21Cr + PVA, 50x, sintered (1250°C, 360 min, vacuum), 55% P

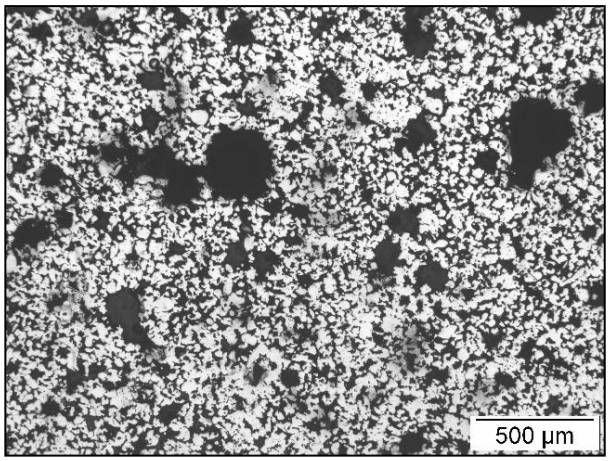

Fig. 4.64: Fe21Cr + PVA, 50x, sintered (1250°C, 360 min, vacuum), 55% P

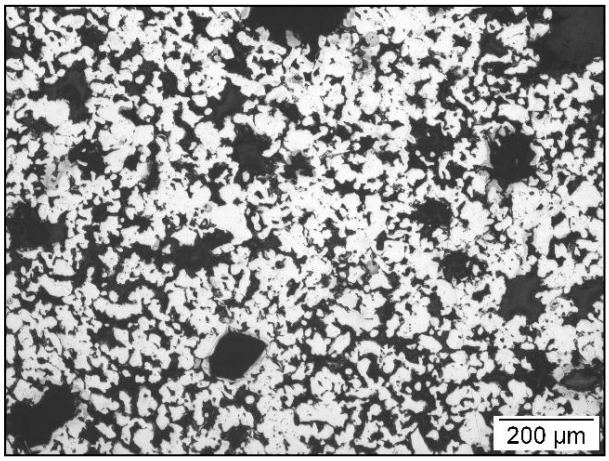

Fig. 4.65: Fe21Cr + PVA, 100x, sintered (1250°C, 360 min, vacuum), 55% P

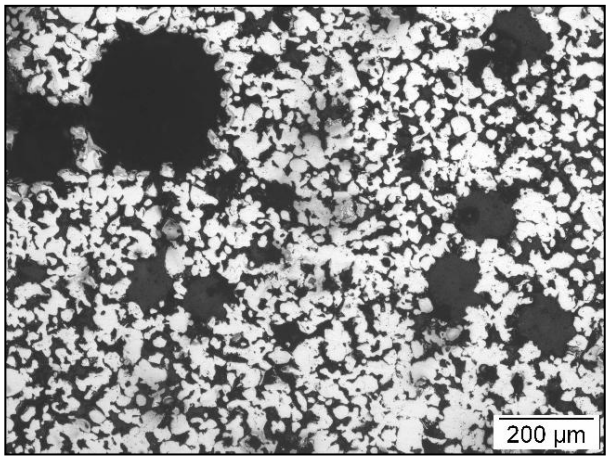

Fig. 4.66: Fe21Cr + PVA, 100x, sintered (1250°C, 360 min, vacuum), 55% P

The porosity of the PVA Nr. 27 sample (1250°C, 360 min, vacuum) is about 55%, i.e. 10% lower than with the other PVA sample, because of the longer sintering time. But still after 360 min of sintering, there are again numerous big pores visible. As is well known, such heterogeneous porosity does not lead to even densification and shrinkage, but the larger pores rather act as "condensation" nuclei for the finer porosity, i.e. this is a case of Ostwald ripening of the pores.

The metallographic investigations of these samples thus show that the PVA method is not suitable for producing these porous metal supports, at least if regular porosity is required, since it is not possible to obtain a homogeneous mix of PVA and powder that would result in a sintered body with homogeneous pore distribution.

4.3.2 Latex binder samples

The Fe21Cr powder was mixed with Styronal, a binder based on a styrene and butadiene copolymer, and cyclohexane for 2 hrs. After decanting of the liquid, the powder was formed by hand and dried overnight. After that the samples was dewaxed (600°C, 60 min, Ar flow rate 2 l/min; H_2 flow rate 0.5 l/min) and sintered (1300°C, 60 min, H_2 flow rate 2 l/min).

The green density is about 1.5 – 2.1 g/cm³ (volumetric method), the sintered density about 4.1 g/cm³ (water displacement method). The linear shrinkage of this sample is about 10.7% and the porosity was calculated as 46%.

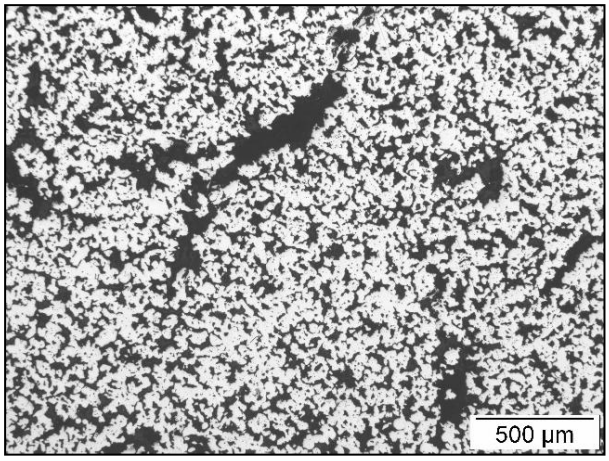

Fig. 4.67: Fe21Cr sample with Styronal binder, 50x, 46% P

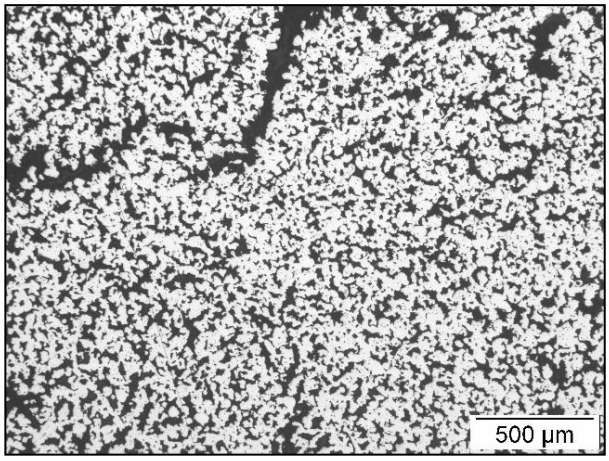

Fig. 4.68: Fe21Cr sample with Styronal binder, 50x, 46% P

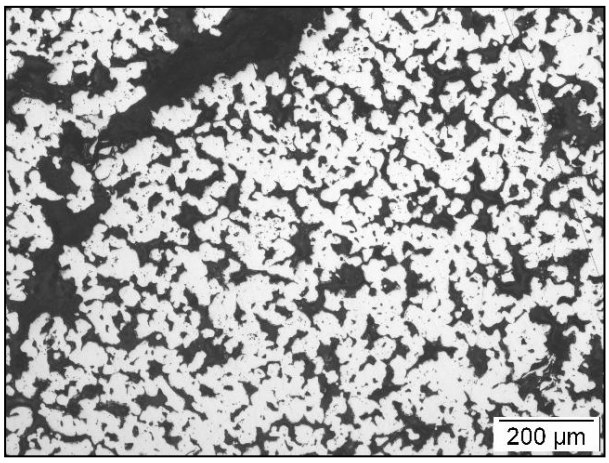

Fig. 4.69: Fe21Cr sample with Styronal binder, 100x, 46% P

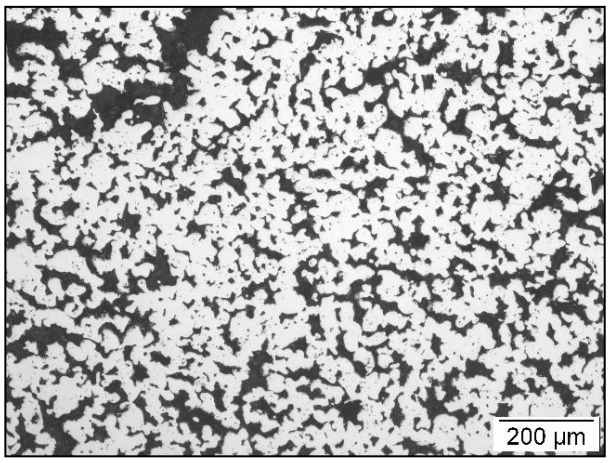

Fig. 4.70: Fe21Cr sample with Styronal binder, 100x, 46% P

In Fig. 4.67 and in Fig. 4.68 can be seen that the pores are rather finely distributed, there are a lot of interconnected pores and some cracks. The idea is to get rid of cracks through consolidation by powder extrusion molding and that was the reason that powder extrusion molding and metal injection molding experiments have been carried out at the UC3M.

4.4 MIM samples

Due to better availability of the powder, a different ferritic (Fe16Cr) and a different lot of the austenitic (Fe25Cr20Ni2.5Si, lot "UC3M") powder was used for the MIM and PEM experiments at UC3M. The feedstock of the ferritic samples consisted of high density polyethylene (HDPE), paraffin wax and stearic acid; the austenitic feedstock only of HDPE and paraffin wax. For both powders the powder loading was in the range of 45 – 55 vol%. The samples were then debinded (solvent and thermal) and sintered at 1300°C for 60 min in vacuum (for the debinding and sintering process see Chapter 3.11). The manufacturing of the samples is described in detail in Chapter 3.9.

Results

DSC and TGA measurements of green parts were performed; the curves are shown in Fig. 4.71 and in Fig. 4.72. The samples were heated up from room temperature to 600°C at 10 K/min in nitrogen atmosphere (20 ml/min). The blue line stands for the TGA and determines the mass loss, in total about 10 wt%. The first pronounced mass loss is about 5 wt% and is finished before reaching 400°C, assigned to removal of the paraffin wax. The second mass loss then comes from the high density polyethylene and is finished at 500°C.

The red line stands for the DSC, with three endothermic reactions. First, the melting of paraffin wax is starting at 50°C, then the melting of the HDPE starting around 130°C, and at last the degradation of the binder starting around 450°C. It is remarkable that there is no pronounced DSC-peak for the first mass loss, between 250 and 450°C, although there should be, because melting, evaporation and decomposition are all endothermic reactions. Apparently these endothermic reactions extend over such a wide temperature "window" that no clear DSC signal is generated.

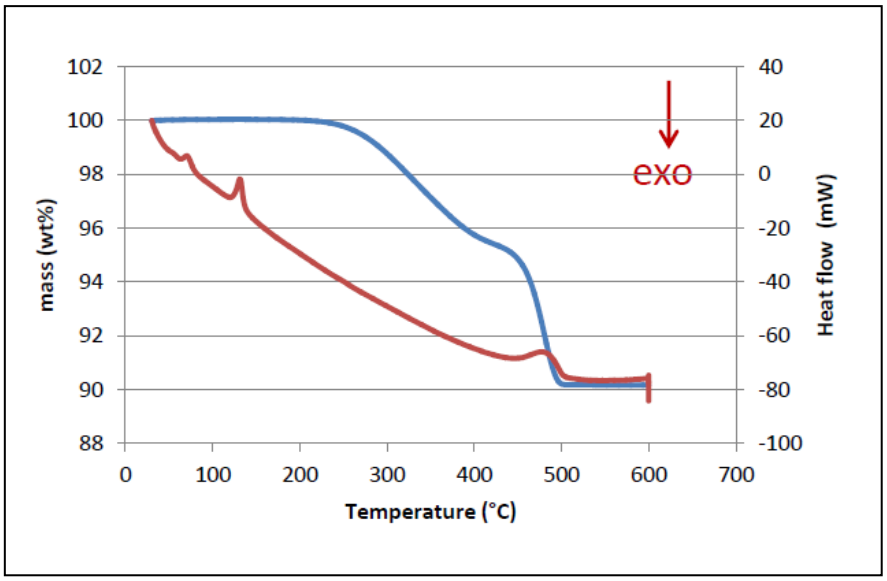

Fig. 4.71: DSC (red) and TGA (blue) curves for the austenitic feedstock (polyethylene and paraffin wax as binder)

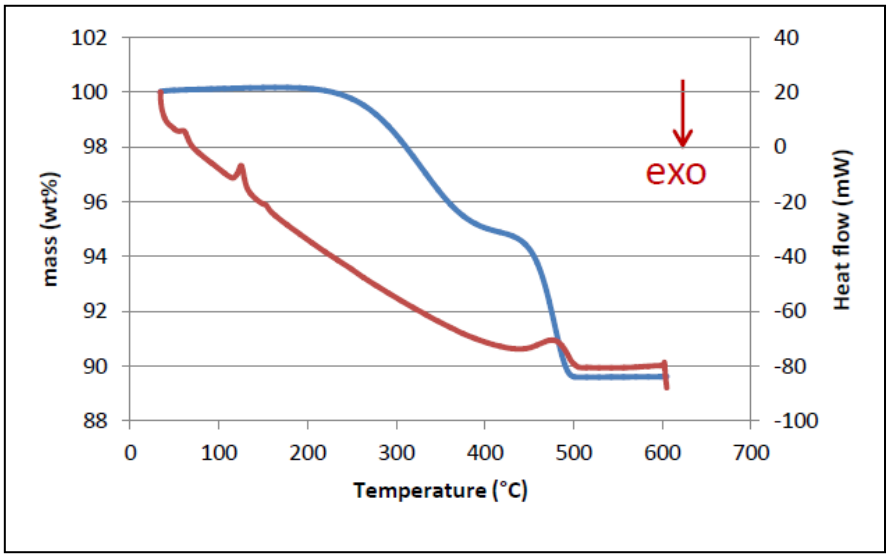

Fig. 4.72: DSC (red) and TGA (blue) curves for the ferritic feedstock (polyethylene, paraffin wax and stearic acid as binder)

The green and sintered density (Archimedes method) of the samples is shown in Fig. 4.73. As a reminder, the green density was measured on the green parts and not on the brown parts. It is obvious that the sintered density decreases with increasing binder content/decreasing powder loading. The sintered density of the austenitic sample is lower than that of the ferritic one. This is in contrast to the results of the gravity sintered samples, where the austenitic samples had a higher density than the ferritic ones. A reason could be that the powders used for MIM and gravity sintering, respectively, were different.

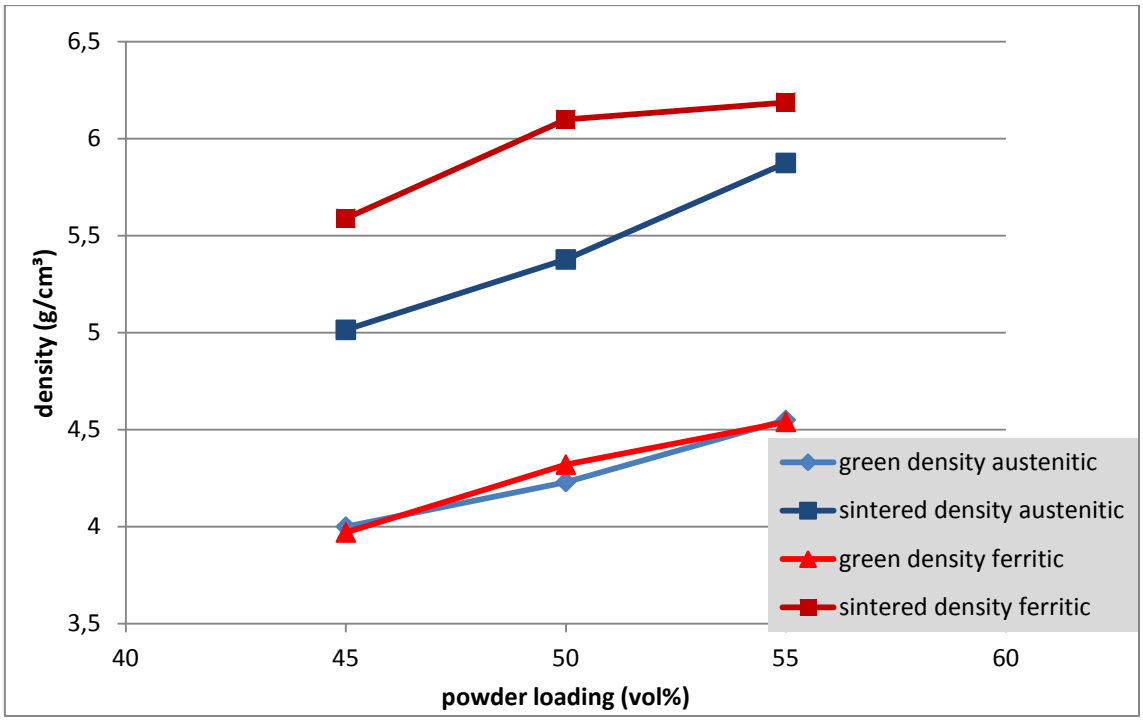

Fig. 4.73: Green and sintered density of the MIM samples

In Table 4.21 the shrinkage of the MIM samples is shown. The shrinkage was calculated by using the following formula:

Linear shrinkage [%] = $[1 - (l_{sintered} / l_{green\ part})] * 100$

The shrinkage in every direction was measured and calculated this way (at least 6 samples per powder loading). It seems that for a given powder loading it is isotropic. Injection moulding itself is always claimed as to be an isotropic forming process. It could also be possible that the shrinkage is not depending on the powder loading in the range from 45 – 55 vol%. It has to be pointed out that the increase in density during sintering correlates well with the decrease of the volume as calculated from the shrinkage data.

Table 4.21: Shrinkage of the vacuum sintered MIM samples (1300°C, 60 min)

		shrinkage (%)		
Sample	powder loading (vol%)	length	Width	height
Fe16Cr	55	13,3	14,5	13,9
Fe16Cr	50	13,5	13,6	11,0
Fe16Cr	45	13,4	14,8	12,8
Fe25Cr20Ni2.5Si	55	10,1	11,0	11,9
Fe25Cr20Ni2.5Si	50	9,5	9,9	10,3
Fe25Cr20Ni2.5Si	45	11,2	12,3	13,1

Table 4.22 shows the carbon, oxygen and nitrogen contents of the ferritic powder and the respective samples throughout the whole manufacturing process. The carbon content of the powder is very low. The feedstock consisted of polyethylene, paraffin wax and stearic acid. It is obvious that, as expected, increasing the binder content in the feedstock increases the carbon content as well. After solvent debinding (cyclohexane, 60°C, 5 hrs) the carbon content is halved, and after thermal debinding in air the content is about 0.03 wt%. The carbon content after sintering is nearly the same as that of the powder. I.e. carbon control during processing should be possible even for this high Cr powder.

The oxygen content of the feedstock and after debinding is about 0.35 – 0.50 wt%.

Table 4.22: C/O/N-content of the ferritic powder (Fe16Cr) and samples

Sample	powder loading (vol%)	wt%C	wt% O	wt%N
Powder	-	0,013 ± 0,001	0,201 ± 0,005	0,007 ± 0,001
Feedstock	45	10,78 ± 1,17	0,369 ± 0,030	0,257 ± 0,033
after solvent debinding	45	5,87 ± 0,07	0,431 ± 0,015	0,179 ± 0,010
after thermal debinding	45	0,029 ± 0,003	0,401 ± 0,031	0,030 ± 0,001
vacuum sintered	45	0,013 ± 0,004	0,341 ± 0,005	0,0005 ± 0,0003
Feedstock	50	9,11 ± 0,03	0,470 ± 0,033	0,226 ± 0,016
after solvent debinding	50	5,57 ± 0,09	0,391 ± 0,014	0,246 ± 0,005
after thermal debinding	50	0,027 ± 0,003	0,366 ± 0,010	0,031 ± 0,001
vacuum sintered	50	0,019 ± 0,033	0,299 ± 0,021	0,002 ± 0,001
Feedstock	55	8,13 ± 0,31	0,355 ± 0,007	0,216 ± 0,006
after solvent debinding	55	4,31 ± 0,11	0,377 ± 0,017	0,122 ± 0,007
after thermal debinding	55	0,036 ± 0,002	0,379 ± 0,007	0,033 ± 0,001
vacuum sintered	55	0,016 ± 0,003	0,325 ± 0,012	0,0006 ± 0,0001

In Table 4.23 the carbon, oxygen and nitrogen content of the austenitic powder and samples is shown. The behaviour is the same as that of the ferritic samples. After solvent debinding the carbon content is halved and further reduced after thermal debinding. After sintering the carbon content is nearly the same as that of the powder.

Table 4.23: C/O/N-content of the austenitic (Fe25Cr20Ni2.5Si) powder and samples

Sample	powder loading (vol%)	wt%C	wt% O	wt%N
Powder	-	0,021 ± 0,001	0,167 ± 0,005	0,083 ± 0,015
Feedstock	45	10,61 ± 0,09	0,535 ± 0,027	0,380 ± 0,029
after solvent debinding	45	5,07 ± 0,07	0,347 ± 0,005	0,153 ± 0,001
after thermal debinding	45	0,032 ± 0,001	0,499 ± 0,003	0,129 ± 0,004
vacuum sintered	45	0,018 ± 0,003	0,2275 ± 0,001	0,0007 ± 0,0001
Feedstock	50	9,01 ± 0,24	0,560 ± 0,082	0,244 ± 0,038
after solvent debinding	50	6,22 ± 0,11	0,403 ± 0,004	0,273 ± 0,001
after thermal debinding	50	0,065 ± 0,006	0,337 ± 0,002	0,140 ± 0,001
vacuum sintered	50	0,130 ± 0,009	0,247 ± 0,006	0,0029 ± 0,0002
Feedstock	55	7,76 ± 0,15	0,457 ± 0,057	0,417 ± 0,019
after solvent debinding	55	4,09 ± 0,02	0,296 ± 0,008	0,211 ± 0,009
after thermal debinding	55	0,031 ± 0,001	0,330 ± 0,002	0,136 ± 0,002
vacuum sintered	55	0,022 ± 0,003	0,221 ± 0,002	0,001 ± 0,001

As can be seen in Fig. 4.74- Fig. 4.91, the distribution of the pores for the ferritic samples is very good. No agglomeration of pores is visible even for the lowest powder loading with 45 vol%. There are no differences between the sections cut in different orientations.

Fig. 4.92 - Fig. 4.109 show the pore distribution for the austenitic samples. Due to their higher porosity, the distribution is not as good as for the ferritic ones. However, compared to other approaches with spaceholders the porosity is still quite regular, except for the austenitic sample with the lowest powder loading (45 vol%), for which agglomerations of pores can be seen. The question is if stearic acid as a surface-active agent has a beneficial effect for the austenitic powder at this low powder loading (it should be remembered that the feedstock used here did not contain stearic acid). Due to the short stay in Leganes for only two months, additional binder experiments with stearic acid were not possible.

Ferritic MIM samples

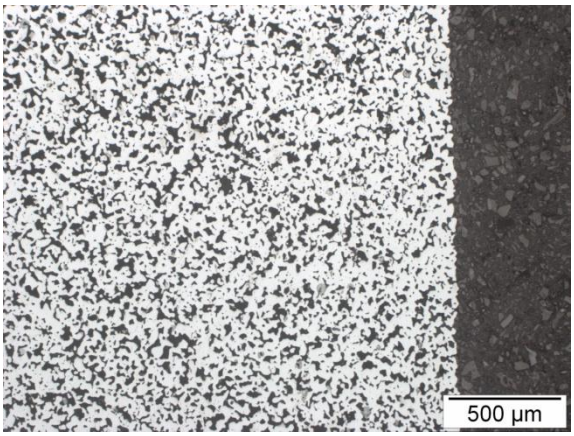

Fig. 4.74: Fe16Cr + 45 vol% powder loading, horizontal plane, 50x, 28% porosity

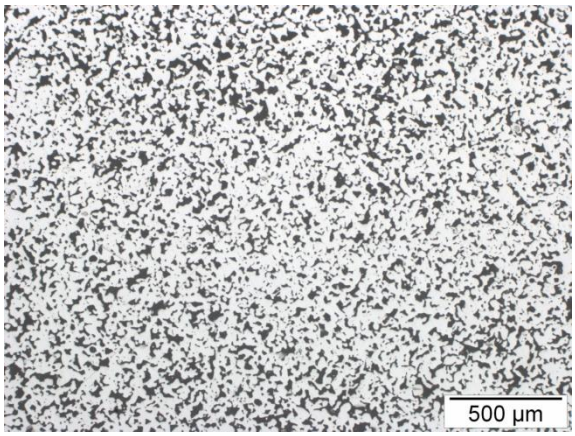

Fig. 4.75: Fe16Cr + 45 vol% powder loading, horizontal plane, 50x, 28% porosity

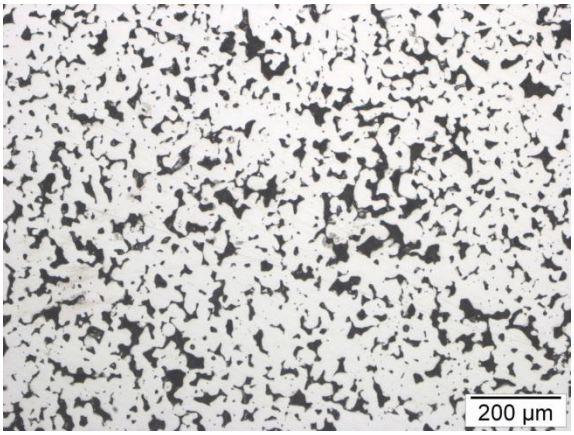

Fig. 4.76: Fe16Cr + 45 vol% powder loading, horizontal plane, 100x, 28% porosity

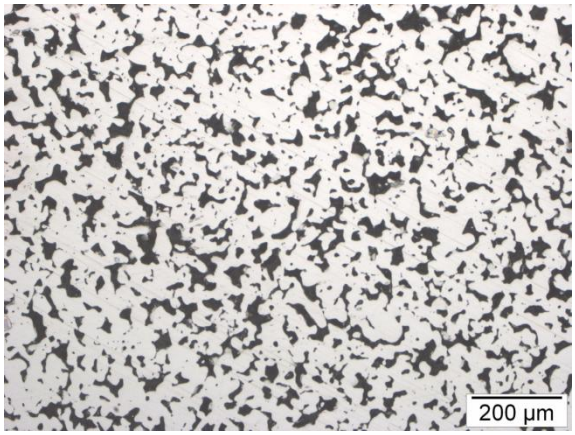

Fig. 4.77: Fe16Cr + 45 vol% powder loading, horizontal plane, 100x, 28% porosity

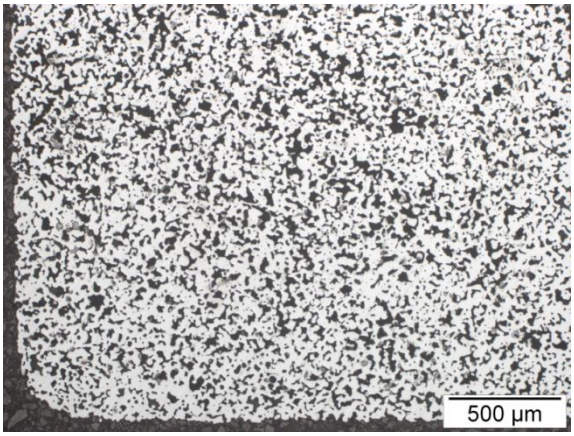

Fig. 4.78: Fe16Cr + 45 vol% powder loading, cross plane, 50x, 28% porosity

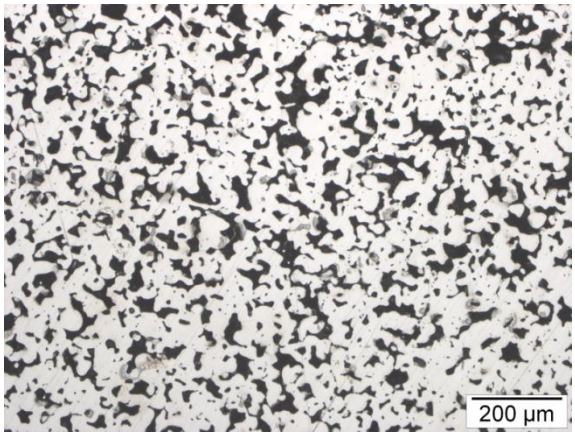

Fig. 4.79: Fe16Cr + 45 vol% powder loading, cross plane, 100x, 28% porosity

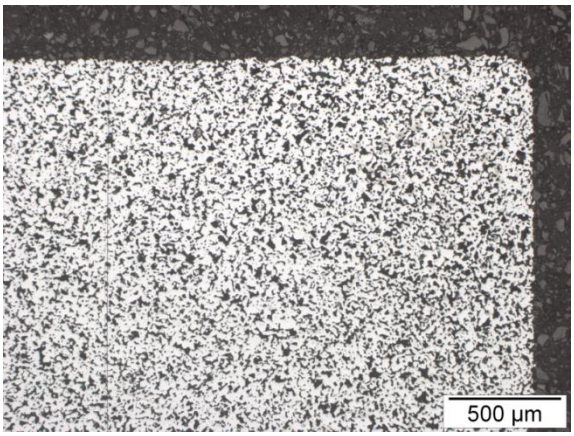

Fig. 4.80: Fe16Cr + 50 vol% powder loading, horizontal plane, 50x, 22% porosity

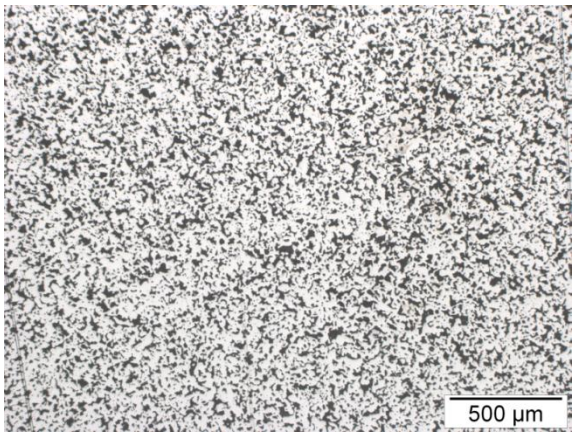

Fig. 4.81: Fe16Cr + 50 vol% powder loading, horizontal plane, 50x, 22% porosity

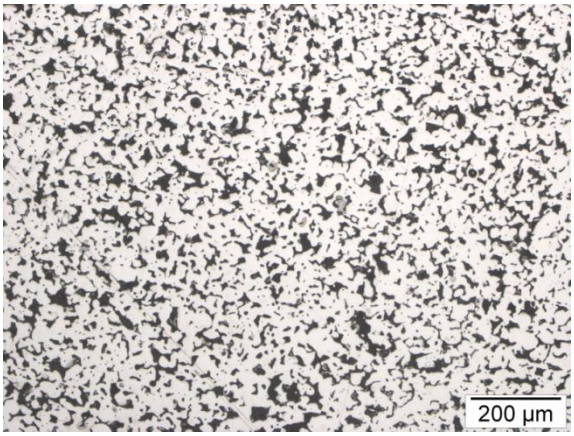

Fig. 4.82: Fe16Cr + 50 vol% powder loading, horizontal plane, 100x, 22% porosity

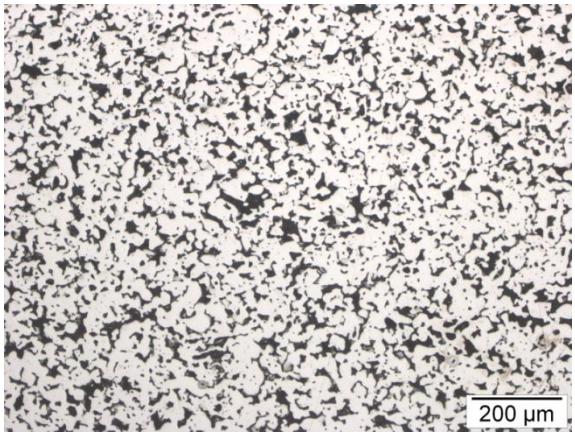

Fig. 4.83: Fe16Cr + 50 vol% powder loading, horizontal plane, 100x, 22% porosity

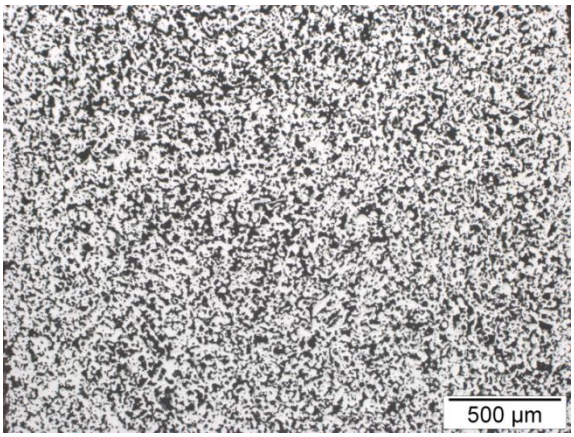

Fig. 4.84: Fe16Cr + 50 vol% powder loading, cross plane, 50x, 22% porosity

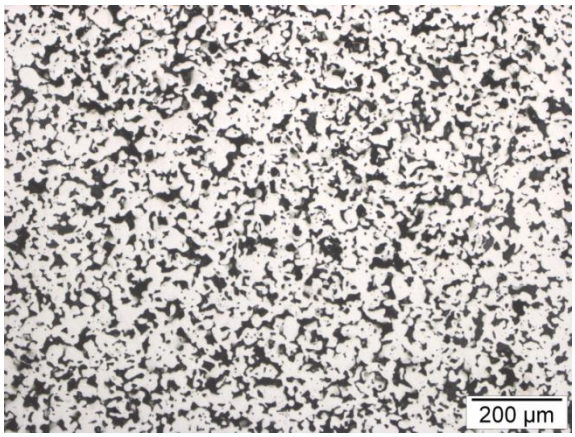

Fig. 4.85: Fe16Cr + 50 vol% powder loading, cross plane, 50x, 22% porosity

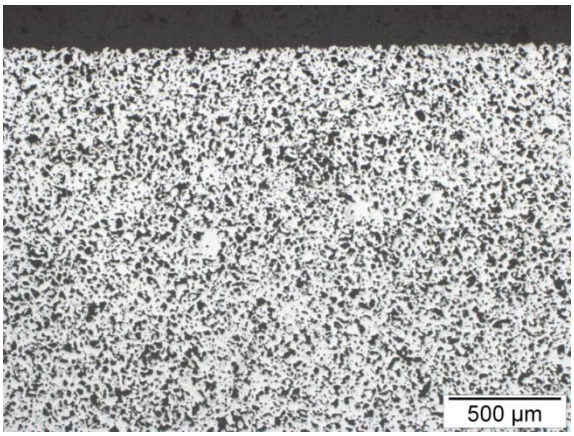

Fig. 4.86: Fe16Cr + 55 vol% powder loading, horizontal plane, 50x, 20% porosity

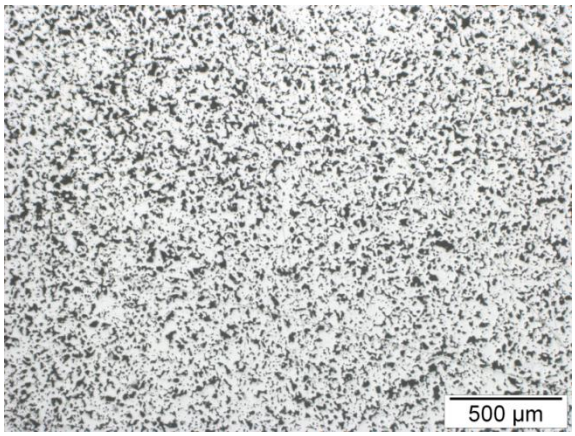

Fig. 4.87: Fe16Cr + 55 vol% powder loading, horizontal plane, 50x, 20% porosity

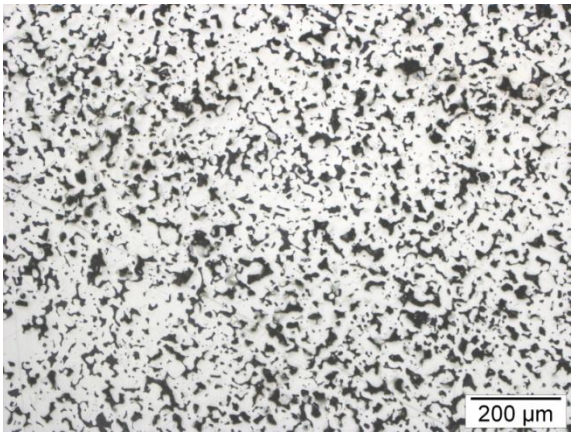

Fig. 4.88: Fe16Cr + 55 vol% powder loading, horizontal plane, 100x, 20% porosity

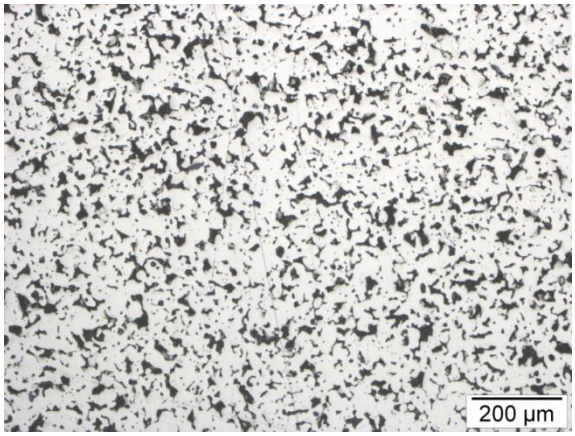

Fig. 4.89: Fe16Cr + 55 vol% powder loading, horizontal plane, 50x, 20% porosity

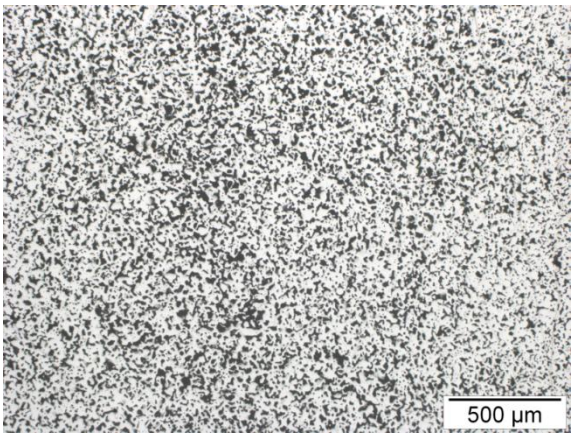

Fig. 4.90: Fe16Cr + 55 vol% powder loading, cross plane, 50x, 20% porosity

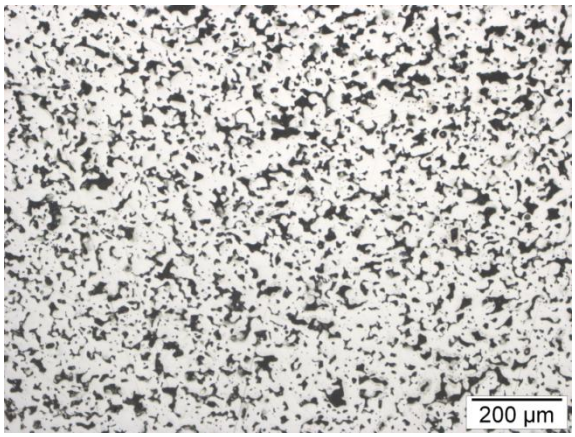

Fig. 4.91: Fe16Cr + 55 vol% powder loading, cross plane, 100x, 20% porosity

Austenitic MIM samples

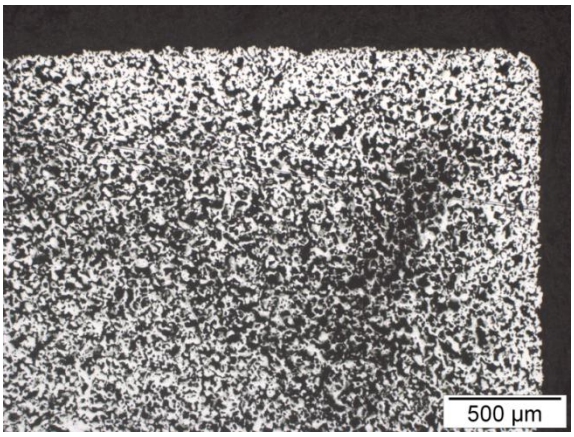

Fig. 4.92: Fe25Cr20Ni2.5Si + 45 vol% powder loading, horizontal plane, 50x, 35% porosity

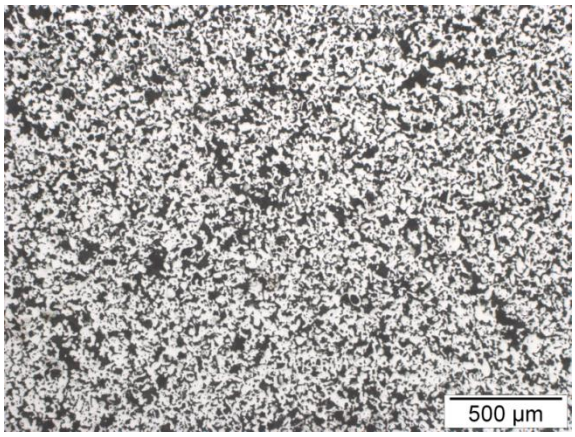

Fig. 4.93: Fe25Cr20Ni2.5Si + 45 vol% powder loading, horizontal plane, 50x, 35% porosity

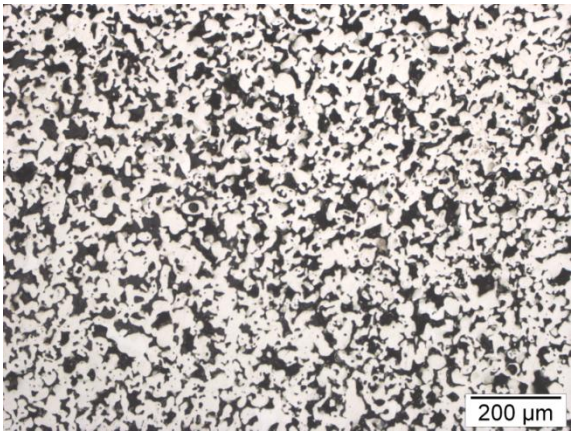

Fig. 4.94: Fe25Cr20Ni2.5Si + 45 vol% powder loading, horizontal plane, 100x, 35% porosity

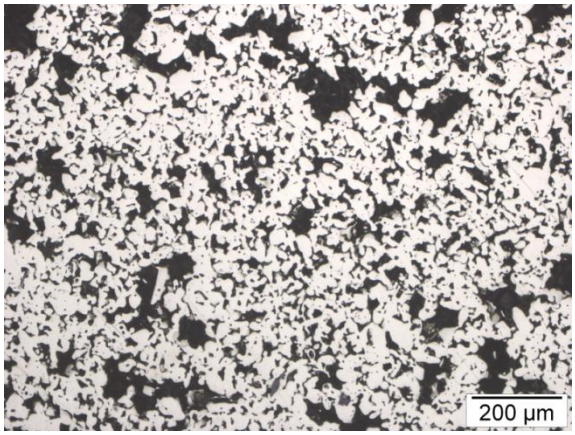

Fig. 4.95: Fe25Cr20Ni2.5Si + 45 vol% powder loading, horizontal plane, 100x, 35% porosity

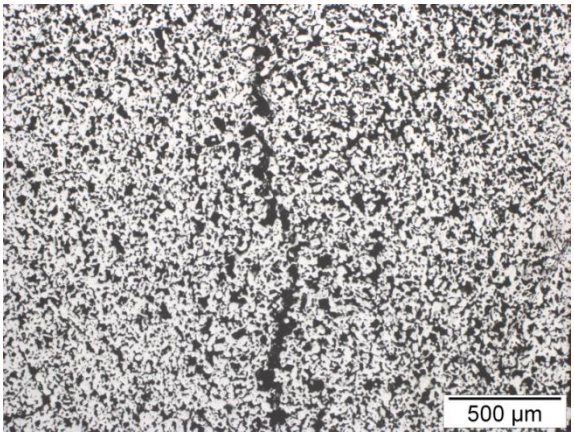

Fig. 4.96: Fe25Cr20Ni2.5Si + 45 vol% powder loading, cross plane, 50x, 35% porosity

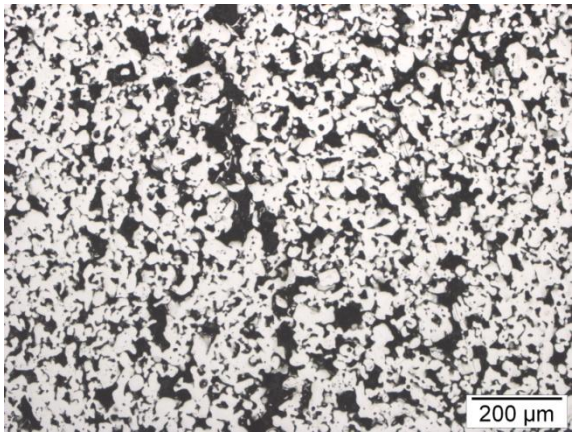

Fig. 4.97: Fe25Cr20Ni2.5Si + 45 vol% powder loading, horizontal plane, 100x, 35% porosity

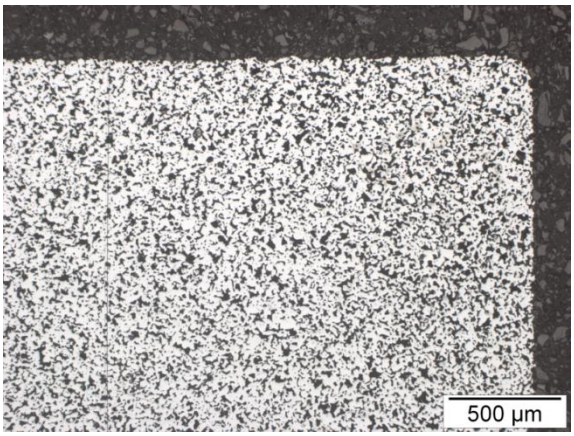

Fig. 4.98: Fe25Cr20Ni2.5Si + 50 vol% powder loading, horizontal plane, 50x, 31% porosity

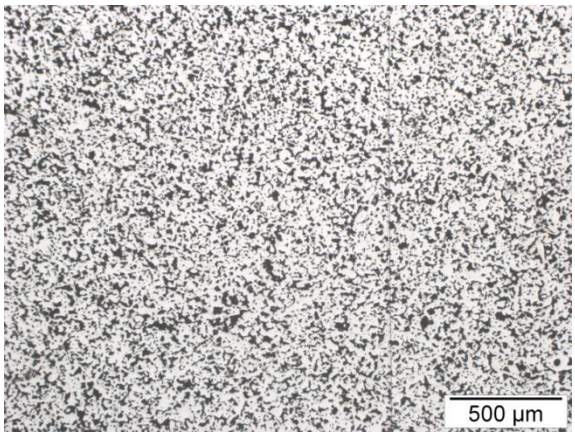

Fig. 4.99: Fe25Cr20Ni2.5Si + 50 vol% powder loading, horizontal plane, 50x, 31% porosity

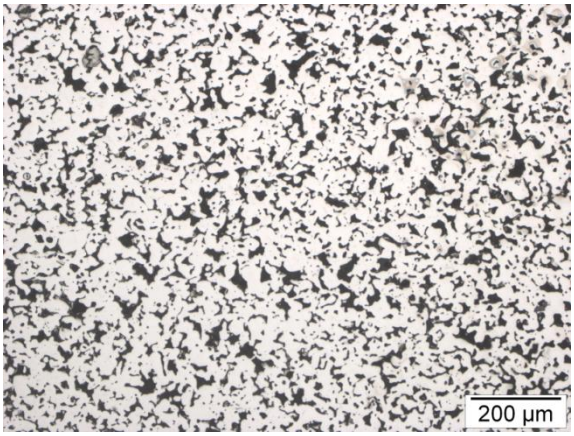

Fig. 4.100: Fe25Cr20Ni2.5Si + 50 vol% powder loading, horizontal plane, 100x, 31% porosity

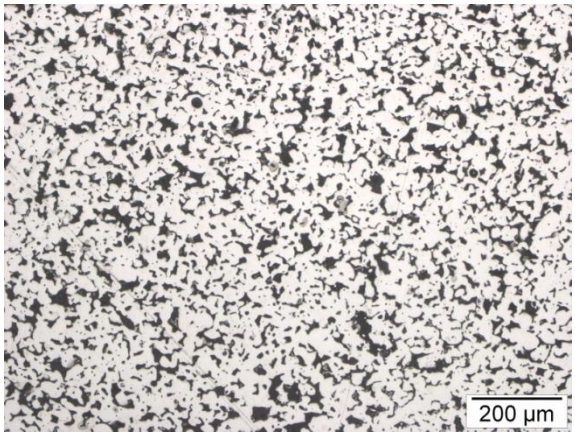

Fig. 4.101: Fe25Cr20Ni2.5Si + 50 vol% powder loading, horizontal plane, 100x, 31% porosity

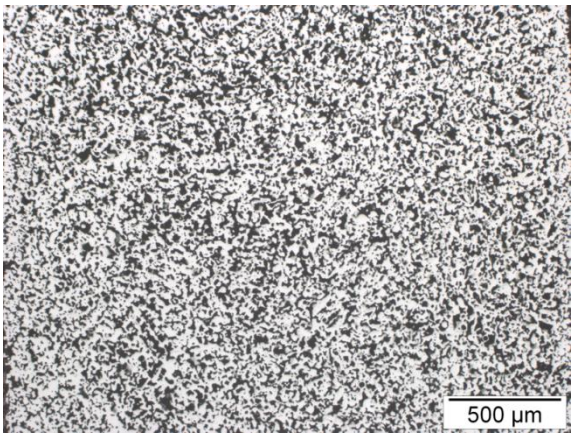

Fig. 4.102: Fe25Cr20Ni2.5Si + 50 vol% powder loading, cross plane, 50x, 31% porosity

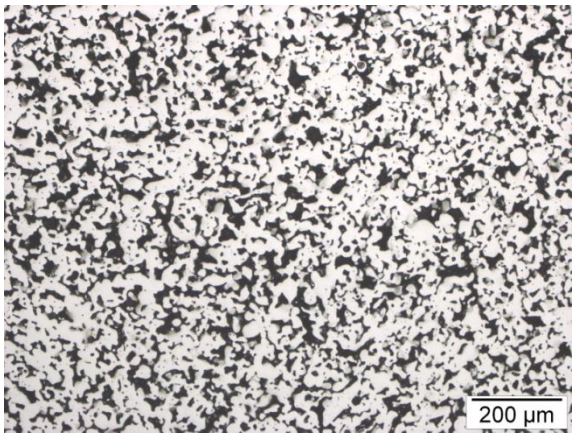

Fig. 4.103: Fe25Cr20Ni2.5Si + 50 vol% powder loading, cross plane, 100x, 31% porosity

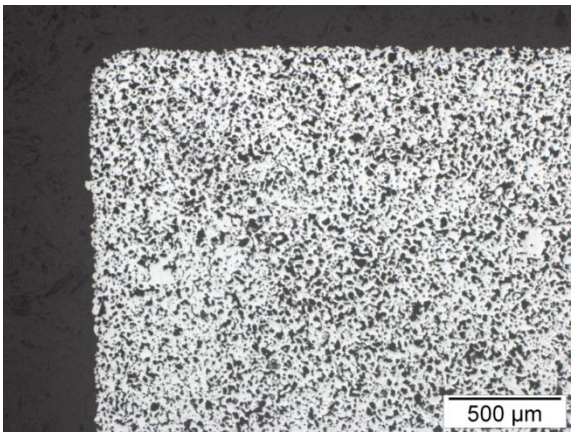

Fig. 4.104. Fe25Cr20Ni2.5Si + 55 vol% powder loading, horizontal plane, 50x, 24% porosity

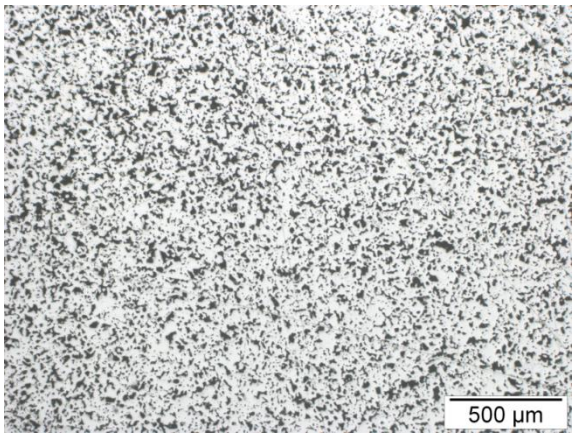

Fig. 4.105: Fe25Cr20Ni2.5Si + 55 vol% powder loading, horizontal plane, 50x, 24% porosity

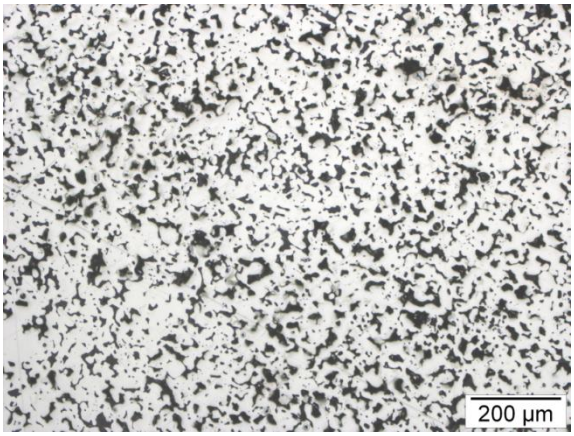

Fig. 4.106: Fe25Cr20Ni2.5Si + 55 vol% powder loading, horizontal plane, 100x, 24% porosity

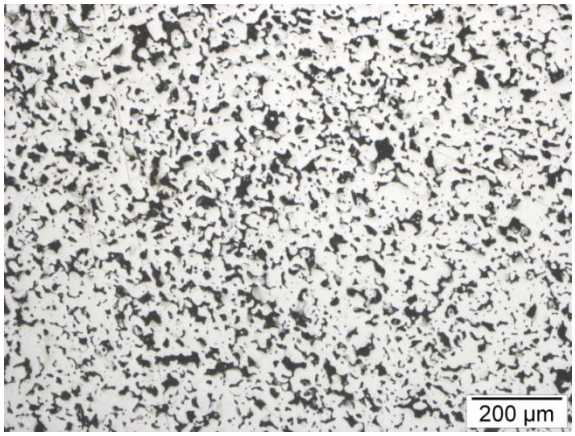

Fig. 4.107: Fe25Cr20Ni2.5Si + 55 vol% powder loading, horizontal plane, 100x, 24% porosity

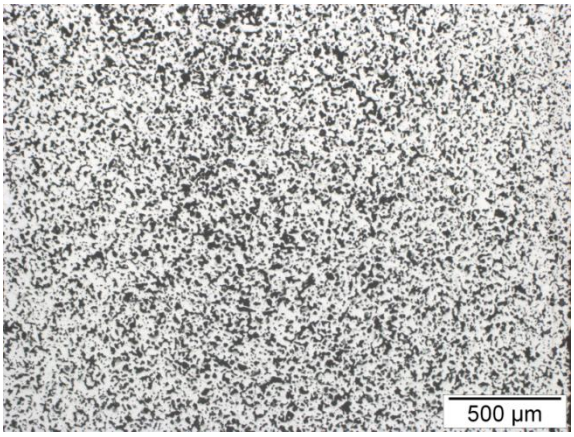

Fig. 4.108: Fe25Cr20Ni2.5Si + 55 vol% powder loading, cross plane, 50x, 24% porosity

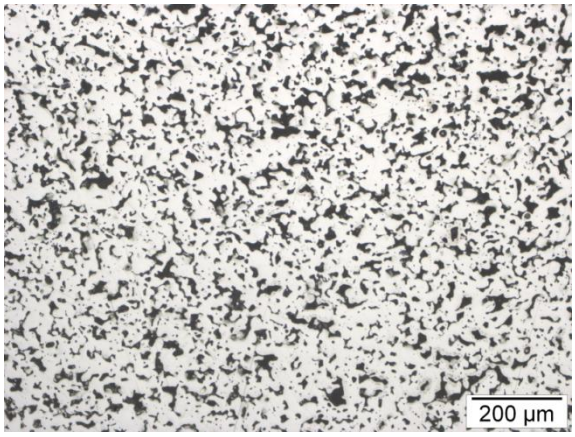

Fig. 4.109: Fe25Cr20Ni2.5Si + 55 vol% powder loading, cross plane, 100x, 24% porosity

The porosity was calculated by using the following formula: porosity [%] = (1 –(ρsintered / ρPycnometer)) * 100 and can be seen in Table 4.24. The higher the binder loading, the lower is the porosity.

Table 4.24: Porosity of the vacuum sintered MIM samples (1300°C, 60 min)

Sample	powder loading (vol%)	sintered density (g/cm³)	theoretical density (g/cm³)	porosity (%)
Fe16Cr	55	6,187	7,766	20,3
Fe16Cr	50	6,099	7,766	21,5
Fe16Cr	45	5,589	7,766	28,0
Fe25Cr20Ni2.5Si	55	5,875	7,758	24,3
Fe25Cr20Ni2.5Si	50	5,377	7,758	30,7
Fe25Cr20Ni2.5Si	45	5,015	7,758	35,4

4.5 PEM samples

Powder and binder system for the powder extrusion molded (PEM) samples were exactly the same as for the MIM experiments. This means the Fe16Cr was mixed with a binder consisting of HDPE, paraffin wax and stearic acid. The Fe25Cr20Ni2.5Si powder was mixed without stearic acid, and only HDPE and paraffin wax were used. In both cases the powder loading was in the range of 45 – 55%. The samples were extruded to cylindrical rods with an average length of 40-50 mm and a diameter of 7-8 mm. The two-step debinding process (solvent and subsequently thermal debinding) and the sintering (1300°C, 60 min, vacuum) were carried out exactly under the same conditions and are described in Chapter 3.11.

Results

The green and sintered densities of the samples are shown in Fig. 4.110. The samples were sintered in vacuum for 1 h at 1300°C. It is obvious that with higher powder loading the green and sintered density is higher. The green density of the austenitic PEM samples is in the same range as that of the ferritic one, but the sintered density of the ferritic samples is higher than that of the austenitic ones. Compared to the MIM samples, the green (and the sintered) density of the MIM samples is higher than that of the PEM samples. This is clear because the injection pressure is higher than the pressure for extrusion which enhances rearrangement of the powder particles towards higher density; the densities of the extrusion samples can be seen in Table 4.25. The shrinkage of the samples in length is in the range 10-15%, not depending on the binder content. The shrinkage in the other directions was not determined because of the irregular shape of the samples; the scatter was too high to give correct numbers.

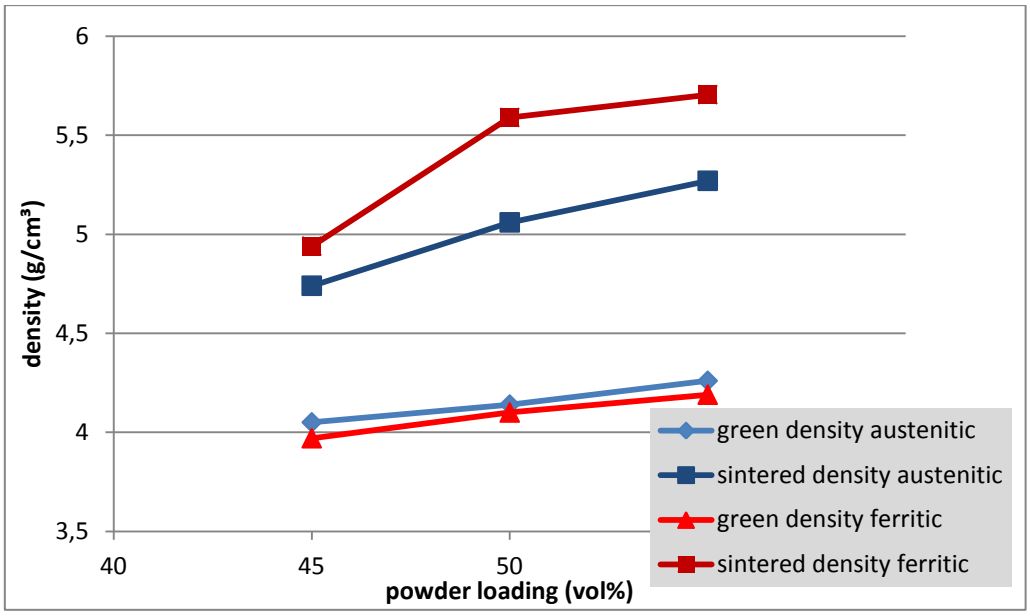

Fig. 4.110. Green and sintered density of the PEM samples (1300°C, 60 min, vacuum)

Table 4.25: Green density, sintered density and porosity of the PEM samples

Sample	powder loading (vol%)	green density (g/cm³	sintered density (g/cm³)	theoretical density (g/cm³)	porosity (%)
Fe21Cr	55	4,19	5,71	7,766	26,5
Fe21Cr	50	4,10	5,59	7,766	28,0
Fe21Cr	45	3,97	4,94	7,766	36,4
Fe25Cr20Ni2.5Si	55	4,26	5,27	7,758	32,1
Fe25Cr20Ni2.5Si	50	4,14	5,06	7,758	34,8
Fe25Cr20Ni2.5Si	45	4,05	4,74	7,758	38,9

For the distribution of the pores, the cross section of the extrusion samples has been investigated. Even the ferritic sample with the highest powder loading (55 vol%; Fig. 4.111 - Fig. 4.114) shows agglomerations of pores. This may come from inhomogeneities of the feedstock. So premixing the powder and the binder in a turbula mixer or mixing it for another round before extruding could be beneficial.

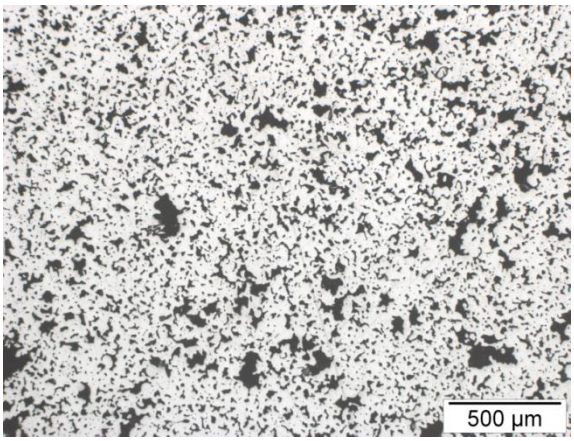

Fig. 4.111: Ferritic PEM sample with 55 vol% powder loading, cross section, 50x, 26,5% porosity

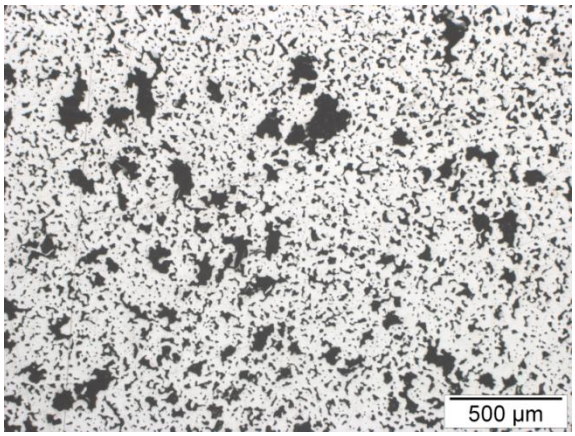

Fig. 4.112: Ferritic PEM sample with 55 vol% powder loading, cross section, 50x, 26,5% porosity

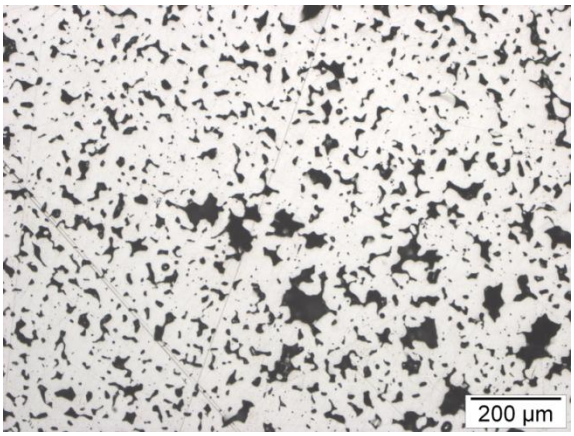

Fig. 4.113: Ferritic PEM sample with 55 vol% powder loading, cross section, 100x, 26,5% porosity

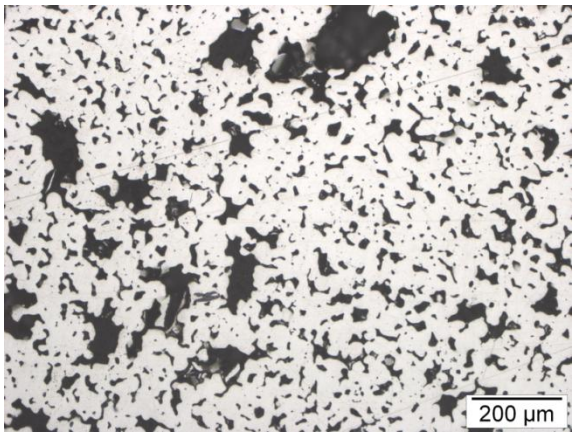

Fig. 4.114: Ferritic PEM sample with 55 vol% powder loading, cross section, 100x, 26,5% porosity

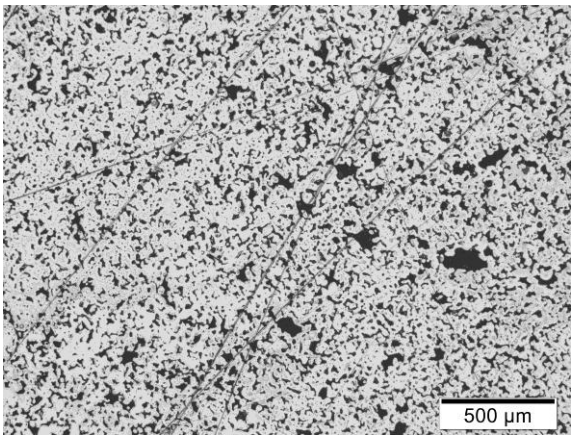

Fig. 4.115: Ferritic PEM sample with 50 vol% powder loading, cross section, 50x, 28,0% porosity

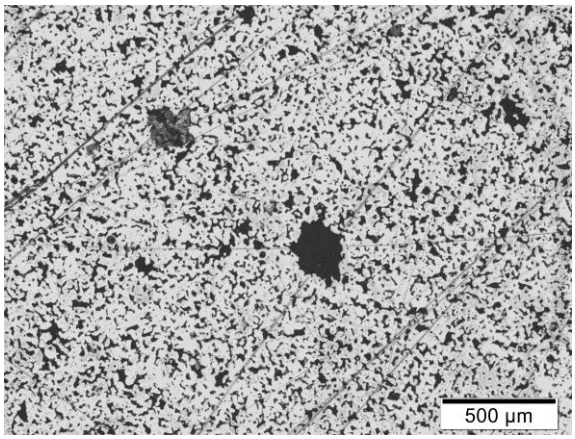

Fig. 4.116: Ferritic PEM sample with 50 vol% powder loading, cross section, 50x, 28,0% porosity

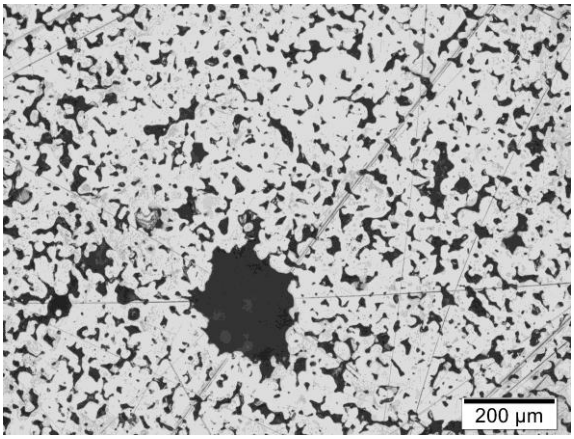

Fig. 4.117: Ferritic PEM sample with 50 vol% powder loading, cross section, 100x, 28,0% porosity

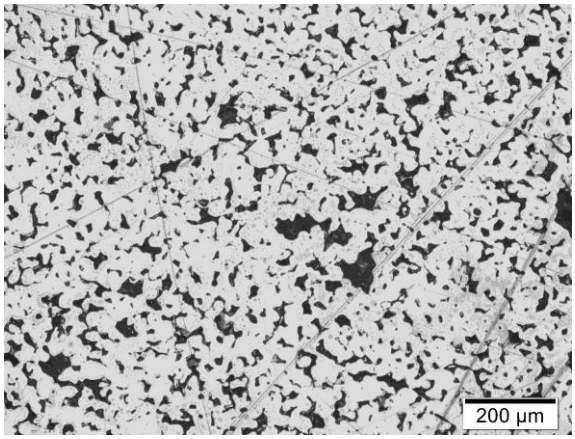

Fig. 4.118: Ferritic PEM sample with 50 vol% powder loading, cross section, 100x, 28,0% porosity

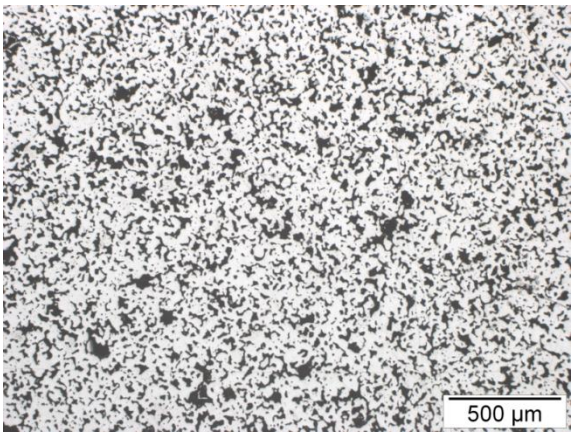

Fig. 4.119: Ferritic PEM sample with 45 vol% powder loading, cross section, 50x, 36,4% porosity

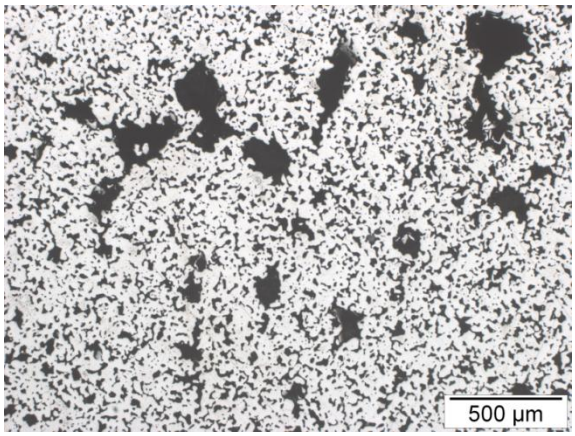

Fig. 4.120: Ferritic PEM sample with 45 vol% powder loading, cross section, 50x, 36,4% porosity

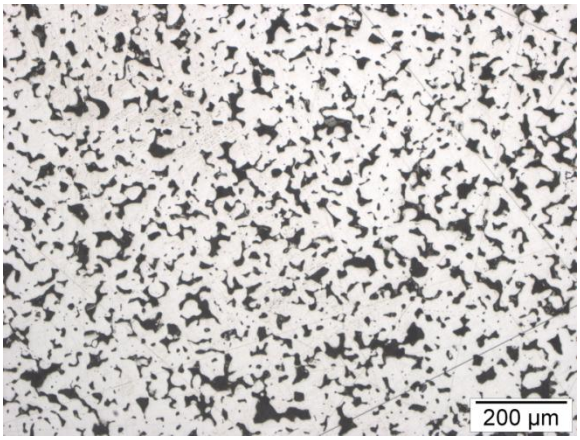

Fig. 4.121: Ferritic PEM sample with 45 vol% powder loading, cross section, 100x, 36,4% porosity

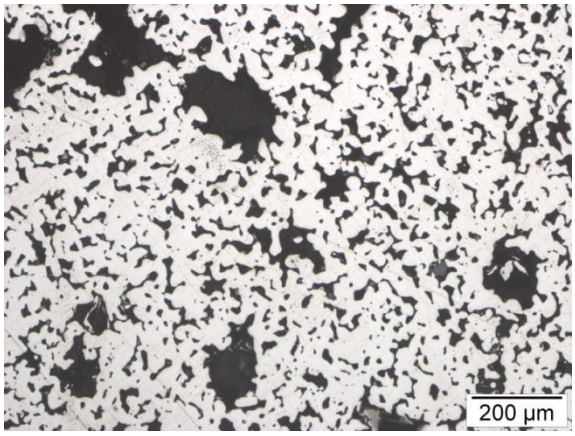

Fig. 4.122: Ferritic PEM sample with 45 vol% powder loading, cross section, 100x, 36,4% porosity

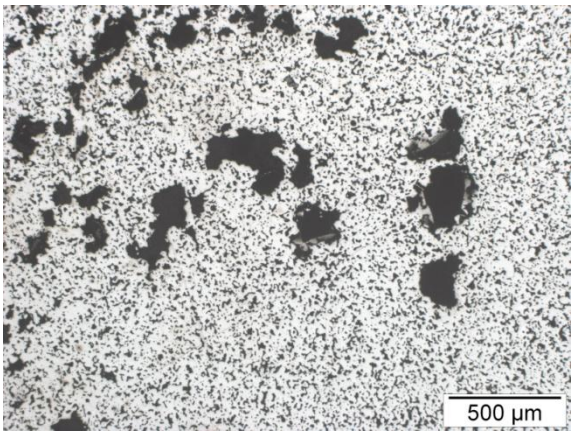

Fig. 4.123: Austenitic PEM sample with 45 vol% powder loading, cross section, 50x, 32,1% porosity

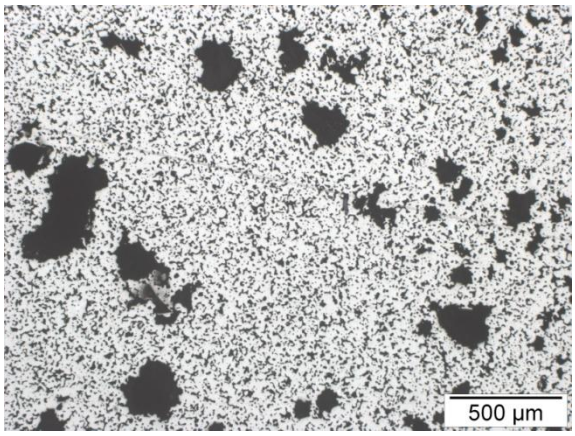

Fig. 4.124: Austenitic PEM sample with 45 vol% powder loading, cross section, 50x, 32,1% porosity

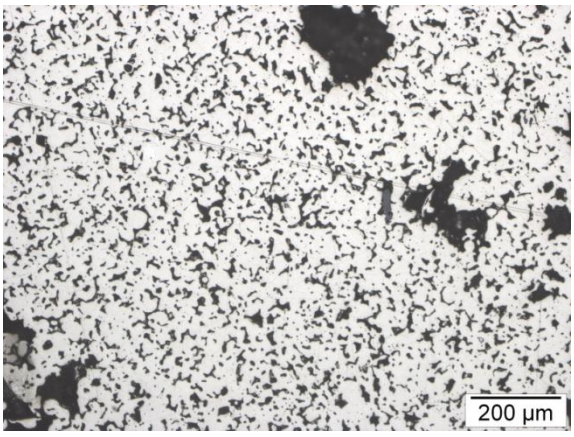

Fig. 4.125: Austenitic PEM sample with 45 vol% powder loading, cross section, 100x, 32,1% porosity

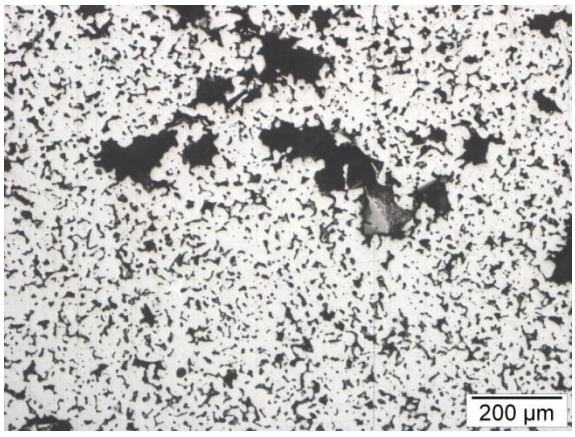

Fig. 4.126: Austenitic PEM sample with 45 vol% powder loading, cross section, 100x, 32,1% porosity

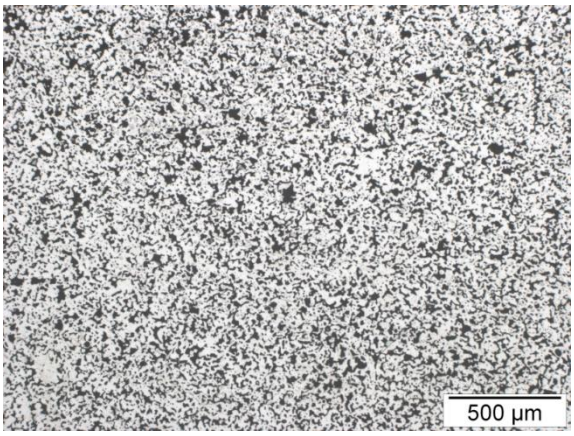

Fig. 4.127: Austenitic PEM sample with 50 vol% powder loading, cross section, 50x, 34,8% porosity

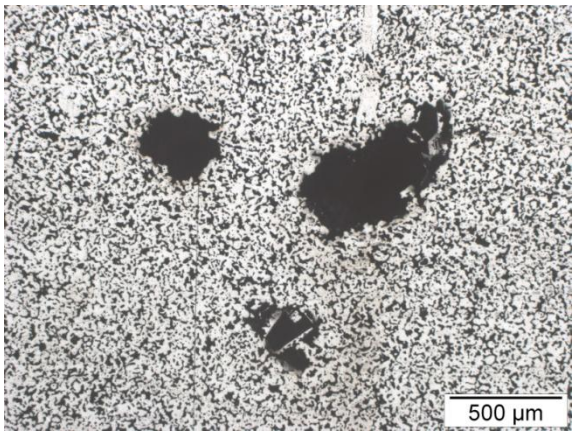

Fig. 4.128: Austenitic PEM sample with 50 vol% powder loading, cross section, 50x, 34,8% porosity

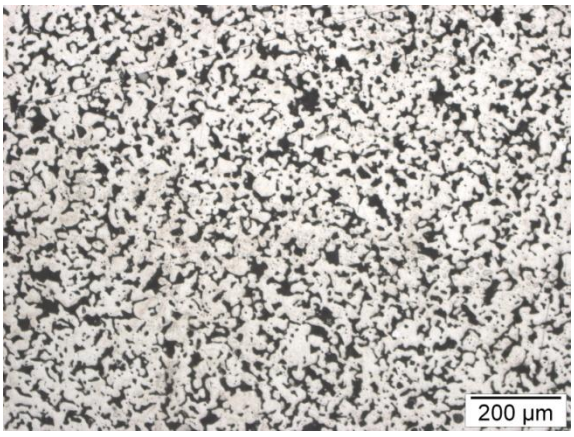

Fig. 4.129: Austenitic PEM sample with 50 vol% powder loading, cross section, 100x, 34,8% porosity

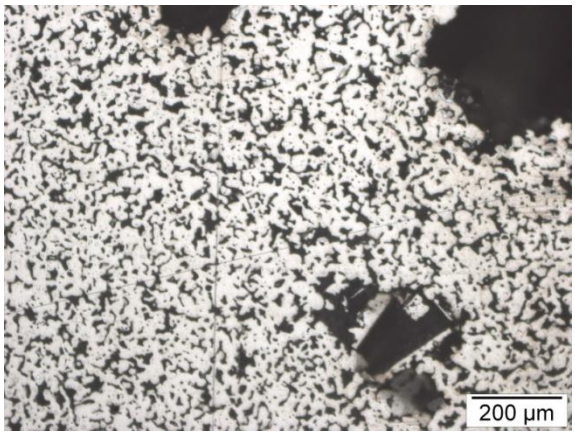

Fig. 4.130: Austenitic PEM sample with 50 vol% powder loading, cross section, 100x, 34,8% porosity

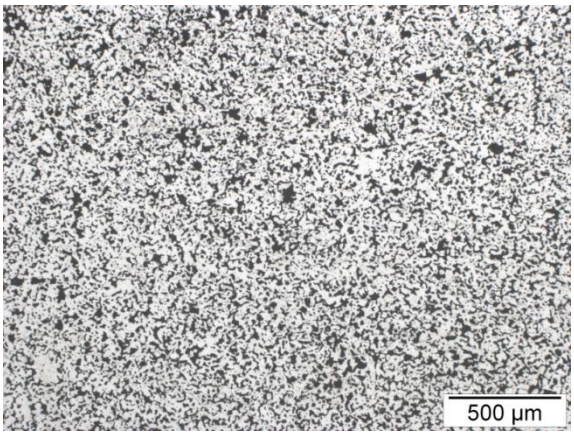

Fig. 4.131: Austenitic PEM sample with 55 vol% powder loading, cross section, 50x, 38,9% porosity

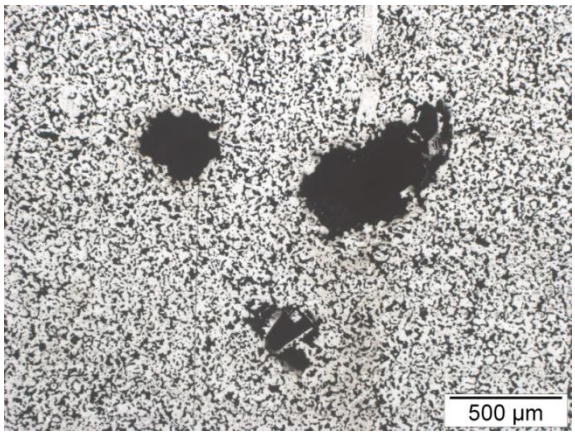

Fig. 4.132: Austenitic PEM sample with 55 vol% powder loading, cross section, 50x, 38,9% porosity

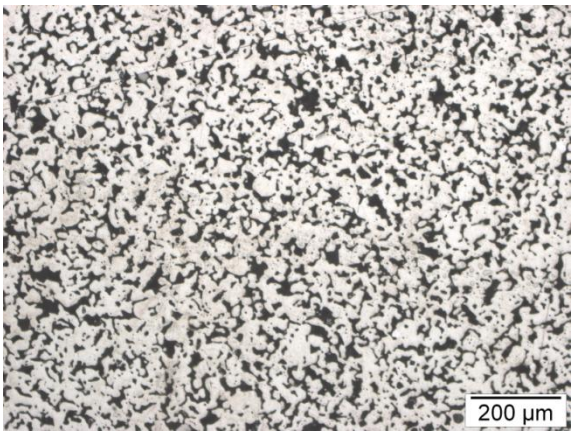

Fig. 4.133: Austenitic PEM sample with 55 vol% powder loading, cross section, 100x, 38,9% porosity

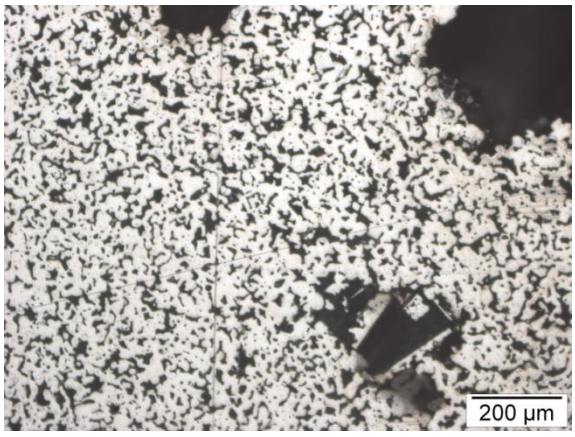

Fig. 4.134: Austenitic PEM sample with 55 vol% powder loading, cross section, 100x, 38,9% porosity

The extrusion molded samples have around 30% porosity (starting powder loading 55 vol%), even higher with higher binder content. The problem is the distribution of the pores. Another problem is that the dimension of the final metal support should be about 100 x 100 x 1 mm, and this could be a very challenging task for the extrusion process.

4.6 Hg-Porosimetry

In Table 4.26 the results of the measurements (Hg-density and Hg-porosity) with the Hg-Porosimeter can be seen. The correlation between the Hg-density and the Archimedes density is very good. This indicates that the impregnation of the samples with a water repellant spray for measuring the Archimedes density did work out well. It is obvious that with higher powder loading the porosity decreases. This behavior is also visible for the values measured with Hg-Porosimetry.

Table 4.26: Comparison of density and porosity with the results from the Hg-Porosimeter

Powder	manufacturing process	powder loading (vol%)	Archimedes density* (g/cm³)	Hg-density (g/cm³)	porosity** (%)	Hg-porosity (%)
Fe16Cr	MIM	45	5,59	**5,57**	28,0	**24,6**
Fe16Cr	MIM	50	6,10	**6,16**	21,5	**16,5**
Fe16Cr	MIM	55	6,19	**6,17**	20,3	**16,2**
Fe25Cr20Ni	MIM	45	5,02	**4,76**	35,4	**34,4**
Fe25Cr20Ni	MIM	50	5,38	**5,38**	30,7	**29,9**
Fe25Cr20Ni	MIM	55	5,88	**5,93**	24,3	**23,0**
Fe21Cr	gravity. sint./bulk	-	3,98	**3,78**	47,5	**49,8**
Fe21Cr	gravity sint./tap	-	4,40	**4,43**	42,0	**40,6**

*Archimedes density: density of sintered samples measured by Archimedes method **porosity [%] = $(1 - (\rho_{Archimedes} / \rho_{theoretical})) * 100$ ($\rho_{theoretical}$ measured by He-Pycnometry)

With Hg-Porosimetry, also a volumetric distribution of the pore size can be obtained. In Fig. 4.135 and in Fig. 4.136 cumulative pore volume and the pore size distribution with the modal pore diameter (µm) of an austenitic MIM and a gravity sintered sample can be seen. The pore size distribution of all ferritic and austenitic MIM samples look rather the same, that is the reason that only the one for the austenitic sample with 45% powder loading is shown. All other diagrams can be seen in the appendix.

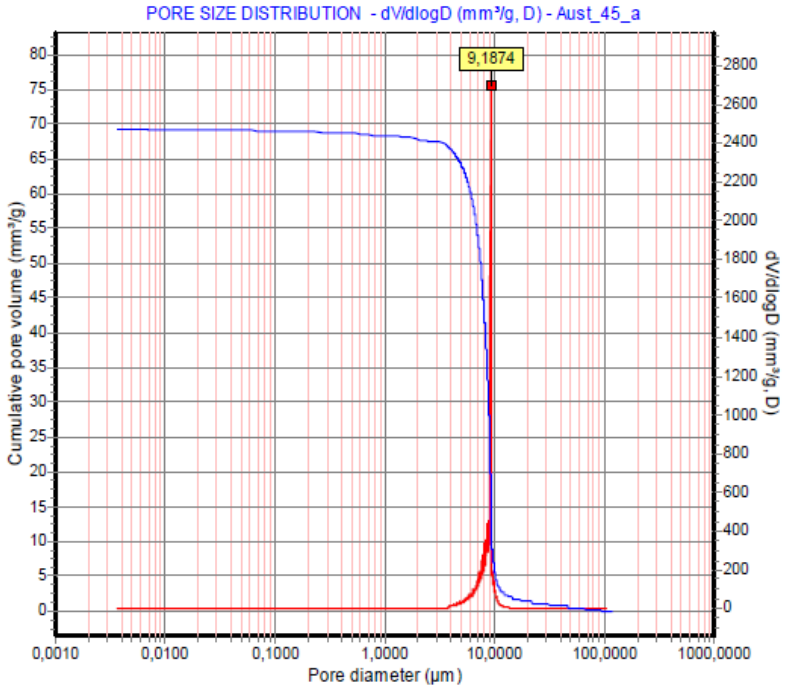

Fig. 4.135: Cumulative pore volume (blue graph) and pore size distribution (red graph) of the Fe25Cr20Ni2.5Si MIM sample (45 vol% powder loading)

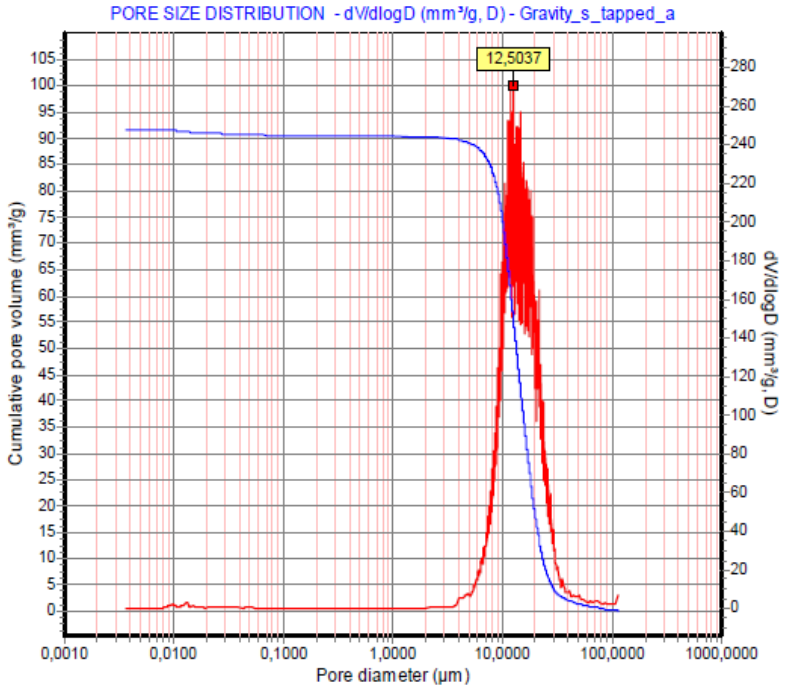

Fig. 4.136: Cumulative pore volume (blue graph) and pore size distribution (red graph) of the Fe21Cr gravity sintered sample (tapped state)

In Table 4.27 characteristic values of the distribution are shown. The modal pore diameter and median pore diameter are quite the same, except for the Fe21Cr gravity sintered sample (tapped state). This results in a broader peak for the pore size distribution, as can be seen in Fig. 4.136. The austenitic MIM sample with 45% powder loading has a Hg-porosity of 34.4% and a pore volume of 69.3 mm³/g, while the gravity sintered sample (tapped state) has a Hg-porosity of 40.6% and a significantly higher pore volume with 91.7 mm³/g. This means - in case of a linear relation between porosity and pore volume - the gravity sintered samples would have a higher Hg-infiltrable pore volume in case of the same porosity.

Table 4.27: Characterisitic values for the pore size distribution

Powder	manufacturing process	powder loading (vol%)	Hg-porosity (%)	modal pore diameter (µm)	median pore diameter (µm)	total pore volume (mm³/g)
Fe16Cr	MIM	45	24,6	10,7	9,4	44,1
Fe16Cr	MIM	50	16,5	6,4	6,0	26,8
Fe16Cr	MIM	55	16,2	5,5	5,1	26,3
Fe25Cr20Ni	MIM	45	34,4	9,2	8,6	69,3
Fe25Cr20Ni	MIM	50	29,9	7,7	7,4	55,7
Fe25Cr20Ni	MIM	55	23,0	5,7	5,7	38,7
Fe21Cr	gravity sint./bulk	-	49,8	18,0	17,3	131,8
Fe21Cr	gravity sint./tap	-	40,6	12,5	14,0	91,7

4.7 Image Analysis

Image analysis has been performed with the program *FIJI*, an open source program based on *ImageJ*. The original image of the metallographic section was grayscaled, and the area porosity was calculated by including the edges. Pore distribution calculations were made by excluding the edges where pores are cut. Also the Feret diameter was calculated with *FIJI*. In this work, the Feret diameter is referred to the maximum caliper of pores and not particles. For detailed description of the image analysis see Chapter 3.18.

In Table 4.28 - Table 4.31 a comparison of the porosity determined with the *Fiji* software and the Archimedes porosity can be seen. It is already known that the separation of the section area into pores and matrix is influenced by the microscope magnification used, and different magnifications can lead to different results for the porosity [**118**]. Kalss also reported that high magnifications can lead to comparably too low values in porosity but high standard deviations and subsequently to broad intervals of confidence. Also in our case, the FIJI porosity obtained with the images of a magnification of 50x is higher than that of the 100x and 200x images. Fig. 4.137 and Fig. 4.138 show the thresholding of the same austenitic MIM sample at different magnifications. At a magnification of 200x, there is a sharp separation between the bright and the dark "part" of the sample, but at a magnification of 50x, this separation is not very clear. There is a broad "band" between the bright and the dark part. It could be possible that because of this blurred boundary the thresholding at 50x is shifted to higher threshold values, resulting in higher porosities.

This blurred definition of the thresholding could also be the reason that the porosity calculated with the images with 50x magnification is higher than that the Archimedes porosity. The best match of Archimedes porosity and FIJI porosity could be obtained in most cases with images at 200x magnification.

The calculated FIJI porosity of the cross section is higher than that of the longitudinal section except for the Fe16Cr sample with 55 vol% powder loading. So no clear trend can be seen.

Also the Feret diameter was calculated with *FIJI*. In this work, the Feret diameter is referred to the maximum caliper of pores and not particles. The average Feret diameter (or caliper diameter) of all pores decreases with increasing magnification, but the diameter is not depending on the powder loading. It can be seen that for a given powder loading and magnification the average Feret diameter for the cross section is in the same range as for the longitudinal section, f. ex.: for the ferritic sample with 50 vol% p.l and a magnification of 100x the average Feret diameter of all pores is calculated as 22.8 µm in cross section and 22.0 µm for the longitudinal section.

Table 4.28: Calculated FIJI porosity of the Fe16Cr MIM samples (cross section) with different powder loading at different magnifications

Sample	powder loading (%)	magnification	FIJI porosity (%)	Archimedes porosity* (%)	Feret diameter (µm)
Fe16Cr	45	50x	33,8 ± 0,7	28,0	34,1 ± 1,4
Fe16Cr	45	100x	29,4 ± 0,2	28,0	22,7 ± 0,8
Fe16Cr	45	200x	27,0 ± 0,8	28,0	13,0 ± 1,6
Fe16Cr	50	50x	29,0 ± 0,6	21,5	29,0 ± 0,6
Fe16Cr	50	100x	25,9 ± 1,0	21,5	22,8 ± 1,0
Fe16Cr	50	200x	24,0 ± 1,4	21,5	16,8 ± 0,3
Fe16Cr	55	50x	21,5 ± 0,9	20,3	21,5 ± 0,9
Fe16Cr	55	100x	18,6 ± 0,6	20,3	16,9 ± 0,7
Fe16Cr	55	200x	17,3 ± 0,6	20,3	11,6 ± 2,2

**This porosity was calculated from the Archimedes density by using the following formula porosity [%] = $(1 - (\rho_{sintered} / \rho_{theoretical})) * 100$*

Table 4.29: Calculated FIJI porosity of the Fe16Cr MIM samples (longitudinal section) with different powder loading at different magnifications

Sample	powder loading (%)	magnification	FIJI porosity (%)	Archimedes porosity (%)	Feret diameter (µm)
Fe16Cr	45	50x	28,4 ± 1,0	28,0	30,7 ± 1,4
Fe16Cr	45	100x	24,6 ± 1,9	28,0	22,0 ± 1,4
Fe16Cr	45	200x	24,4 ± 2,0	28,0	14,3 ± 2,5
Fe16Cr	50	50x	27,8 ± 2,2	21,5	28,8 ± 1,8
Fe16Cr	50	100x	23,4 ± 2,1	21,5	22,0 ± 0,5
Fe16Cr	50	200x	23,0 ± 1,8	21,5	13,2 ± 1,1
Fe16Cr	55	50x	27,4 ± 1,0	20,3	28,7 ± 0,6
Fe16Cr	55	100x	22,6 ± 2,4	20,3	19,4 ± 1,2
Fe16Cr	55	200x	21,4 ± 1,5	20,3	12,5 ± 0,7

Table 4.30: Calculated FIJI porosity of the Fe25Cr20Ni2.5Si MIM samples (cross section) with different powder loading at different magnifications

Sample	powder loading (%)	magnification	FIJI porosity (%)	Archimedes porosity (%)	Feret diameter (µm)
Fe25Cr20Ni2.5Si	45	50x	42,0 ± 0,9	35,4	29,6 ± 1,6
Fe25Cr20Ni2.5Si	45	100x	36,9 ± 1,7	35,4	23,1 ± 1,5
Fe25Cr20Ni2.5Si	45	200x	35,3 ± 1,4	35,4	15,5 ± 1,7
Fe25Cr20Ni2.5Si	50	50x	38,5 ± 1,9	30,7	29,5 ± 1,1
Fe25Cr20Ni2.5Si	50	100x	32,8 ± 2,2	30,7	21,6 ± 1,2
Fe25Cr20Ni2.5Si	50	200x	30,2 ± 1,7	30,7	15,7 ± 0,8
Fe25Cr20Ni2.5Si	55	50x	32,7 ± 2,2	24,3	24,3 ± 1,9
Fe25Cr20Ni2.5Si	55	100x	28,5 ± 1,9	24,3	19,6 ± 1,1
Fe25Cr20Ni2.5Si	55	200x	25,5 ± 1,9	24,3	14,3 ± 0,8

Table 4.31: Calculated FIJI porosity of the Fe25Cr20Ni2.5Si MIM samples (longitudinal section) with different powder loading at different magnifications

Sample	powder loading (%)	magnification	FIJI porosity (%)	Archimedes porosity (%)	Feret diameter (µm)
Fe25Cr20Ni2.5Si	45	50x	37,9 ± 1,3	35,4	29,4 ± 2,1
Fe25Cr20Ni2.5Si	45	100x	35,7 ± 2,7	35,4	22,0 ± 3,8
Fe25Cr20Ni2.5Si	45	200x	34,6 ± 2,9	35,4	14,3 ± 1,1
Fe25Cr20Ni2.5Si	50	50x	33,1 ± 0,4	30,7	26,4 ± 0,6
Fe25Cr20Ni2.5Si	50	100x	27,8 ± 0,6	30,7	19,7 ± 1,1
Fe25Cr20Ni2.5Si	50	200x	25,2 ± 0,3	30,7	13,6 ± 0,3
Fe25Cr20Ni2.5Si	55	50x	31,5 ± 2,9	24,3	23,7 ± 0,9
Fe25Cr20Ni2.5Si	55	100x	26,2 ± 0,5	24,3	17,9 ± 1,0
Fe25Cr20Ni2.5Si	55	200	23,6 ± 0,4	24,3	12,6 ± 1,0

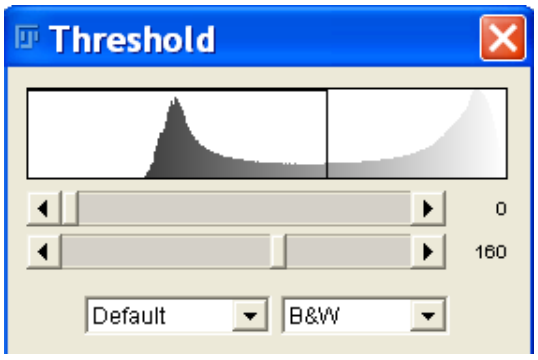

Fig. 4.137: Thresholding of the Fe25Cr20Ni2.5Si (45 vol% p.l.) at 50x magnification

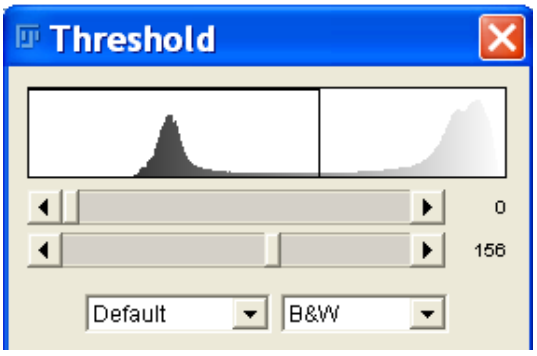

Fig. 4.138: Thresholding of the same sample (Fe25Cr20Ni2.5Si; 45 vol% p.l.) at 200x magnification

Also the distribution of the pores can be calculated. In our case, the distribution only for the austenitic sample with 45 vol% powder loading at a magnification of 100x was calculated. The reason is that it is the only sample at a magnification of 50x or 100x where the porosity calculated with FIJI is in the same range as the Archimedes porosity.

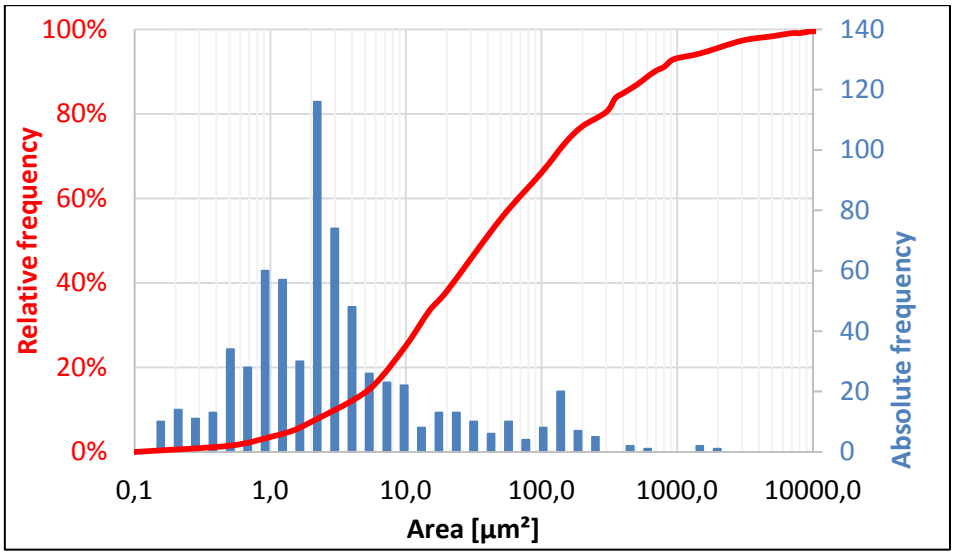

Fig. 4.139: Pore size distribution of the Fe25Cr20Ni2.5Si MIM sample with 45 vol% p.l. Calculation based on surface area

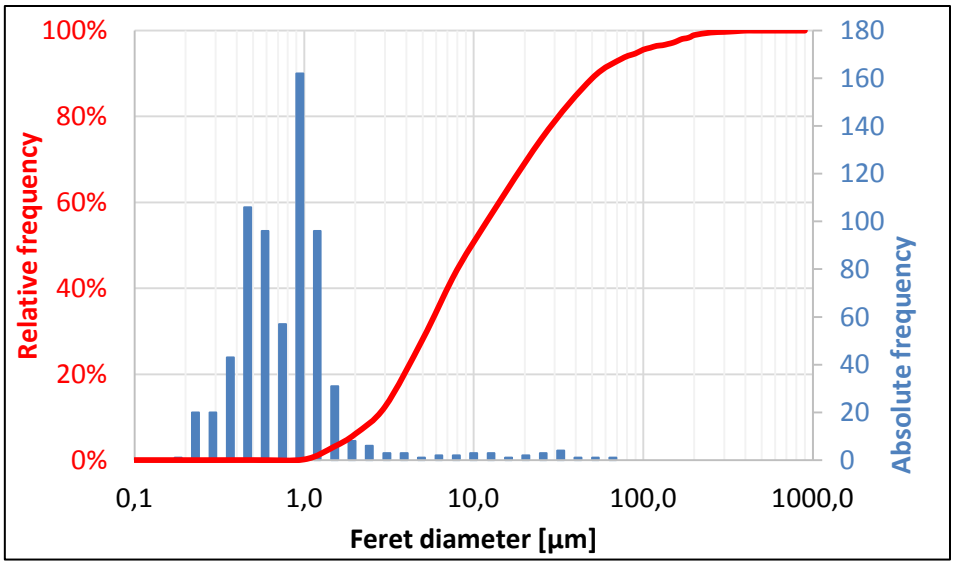

Fig. 4.140: Pore size distribution of the Fe25Cr20Ni2.5Si MIM sample with 45 vol% p.l. Calculation based on Feret diameter

As already mentioned, in this work the basic geometrical parameter of choice for pore size distribution calculations is the parameter “pore surface area” (Fig. 4.139). For comparison, also the Feret diameter has been used (see Fig. 4.140). Because of the irregular shape of the pores, the Feret diameter is not the optimal choice for these calculations. Nevertheless, in both cases it is obvious that there are a lot of small pores with an area around 1-10 µm² (5-25 µm diameter resp.). Some large pores are identified on the other end of the scale.

It has to be said that only a few images of the sample were taken in order to calculate the size distribution. After the removal of pores that are cut by edges, there is only a relatively small image left that should represent the sample well. However, the calculations were performed and the result is that there are a lot of small pores and some big pores.

Image analysis is a powerful tool to gain quantitative information like porosity, but one has to keep in mind if the original image is representative of the whole sample or not.

4.8 Plates Höganäs

Very thin austenitic and ferritic plates with a thickness of around 0.40 mm, produced by tape casting, have been supplied by Höganäs AB for further analysis at TUW. The chemical composition measured at TUW can be seen in Table 4.32. Measurement of the density with the He-Pycnometer did not work out because of the high death volume of the cell.

Table 4.32: Chemical composition of the plates

	Chemical composition (wt%)							
Sample	**Fe**	**Cr**	**Ni**	**Si**	**Mn**	**C**	**O**	**N**
Austenite	58,18	20,86	18,39	2,27	0,11	0,12	0,09	0,05
Ferrite	72,39	26,88	0,14	0,29	0,11	0,03	0,04	0,02

4.8.1 Thermal Analysis

TG/DTA measurements have been carried out. The samples were heated up from 40°C to 1590°C and then cooled down back to 50°C (20 K/min) in dry or wet hydrogen atmosphere (flow rate: ca. 10 ml/min). The reason for these measurements was to expose the materials to operating conditions similar to those on the SOFC hydrogen site (anode). For the wet hydrogen measurements, the gas was piped through a gas washing flask filled with distilled water (kept at 22°C).

It is already known that Cr-rich oxide scales lose chromium by evaporation of CrO3 at high temperatures [**119**,**120**], but at lower temperatures the evaporation of chromium is not completely understood. Therefore it was tried to detect some possibly formed volatile chromium species like CrO (mass 68), $CrO*(H_2O)$ (mass 86), $CrO(OH)_2* H_2O$ (mass 120). For comparison a blank value (mass 148, no specific chromium oxyhydroxide species) was chosen.

Fe27Cr plate

Fe27Cr in dry hydrogen

Fig. 4.141 shows the TG/DTA graph for the Fe27Cr plate in dry hydrogen. The black/blue solid graph is for the DTA measurement, the black broken line for the TG analysis. A slight oxidation beginning at 650°C is visible, before the reduction with a weight loss of 0.05 wt% is starting, also the melting of the sample above 1500°C is visible. Fig. 4.142 shows the TGA/DTA-MS graph for the ferritic plate. The red graph m28 with a maximum at 1023°C shows the formation of N_2 and it is identical in shape (of course not in intensity) to the green line with mass 14. The blue line with mass 18 has a pronounced peak at 1096°C, indicating the reduction reaction. There is also a maximum at 426°C, probably due to the reduction of surface (iron?) oxides.

In Fig. 4.143 the TG/DTA-MS graphs for Fe27Cr in dry H_2 atmosphere is shown. It is not possible to say if there is a signal for the graph with mass 68 (CrO), because the intensity is very low (ion current $2*10^{-13}$ A).

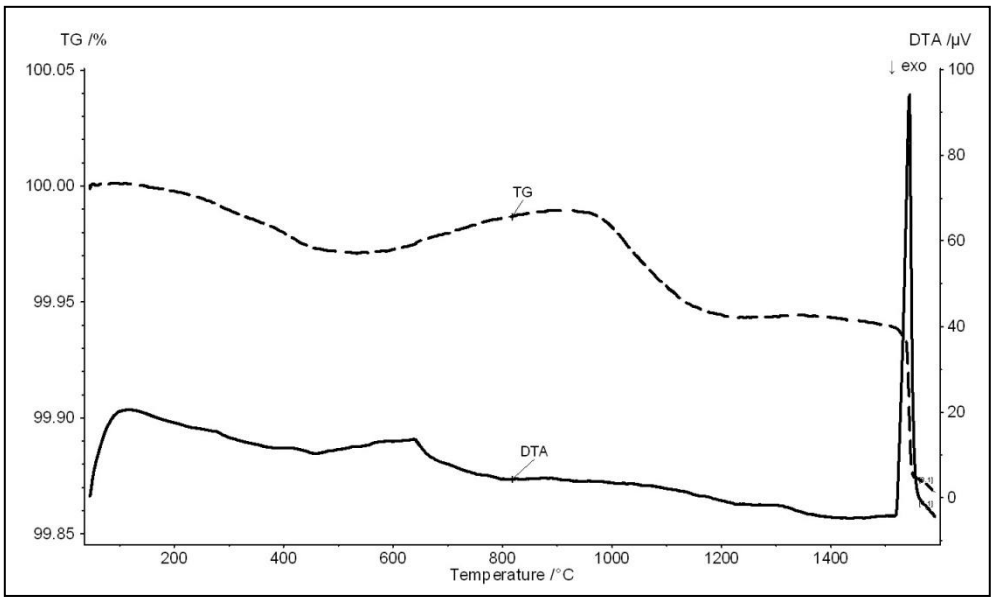

Fig. 4.141: TG/DTA graphs for Fe27Cr in dry H_2 atmosphere. The black broken line stands for the TGA, the solid line for the DTA

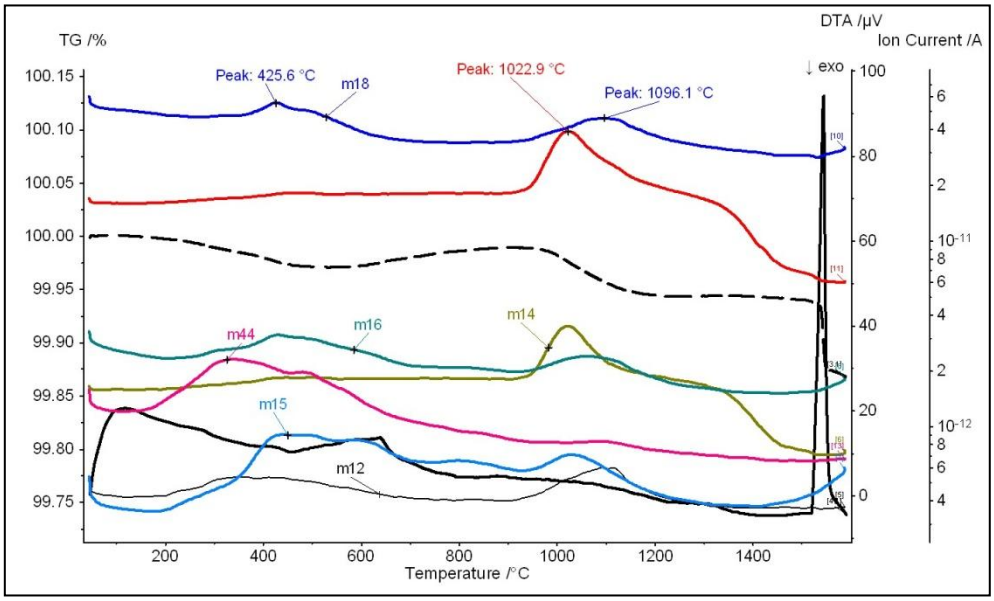

Fig. 4.142: TG/DTA-MS graphs for Fe27Cr in dry H_2 atmosphere, logarithmic Y axis. The black broken line stands for the TGA, the black solid line for the DTA. The red defines mass 28, the blue mass 18, the green line mass 14.

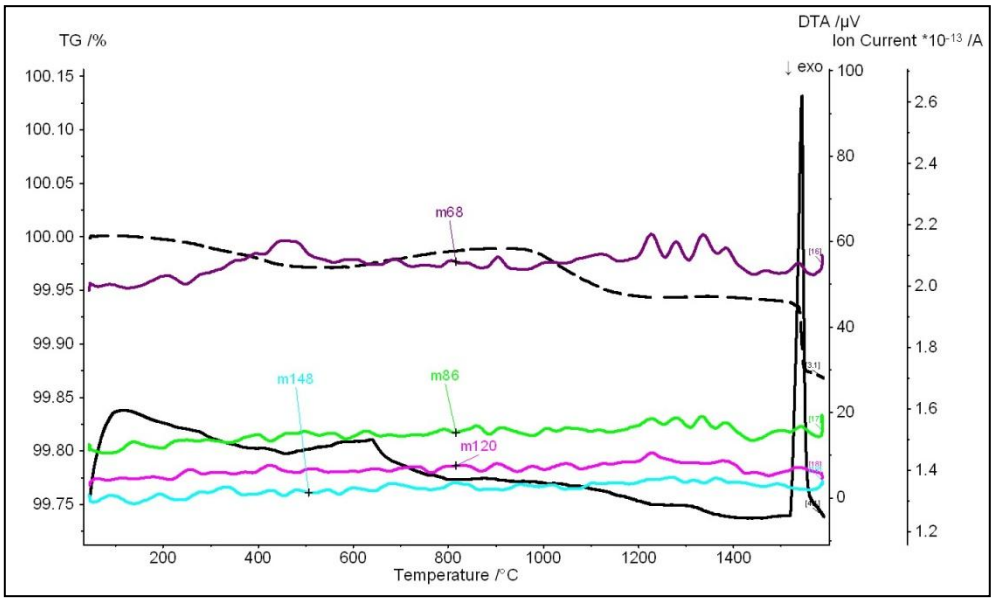

Fig. 4.143: TG/DTA-MS graphs for Fe27Cr in dry H_2 atmosphere, linear MS y axis. The black broken line stands for the TGA, the black solid line for the DTA. The purple line defines mass 68 [CrO], the green mass 86 [CrO*(H_2O)], the pink mass 120 [$CrO(OH)_2$* H_2O] and the light blue mass 148 [no specific chromium oxyhydroxide species]

Fe27Cr in wet hydrogen

Fig. 4.144 shows the TG/DTA graph for the Fe27Cr plate in wet hydrogen, where the black solid graph is for the DTA measurement and the black broken line for the TG analysis in wet hydrogen atmosphere. A weight gain about 2% starting around 650°C and extending over the whole temperature range can be seen. The TGA graph shows two peaks with one maximum a little bit below 800°C and the other is around 1100°C. This indicates two different reactions or one reaction with different reaction rates. To verify this, annealing experiments in the temperature range from 600-900°C have been carried out (see Chapter 4.8.2).

It is evident that in wet hydrogen the Fe27Cr sample gets heavily oxidized. If you look at the blue graph (mass 18) in Fig. 4.145, one may say that in this atmosphere the Fe27Cr plate works like a getter, since the level of water in the atmosphere drops significantly. When comparing the DTG signal in with the m18 signal in it is evident that both are virtually mirror-like.

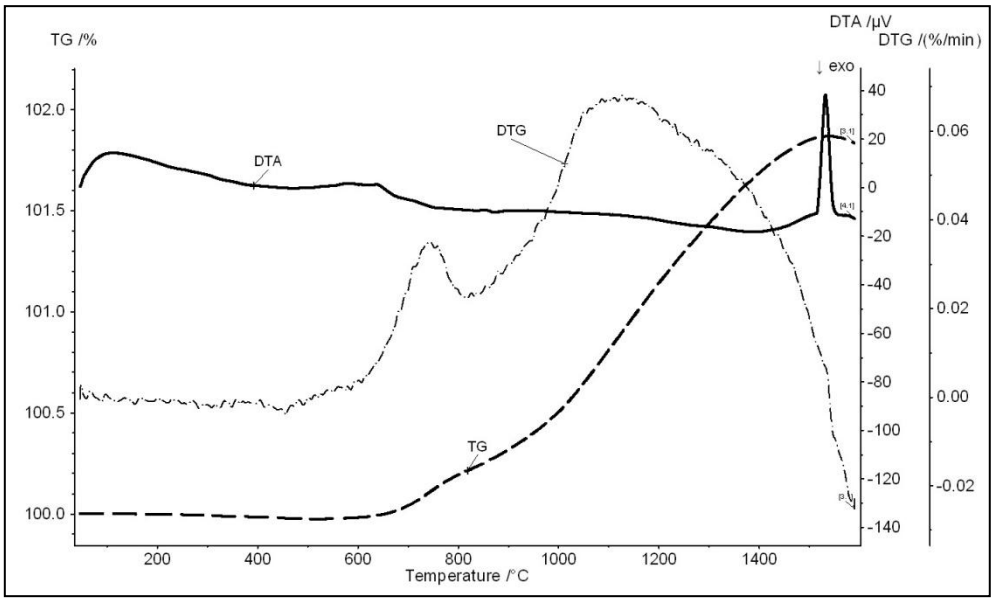

Fig. 4.144: TG/DTA graphs for Fe27Cr in wet H_2 atmosphere. The black broken line stands for the TGA, the solid line for the DTA

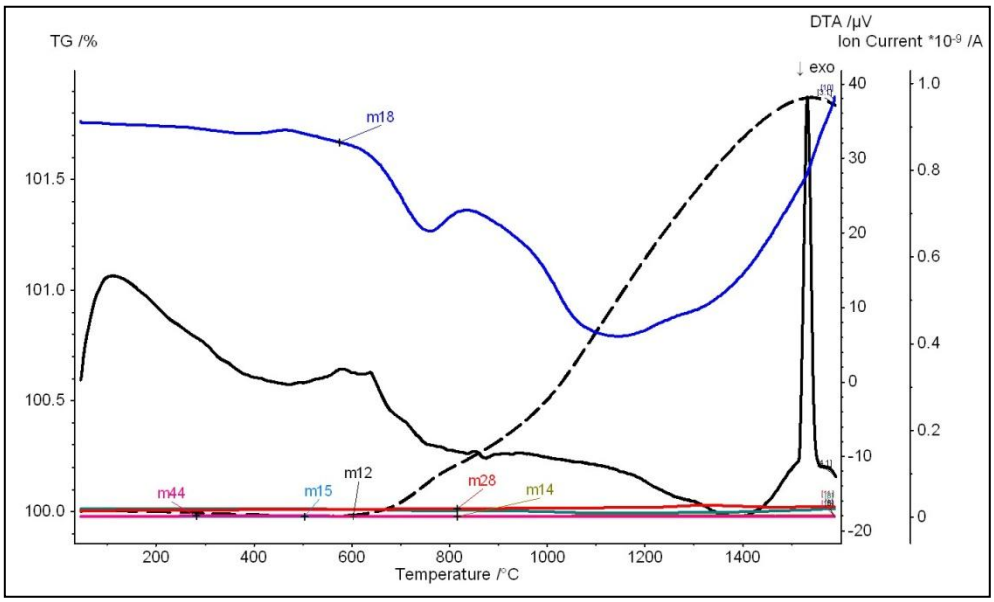

Fig. 4.145: TG/DTA-MS graphs for Fe27Cr in wet H_2 atmosphere. The black broken line stands for the TGA, the black solid line for the DTA. The blue line defines mass 18

Fe21Cr18Ni2.3Si plate

Fe21Cr18Ni2.3Si in dry hydrogen

The behaviour of the austenitic plate in dry hydrogen is very similar to the ferritic one and can be seen in Fig. 4.146 and in Fig. 4.147. Also the austenitic sample shows slight oxidation behavior before the reduction reaction starts. The red line m28 indicates the formation of N_2

(maximum at 1021°C, identical in shape to the green line with mass 14), the blue line the formation of H_2O, with a maximum at 1074°C, 20°C lower than for the ferritic plate.

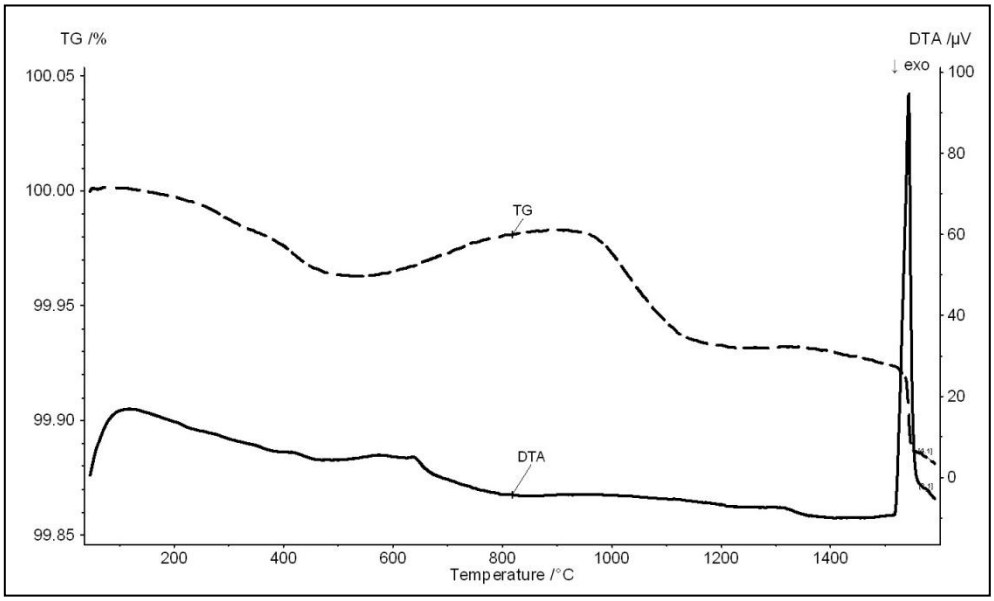

Fig. 4.146: TG/DTA graphs for Fe21Cr18Ni2.3S in dry H_2 atmosphere. The black broken line stands for the TGA, the solid line for the DTA

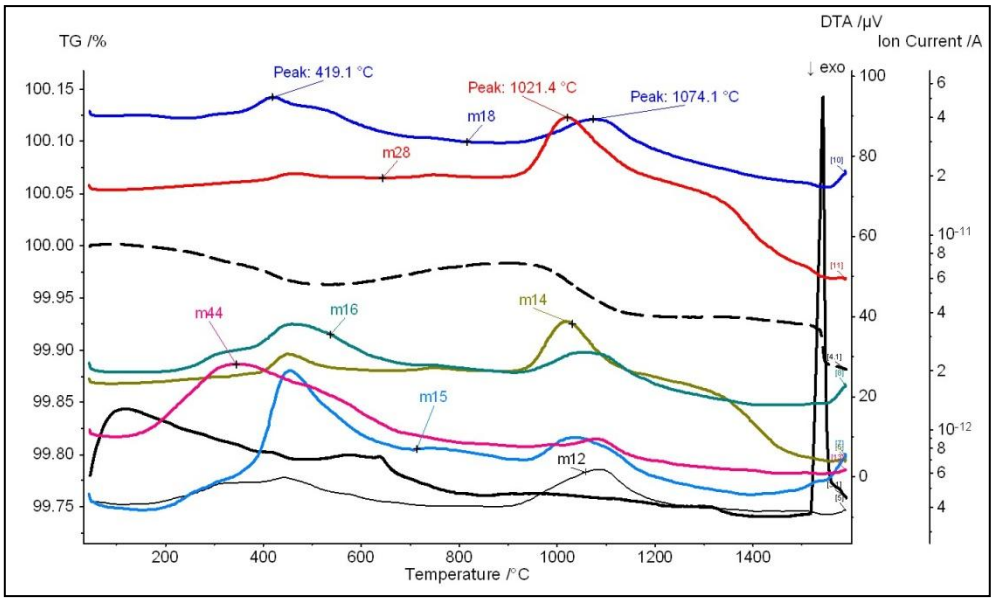

Fig. 4.147: TG/DTA-MS graphs for Fe21Cr18Ni2.3Si in dry H_2 atmosphere, logarithmic MS y axis. The black broken line stands for the TGA, the black solid line for the DTA. The red defines mass 28, the blue mass 18, the green line mass 14.

Fe21Cr18Ni2.3Si in wet hydrogen

Fig. 4.148 shows the TG/DTA graph for the austenitic plate in wet hydrogen. Also the austenitic sample shows heavy oxidation; a mass gain of 2 wt% starting at 650°C can be seen. Also a formation of N_2 and a little bit of CO can be seen at 1269°C (Fig. 4.149). A hint why also some CO could be formed is that the shapes of the graphs with mass 28 and with mass 14 are not identical. It can be seen that the graph with mass 28 has a broader peak than the one with mass 14. Also the carbon content of the base powder with 0.12 wt% is higher than the nitrogen content (0.05 wt%).

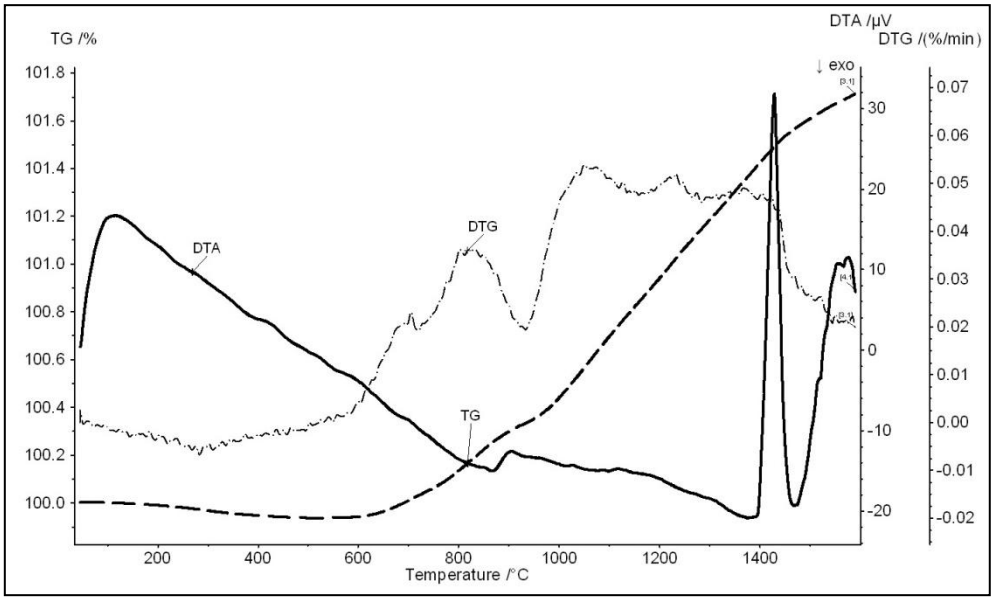

Fig. 4.148: TG/DTA graphs for Fe21Cr18Ni2.3Si in wet H_2 atmosphere. The black broken line stands for the TGA, the solid line for the DTA

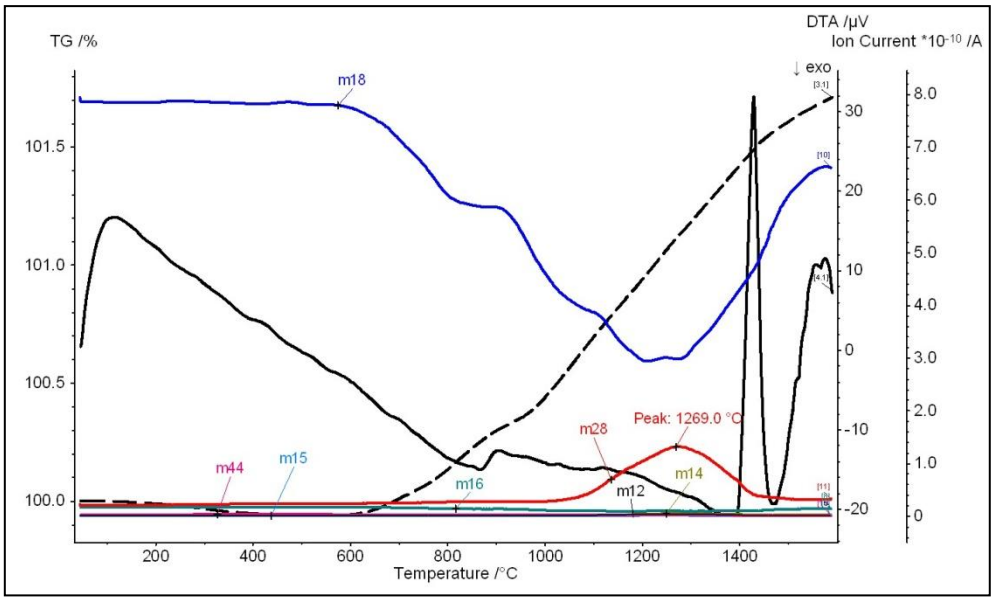

Fig. 4.149: TG/DTA-MS graphs for Fe21Cr18Ni2.3Si in wet H_2 atmosphere, linear MS y axis. The black broken line stands for the TGA, the black solid line for the DTA. The blue line defines mass 18

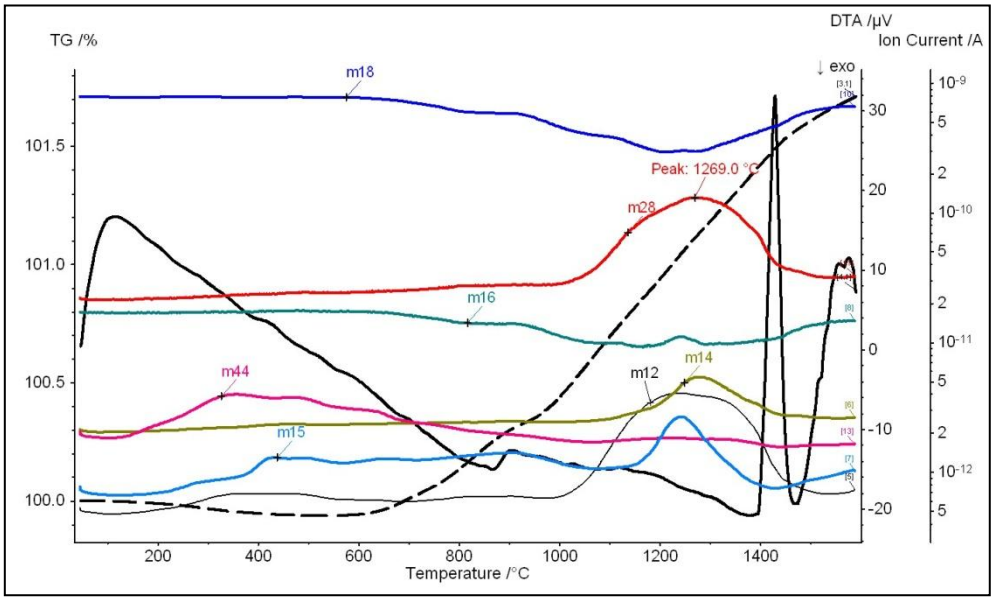

Fig. 4.150: TG/DTA-MS graphs for Fe21Cr18Ni2.3Si in wet H_2 atmosphere, logarithmic MS y axis. The black broken line stands for the TGA, the black solid line for the DTA. The red line defines mass 28, blue line mass 18, green line m14 and the thin black line mass 12

Formation of volatile chromium oxide hydroxide species

Reduction of Cr_2O_3 in hydrogen

The Fe27Cr and Fe21Cr18Ni2.3Si plates in wet hydrogen did not show any signals of possibly formed volatile chromium species like CrO (mass 68), $CrO*(H_2O)$ (mass 86), $CrO(OH)_2* H_2O$ (mass 120). Therefore a Cr_2O_3 specimen was taken and reduced and the volatile chromium species were tried to detect with mass spectroscopy

In Fig. 4.151 the TG/DTA graph for a test run with a Cr_2O_3 specimen in hydrogen atmosphere can be seen. For the measurement a coarse chromium oxide powder from the stock was taken (no detailed description available). There is no weight loss over the whole temperature range, which means that no reduction reaction is happening, i.e. at least the Cr_2O_3 powder grade used here is not reduced by hydrogen up to 1600°C, which is actually surprising, because in the Richardson-Ellingham diagram the Cr_2O_3 is reduced in dry hydrogen at a temperature about 700°C.

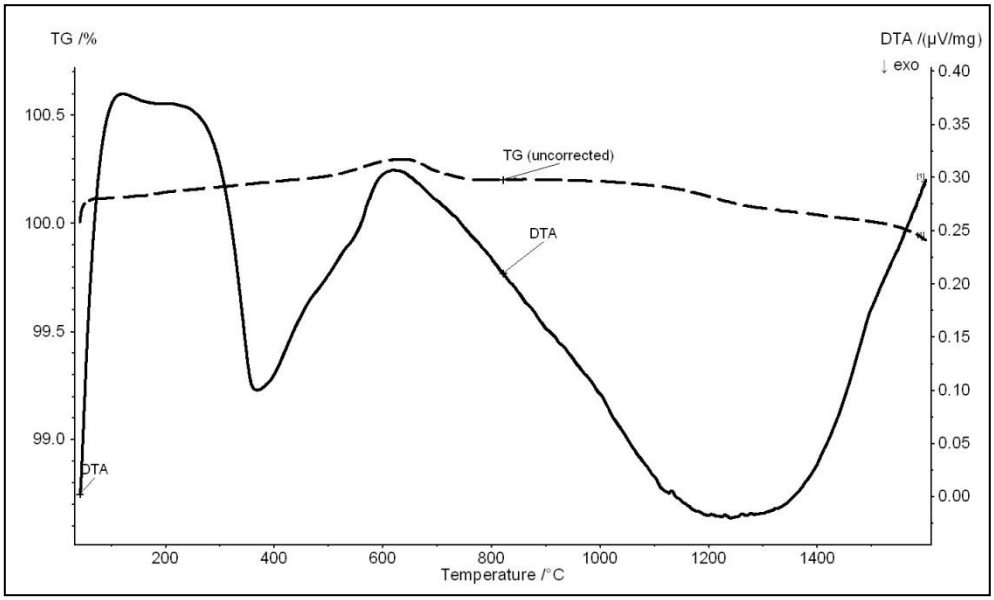

Fig. 4.151: TG/DTA graphs for Cr_2O_3 in hydrogen. The black broken line stands for the TGA, the solid line for the DTA

Reduction of Cr_2O_3 + carbon in hydrogen

In Fig. 4.152 shows the TG/DTA graph for the Cr_2O_3 sample with carbon added (overstoichiometric). The reduction starts at 1063°C and ends at 1171°C with a total weight loss of about 38%. The DTA peak for this reaction is in good correlation with the red line, mass 28, with a maximum at 1134°C. It is possible that the red line not only shows the formation of CO, but also some formation of N_2 (see green line, mass 14, Fig. 4.153). Also interesting is the turquoise line (mass 15, CH_3?) in Fig. 4.153, indicating a slight methane formation, but there is a small difference compared to the light green graph with mass 16, especially in the temperature range from 1000°C – 1200°C.

Further it was tried to detect some volatile chromium oxyhydroxide species (Fig. 4.154), but it is not possible to say if there is a signal for the graph with mass 68 (CrO), because the intensity is very low (ion current $2*10^{-13}$ A).

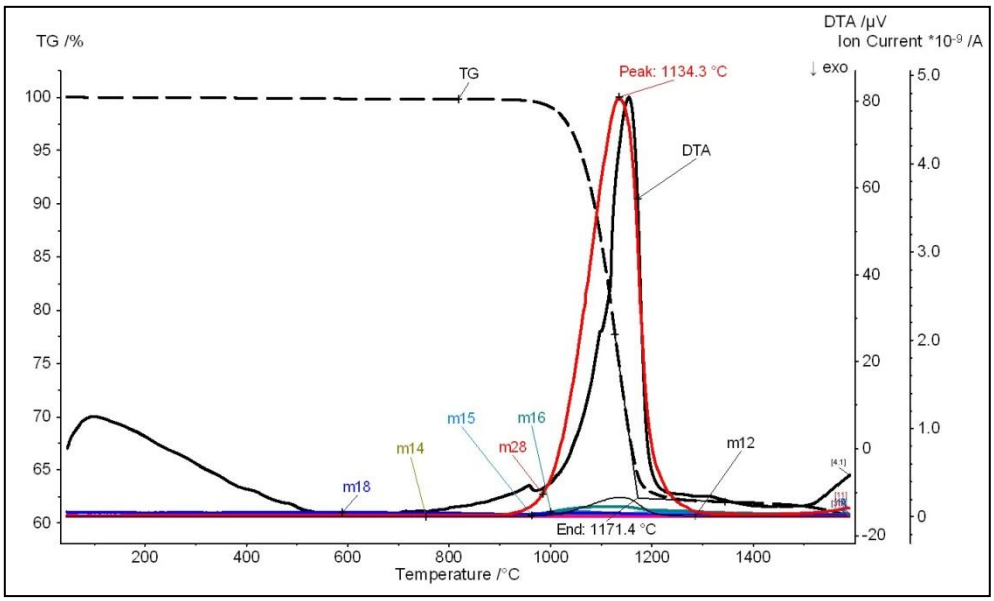

Fig. 4.152: TG/DTA-MS graphs for Cr_2O_3 + carbon in hydrogen, linear MS.y axis. The black broken line stands for the TGA, the black solid line for the DTA, the red defines mass 28

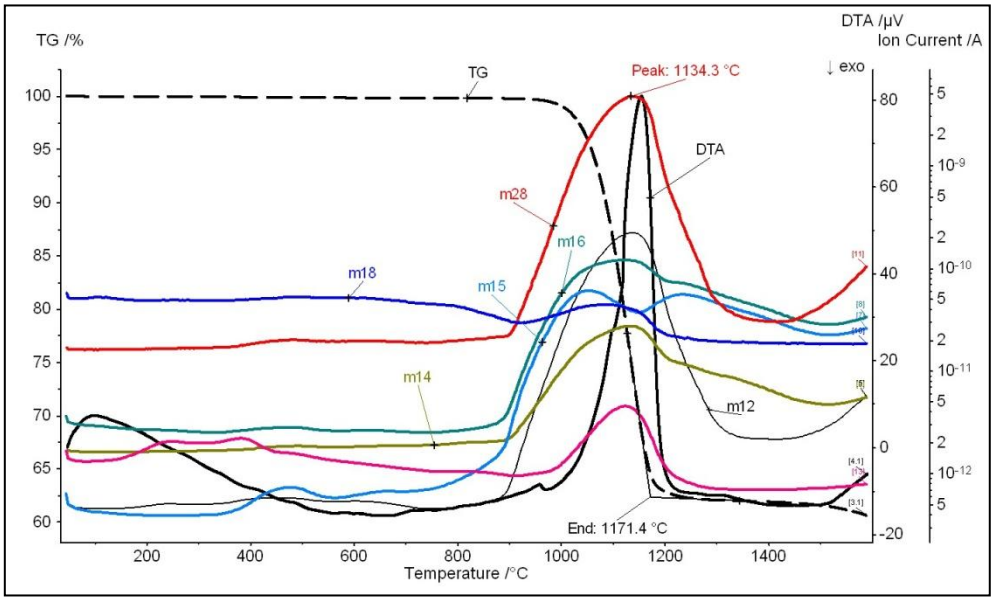

Fig. 4.153: TG/DTA-MS graphs for Cr_2O_3 + carbon in hydrogen, logarithmic MS y axis. The black broken line stands for the TGA, the black solid line for the DTA. The red line defines mass 28, blue line mass 18 and light blue mass 15

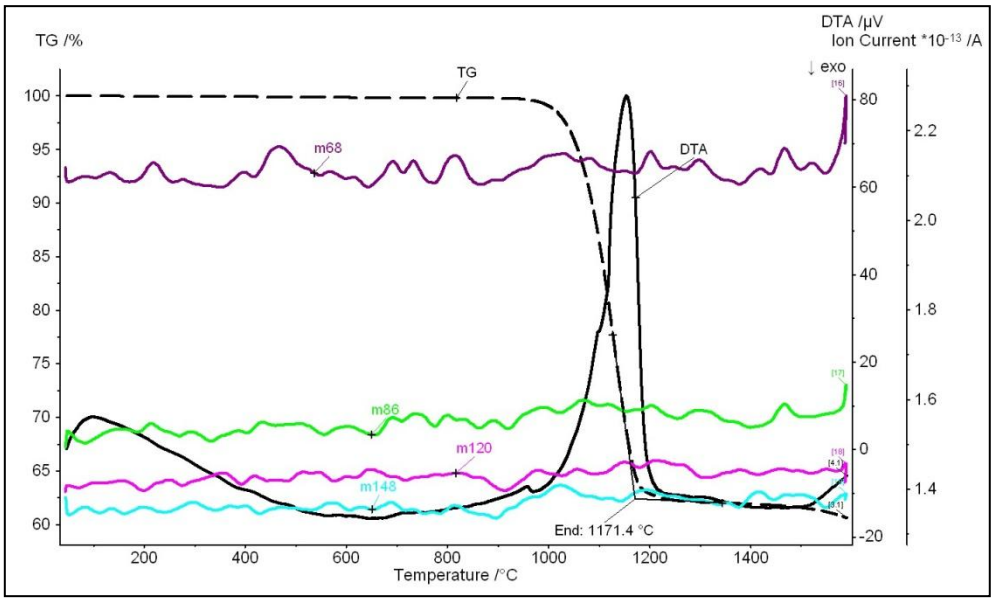

Fig. 4.154: TG/DTA-MS graphs for Cr_2O_3 + carbon in hydrogen atmosphere, linear MS y axis. The black broken line stands for the TGA, the black solid line for the DTA. The purple line defines mass 68 [CrO], the green mass 86 [CrO*(H_2O)], the pink mass 120 [$CrO(OH)_2$* H_2O] and the light blue mass 148 [no specific chromium oxyhydroxide species]

4.8.2 Annealing experiments

As shown before, in the thermoanalytical studies the austenitic and ferritic tape cast plates suffered severe mass increase in wet hydrogen atmosphere. That is the reason why some annealing tests in wet hydrogen atmosphere were carried out (Netzsch STA 449). The samples were heated up to temperatures between 600 and 900°C, held there for 1 hour and then cooled down again. These measurements were made in order to see if there is any relationship between mass gain and annealing temperature or if there is a certain temperature where the sample exhibits severe mass gain.

The mass change was measured by subtracting the minimum from the maximum value in the TG graph. In addition, the oxygen content was measured after the annealing experiments and SEM pictures of the oxidized surface of the samples were taken. Also XRD measurements of the annealed samples have been made.

Fe27Cr plates

In Fig. 4.155 the TG graph for the ferritic samples can be seen. At each temperature a mass gain is visible. The values for every mass gain are shown in Table 4.33. The higher the annealing temperature, the higher is the mass gain and the oxygen content. The ferritic sample with an annealing temperature at 900°C - which is a normal operating temperature for SOFCs - exhibits severe mass gain of 0.68% in only 1 hour.

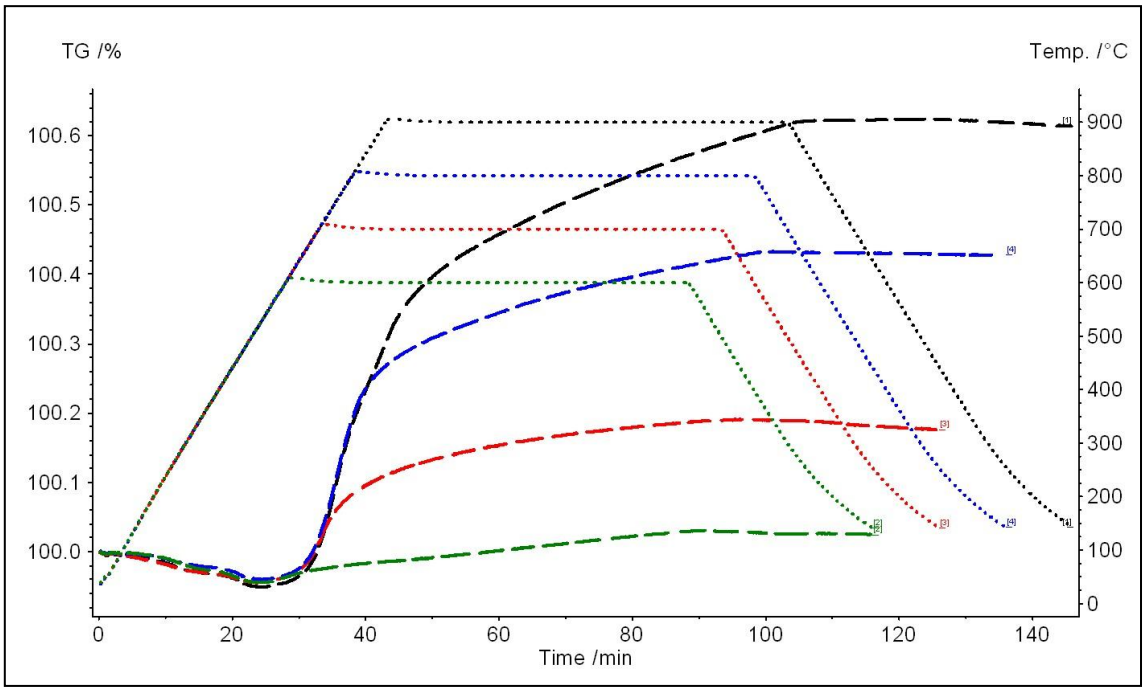

Fig. 4.155: TG graphs for the Fe27Cr sample treated in wet H2. Green broken line stands for a hold at the oxidation temperature of 600°C, the red broken line for a hold at 700°C, the blue line for a hold at 800°C, the black broken line for a hold at 900°C

Table 4.33: Mass gain, oxygen and nitrogen content of the ferritic Fe27Cr plates at room temperature and for different oxidation temperatures (treated in wet H_2)

Sample	annealing temperature (°C)	mass change (%)	wt%O	wt%N
Fe27Cr	22	-	0,037 ± 0,006	0,020 ± 0,001
Fe27Cr	600	+ 0,07	0,121 ± 0,016	0,023 ± 0,001
Fe27Cr	700	+ 0,23	0,265 ± 0,029	0,023 ± 0,001
Fe27Cr	800	+ 0,47	0,478 ± 0,046	0,023 ± 0,001
Fe27Cr	900	+ 0,68	0,696 ± 0,032	0,024 ± 0,001

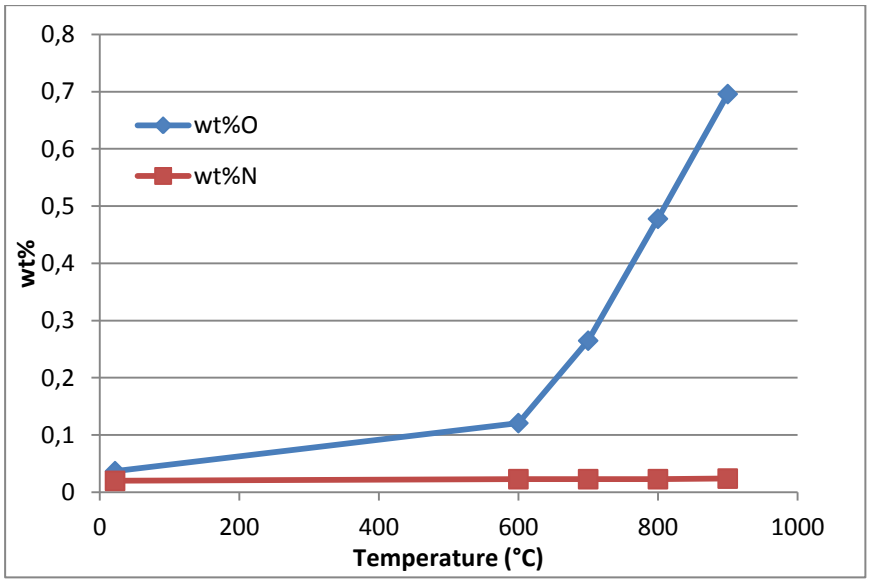

Fig. 4.156: Oxygen and nitrogen content (wt%) of the Fe27Cr samples at different temperatures

Fig. 4.156 demonstrates the increase of the oxygen content depending on the temperature and Fig. 4.165 the mass gain depending on the temperature. The nitrogen content does not change over the whole temperature range.The oxygen content of the ferritic samples at room temperature with 0.04 wt% is very low.The higher the annealing temperature, the higher was the oxygen content.

In Fig. 4.157 - Fig. 4.159 SEM images of the oxidized surfaces can be seen. For comparison, also the plate at the initial state (no "forced" oxidation) is shown. The oxide layers covering the surface of the annealed specimens are clearly visible. In addition, also an EDAX measurement has been made; Fig. 4.160 shows the measurement for the Fe27Cr plate oxidized at 900°C. Only Fe, Cr, O and some C and Si could be identified, which means that the oxide layer consists of chromium oxides.

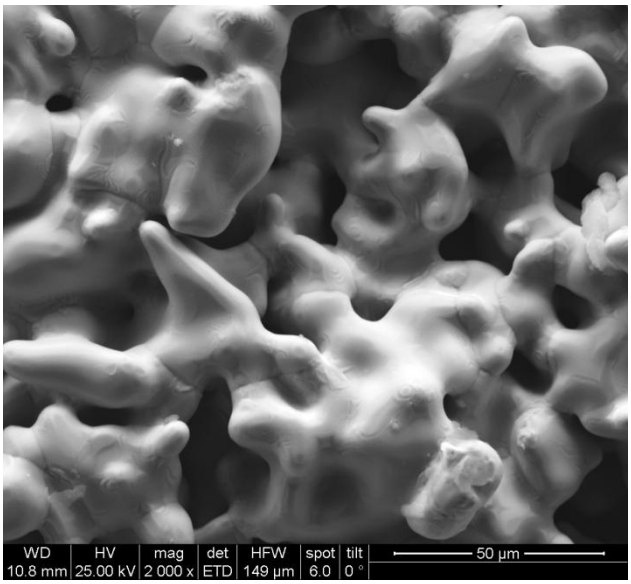

Fig. 4.157: SEM image of the Fe27Cr plate, room temperature as delivered

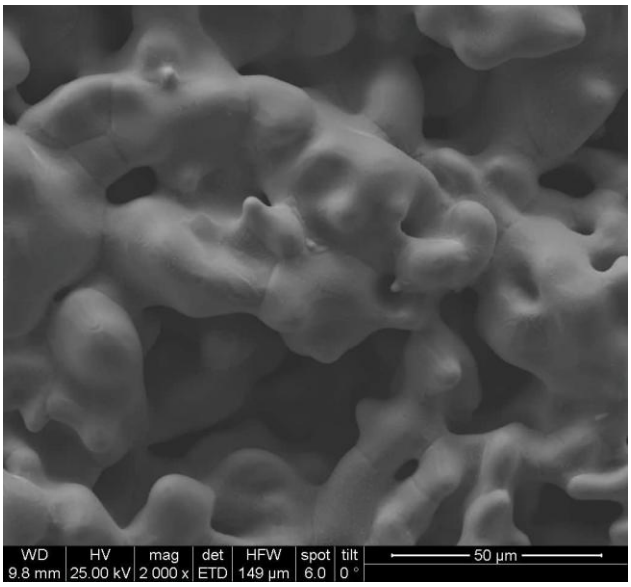

Fig. 4.158: SEM image of the Fe27Cr plate, oxidation temperature 600°C, 1h

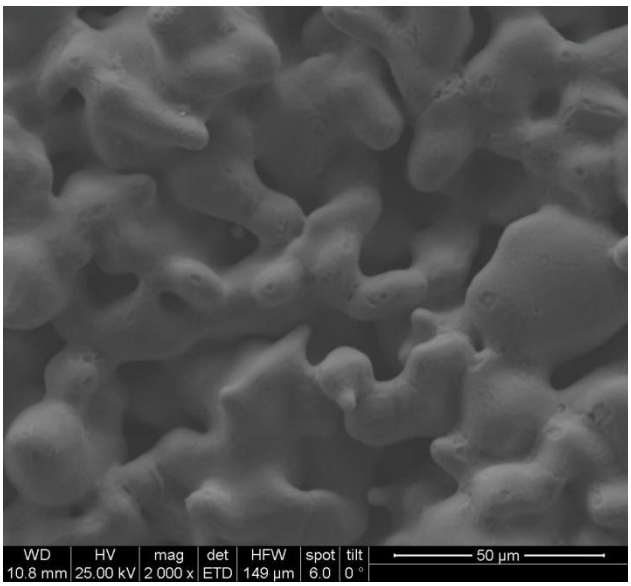

Fig. 4.159: SEM image of the Fe27Cr plate, oxidation temperature 900°C, 1h

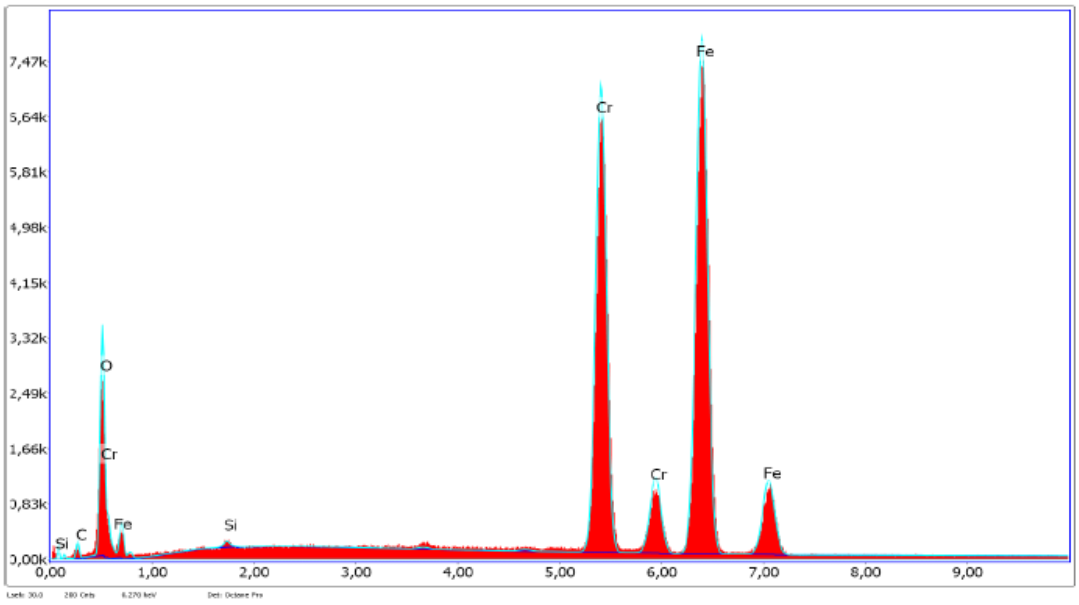

Fig. 4.160: EDAX measurement of the Fe27Cr plate, annealed at 900°C

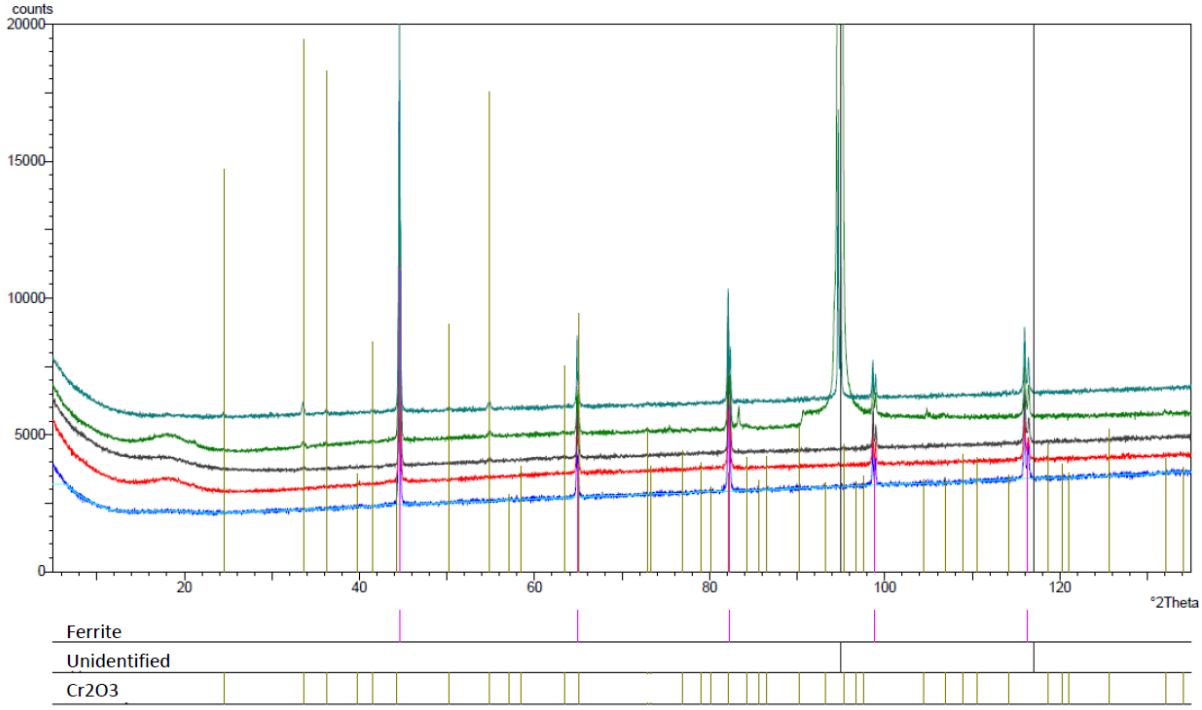

Fig. 4.161: Diffractogram of the Fe27Cr plate; the turquoise line stands for an annealing temperature of 900°C, green = 800°C, grey= 700°C, red = 600°C, blue = no heat treatment, starting state

In Fig. 4.161 the diffractogram of the Fe27Cr plate can be seen. The higher the annealing temperature, the more Cr2O3 is formed. An unidentified reflex at 800°C and 900°C can be seen.

In order to identify the reflex at 800°C and 900°C, a grazing incidence measurement of the 27Cr plate annealed at 800°C was performed (Fig. 4.162), but here only the reflexes of the ferrite are visible and no additional reflex occurs.

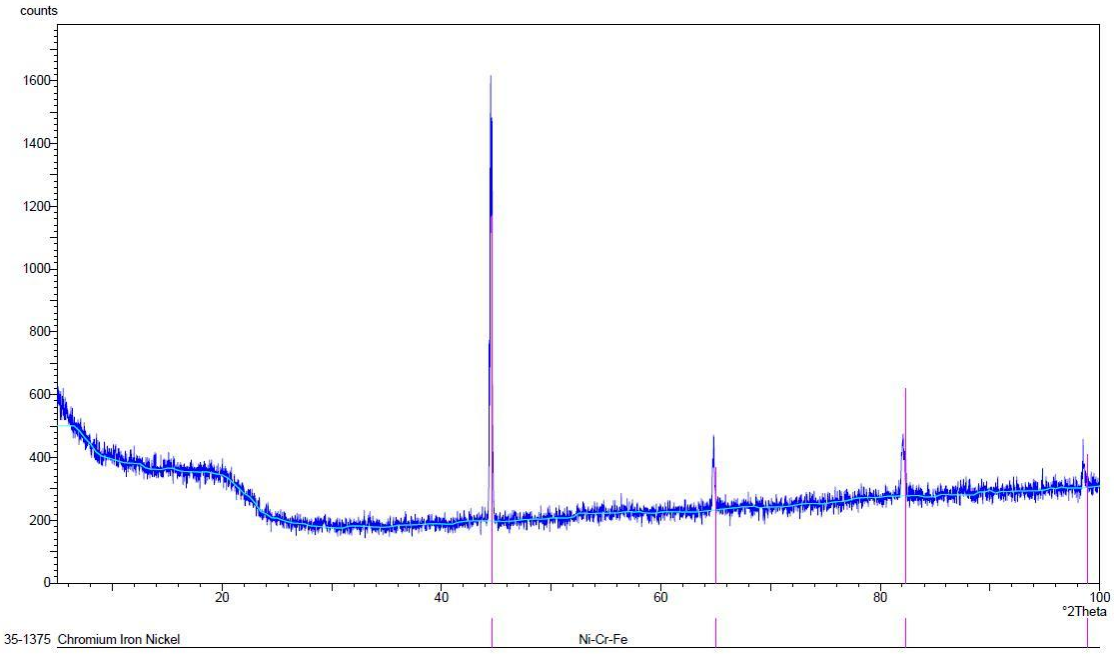

Fig. 4.162: Grazing incidence measurement of the Fe27Cr plate annealed at 800°C

Fe21Cr18Ni2.3Si plates

The austenitic plate Fe21Cr18Ni2.3Si was subjected to the same oxidation experiments as the ferritic plate. The TG graph for the four different isothermal stages (600 – 900°C) can be seen in Fig. 4.163. The TG/DTA measurement for every temperature can be found in the appendix, SEM images of the oxidized surfaces included. In Table 4.34 mass changes, oxygen and nitrogen content of the samples are shown. Again, the higher the oxidation temperature, the higher is the mass gain and oxygen content. Except for the mass gain at 900°C, the increase in mass is lower than for the ferritic grade. Also the slope of the linear regression between temperature and mass change for the austenitic samples is lower than that of the ferritic one (316 vs. 480 resp.). The SEM images demonstrate the formation of the oxide layer on the surface of the former powder particles at elevated temperatures.

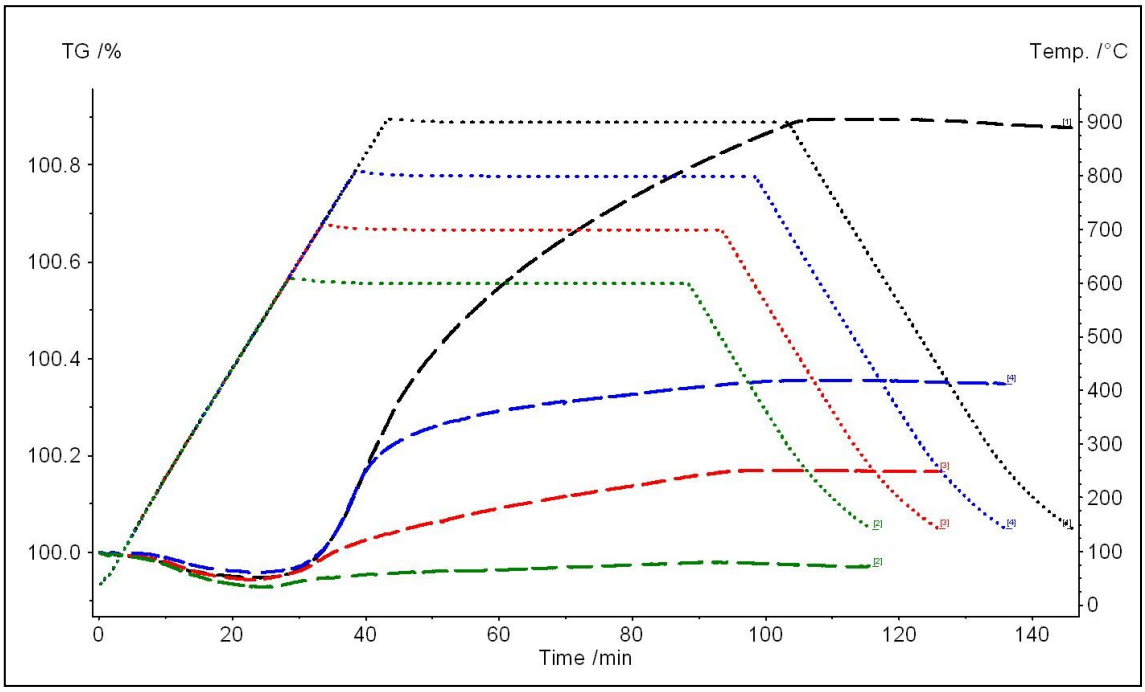

Fig. 4.163: TG graphs for the Fe21Cr18Ni2.3Si sample, treated in wet H_2. Green broken line stands for a hold at the oxidation temperature of 600°C, the red broken line for a hold at 700°C, the blue line for a hold at 800°C, the black broken line for a hold at 900°C

Table 4.34: Mass gain, oxygen and nitrogen content of the austenitic Fe21Cr18Ni2.3Si plates at room temperature and for different oxidation temperatures

Sample	Oxidation temperature (°C)	mass change (%)	wt%O	wt%N
Fe21Cr18Ni2.3Si	22	-	0,086 ± 0,003	0,047 ± 0,004
Fe21Cr18Ni2.3Si	600	0,05	0,129 ± 0,016	0,058 ± 0,002
Fe21Cr18Ni2.3Si	700	0,23	0,349 ± 0,025	0,068 ± 0,001
Fe21Cr18Ni2.3Si	800	0,40	0,565 ± 0,076	0,074 ± 0,002
Fe21Cr18Ni2.3Si	900	0,95	0,678 ± 0,069	0,068 ± 0,005

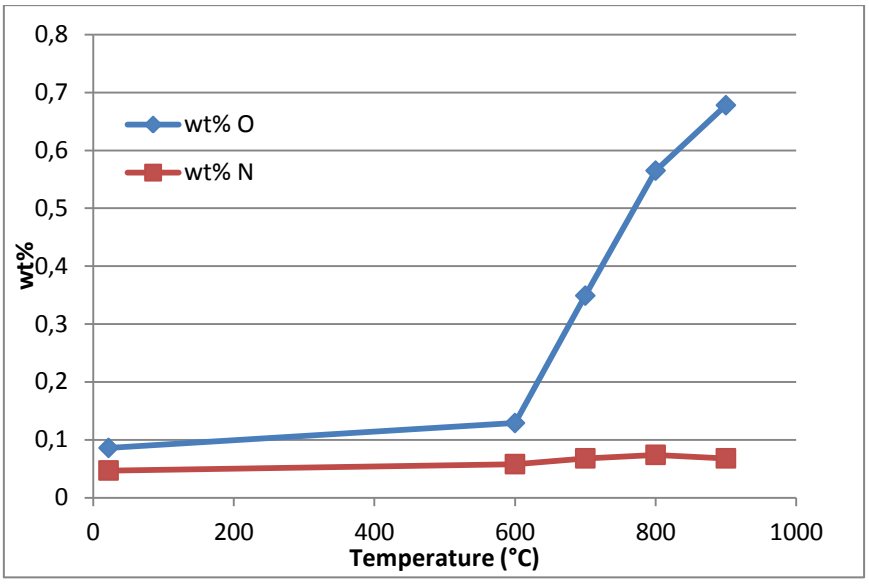

Fig. 4.164: Oxygen and nitrogen content (wt%) at different temperatures of the Fe21Cr18Ni sample

In Fig. 4.165 the mass change as a function of the temperature can be seen. Instead of a specific temperature at or above which severe oxidation and mass gain are pronounced, there is a rather linear relationship between mass change and temperature. The slope of the austenitic Fe21Cr182.3Si sample with 316 is lower than that of the ferritic sample with 480 and naturally, a higher slope results in higher mass gain.

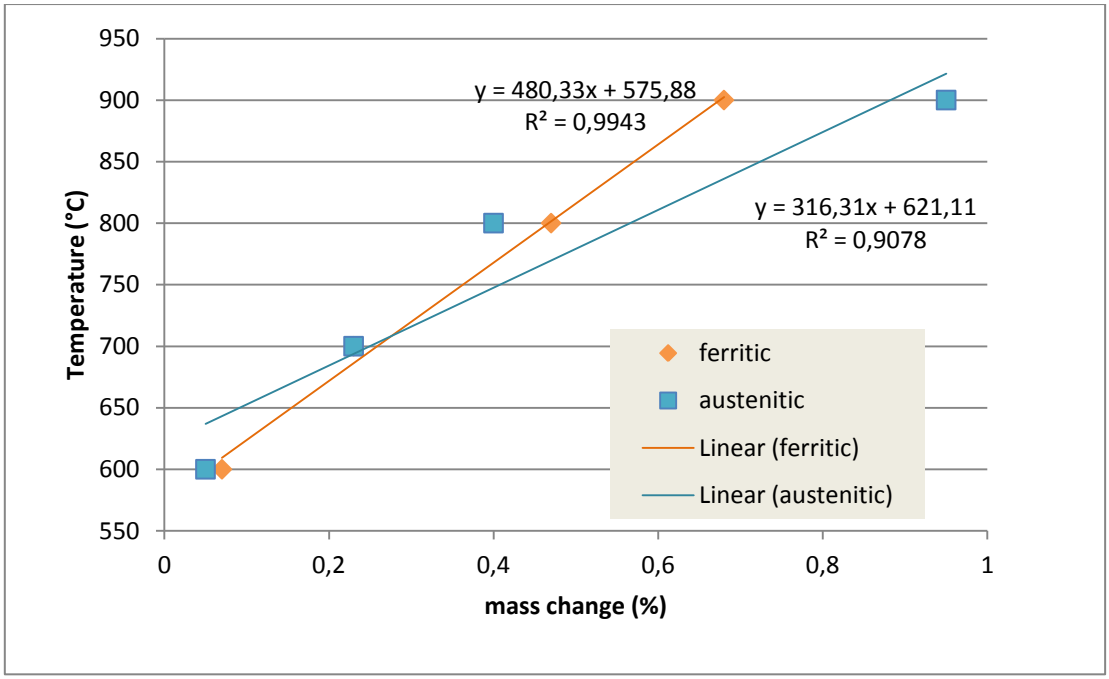

Fig. 4.165: Mass change (%) depending on the temperature of the Fe21Cr18Cr2.3Si sample

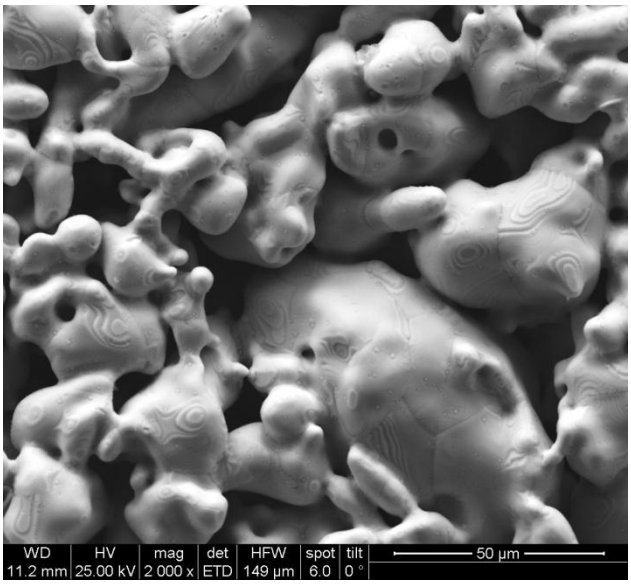

Fig. 4.166: SEM image of the Fe21Cr18Ni2.3Si plate, room temperature

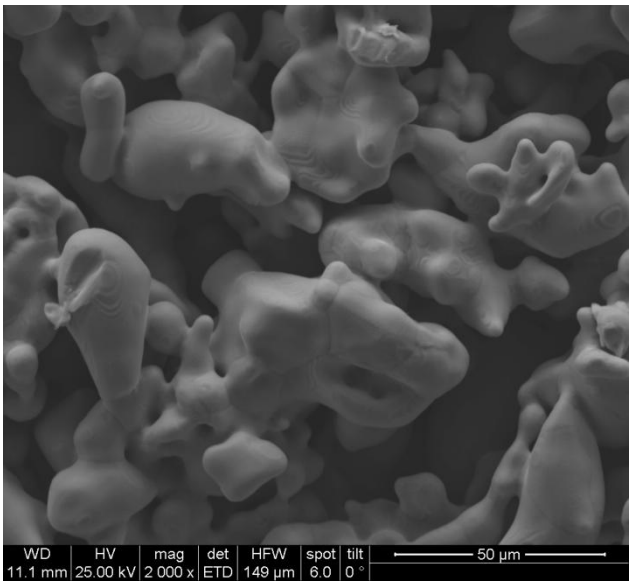

Fig. 4.167: SEM image of the Fe21Cr18Ni2.3Si, oxidation temperature 600°C, 1h

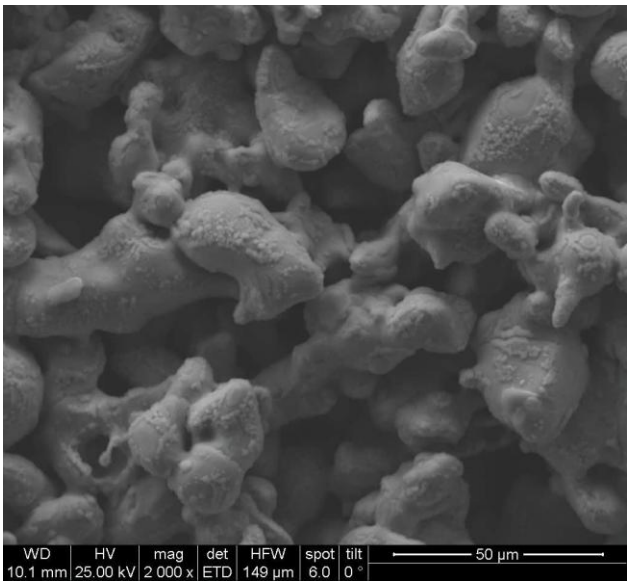

Fig. 4.168: SEM image of the Fe21Cr18Ni2.3Si, oxidation temperature 900°C, 1h

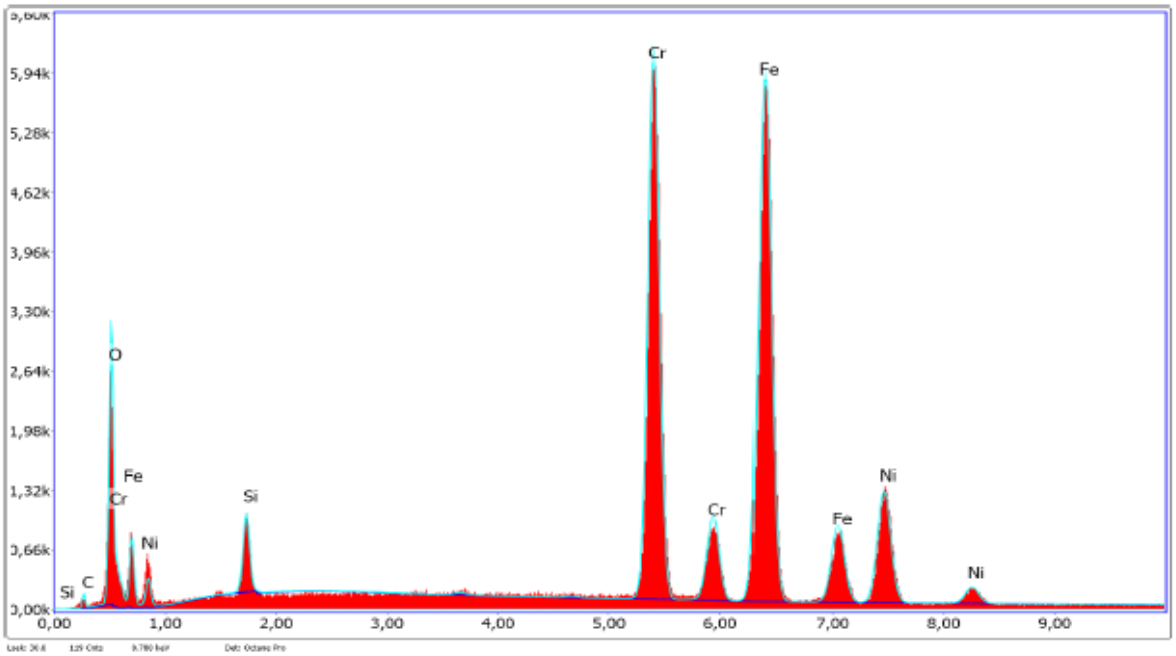

Fig. 4.169: EDAX measurement of the Fe21Cr18Ni2.3Si plate, annealed at 900°C

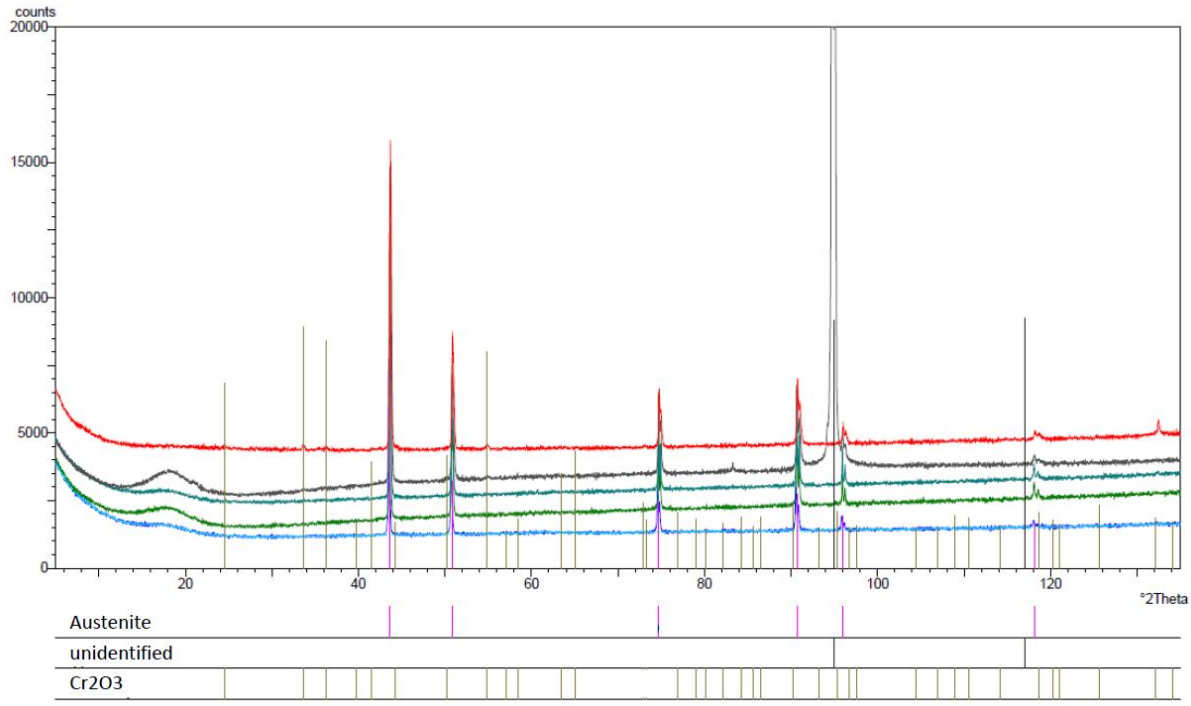

Fig. 4.170: Diffractogram of the Fe21Cr18Ni2.3Si plate; the red line stands for an annealing temperature of 900°C, grey = 800°C, turquoise = 700°C, green = 600°C, blue = no heat treatment, starting state

In Fig. 4.170 the diffractogram of the Fe21Cr18Ni2.3Si plate can be seen. The higher the annealing temperature, the more Cr_2O_3 could be detected. At 800°C (grey line), an unidentified reflex is visible (face centered cubic). It is interesting, that this reflex is only visible at 800°C and not at any other temperature. Again, a grazing incidence measurement was performed (see Fig. 4.171) and in contrast to the ferritic sample, an unidentified reflex can be seen at $2\theta = 55°$. For comparison, XRF measurements of the sample annealed at 800°C and of the starting state were done. The composition of the metallic alloy elements were the same.

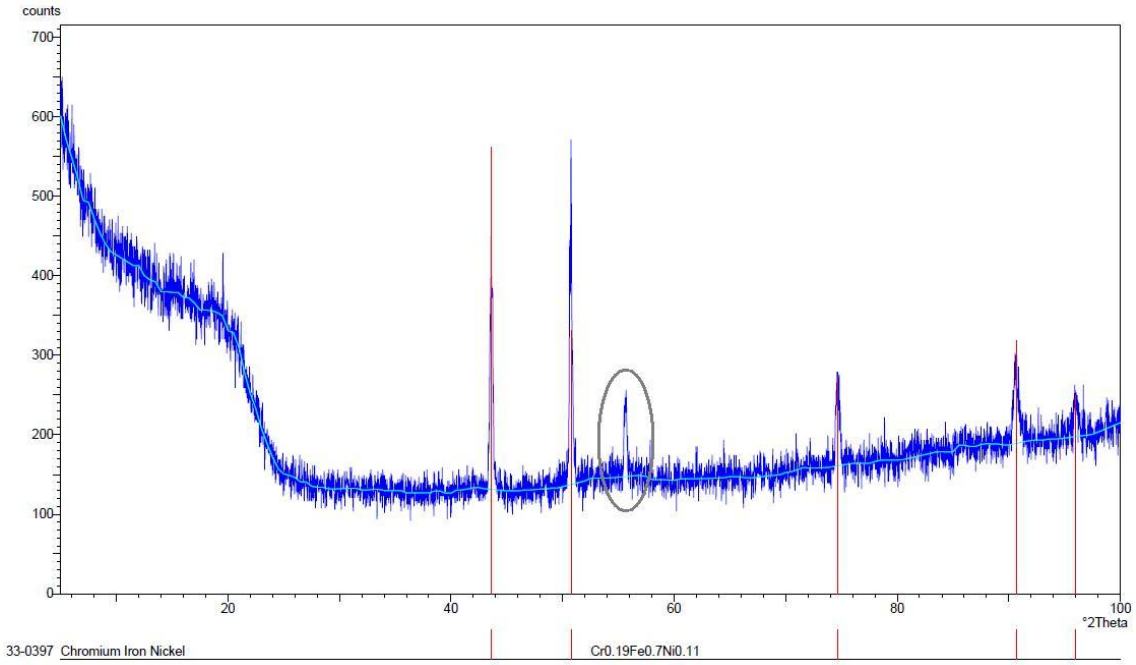

Fig. 4.171: Grazing incidence measurement of the Fe21Cr18Ni2.3Si plate annealed at 800°C

5. Summary and Conclusions

A porous metal support for a SOFC is usually produced by tape casting or spray deposition. In this present work, alternative methods like uniaxial pressing and sintering, gravity sintering or metal injection molding were tried. Also the question arises if co-sintering of the metal support together with ceramic layers is possible. For co-sintering, a linear shrinkage of 15-20% of the metal support is needed to match that of the ceramic functional layers. Another requirement was open and fully interconnected porosity of about 30-50%. Therefore the samples were analyzed with regard to density, porosity and shrinkage. A short summary of the results is now given focused more on the results of the ferritic samples, because commercially available porous metal supports are made of ferritic grades for a better matching of the CTE of the ceramics layers.

Pressing and sintering:

The first method to try was pressing and sintering, so the Fe21Cr powder was uniaxially compacted into the die for Charpy bars (55 x 10 mm) and then sintered at 1300°C for 60 min in H_2. The powder was either mixed with 0.6 wt% Kenolube P11 as a pressing lubricant or compacted with die wall lubrication. In either case the compacting pressure started from 800 MPa and then the pressure was lowered progressively to increase the (green and final) porosity. With die wall lubrication, the pressure could be lowered to a minimum of 100 MPa, with pressing lubricant to 150 MPa. Reducing the compacting pressure even further was not possible, since then the samples disintegrated on ejection. The green and sintered density of the die wall lubricated samples is lower than that of the samples with pressing lubricant (for comparison of the austenitic and ferritic samples see Table 4.5).

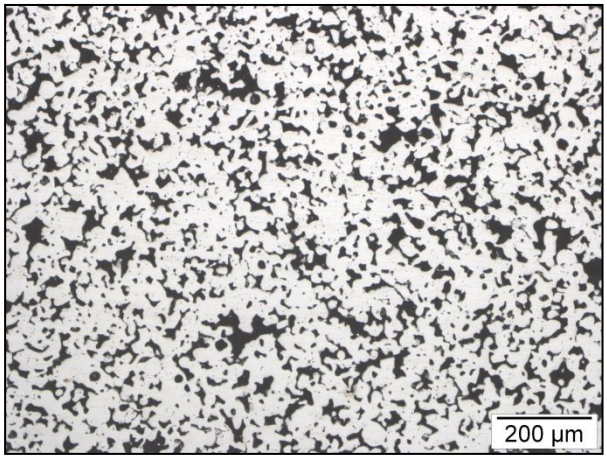

Fig. 5.1: Fe21Cr, pressed with 150 MPa, die wall lubricated, 31.2% porosity, 100x, sintered in H_2, 1 h 1300°C

For example, the Fe21Cr sample compacted at 150 MPa with die wall lubrication has a low green (3.88 g/cm³) and sintered density (4.82 g/cm³, Archimedes method). The pycnometric density of the powder was measured as 7.54 g/cm³. The porosity is 31.2% and as can be seen in Fig. 5.1, the pores are homogeneously distributed. The linear shrinkage of the sample is about 7.7% and clearly not in the desired range of 15-20% shrinkage. In order to get more shrinkage, gravity sintering was tried.

Gravity sintering:

The powder was filled into Al_2O_3 crucibles (from the LECO CS analyzer) and the sintered for 60 min at 1300°C in H_2. Two different filling techniques were tried (with or without tapping, in order to check the influence of tapping on the shrinkage). The green and sintered density of the tap-filled samples is higher than that of the samples filled without tapping. For example, the green density of the tapped Fe21Cr sample (= tap density) was measured as 3.44 g/cm^3, the sintered density is 4.40 g/cm³. For comparison, the sintered density of the Fe21Cr filled without tapping is markedly lower with 3.98 g/m^3. The starting state of this sample is not exactly the apparent density; it is more likely between apparent and tap density. The reason is that while putting the sample carefully in the furnace, densification of the powder is happening, due to small impacts of the sinter boat against the wall ("pseudo-tapping").

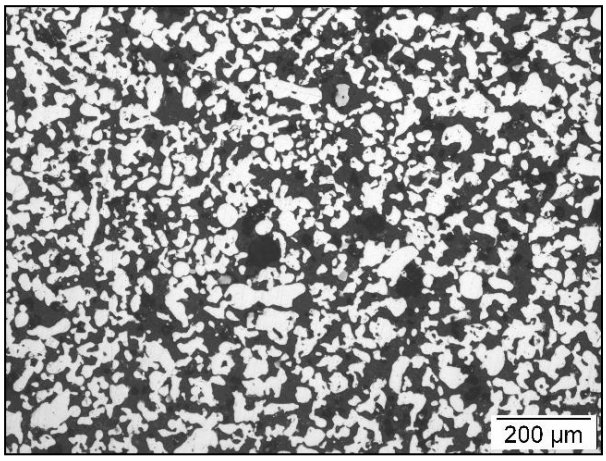

Fig. 5.2: Fe21Cr, bulk state, longitudinal plane, 100x, 48% P, sintered in H_2, 60 min 1300°C

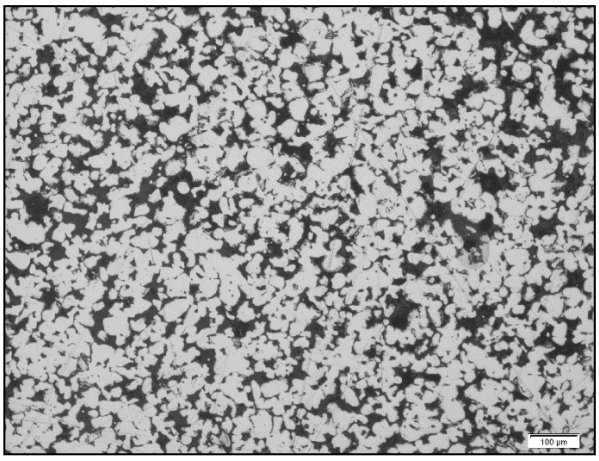

Fig. 5.3: Fe21Cr, bulk state, cross plane, 100x, 48% P, sintered in H_2, 60 min 1300°C

The porosity of the Fe21Cr sample starting from tapped state is 42.0%, from the sample starting from the bulk state is higher with 47.5%. The pores are well distributed in both plane directions and almost no agglomerations can be seen (Fig. 5.2 and Fig. 5.3). The porosity of the Fe25Cr20Ni2.5Si sample is a bit lower (43.8% for the bulk state and 34.1% for the tapped state), and the distribution is also very fine. A comparison of the pycnometric density of the powder and the sintered density revealed that almost exclusively open porosity in the sintered parts is present, which is required for porous metal supports.

To measure the shrinkage in every direction more precisely, gravity sintering experiments of the powder in an Al_2O_3 boat were performed, and the results for the austenitic and ferritic powder can be seen in Table 5.1.

Table 5.1: Shrinkage of the gravity sintered samples

	shrinkage (%)		
Sample	**length**	**width**	**height**
Fe21Cr bulk	2,4	6,4	16,0
Fe21Cr tapped	0,5	8,6	10,4
Fe25Cr20Ni2.5Si bulk	7,1	11,5	22,8
Fe25Cr20Ni2.5Si tapped	6,7	10,1	13,6

There is a big difference in shrinkage of the height (in direction of the gravity force) between the bulk and the tap starting state, meaning that about 5 - 10% are enforced by "pseudo-tapping" and partly also by gravity. The shrinkage in the other directions is lower and the reason could be that the powder was stuck to the ceramic case, which inhibited higher shrinkage.

Binder experiments:

A binder system based on polyvinyl alcohol was tested out, but the metallographic images showed that this method was not suitable for producing porous metal supports because the sintered samples have numerous big pores. Another binder system tested was with a Styronal, a binder based on a styrene und butadiene copolymer. The sintered samples showed better pore distribution, but still there were cracks and agglomerations of pores visible. Also shaping of the wet powder was a problem. To avoid the cracks, powder extrusion and metal injection molding experiments were performed at the UC3M in Leganes. But two problems showed up with extrusion molding that could not be overcome due to the short period of time (only 2 months stay at Leganes). First, typically one out of four samples cracked while debinding, and the second problem was the distribution of the pores. Even at the highest powder loading with 55 vol% big agglomerations of pores of around 200 µm could be seen. Better results could however be obtained with injection molding.

Metal Injection Molding:

Fig. 5.4: Comparison of green (above) and sintered MIM parts (1300°C, 60 min, vacuum)

It can be seen that the shrinkage is rather isotropic and in the range of 13% (independent of the powder loading), which is rather close to the desired 15-20%.

For all three binder contents of the Fe16Cr samples could be shown that the pores are very well distributed and no agglomerations can be seen (for example, Fe16Cr + 50 vol% powder loading, see Fig. 5.5).

Naturally, the higher the powder content, the lower the porosity. There is also a good correlation between the Archimedes porosity and the porosity measured with the Hg-porosimetry (Table 5.3).

For these experiments, a Fe16Cr powder, due to better availability, was used. The binder consisted of high density polyethylene, paraffin wax and stearic acid; three different powder loadings, 45, 50 and 55 vol%, were tried. The samples were debinded (solvent and thermal) and then sintered at 1300°C for 60 min in vacuum. The shrinkage is evident (Fig. 5.4), and the values of the shrinkage are listened in Table 5.2.

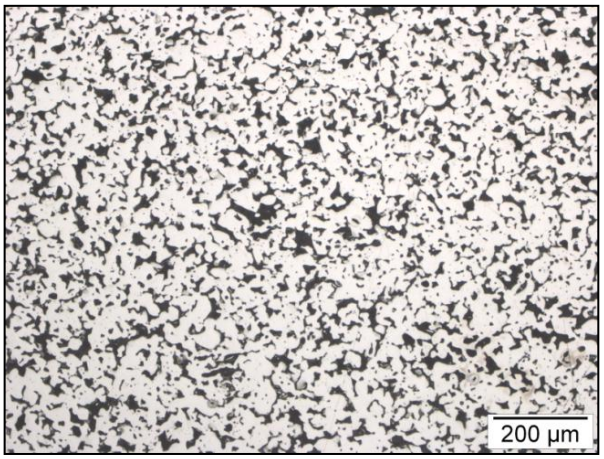

Fig. 5.5: Fe16Cr + 50 vol% powder loading, horizontal plane, 100x, 22% porosity

Table 5.2: Shrinkage and porosity of the vacuum sintered MIM samples (1300°C, 60min)

		shrinkage (%)		
Sample	powder loading (vol%)	length	width	height
Fe16Cr	55	13,3	14,5	13,9
Fe16Cr	50	13,5	13,6	11,0
Fe16Cr	45	13,4	14,8	12,8
Fe25Cr20Ni2.5Si	55	10,1	11,0	11,9
Fe25Cr20Ni2.5Si	50	9,5	9,9	10,3
Fe25Cr20Ni2.5Si	45	11,2	12,3	13,1

Table 5.3: Comparison of Archimedes-, Hg- and FIJI-porosity

Powder	manufacturing process	powder loading (vol%)	Archimedes porosity* (%)	Hg-porosity (%)	FIJI porosity** (%)
Fe16Cr	MIM	45	28,0	24,6	27,0 ± 0,8
Fe16Cr	MIM	50	21,5	16,5	24,0 ± 1,4
Fe16Cr	MIM	55	20,3	16,2	17,3 ± 0,6
Fe25Cr20Ni	MIM	45	35,4	34,4	35,3 ± 1,4
Fe25Cr20Ni	MIM	50	30,7	29,9	30,2 ± 1,7
Fe25Cr20Ni	MIM	55	24,3	23,0	25,5 ± 1,9

*porosity [%] = $(1 - (\rho_{Archimedes} / \rho_{theoretical})) * 100$ ($\rho_{theoretical}$ measured by He-Pycnometry)
**values are given only for the images with a magnification of 200x

Image analysis

has been performed with *FIJI*, an open source image processing program based on *ImageJ*. For porosity quantification, the values are shown in Table 5.3. As already known, different magnifications of one image can lead to different values for the porosity. Also the thresholding of the images is a key factor. In this work, a good correlation of the calculated *FIJI* porosity and the Archimedes porosity could be obtained for the images with a magnification of 200x. With the *FIJI* software, also the distribution of the pores can be calculated. Fig. 5.6 shows the pore size distribution of an austenitic MIM sample. It can be seen that there are a lot of small pores (1 – 10 µm² pore surface area) and a few big ones on the other end of the scale. Image analysis could be a very powerful tool for gathering information about porosity, but one has to keep in mind if the images used for the calculations are representative of the sample or not.

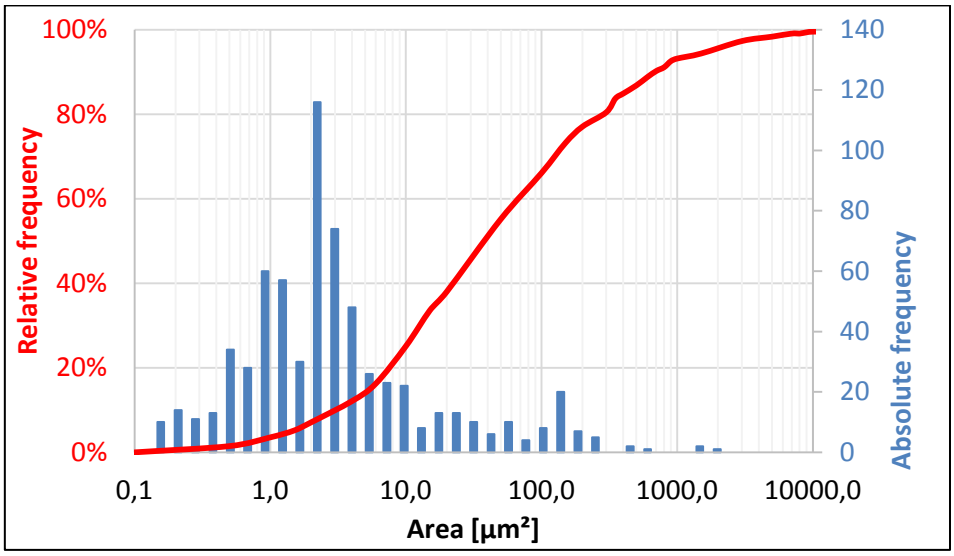

Fig. 5.6: Pore size distribution of Fe25Cr20Ni2.5Si MIM sample with 45 vol% p.l. Calculation based on surface area

Summarizing it can be stated that different alternative manufacturing processes for a porous metal support have been tried. The uniaxial pressing and sintering experiments resulted in insufficient shrinkage; for that reason, gravity sintering experiments were performed. This was an interesting approach, although over 40% porosity, the pores were finely distributed, but one problem was the anisotropic shrinkage of these samples. The most promising method was metal injection molding. Also there the distribution of the pores was very even, the shrinkage was isotropic and in the area of 13%, which is not surprising, because MIM itself is always claimed to be an isotropic forming process. In any case the results prove that MIM is not only a process suited for producing small, fully dense precision parts – as is industrial practice today - but that it can also yield highly porous structures, the prominent feature being the regular, well defined and evenly distributed porosity that can be attained.

If MIM then could replace tape casting for production of these metal supports is questionable, because on the one hand, it has to be proved that the dimension of the support with 10 x 10 x 1 mm can be produced; on the other hand, tape casting is already a well established process and manufacturing the entire cell is not at all an easy task if you think of all the processes involved like PVD coating of the thin film diffusion barrier layers. Switching from tape casting to metal injection molding for sure will have an impact on the whole production route. And last, but not least, it will be interesting to see if the SOFC - or the fuel cell in general – with all its positive properties like efficiency and low-emission energy supply will enter the market competitive or it will remain a niche product.

6. References

[**1**] http://www.bp.com, BP Statistical Review of World Energy 2013, (2013)

[**2**] Positionspapier – Chemie als ein Innovationstreiber in der Materialforschung, Dechema, Dezember 2012

[**3**] W.R. Grove, On a Gaseous Voltaic Battery, *Phil. Mag. XXI*, 417-420 (1842)

[**4**] http://www.bloomenergy.com

[**5**] W. Nernst, "Über Die Elektrolytische Leitung Fester Körper Bei Sehr Hohen Temperaturen", *Z. Elektrochem.*, 6, 41-43, (1899)

[**6**] S. Gottesfeld., T. Zawodinski, "Polymer electrolyte fuel cells", *Adv. Electrochem. Sci. Eng.*, Vol. 5, 195 – 301, (1997)

[**7**] P. Costamagna, S. Srinivasan, "Quantum jumps in the PEMFC science and technology from the 1960s to the year 2000 Part 1 Fundamental scientific aspects", *Journal of Power Sources*, Vol. 102, 242 – 252, (2001)

[**8**] L. Xianguo, S. Imran, "Review of bipolar plates in PEM fuel cells: Flow-field design", *Int. Journal of Hydrogen Energy*, Vol. 30, 359 – 371, (2005)

[**9**] Kinoshota, *Electrochemical Oxygen Technology*, John Wiley & Sons, New York, Chapter 2, 19 – 112, (1992)

[**10**] M. Cifrain, K. Kordesch, *Handbook of Fuel Cells – Fundamentals., Technology and Applications*, Vol. 1, Part 4, 267 – 280, Edited by Wolf Vielstich, Wiley & Sons, Chichester, ISBN: 0-471-49926-9, (2003)

[**11**] K. Kordesch, G. Simader, *Fuel Cells and Their Applications*, 54 – 72, VCH, Weinheim, Germany, ISBN: 3-527-28579-2, (1996)

[**12**] O. Lindström, M. Lavers, "Cost Engineering of Ammonia and AFC power plants", Fuel Cell Seminar, San Diego (CA), USA; 196-198, (1994)

[**13**] J. Appleby, Proceedings of the Workshop on the Electrochemistry of Carbon, Edited by S. Sarangapani, et al., The Electrochemical Society, Inc., Pennington, NJ, p. 251, (1984)

[**14**] G. Hoogers, *Fuel Cell Technology Handbook*, CRC Press LLC, Boca Raton (FL), USA; ISBN: 0-8493-0877-1, (2003)

[**15**] M.L. Orfield, D.A. Shores, Corrosion 86, Paper No. 88, National Association of Corrosion Engineers, Houston (TX), (1986)

[**16**] R.J. Selman, *Energy*, 11, 153, (1986)

[**17**] N. Minh, *High Temperature Fuel Cells*, CHEMTECH, journal published by the American Chemical Society, Vol. 21, No. 1, January, 32-37, (1991)

[**18**] P. Berger, „HotModule Brennstoffzellen-Kraftwerk-Verstromung regenerativer Gase in der MCFC“, VDI-Berichte, Nr. 1874, 87-100, published by the German National Library, ISBN: 3-18-091874-8, (2005)

[**19**] L. Hu, I. Rexed, et al., “Electrochemical performance of reversible molten carbonate fuel cells”, *Int. Journal of Hydrogen Energy*, Vol. 39, 12323-12329, (2014)

[**20**] EG&G Technical Services, Fuel Cell Handbook, 7th Edition. (2004)

[**21**] http://www.fz-juelich.de

[**22**] N.Q. Minh, “Ceramic Fuel Cells”, *J. Americ. Chem. Soc.*, Vol. 76, Nr. 3, 563-588, (1993)

[**23**] E. Baur and H. Preis; *Zeitung für Elektrochemie*, 43; p. 727 – 732, (1937)

[**24**] Advances in Ceramics, *Science and Technology of Zirconia*, Vol. 3; Edited by A. H. Heuer and L. W. Hobbs, American Ceramic Society, Columbus (OH), United States, (1981)

[**25**] Advances in Ceramics, *Science and Technology of Zirconia II*, Vol. 12; Edited by N. Claussen, M. Rühle, and A.H. Heuer. American Ceramic Society, Columbus (OH), United States, (1984)

[**26**] Advances in Ceramics, *Science and Technology of Zirconia III*, Vol. 24; Edited by S. Somiya, N. Yamamoto, and H. Yanagida. American Ceramic Society, Westerville (OH), United States, (1988)

[**27**] R. Stevens, “An Introduction to Zirconia”, Magnesium Elektron, London, U.K., (1986)

[**28**] T.H. Etsell and S.N. Flengas, “The Electrical Properties of Solid Oxide Electrolytes”, *Chem. Rev.*, Vol. 70, 339-376, (1970)

[**29**] E.C. Subbarao and H.S. Maiti, “Solid Electrolytes with Oxygen Ion Conduction”, *Solid State Ionics*, Vol. 11, 317-338, (1984)

[**30**] O. Kanert, “Dynamical properties of defects in solids”, *Phys. Rep.*, Vol. 91, 183-232, (1982)

[**31**] J:B. Goodenough, K. Huang, “Lanthanum Gallate as a New SOFC Electrolyte”, Proceedings of the Fuel Cells 1997 Review Meeting, (1997)

[**32**] F.M. B. Figureido and F.M.B. Marques, “Electrolytes for solid oxide fuel cells”, *WIREs Energy Environ*, 2, 52-72, (2013)

[**33**] H.S. Spacil, U.S. Pat No. 3,558,360, (1970)

[**34**] D.W. Dees, T.D. Claar, et al, “Conductivity of porous Ni / ZrO_2-Y_2O_3 cermets”, *Journal of Electrochemical Society*, Vol. 134 (9), 2141 – 2146, (1987)

[**35**] A. N. Busawon, D. Sarantaridis, A. Atkinson, “Ni Infiltration as a Possible Solution to the Redox Problem of SOFC Anodes”, *Electrochem. Solid-State Lett.*, Vol. 11 (10), B186-B189, (2008)

[**36**] Y. Matsuzaki, I. Yasuda, “The poisoning effect of sulfur containing impurity gas on a SOFC anode: Part I. Dependence on temperature, time, and impurity concentration”, *Solid State Ionics*, 132, 261-269, (2000)

[**37**] S.C. Singhal, et al., "Anode Development for Solid Oxide Fuel Cells", United States Department of Energy, Pittsburgh, USA, (1986)

[**38**] H. Kurokawa, T.Z. Sholklapper, S.J. Visco, et al., "Ceria nanocoating for sulfur tolerant Ni-based anodes of solid oxide fuel cells", *Electrochemical and Solid State Letters*, Vol. 10, 135-138, (2007)

[**39**] J.R. Rostrup-Nielsen, et al., "Sites for catalysis and electrochemistry in solid oxide fuel cell (SOFC) anode", Applied Physics A – Materials Science Processing, Vol. 85 (4), 427-430, (2006)

[**40**] M.L. Toebes , J.H. Bitter, et al., "Impact of the structure and reactivity of nickel particles on the catalytic growth of carbon nanofibers", *Catalysis Today*, Vol. 76, 33-42, (2002)

[**41**] H. He, J:M: Hill, "Carbon deposition on Ni/YSZ composites exposed to humidified methane", *Applied Catalysis A: General*, Vol. 317, 284-292, (2007)

[**42**] J. Woo Yun, et al., "Ceria coating effect in H_2S poisoning of Ni/YSZ anodes for Solid Oxide Fuel Cells", *Journal of the Electrochemical Society*, Vol. 157 (12), 1825-1830, (2010)

[**43**] O. Marina, C. Bagger. S. Primahl, M. Mogensen, "A solid oxide fuel cell with a gadolinia-doped ceria anode: preparation and performance", *Solid State Ionics*, Vol. 123, 199-208, (1999)

[**44**] S. A. Barnett, Handbook of Fuel Cell Technology, Vol. 4, 198, Wiley, New Jersey, USA, (2003)

[**45**] H. He, R.J. Gorte, J.M. Vohs, "Highly Sulfur Tolerant Cu-Ceria Anodes for SOFCs", *Electrochem. Solid-State* Lett., Vol. 8 (6), 279-280, (2005)

[**46**] S. Park, et al., "Direct oxidation of hydrocarbons in a Solid Oxide Fuel Cell", *Nature* (London), Vol. 404, 261-267, (2000)

[**47**] M.D. Gross, J.M. Vohs, R.J. Gorte, "A study of thermal stability and methane tolerance of Cu-based SOFC anodes with electrodeposited Co", *Electrochimica Acta*, Vol. 52, 1951-1957, (2007)

[**48**] Y.H. Hunag, et al., "Double Perovskites as Anode Materials for Solid Oxide Fuel Cells", *Science*, Vol. 312, 254-257, (2006)

[**49**] Z.H. Bi and J.H. Zhu, "Effect of Current Collecting Materials on the Performance of the Double-Perovskite $Sr_2MgMoO_{6-\delta}$ Anode", J. Electrochem. Soc., Vol. 158 (6), 605-613, (2011)

[**50**] G.H. Jonker, "Semiconducting properties of mixed crystals with perovskite structure", *Physica*, Vol. 20, 1118-1122, (1954)

[**51**] J. Tanaka, K. Takahashi, K. Yukino, S. Horiuchi, "Electrical Conduction of $(La_{0.8}Ca_{0.2})MnO_3$ with Homogenous Ionic Distribution", *Physica Status Solidi (a)*, Vol. 20 (2), 621-630, (1983)

[**52**] A. Wold, R.J. Arnott and J.B. Goodenough, "Some magnetic and crystallographic properties of the system $LaMn_{1-x}Ni_xO_{3+\lambda}$," *J. Appl. Phys.*, Vol. 29, 387-389, (1958)

[**53**] J.B. Goodenough, "Electronic and ionic transport properties and other physical aspects of perovskites", *Reports on Progress in Physics*, Vol. 67, 1915-1993, (2004)

[**54**] R. Hildrum, S. Aasland, O. Johannesen, "Electric and catalytic properties of doped $LaMnO_3$", *Solid State Ionics*, Vol. 66 (3-4), 207-218, (1993)

[**55**] J.H. Kuo, H.U. Anderson, D.M. Sparlin, "Oxidation-reduction behavior of undoped and Sr-doped LaMnO3: Defect structure, electrical conductivity and thermoelectric power", *Journal of Solid State Chemistry*, Vol. 87 (1), 55-63, (1990)

[**56**] M. Kertesz, et al., "Structure and electrical conductivity of $La_{0.84}Sr_{0.16}MnO_3$", *Journal of Solid State Chemistry*, Vol. 42 (2), 125-129, (1982)

[**57**] T. Hashimoto, et al., "Electrical resistivity and Seebeck coefficient of $La_{1-x}M_xMnO_3$ (M=Ca, Sr) single crystals", *J. of Materials Science*, Vol. 23 (3), 1102-1105, (1988)

[**58**] K. Katayama, et al., "Sintering and Electrical Conductivity of $La_{1-x}Sr_xMnO_3$", *J. Ceramic Society of Japan*, Vol. 97, 1327-1333, (1989)

[**59**] A. Hammouche, E. Siebert, A. Hammou, "Crystallographic, Thermal and Electrochemical Properties of the System $La_{1-x}Sr_xMnO_3$ for High-Temperature Solid Electrolyte Fuel Cells", *Mat. Res. Bull*., Vol. 24, 367-380, (1989)

[**60**] S. Simner, J. Stevenson, "Cathode – Chromia Interactions", in SECA 2004 Annual Meeting and Core Program Review, Boston,(2004)

[**61**] N.Q. Minh, "Ceramic Fuel Cells", *J. American Ceramic Society*, Vol. 76 (3), 570-572, (1993)

[**62**] W.J. Quadakkers, H. Greiner, W. Köck, "Metals and Alloys for High Temperature SOFC Applications", *Proceedings of the First European Solid Oxide Fuel Cell Forum*, Vol. 1, 525-541, compiled by V. Bossel, Lucerne, Switzerland, (1994)

[**63**] P. Kofstad, *Proceedings of the Second European Solid Oxide Fuel Cell Forum*, Vol. 2, 297-306, compiled by B. Thorstensen, Oslo, Norway, (1996)

[**64**] W.J. Quadakkers, H. Greiner, et al., "The Chromium Base Metallic Bipolar Plate – Fabrication, Corrosion and Cr Evaporation", *Proceedings of Second European Solid Oxide Fuel Cell Forum*, Vol. 2, 297-306, compiled by B. Thorstensen, Oslo, Norway, (1996)

[**65**] G. Yang, et al., "Adavanced Metallic Interconnect Development", in SECA 2004 Annual Meeting and Core Program Review, Boston, U.S.A., US DOE NETL, (2004)

[**66**] W.J. Quadakkers, L. Singheiser, "Practical Aspect of the Reactive Element Effect", *Material Science Forum*, Vol, 369-372, 77-92, (2001)

[**67**] C.L. Chu, J.Y. Wang, et al., "Evaluation on Some Metallic Alloys for SOFC Interconnect", *Materials Science Forum*, Vol. 544-545, 989-992, (2007)

[**68**] A. Venskutonis, W. Glatz, G. Kunschert, "P/M Processing of ODS Cr- and FeCrr-based alloys for SOFC Applications", *Proceedings 17th Int. Plansee Seminar*, Reutte, Austria, 534-544, (2009)

[**69**] L. Blum, et al., "Recent results in Jülich solid oxide fuel cell technology development", *Journal of Power Sources*, Vol. 241, 477-485, (2013)

[**70**] K.D. Meinhardt, et al., "Glass-ceramic material and method of making", US Patent No. 6,430,966, August 13, (2002)

[**71**] C. Günther, G. Hofer, W. Kleinlein, in *Solid Oxide Fuel Cells-V*, compiled by U. Stimmig, S. Singhal, H. Tagawa, W. Lehnert, The Electrochemical Society Proceedings, PV 97-40, p.746, Pennington, NJ, (1997)

[**72**] K.L. Ley, M. Krumpelt, R. Kumar, J.H. Meiser and I. Bloom, "Glass-ceramic sealants for solid oxide fuel cells: Part 1. Physical properties", *Journal of Material Research*, Vol. 11 (06), 1489-1493, (1996)

[**73**] N. Lahl, et al., "Crystallisation kinetics in $AO\text{-}Al_2O_3\text{-}SiO_2\text{-}B_2O_3$ glasses (A=Ba, Ca, Mg)", J. *of Materials Science*, Vol. 35, 3089-3096, (2000)

[**74**] D. Bahadur, et al., "Influence if Nucleating Agents on the Chemical Interaction of $MgO\text{-}Al_2O_3\text{-}SiO_2\text{-}B_2O_3$ Glass Sealants with Components of SOFCs", *Journal of the Electrochemical Society*, Vol. 151 (4), A558-A562, (2004)

[**75**] S. P. Simner, J.W. Stevenson, "Compressive mica seals for SOFC applications", *Journal of Power Sources*, Vol. 102, 310-316, (2001)

[**76**] M. Bram, et al., "Deformation behavior and leakage tests of alternate sealing materials for SOFC stacks", *Journal of Power Sources*, Vol. 138, 111-119, (2004)

[**77**] D. Stöver, H.P. Buchkremer, N. Menzler, S. Uhlenbruck, „Die Hochtemperatur-Brennstoffzelle (SOFC) – Ein Energiewandler der Pulvermetallurgie", Pulvermetallurgie in Wissenschaft und Praxis, compiled by H. Kolaska, Fachverband Pulvermetallurgie, Hagen, Band 19, 127-156, (2003)

[**78**] Courtesy of Siemens Westinghouse

[**79**] K. Huang, S. Singhal, "Cathode-supported tubular solid oxide fuel cell technology: A critical review", *J. of Power Sources*, Vol. 237, 84-97, (2013)

[**80**] National Energy Technology Laboratory, Office of Fossil Energy Fuel Cell Handbook, Sixth Edition, U.S. Department of Energy, Morgantown, U.S.A., (2002)

[**81**] H. Kurokawa, et al., "Water-based binder system for SOFC porous steel substrates", *Journal of Materials Processing Technology*, Vol. 182, 469-476, (2007)

[**82**] M. Tucker, "Progress in metal-supported Solid Oxide Fuel Cells: A review", *Journal of Power Sources*, Vol. 195, 4570-4582, (2010)

[**83**] M. Bram, S. Vieweger, M. Brandner, T. Franco, N. H. Menzler, D. Stöver, and H. P. Buchkremer, "Development of Metal Supported Solid Oxide Fuel Cells (SOFC) for Future Energy Supply," in *Euro PM Proceedings 2013*, Göteborg, Sweden, (2013)

[**84**] L. Kuo, et al., "Plasma Spraying of Lanthanum Chromite Films for Solid Oxide Fuel Cell Interconnection Application", *J. of American Ceramic Society*, Vol. 80 (3), 589-593, (1997)

[**85**] R.J. Gorte, Course notes International APT Course "Advances in Medium and High Temperature SOFC Technology, Udine, Italy, (2014)

[**86**] Y.J. Leng, et al., "Effect of characteristics of Y_2O_3/ZrO_2 powders on fabrication of anode-supported solid oxide fuel cells", *Journal of Power Sources*, Vol. 117, 26-34, (2003)

[**87**] T. Hikita, in "Science and Technology of Zirconia V", edited by S.P.S. Badwal, M.J. Bannister and R.H.J. Hannink, Technomic Publishing Co., Lancaster, PA, U.S.A., p. 647, (1993)

[**88**] W. Bao, Q. Chang, G. Meng, "Effect of NiO/YSZ compositions on the co-sintering process of anode-supported fuel cells", *Journal of Membrane Science*, Vol. 259, 103-109, (2005)

[**89**] K. Chen, et al., "Performance evolution of NiO/yttria-stabilized zirconia anodes fabricated at different compaction pressures", *Electrochimica Acta*, Vol. 54, 1355-1361, (2009)

[**90**] D. Simwonis et al, "Properties of Ni/YSZ porous cermets for SOFC anode substrates prepared by tape casting and coat-mix process", *J. Materials Processing Technology*, Vol. 92-93, 107-111, (1999)

[**91**] S.P. Jiang, S.H. Chan, "A review of anode materials development in solid oxide fuel cells", *J. Mat. Science*, Vol. 39 (14), 4405-4439, (2004)

[**92**] M. Cologna, V.M. Sglavo, "Sintering and Deformation of Solid Oxide Fuel Cells produced by Sequential Tape Casting", *Int. J. Appl. Ceram. Techn.*, Vol. 7 (6), 803-813, (2010)

[**93**] S.H. Lee, G. Messing, M. Awano, "Sintering Arches for Cosintering Camber-Free SOFC Multilayers", *J. Am. Ceram. Soc.*, Vol. 91 (2), 421-427, (2008)

[**94**] H. Frandsen, et al., "Modeling Sintering of Multilayers Under Influence Of Gravity", *J. Am. Ceram. Soc.*, Vol. 96 (1), 80-89, (2013)

[**95**] J. Malzbender, "Curvature and stresses for bi-layer functional ceramic materials", *J. of the Europ. Ceram. Society*, Vol. 30, 3407-3413, (2010)

[**96**] K. Mikeska, D, Schaefer, H. Jensen, „Method for reducing shrinkage during firing of green ceramic bodies", U.S. Patent No. 5,085,720, (1992)

[**97**] Th. Franco, et al., "Development of Metal-Supported Solid Oxide Fuel Cells", *ECS Transactions*, Vol. 35 (1), 147-155, (2011)

[**98**] L. Sigl, "Pulvertechnologie: Eine Quelle für innovative Energietechnik", *Pulvermetallurgie in Wissenschaft und Praxis*, compiled by H. Kolaska, Fachverband Pulvermetallurgie, Hagen, Band 28, 5-36, (2012)

[**99**] B. Tabernig, et al., „P/M FeCr Alloy as Interconnector and Substrate Materials for Metal Supported Solid Oxide Fuel Cells", in *Euro PM2011 Proceedings*, Barcelona, Spain, Vol. 3, p. 449, (2011)

[**100**] M. Santarelli, Course notes, International APT Course "Advances in Medium and High Temperature SOFC Technology, Udine, Italy, (2014)

[**101**] S.Strobl, H.Danninger: *PM-Verfahren zur Herstellung metallischer Zellularwerkstoffe*. Proc. 15th Int. Plansee Seminar, Reutte 2001, G.Kneringer, P.Rödhammer, H.Wildner eds., Plansee Holding AG, Reutte, Austria, Vol.3, 300-313, (2001)

[**102**] G. Davis, S. Zhen, "Metallic foams: their production, properties and applications", *Journal of Materials Science*, Vol. 18 (7), 1899-1911, (1983)

[**103**] W. Schatt, K.-P. Wieters, B. Kieback, *Pulvermetallurgie – Technologie und Werkstoffe*, Second Edition, Springer-Verlag, Berlin Heidelberg, (2007)

[**104**] http://www.gammatec.com/grobritannien-uk/densitometer/index.php

[**105**] M. Dlapka; PhD thesis, Vienna University of Technology (2011)

[**106**] Quantachrome Instruments, user manual, (2006)

[**107**] P. Schmidt, et al, Praxis der Rasterelektronenmikroskopie und Mikrobereichsanalyse, expert, Renningen-Malsheim, Germany, (1994)

[**108**] Leco CS230 Carbon/Sulfur Determinator, user manual, (2007)

[**109**] Leco TC400 Nitrogen/Oxygen Determinator, user manual, (2007)

[**110**] Porotec Pascal 140/240/440, user manual

[**111**] E.W. Washburn, Proc. Natl. Acad. Sci. USA, Vol. 7, p.115, (1921)

[**112**] T. Daniels, Thermal Analysis, Kogan Page, London, Ch.5, (1973)

[**113**] DIN-Norm 51005

[**114**] S. Paciornik and M. H: de Pinho Mauricio, "*Digital Imaging*", ASM Handbook Vol. 9 Metallography and Microstructure, p. 368-402, (2004)

[**115**] D: Simwonis, F. Tietz, D. Stöver, "Nickel coarsening in annealed Ni/YSZ abide substrate for solid oxde fuel cells, *Solid State Ionics*, Vol. 132 (3-4), 241-251, (2000)

[**116**] A. Lanzini, P. Leone, P. Asinari, "Microstructural characterization of solid oxide fuel cell electrodes by image analysis technique", *Journal of Power Sources*, Vol. 194, 408-422, (2009)

[**117**] T. Ferreira, W. Rasband, ImageJ User Guide, (2012)

[**118**] Kalss, G. et al., "Quantification of porosity of a powder metallurgical steel by image analysis", Prakt. Met. Sonderband,, Vol. 38, pp. 105 – 112, (2006)

[**119**] D. Caplan, M. Cohen, *J. Electrochem. Society*, Vol. 108, pp. 438, (1961)

[**120**] C.S. Tedmond Jr., *J. Electrochem. Society*, Vol. 113, pp. 766, (1966)

7. Appendix

7.1 List of abbreviation

AFC	Alkaline Fuel Cell
APS	atmospheric plasma spraying
APU	auxiliary power units
CGO	ceria doped gadolinium oxide
CHP	combined heat and power
CTE	thermal expansion coefficient
EVD	electrochemical vapor deposition
GDC	gadolinium doped ceria
HAB	Höganäs AB
IC	Interconnector
LSM	strontium doped lanthanum manganate
MCFC	Molten Carbonate Fuel Cell
MS-SOFC	metal supported SOFC
ODS	oxide dispersion strengthened
PAFC	Phosphoric Acid Fuel Cell
PEFC	Polymer Electrolyte Fuel Cell / Proton Exchange Membrane Fuel Cell
pl	powder loading
TPB	triple phase boundaries
SDZ	scandium doped zirconia
SEM	scanning electron microscope
SOFC	Solid Oxide Fuel Cell
TUW	Vienna University of Technology
UC3M	University of CarlosIII Madrid
YSZ	yttrium stabilized zirconia

7.2 Hg-Porosimetry

Pore size distribution (red graph) and cumulative pore volume (blue graph) of Fe25Cr20Ni2.5Si MIM sample (50 vol% powder loading); as sintered sample

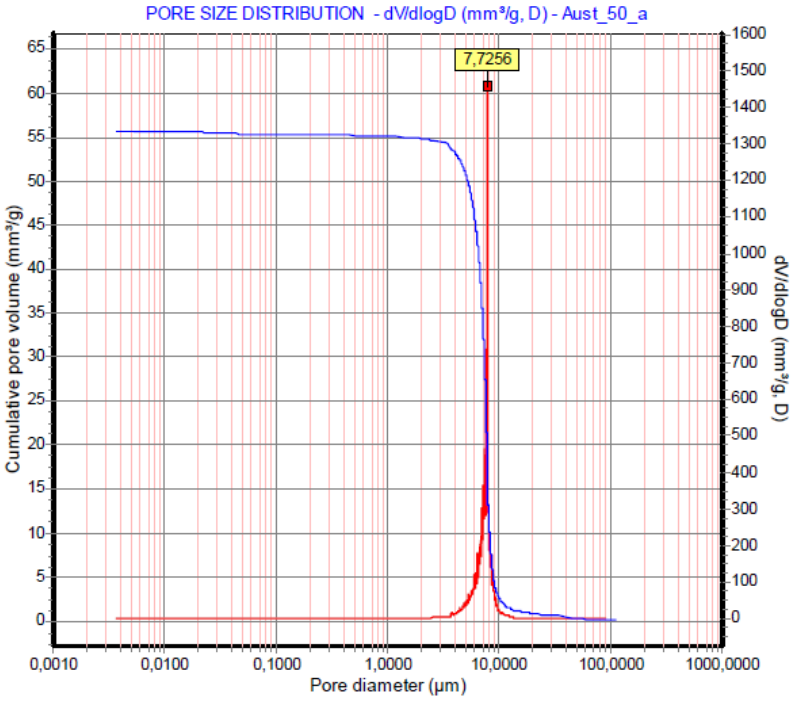

Pore size distribution (red graph) and cumulative pore volume (blue graph) of Fe25Cr20Ni2.5Si MIM sample (55 vol% powder loading); as sintered sample

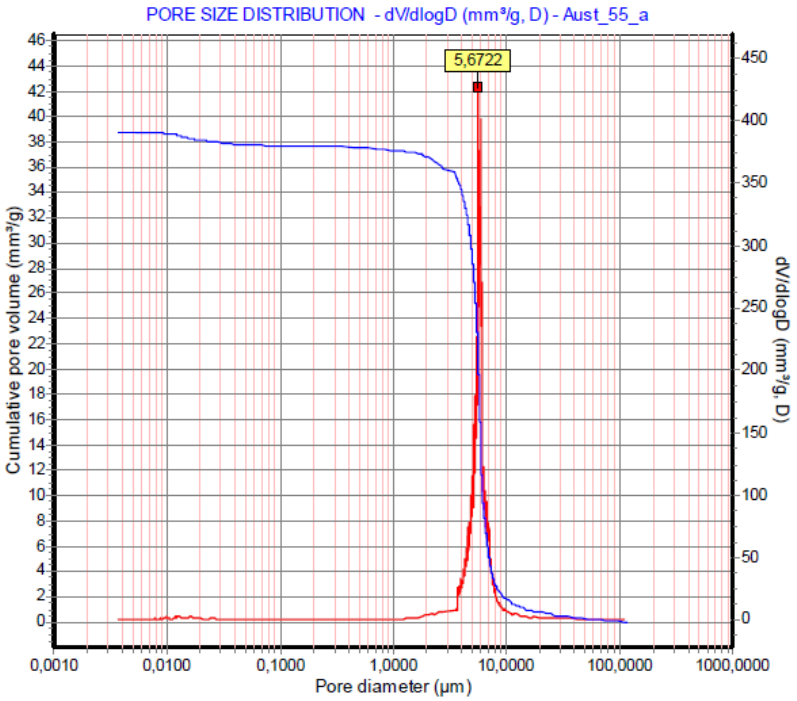

Pore size distribution (red graph) and cumulative pore volume (blue graph) of Fe16Cr MIM sample (45 vol% powder loading); as sintered sample

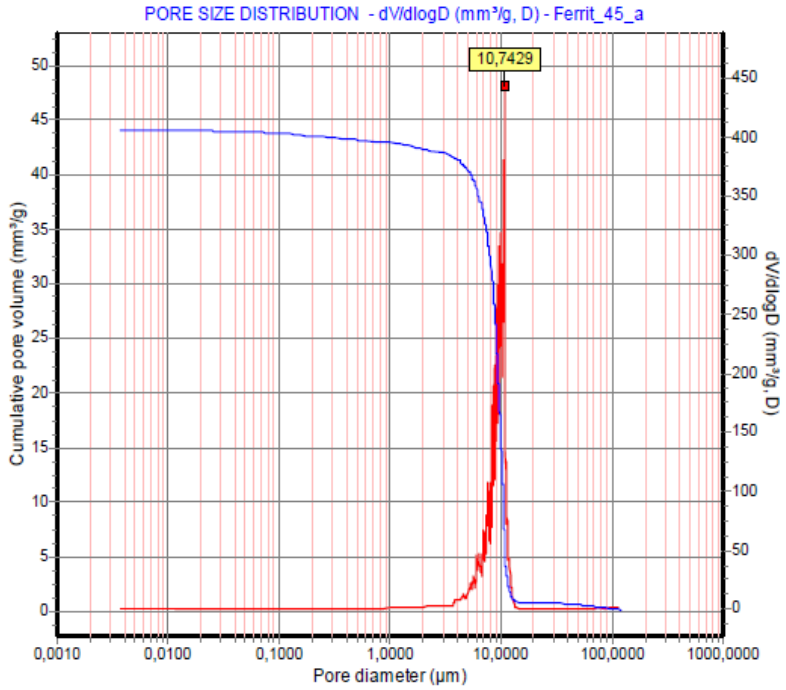

Pore size distribution (red graph) and cumulative pore volume (blue graph) of Fe16Cr MIM sample (50 vol% powder loading); as sintered sample

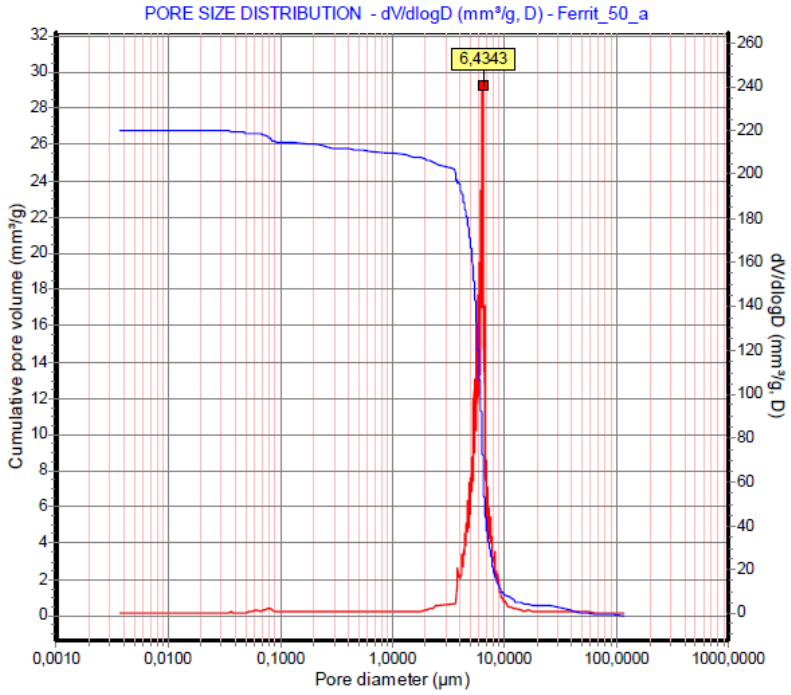

Pore size distribution (red graph) and cumulative pore volume (blue graph) of Fe16Cr MIM sample (55 vol% powder loading); as sintered sample

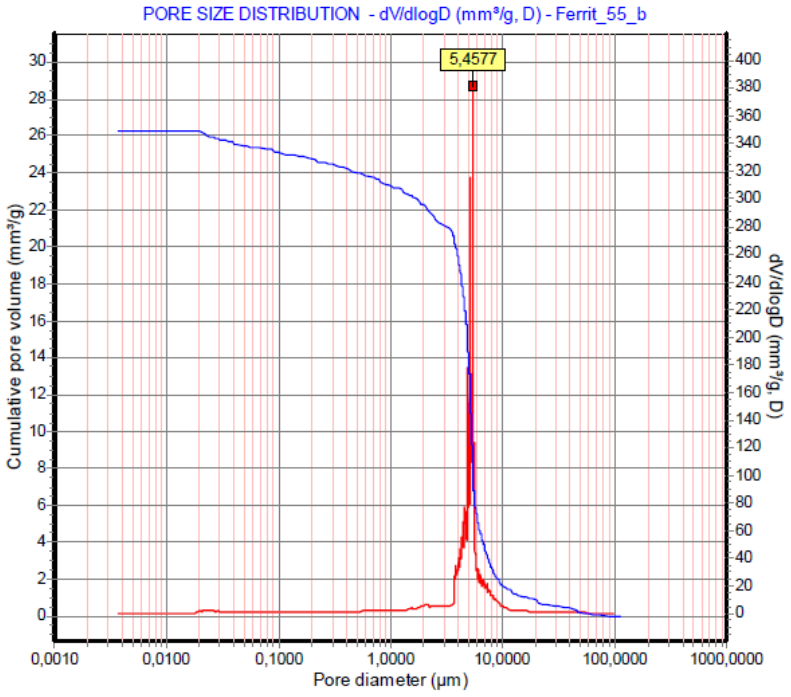

Pore size distribution (red graph) and cumulative pore volume (blue graph) of Fe21Cr gravity sintered sample (bulk initial state)

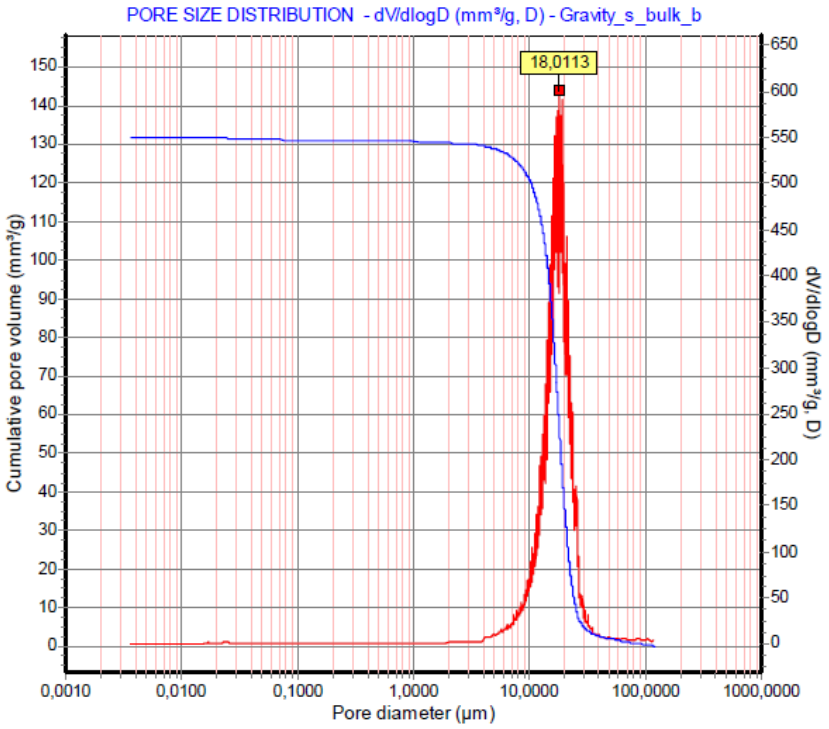

Pore size distribution (red graph) and cumulative pore volume (blue graph) of Fe21Cr gravity sintered sample (tapped initial state)

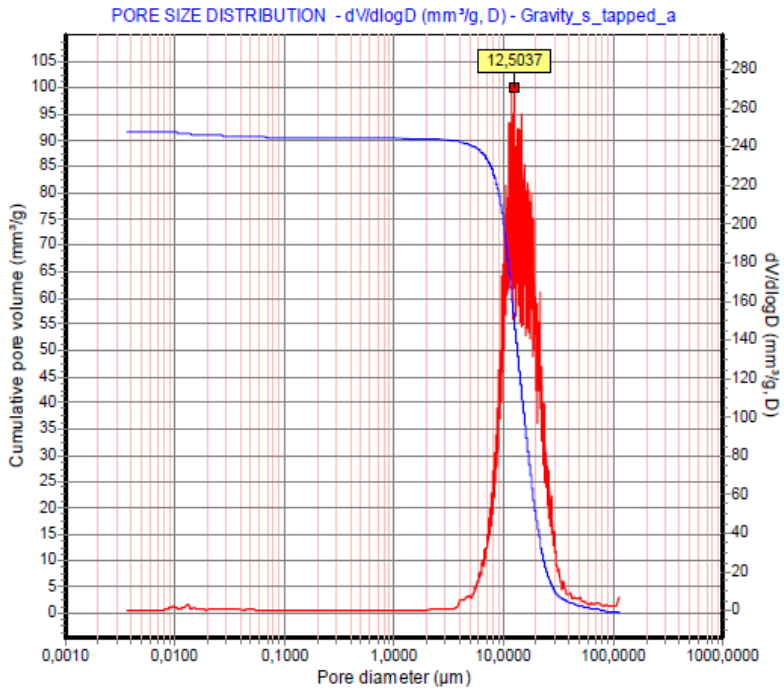

7.3 Dilatometer

Dilatometric graph of the Fe25Cr20Ni2.5Si (blue line) sample and first derivative (broken black line); double action pressed at 400 MPa (die wall lubricated); measurement perpendicular to the pressing direction, H_2-atmosphere

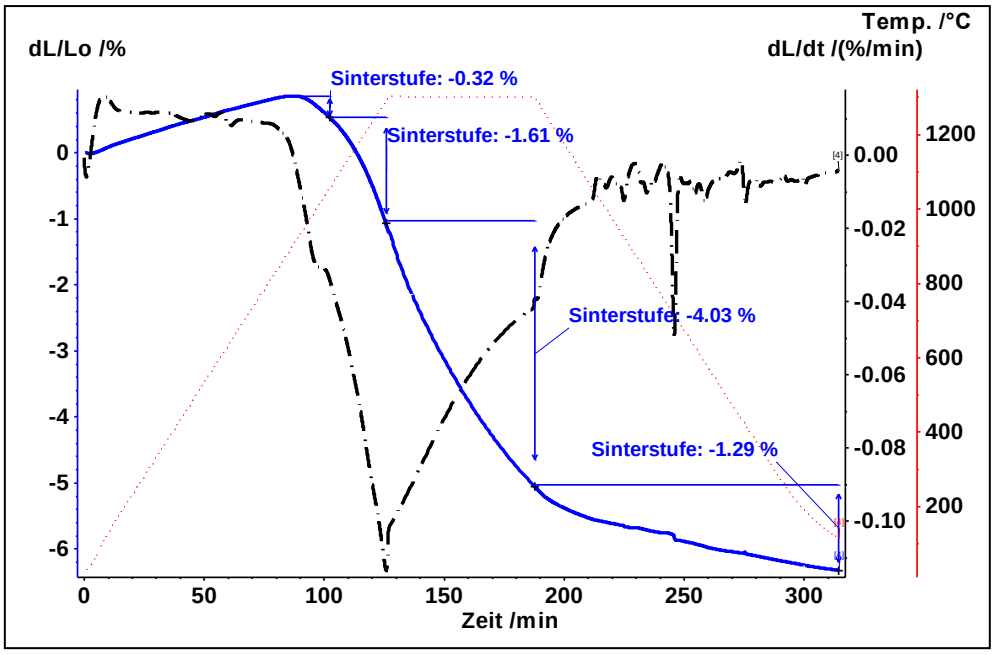

Dilatometric graph of the Fe18Cr0.3Mn0.5Nb (red line) sample and first derivative (broken black line); double action pressed at 400 MPa (die wall lubricated); measurement perpendicular to the pressing direction, H_2-atmosphere

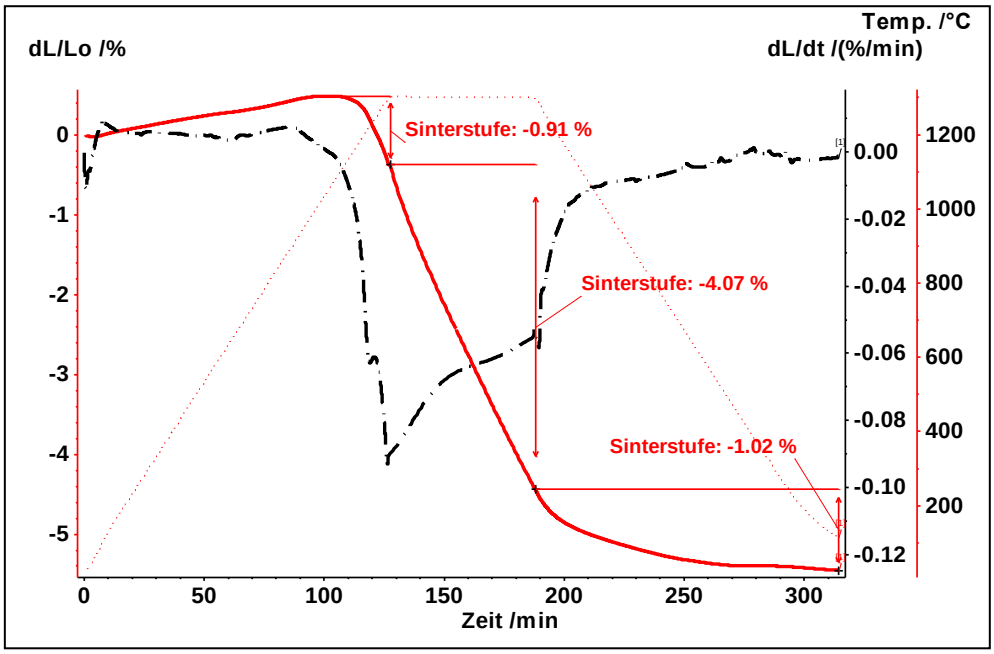

Dilatometric graph of the Fe21Cr (green line) sample and first derivative (broken black line); double action pressed at 400 MPa (die wall lubricated); measurement perpendicular to the pressing direction, H_2-atmosphere

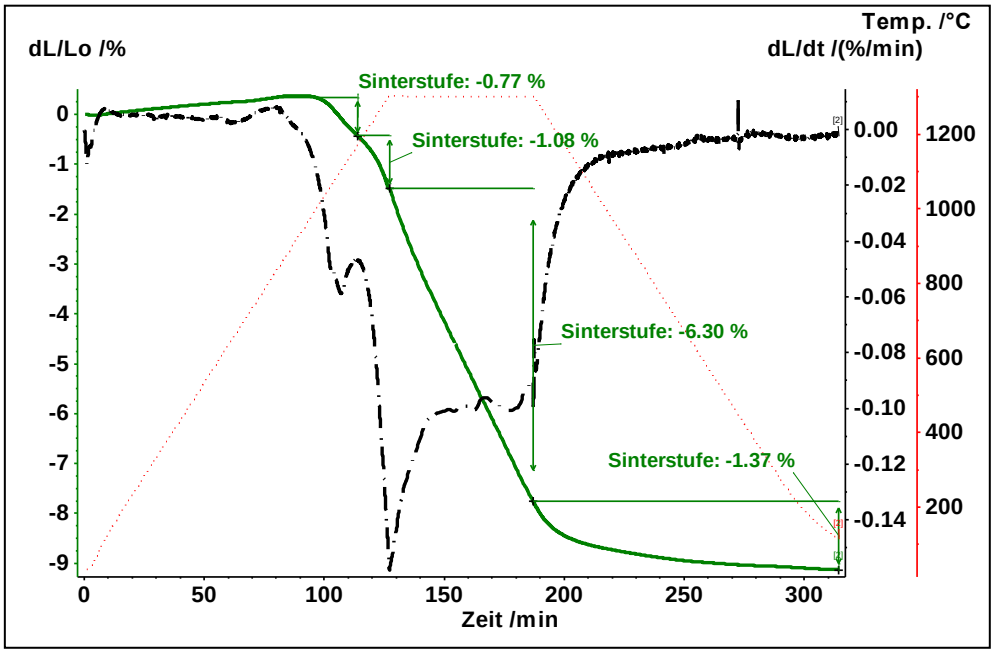

Dilatometric graph of the Fe21Cr0.5Nb (purple line) sample and first derivative (broken black line); double action pressed at 400 MPa (die wall lubricated); measurement perpendicular to the pressing direction, H_2-atmosphere

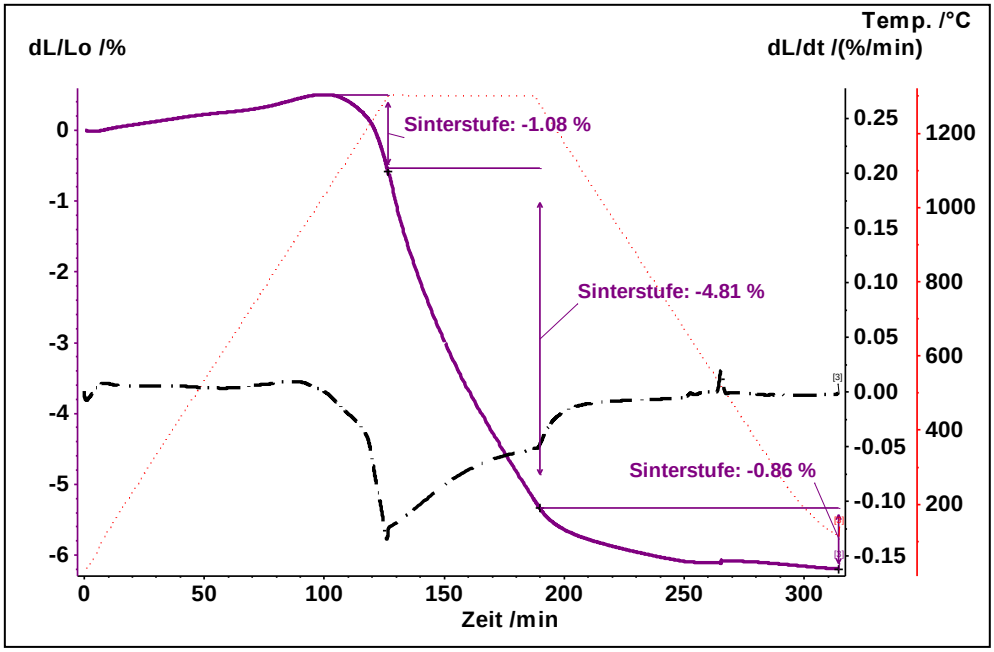

TG/DTA measurement of the Fe27Cr plate, annealed at 600°C, 1 h, wet hydrogen

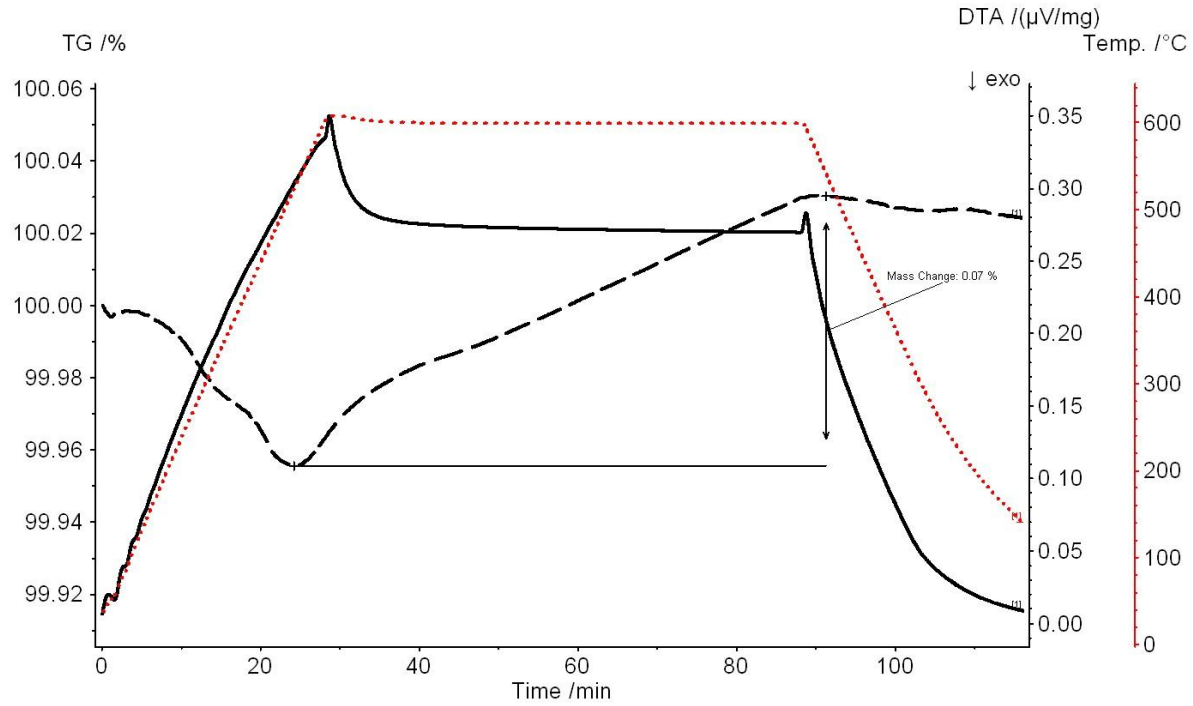

SEM images of the Fe27Cr plate, annealed at 600°C, 1 h, wet hydrogen

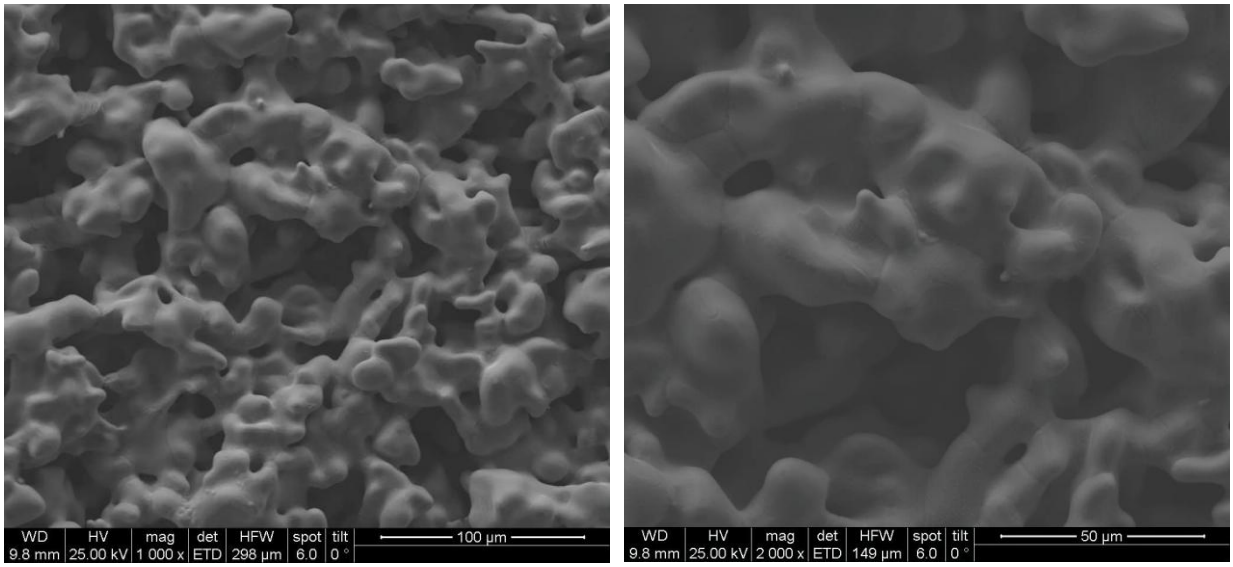

TG/DTA measurement of the Fe27Cr plate, annealed at 700°C, 1 h, wet hydrogen

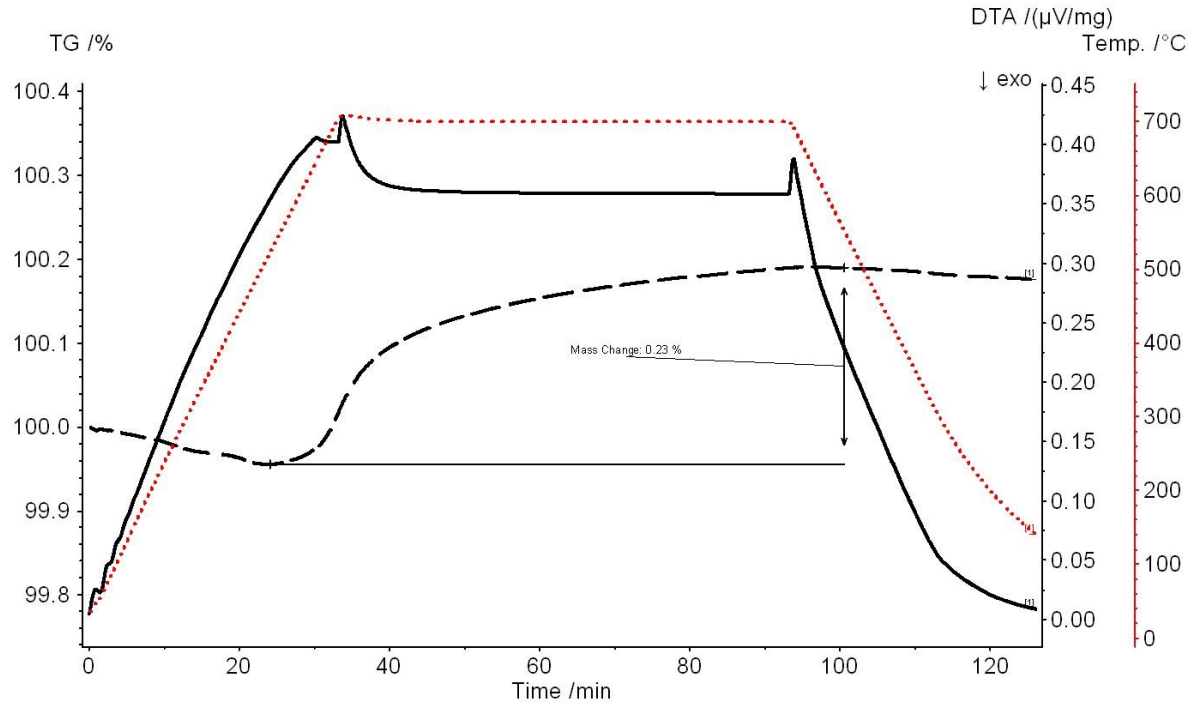

SEM images of the Fe27Cr plate, annealed at 700°C, 1 h, wet hydrogen

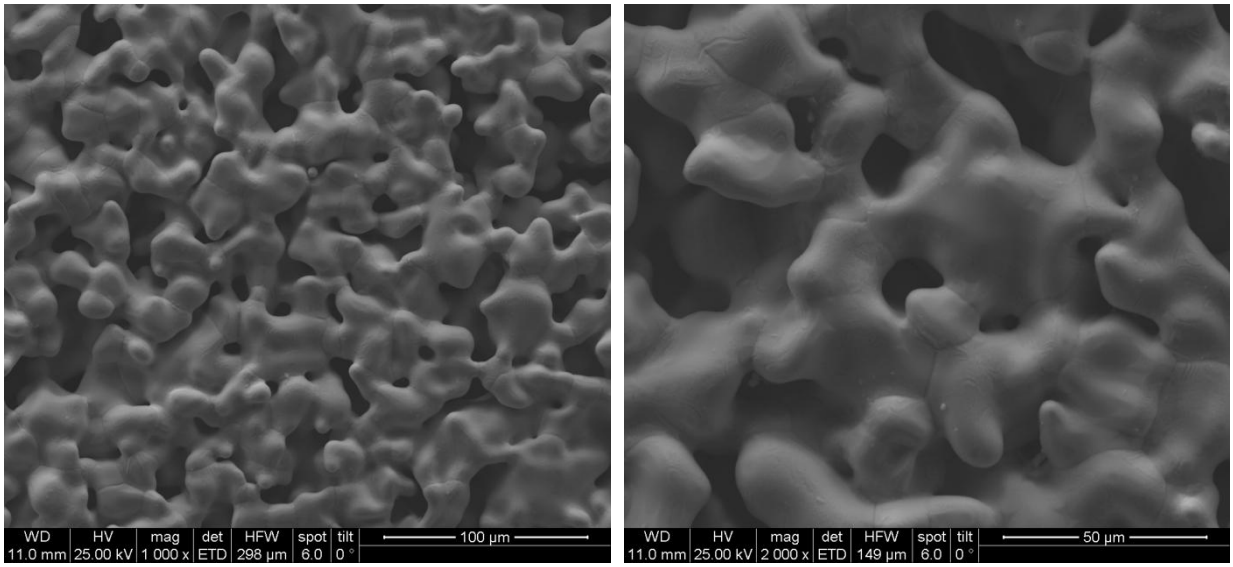

TG/DTA measurement of the Fe27Cr plate, annealed at 800°C, 1 h, wet hydrogen

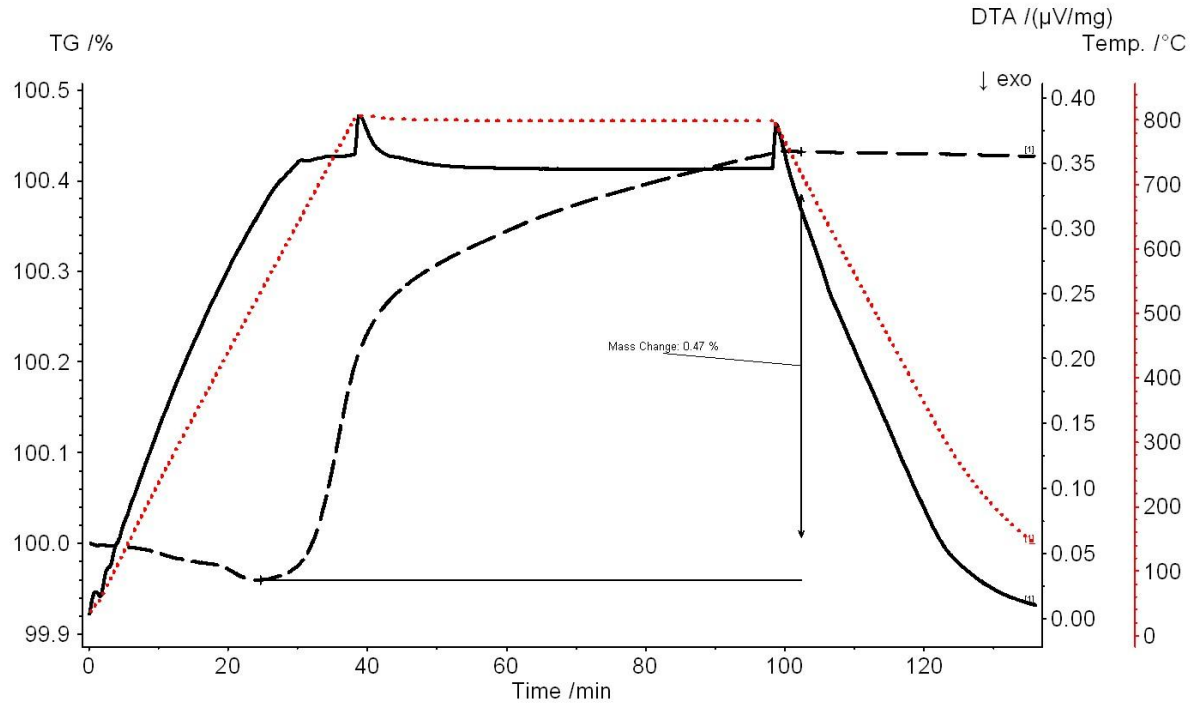

SEM images of the Fe27Cr plate, annealed at 800°C, 1 h, wet hydrogen

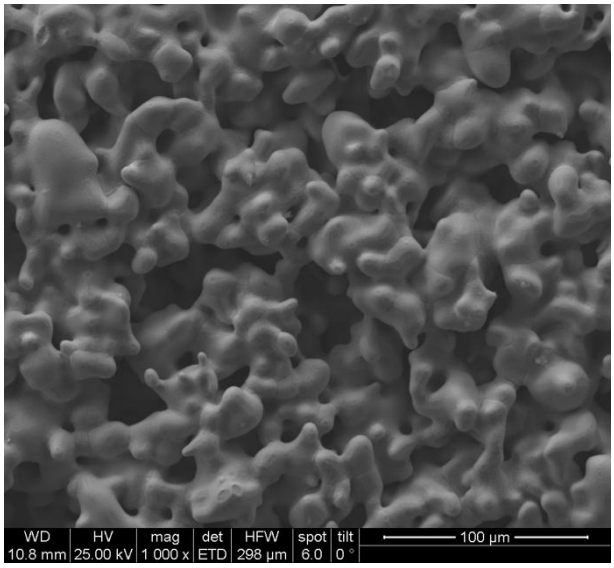

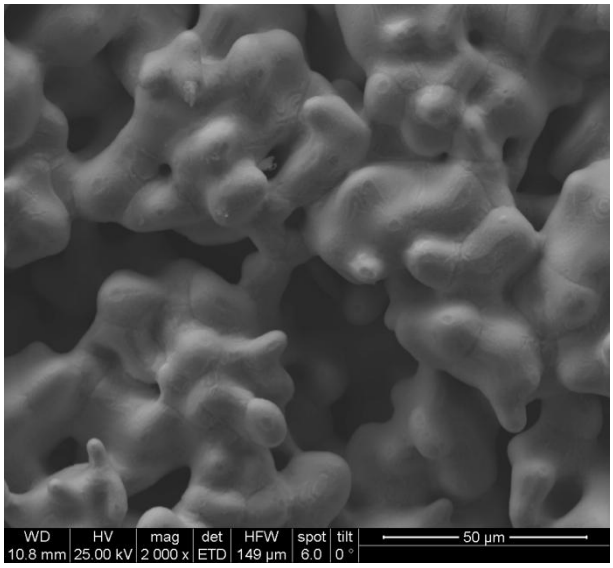

TG/DTA measurement of the Fe27Cr plate, annealed at 900°C, 1 h, wet hydrogen

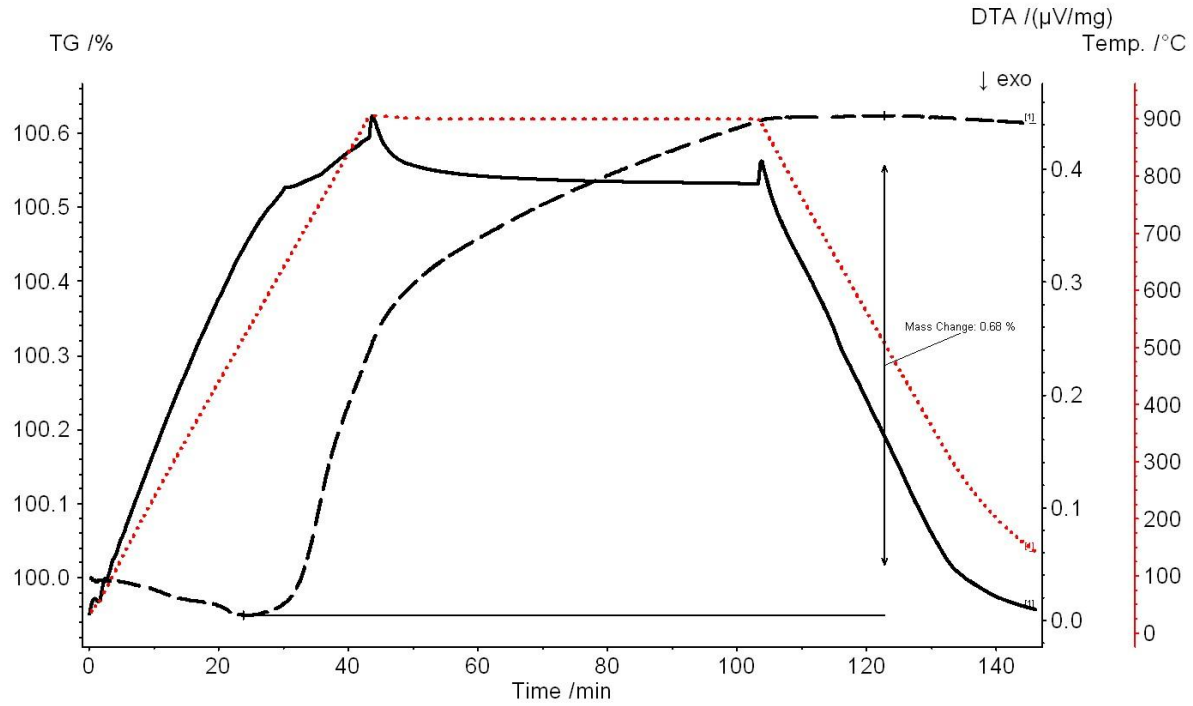

SEM images of the Fe27Cr plate, annealed at 900°C, 1 h, wet hydrogen

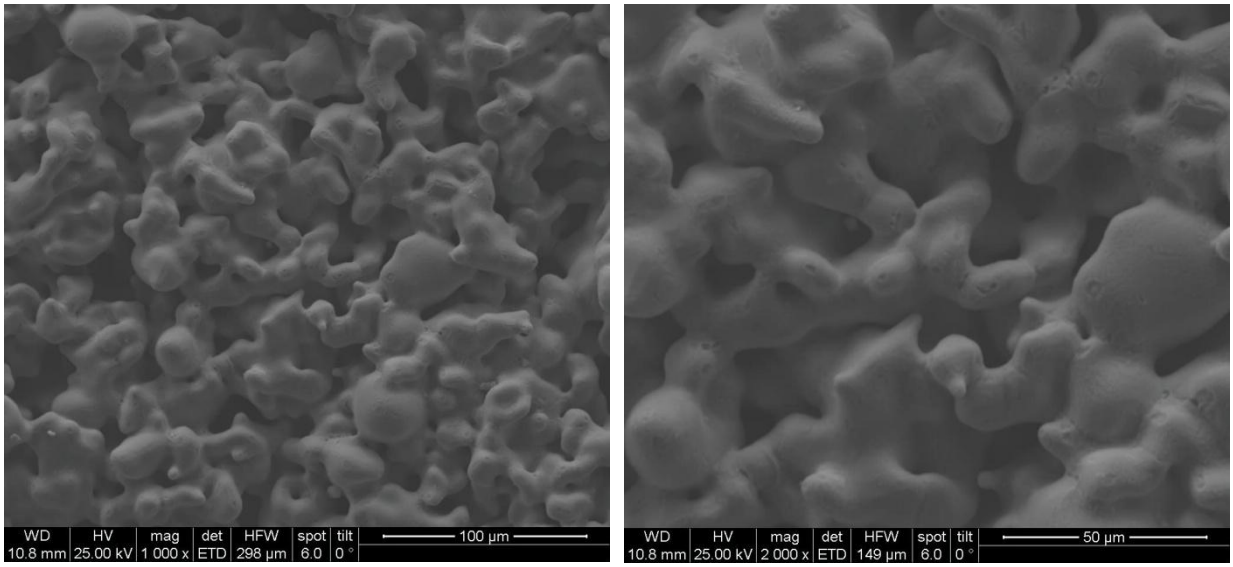

TG/DTA measurement of the Fe21Cr18Ni plate, oxidized at 600°C, 1 h, wet hydrogen

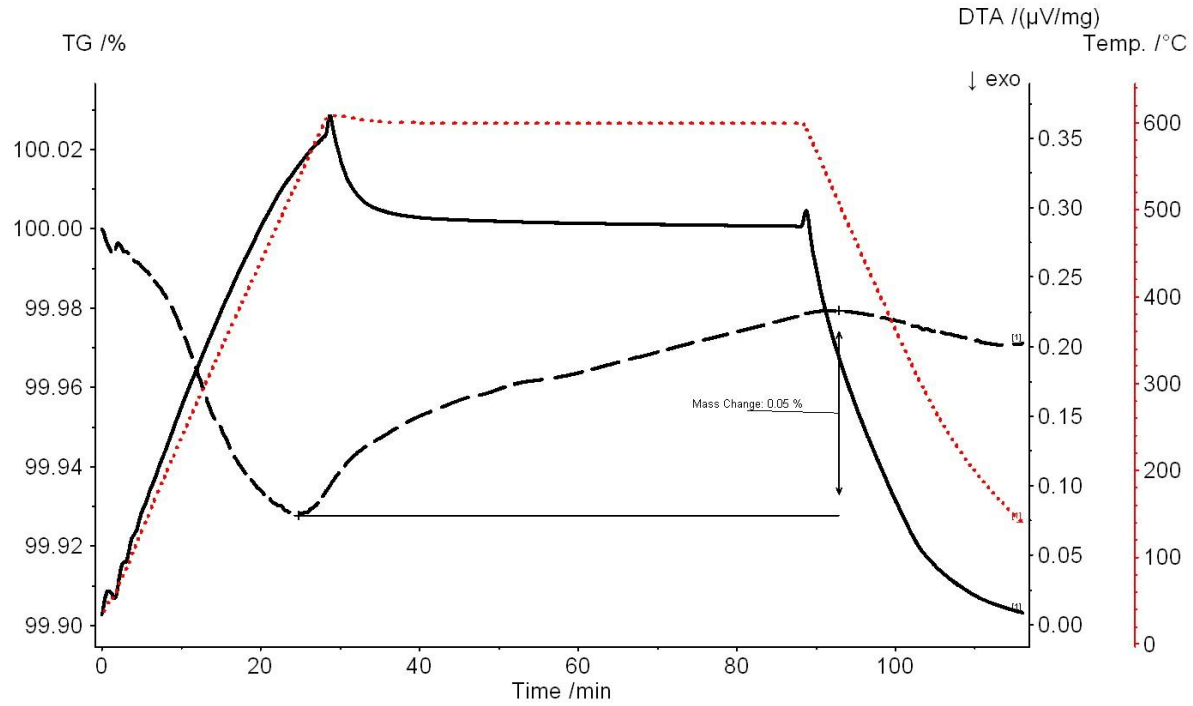

SEM images of the Fe21Cr18Ni plate, annealed at 600°C, 1 h, wet hydrogen

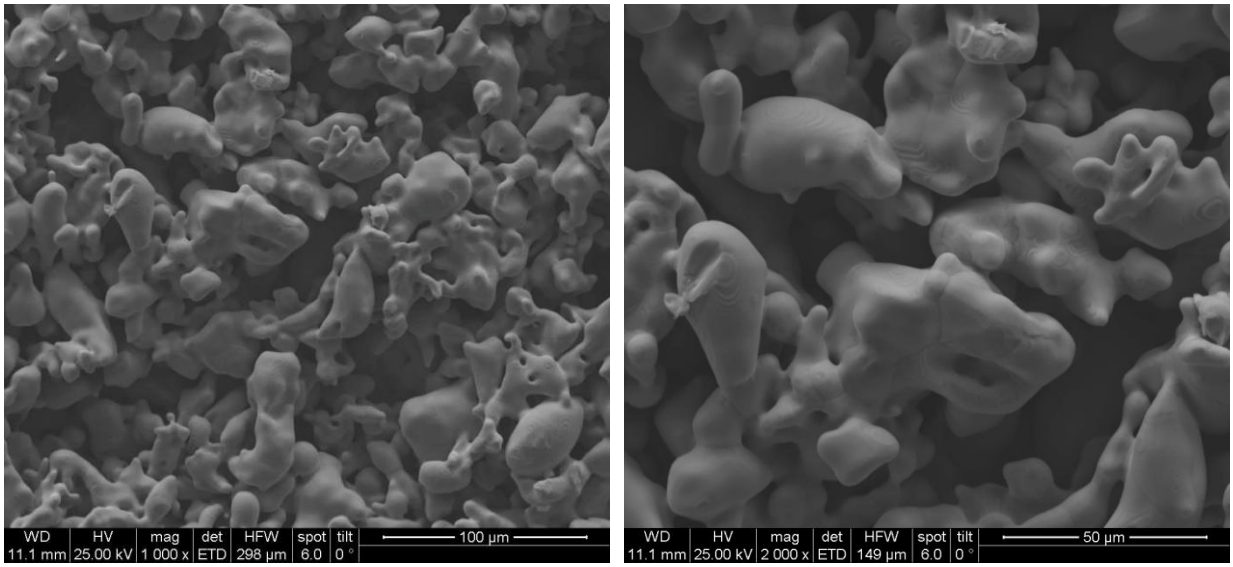

TG/DTA measurement of the Fe21Cr18Ni plate, annealed at 700°C, 1 h, wet hydrogen

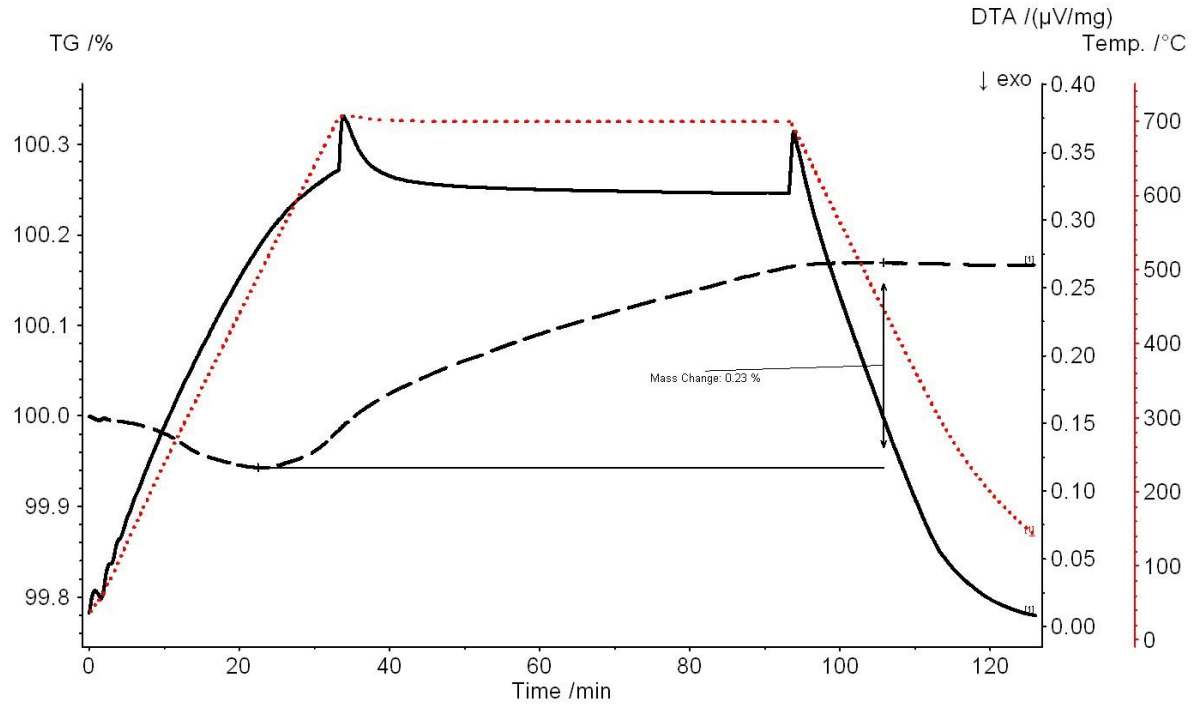

SEM images of the Fe21Cr18Ni plate, annealed at 700°C, 1 h, wet hydrogen

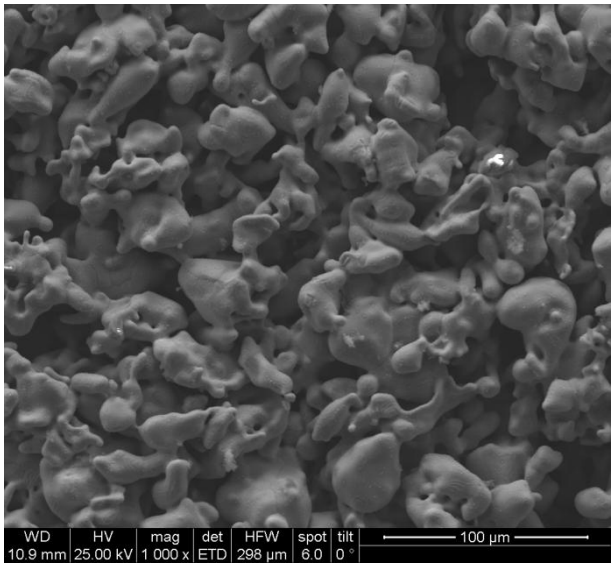

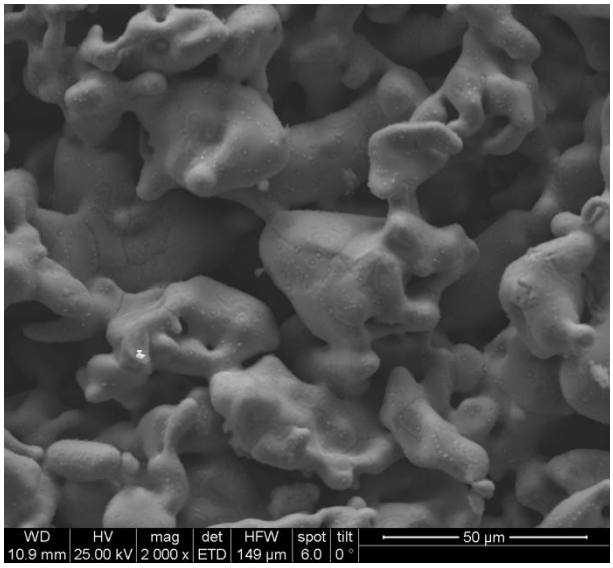

TG/DTA measurement of the Fe21Cr18Ni plate, annealed at 800°C, 1 h, wet hydrogen

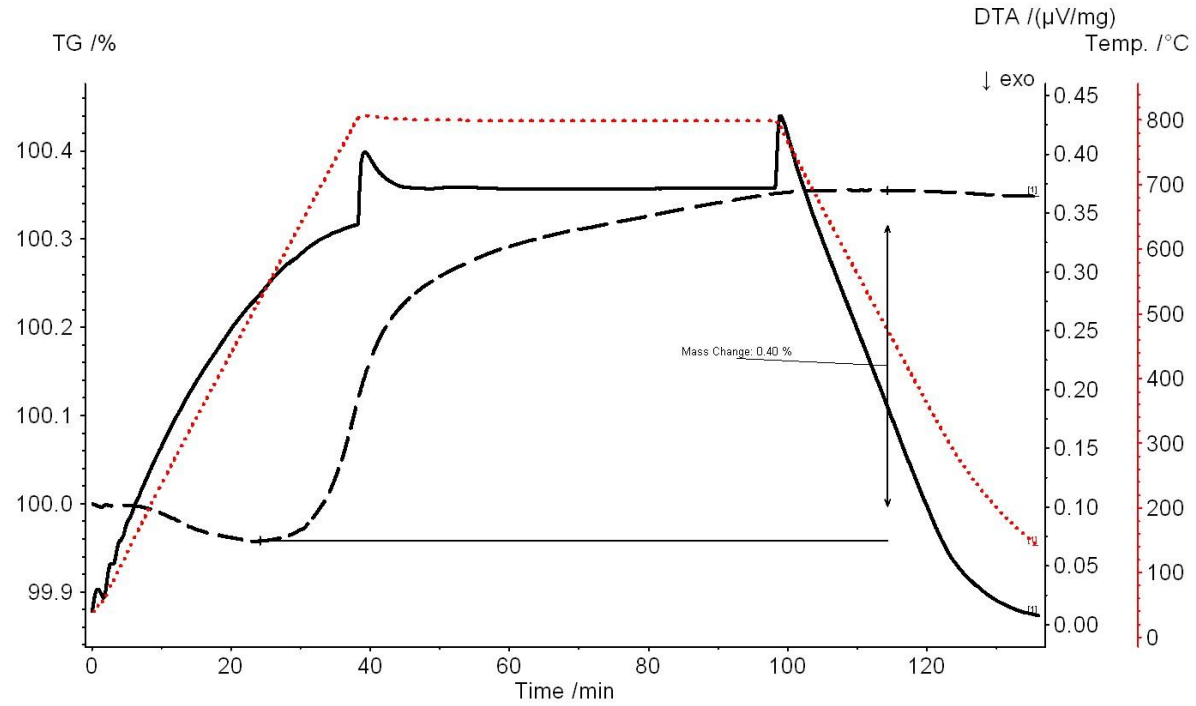

SEM images of the Fe21Cr18Ni plate, annealed at 800°C, 1 h, wet hydrogen

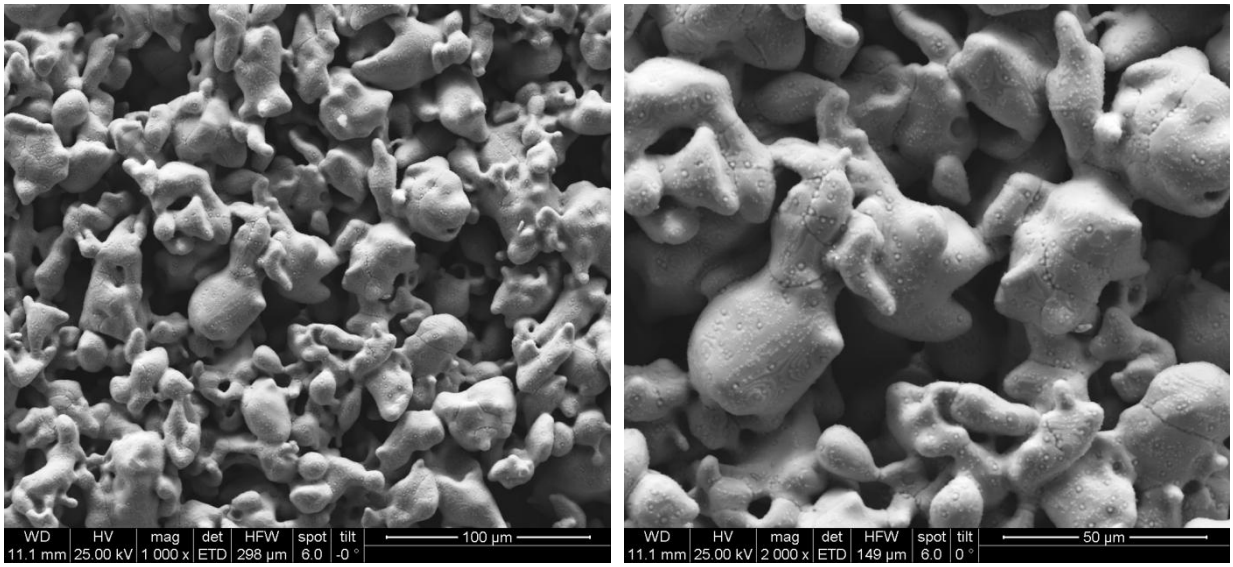

TG/DTA measurement of the Fe21Cr18Ni plate, annealed at 900°C, 1 h, wet hydrogen

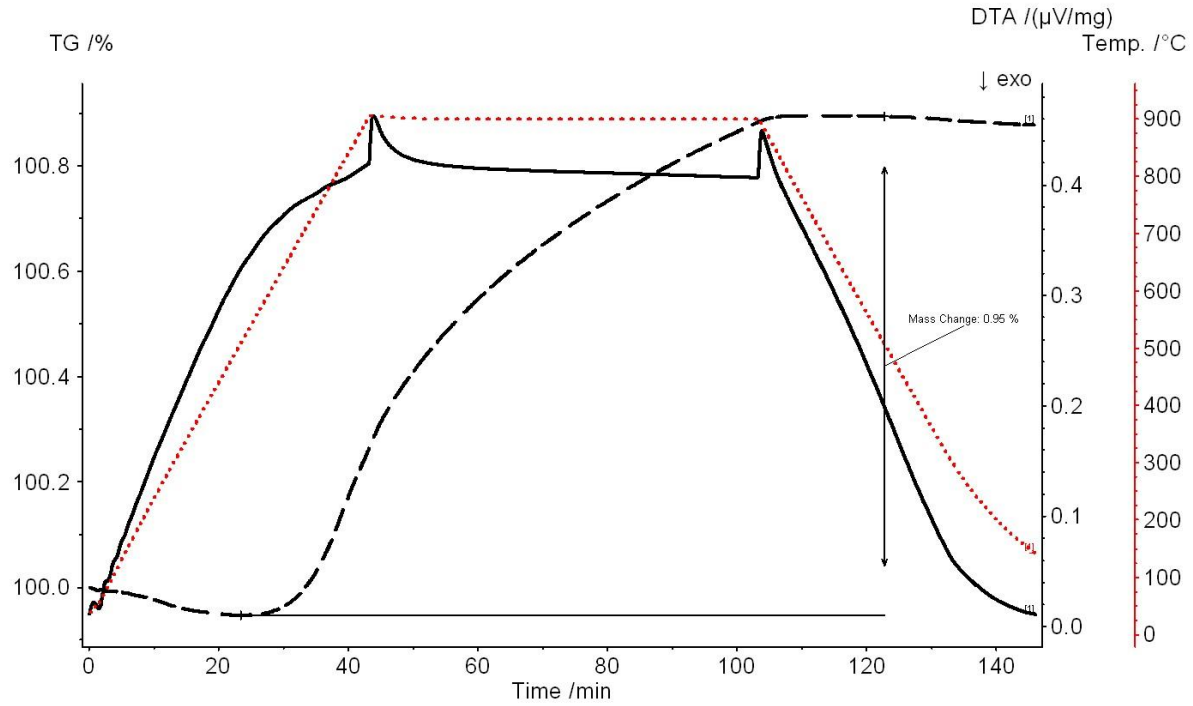

SEM images of the Fe21Cr18Ni plate, annealed at 900°C, 1 h, wet hydrogen